The regulation of 3-deoxy-D-*arabino*-heptulosonate 7-phosphate synthase from *Mycobacterium tuberculosis*

A thesis submitted in partial fulfilment
of the requirements for the degree
of
Doctor of Philosophy in Biochemistry
at the University of Canterbury
by
Nicola Jean Blackmore

September 2014

Acknowledgements

There are so many people who should be thanked for helping me get here that it is hard to know where to start. I will begin by thanking my supervisor Emily Parker for inspiring me to enter postgraduate study with her enthusiasm for science and for providing me the opportunity to work with her on such a fascinating project. Thanks to Emily and her research group I have learnt to survive and enjoy the world of scientific research and I have learnt a lot about myself along the way.

I wish to thank all the past and present members of the Parker group. I have really enjoyed getting to know you all and I consider myself incredibly fortunate over the last few years to work with so many amazing people who have made research fun and exciting. I cannot thank Frances, Tammie, Wanting, Richard, Sarah, Dmitri, Eric, Tom, Leah and Michael (an honorary office member) enough for making our office a haven for when research got tough and just simply enjoying life.

I owe a special thanks to all of those people who have collaborated on *Mtu*DAH7PS in the past and present. Particular thanks must go to Richard Hutton who kindly introduced me to the ways of the biochemistry lab and *Mtu*DAH7PS. Wanting Jiao who laid the groundwork for a considerable portion of this thesis through her computational studies and has proven to be a great friend. I must thank Sebastian Reichau for his work on *Mtu*DAH7PS, particularly the crystallography and Ali Nazmi for all his time running and analysing AUC samples.

Thank you to the many technical staff of the Chemistry and Biology Departments, who have analysed samples, fixed, ordered and made things and basically kept our lab functioning smoothly over the years. Thank you Grant Pearce for taking the time to teach me how to use several pieces of equipment housed in the biology department. Thank you to the members of the SAXS/WAXS and MX beamlines at the Australian Synchrotron for access to the beamlines and their invaluable expertise and the NZSG for the funding that made it possible.

I would like to acknowledge the funding I have received from the Maurice Wilkins Centre and the University of Canterbury that have made my postgraduate study possible. I would also like to thank BIC for supplying so many useful pieces of equipment.

One of the first people to offer friendship and support when I started my postgraduate career was Sarah Wilson-Coutts and I cannot thank her enough for all her support through the ups and downs of my research – and more importantly for introducing me to Sporcle and Simon's cat. I must also give a special mention to Michael Hunter who has helped me find my way though numerous scientific conundrums and for being one of the few people willing and able to discuss my research who does not actually work on *Mtu*DAH7PS. I would like to thank David Tran and Frances Huisman for their friendship and for reminding me there is a real world beyond the lab doors. Thank you to Gerd Mittlestaedt who has been incredibly kind and helpful to me and deserves special thanks for all his technical help and support.

I wish to thank my family for their support, in every sense of the word. Thank you to my Mum for her unwavering support in everything I do and for always being there when things got tough. Thank you to my Dad for being a Dad and always being there.

Finally, I want to thank Raweri for putting up with me for all these years. We have experienced many highs and lows (and a few hundred shakes) together and I have never once wanted any one but you at my side. You constantly inspire me to better myself and have made me a better person in every way and I am forever grateful to you.

Abstract

Allosteric regulation of important enzymes is a mechanism frequently employed by organisms to exert control over their metabolism. The work presented in this thesis focused on further developing our understanding of the sophisticated synergistic regulation of the 3-deoxy-D-*arabino*-heptulosonate 7-phosphate synthase (DAH7PS) from *Mycobacterium tuberculosis*.

The shikimate pathway is ultimately responsible for the biosynthesis of the aromatic amino acids in plants, microorganisms and apicomplexans. DAH7PS catalyses the first committed step of the shikimate pathway. Chorismate mutase (CM) is positioned at a critical branch point of the aromatic amino acid biosynthetic pathway and is the first committed step toward the biosynthesis of Phe and Tyr. Due to the critical position of these two enzymes, the activity of DAH7PS and CM are often tightly feedback regulated in order to control the flux of metabolites through the pathway. The shikimate pathway is absent in mammals making the enzymes of the pathway excellent targets for the development of novel antimicrobial drugs for pathogens such as *M. tuberculosis*, the causative agent of tuberculosis.

The kinetic and biophysical characterisation of the DAH7PS from *M. tuberculosis* (*Mtu*DAH7PS) described in Chapter 2 of this thesis, revealed for the first time that *Mtu*DAH7PS is subject to synergistic feedback regulation by all three aromatic amino acids. Structural characterisation of *Mtu*DAH7PS revealed that *Mtu*DAH7PS exists as a mixture of oligomeric species with the homotetrameric species favoured as the protein concentration increases.

The feedback regulation of the *Mtu*DAH7PS is highly sophisticated; *Mtu*DAH7PS activity is only inhibited when Trp is present in combination with either Phe or Tyr. Crystallographic studies of *Mtu*DAH7PS have shown the aromatic amino acids bind to three distinct allosteric binding sites. Designated here as the Trp site, site 1 and site 2. Trp has only been observed to occupy the Trp site, but Phe and Tyr have been observed to occupy both site 1 and site 2. Site-directed mutagenesis (SDM) was used to generate two *Mtu*DAH7PS variants with an amino acid substitution at either site 1

(Arg171Ala) or site 2 (Arg256Ala), in order to disrupt ligand binding. The results of the functional analysis of these two variants are described in Chapter 3. Kinetic analysis revealed Phe binding to site 1 was required for the regulatory response of *Mtu*DAH7PS to Trp and Phe, and that Tyr binding to site 2 was required for the proper regulatory response to Trp and Tyr. Biophysical analysis showed Tyr could bind to both site 1 and site 2, but Tyr had a greater affinity for site 2. Phe only displayed a significant affinity for site 1. These observations have lead to the designation of site 1 as the Phe-selective binding site and site 2 as the Tyr selective binding site.

*Mtu*DAH7PS can form a non-covalent complex with *Mtu*CM, boosting *Mtu*CM activity by more than 100-fold and endowing *Mtu*CM with regulatory sensitivity to Phe and Tyr. Chapter 4 describes the functional and structural characterisation of the interaction of *Mtu*DAH7PS with *Mtu*CM. *Mtu*DAH7PS was also found to endow *Mtu*CM with synergistic regulatory sensitivity when Trp was added in combination with Phe or Tyr. The functional and biophysical characterisation of the interaction of *Mtu*CM with the two *Mtu*DAH7PS variants used in the studies presented in Chapter 3 were also used to show that the allosteric binding sites of *Mtu*DAH7PS were responsible for the synergistic regulation of *Mtu*CM. The results from analytical ultracentrifugation (AUC), native polyacrylamide gel electrophoresis (PAGE) and kinetic analysis found that the binding of Phe lowered the affinity of *Mtu*DAH7PS for *Mtu*CM and resulted in poorer activation of *Mtu*CM activity.

Crystallographic studies have shown the binding of the aromatic amino acids to *Mtu*DAH7PS do not cause a significant change in the conformation of *Mtu*DAH7PS. Molecular dynamics (MD) simulations reveal the synergistic regulation of *Mtu*DAH7PS by Trp and Phe is likely to be primarily entropically driven, mediated by subtle changes in the molecular dynamics of the substrate and allosteric binding sites to facilitate aromatic acid binding at other allosteric binding sites or disfavour erythrose 4-phosphate (E4P) binding at the active site. Statistical coupling analysis (SCA) was combined with MD simulations to predict a cluster of residues that may be involved in transmitting ligand occupancy between allosteric binding sites and to the active site. Four of these residues were selected for substitution via SDM. The structural and functional characterisation of these four *Mtu*DAH7PS

variants, described in chapter 5, found that all four residues play a role in the transmission of regulatory signals of *Mtu*DAH7PS validating the computational studies.

SDM was also used to produce two *Mtu*DAH7PS variants that contained an amino acid substitution (Lys123Met or Asn237Ala) at the Trp site as described in Chapter 6. These modifications to the Trp site were found to disrupt the quaternary structure equilibrium of *Mtu*DAH7PS. Kinetic and biophysical analysis found that the synergistic regulation of *Mtu*DAH7PS had been disrupted but that sensitivity to Phe and Tyr had been enhanced.

The substitution of several residues resulted in the disruption of the homotetrameric structure of *Mtu*DAH7PS, providing a serendipitous opportunity to study the structural and functional properties of the *Mtu*DAH7PS dimer. The kinetic characterisation described in Chapter 7 found the catalytic efficiency and regulation of the dimeric *Mtu*DAH7PS variants was severely compromised.

All the results presented in this thesis are discussed in Chapter 8. Overall this work has emphasised the remarkable complexity by which *Mtu*DAH7PS is regulated and its unusual ability to share its sophisticated regulatory machinery with *Mtu*CM.

Table of contents

List of abbreviations

ACT	aspartate kinase-chorismate-mutase-tyrA
Ala (A)	Alanine
AMP	Ampicillin
Arg (R)	Arginine
Asn (N)	Asparagine
Asp (D)	Aspartic acid
AUC	Analytical ultracentrifugation
bp	Base pairs
BSA	Bovine serum albumin
BTP	1,3-*bis*(tris(hydroxymethyl)methylamino)propane
CAM	Chloramphenicol
CD	Circular dichroism
CM	chorismate mutase
Cys (C)	Cysteine
DAH7P	3-deoxy-D-*arbino*-heptulosonate 7-phosphate
DAH7PS	3-deoxy-D-*arbino*-heptulosonate 7-phosphate synthase
DNA	Deoxy-ribose nucleic acid
DSF	Differential scanning fluorimetry
E4P	D-Erythrose 4-phosphate
EDTA	Ethylenediamine tetra-acetic acid
ESI-MS	Electrospray ionisation mass spectrometry
FPLC	Fast protein liquid chromatography
Gln (Q)	Glutamine
Glu (E)	Glutamic acid
Gly (G)	Glycine
GST	glutathione *S*-transferase

HCl	Hydrochloric acid
His (H)	Histidine
Ile (I)	Isoleucine
IMAC	Immobilised metal affinity chromatography
IPTG	Isopropyl-1-thio-β-D-galactopyranoside
ITC	Isothermal titration calorimetry
k_{cat}	Turnover number
KDO8PS	3 Deoxy-D-*manno*-octulosonate 8-phosphate
K_m	Michaelis-Menten constant
KNF	Koshland-Nemethy-Filmer
LB	Lysogeny broth
Leu (L)	Leucine
Lys (K)	Lysine
MD	Molecular dynamics
MDR-TB	Multidrug resistant TB
Met	Methionine
$MnSO_4$	Manganese sulphate
MW	Molecular weight
MWC	Monod-Wyman-Changeux
MWCO	Molecular weight cut-off
NaCl	Sodium chloride
NaOH	Sodium hydroxide
NMR	Nuclear magnetic resonance
OD	Optical density
PAGE	Polyacrylamide gel electrophoresis
PCR	Polymerase chain reaction
PDB	Protein Data Bank
PEP	Phosphoenolpyruvate
Phe (F)	Phenylalanine

Pro (P)	Proline
RMSD	Root-mean square deviation
RNA	Ribonucleic acid
RPM	Revolutions per minute
SAXS	Small angle X-ray scattering
SCA	Statistical coupling analysis
SDM	Site-directed mutagenesis
SDS	Sodium dodecyl sulphate
SEC	Size exclusion chromatography
Ser (S)	Serine
SOC	Super optimal broth
TAE	Tris base-acetic acid-EDTA
TB	Tuberculosis
TCEP	Tris(2-carboxyethyl)phosphine
TEV	Tobacco etch virus
Thr (T)	Threonine
TIM	Triose phosphate isomerase
Trp (W)	Tryptophan
Tyr (Y)	Tyrosine
UV	Ultraviolet
Val (V)	Valine
WAXS	Wide angle X-ray scattering
WHO	world health organisation
XDR-TB	Extensively drug resistant T

Index of figures

Index of tables

Publications

- **Blackmore, N. J**.; Reichau, S**.**; Jiao, W.; Hutton, R. D.; Baker, E. N.; Jameson, G. B.; Parker, E. J., Three sites and you are out: ternary synergistic allostery controls aromatic amino acid biosynthesis in *Mycobacterium tuberculosis*. *J. Mol. Biol.* **2013**, *425* (9), 1582-1592.

- Webby, C. J., Jiao, W., Hutton, R. D., **Blackmore, N. J**., Baker, H. M., Baker, E. N., Jameson, G. B., and Parker, E. J. Synergistic allostery, a sophisticated regulatory network for the control of aromatic amino acid biosynthesis in *Mycobacterium tuberculosis*, *J. Biol. Chem.* **2010** *285*, 30567-30576.

1. Introduction

All living cells are dependent on the wide range of enzyme-catalysed chemical reactions for their survival. Biological pathways are a series of chemical reactions responsible for the formation of a particular product or which lead to a specific cellular change. Typically biological pathways are responsible for the biosynthesis of necessary metabolites or the degradation of potentially harmful chemicals. Every living cell possesses a huge array of integrated biological pathways, which need to be tightly controlled to ensure that the rates of these chemical reactions are appropriate to meet cellular needs. Regulation of these biological pathways is achieved chiefly by either directly controlling the enzymatic activity of critical enzymes along the pathways or by controlling the expression of the genes that encode the enzymes. Regulation of enzymatic activity is commonly accomplished by either covalent modification of the enzyme, the use of inactive enzymatic precursors, called zymogens, or by allosteric regulation of the enzyme.[1-3]

1.1. Allostery

Allosteric regulation is generally defined as the activation or inhibition of protein functionality by non-covalent interactions with an effector molecule(s). The term allostery is derived from *allos* meaning "other" and *stereos* meaning "solid", in reference to an effector molecule binding to a site on the enzyme remote from the active site.[2,4] In general terms the binding of the effector molecule to the allosteric binding site of an enzyme confers some change that affects enzyme activity at the remote active site.[2,4] Allostery is a general property of proteins and non-enzyme proteins, such as cell receptors, and metabolite binding proteins can also display allostery with the binding of an allosteric effector conferring some change that affects another site responsible for protein function. The concept of allostery can also be broadened to include the interactions between the similar sites on a multisubunit protein, which is sometimes referred to as cooperativity.[2] There are two classical models used to describe allostery: the MWC model and the KNF model. These models have evolved and in

some cases merged as our understanding of allostery has grown leading to new models such as the morpheein and dynamic energy landscape models of allostery.[5,6]

1.1.1. Monod-Wyman-Changeux (MWC) model

The first proposed model of allostery was put forward by Monod Wyman and Changeux, after whom it was named.[7] The model was proposed based on correlating the structural organisation of a protein with observed cooperativity.[7,8] The model states that in the absence of ligand an oligomeric protein exists as an equilibrium between two conformational states usually referred to as the relaxed (R) and tense (T) states.[4,7,8] The addition of an effector molecule perturbs this equilibrium to favour a particular state with a higher affinity for the effector (Figure 1.1).

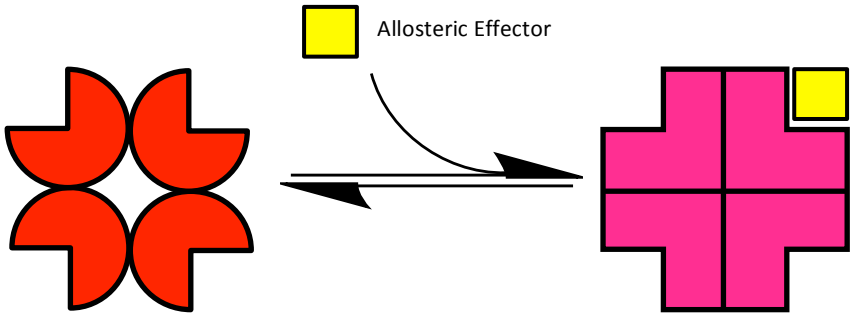

Figure 1.1 Schematic of MWC model of allostery. A symmetric oligomeric protein can either exist in a relaxed (R) or tense (T) conformational state. These two conformational states may vary in their affinity for the allosteric effector.

This model also assumes the subunits of a protein are arranged together so as the oligomeric state of the protein possesses at least one axis of symmetry. The model also assumes all (or none) of the subunits of the protein undergo the transition between the R and T states in a concerted manner, thus conserving the symmetry of the enzyme (Figure 1.1). Consequently this model is also referred to as the concerted model.

1.1.2. Koshland-Némethy-Filmer (KNF) model

A year after the MWC was proposed the KNF model of allostery was put forward by Koshland, Némethy and Filmer.[9] This model was derived from the concept of induced fit theory, where the binding of an effector molecule causes a change in the protein's structure to accommodate the effector molecule.[4,9,10] In the KNF model the binding of an effector to a protein subunit induces conformational change to that subunit to enable the effector to bind (Figure 1.2). [4,9,10] This conformational change that occurs at the subunit to which the effector bound can also induce changes to other subunits, which affect effector binding at those subunits. [1,4,9,10] For this reason the KNF model is commonly referred to as the sequential model of allostery.[1,4,10]

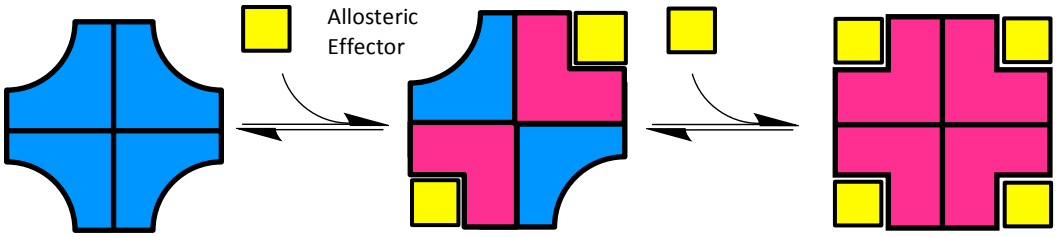

Figure 1.2 Schematic of the KNF model of allostery. The subunit of an oligomeric enzyme undergoes conformational change to facilitate the binding of an allosteric effector. This conformational change induces changes in other subunits affecting effector binding and/or substrate binding at other subunits.

The KNF model assumes that one conformation will only exist in the absence of ligand and that a second conformation will only exist when an effector molecule binds to the protein and induces a change to the structure of the protein (Figure 1.2).[1,4,9,10] The change that occurs at one subunit due to effector binding can make changes to other subunits take place more readily but this change is not propagated to all associated subunits as proposed in the MWC model. Furthermore the KNF model does not require all the subunits of an protein to adopt the same conformation, thus the protein does not need to be symmetrical.[1,2] Moreover the KNF model introduces the idea that a protein can occupy different conformations between the initial and final states of a conformational equilibrium.[11]

The KNF model allows for both positive and negative heterotropic and homotropic effects on effector (and substrate) binding.[1] Molecules that influence the binding of different molecules to a protein have a heterotropic effect, whereas molecules that influence the binding of the same molecules to

the protein have a homotropic effect. This is particularly advantageous when considering negative cooperativity, which is when the binding of an effector to one protein subunit may cause changes in other subunits that decrease the affinity of the protein for the effector, encumbering effector binding.[1,4,9,10]

1.1.3. Morpheein model

The morpheein model of allostery can be viewed as an extension of the MWC and KNF models of allostery and proposes that an oligomeric protein dissociates into smaller subunits. Jaffe coined the term morpheein in 2005 to describe homooligomeric proteins that reversibly dissociate and change conformation in their dissociated state.[5,12] The morpheein model of allostery requires the dissociated state of the homooligomeric protein to undergo a conformational change and may reassemble to form another structurally and functionally distinct oligomer (Figure 1.3).[5,12] In the morpheein model of allostery all subunit forms are accessible in the presence and absence of an allosteric effector, but the allosteric effector may shift the position of the dynamic equilibrium between the different conformational states to favour a particular oligomeric state.[12]

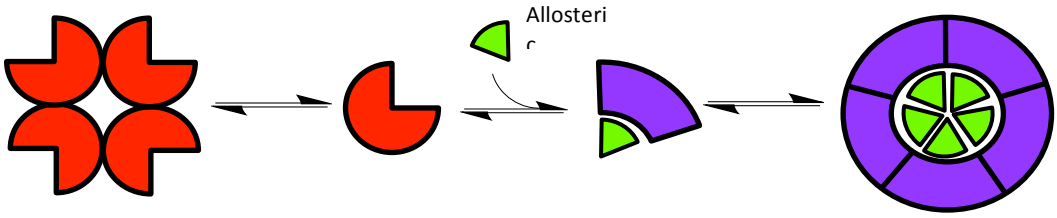

Figure 1.3 Schematic of the morpheein model of allostery. A homooligomeric enzyme reversibly dissociates into smaller subunits that may undergo conformational change in their dissociated state. These subunits with an altered conformation can then reassemble to form an alternative structurally and functionally distinct oligomeric structure. The addition of an allosteric effector may shift the equilibrium to favour a particular homo-oligomer.

1.1.4. Dynamic energy landscape model

The MWC and KNF models of allostery were originally proposed as conceptual models to explain the observed cooperative binding of oxygen to haemoglobin.[3,7,9] Many authors have noted these two models could be considered as special cases of more general models in which neither induced fit or

conformational symmetry are conserved.[4,6,10,13-15] In recent years the concepts of allostery provided by these models and their application have been expanded to encompass monomeric proteins (i.e. chemotaxis protein Y, and trypsin-like proteases), unstructured allosteric proteins (i.e. glucokinase and protein kinase A) and allosteric proteins that show no evidence of conformational change (i.e. catabolite activator protein).[8,10,16-19] It should also be noted that the concept of the allosteric effector has also developed as the study of allosteric proteins has grown, the allosteric effector is no longer constrained to being a small molecule; the effector can be as large as another protein.[16]

The current understanding of allostery is based on the premise that proteins exist as an ensemble of possible conformational states populated according to their Boltzmann distribution.[11,20-22] Proteins are considered to populate a dynamic energy landscape with multiple energy minima (Figure 1.4).[6,15] The protein can sample these minima via its natural molecular dynamic fluctuations, but will primarily occupy the lowest energy state.[6,15] Effector binding to the protein changes the energy landscape and the protein population is redistributed favouring the new lowest energy state.[11,20] Okazaki proposed that both induced-fit and population shift (derived from the KNF and MWC models of allostery respectively) can allow proteins to jump between the unbound protein and effector-bound protein energy landscapes.[6]

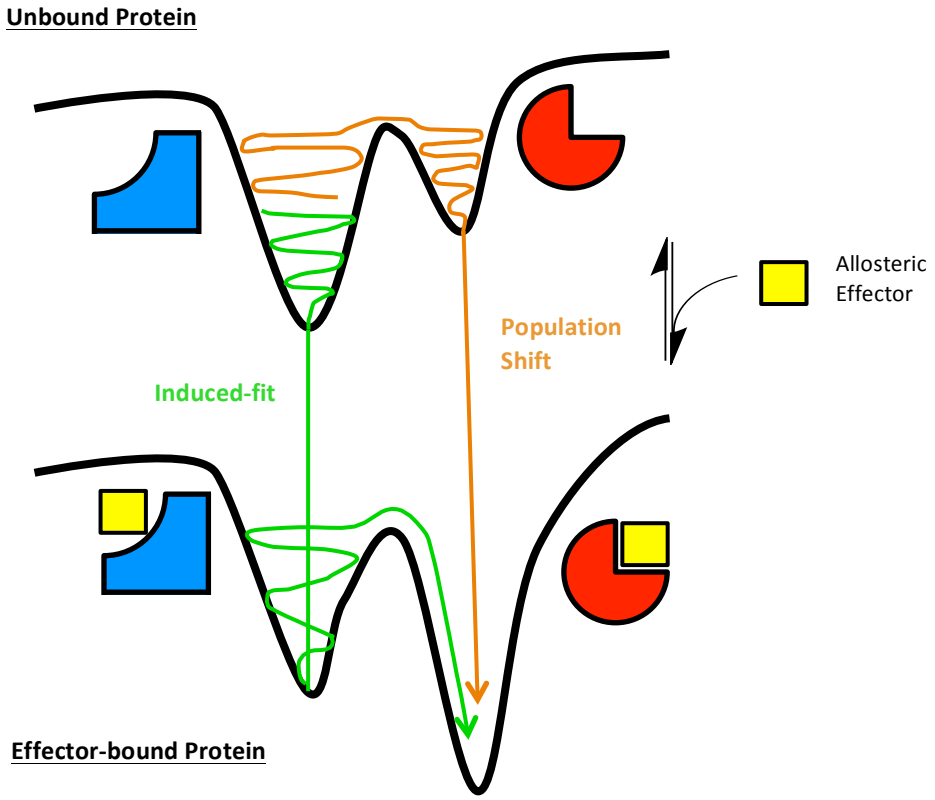

Figure 1.4 Schematic of a dynamic energy landscape of a protein. On top is the energy landscape populated by a protein with no effector bound (unbound protein) and below the energy landscape of the effector-bound protein. The ligand can jump between the two energy landscapes by effector binding or unbinding. Both an induced-fit or population shift model of allostery can represent the jump between the energy landscapes. Schematic adapted from Okazaki *et al.*.[6]

The MWC and KNF models of allostery, are phenomenological and do not directly address how the binding of an effector causes the observed allosteric effect in atomic detail.[4,10] The classic view of allostery, which considered allostery in terms of two distinct conformations, sought one well-defined communication pathway between the allosteric binding site and the active site (Figure 1.5A).[16,23] The binding signal of an allosteric effector is transmitted along this molecular communication pathway and alters the conformation of the active site to better facilitate or impede catalysis. Communication pathways refer to a set of residues that dynamically contact, creating a structural pathway that energetically couples two (or more) binding sites.[11,23]

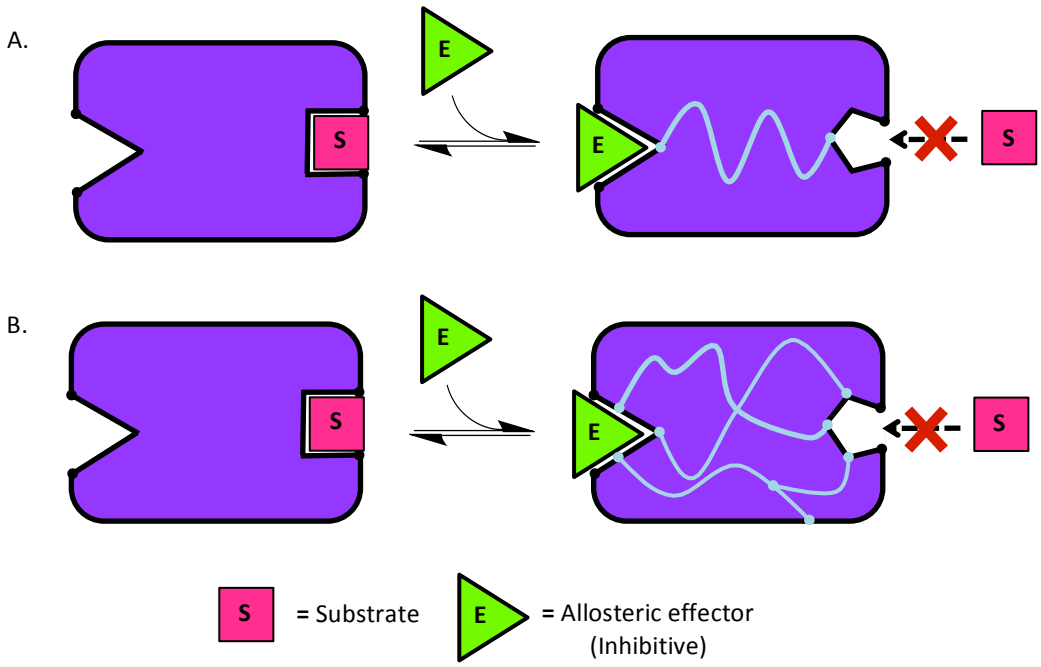

Figure 1.5 Schematic representation of the molecular communication pathways that connect the allosteric effector binding site and the active site. In this scenario the effector acts as an inhibitor; the binding of the effector at the allosteric binding site is communicated to the active site preventing substrate binding. According the classic view (A) a single pathway exists between the active site and the allosteric binding site, whereas multiple connected pathways link the two sites in the current view (B).

Overtime this view has evolved to the current view that enzymes exist as ensembles thus permitting networks of communication pathways to exist.[16,23] The binding of the allosteric effector can be transmitted along multiple pathways, each pathway contributing to the changes that occur at the active site (Figure 1.5B). The changes that occur at the active site are not restricted to detectable conformational changes. [16,23] Alternatively, effector binding may change the flexibility or dynamic motion of an enzyme, which thermodynamic affects the affinity of an enzyme for its substrate without changing the average conformation of the enzyme.[16,22-24] The catabolite activator protein (CAP) is the most prominent example of an allosteric enzyme that does not undergo conformational change.[8,22,25] The binding of cyclic adenosine monophosphate (cAMP) to CAP switches the enzyme from inactive to active without any evidence of structural change.[8,25] Nuclear magnetic resonance analysis revealed the intrinsic motion of the unliganded CAP was strongly affected by the addition of cyclic adenosine monophosphate (cAMP).[8,16,25] CAP was one of the first examples of an allosteric mechanism that is entropically driven. [8,16,25]

1.1.5. Allostery and drug discovery

In the past drug development has almost exclusively focused on developing compounds that bind to the orthosteric site of a protein to effectively inhibit protein function.[3,16] More recently drugs that bind to the allosteric binding site of a protein are being more actively pursued. [3,16] There is a range of allosteric drugs currently available on the market including Valium and the benzodiazepines, which target the ionotropic γ-aminobutyric acid (GABA) receptor.[3,26]

One advantage of drugs developed based on allosteric ligands is that they can either activate or inactivate their target protein opening up a new range of novel therapeutic drug targets. [3,16] One example of a potential drug target where activation of the target enzyme may be beneficial is the sirtuins. The sirtuins are a class of deacetylases being explored as potential therapeutic targets for the treatment of age-related diseases such as type-2 diabetes.[27,28] The activation of the silent information regulator protein 2 (Sir2p) from yeast has been correlated to increased longevity in response to calorie restriction.[28] Investigation into the human orthologue of Sir2p, SIRT1, has identified small molecules, which activate SIRT1 and may mimic the beneficial effects of calorie restriction.[27,28]

Allosteric drugs have other potential advantages over orthosteric drugs. Allosteric drugs are typically highly specific as the allosteric binding sites are less conserved across protein families compared to the active site. [3,26] Higher specificity in turn can also lead to a lower risk of side effects.[3,26] Allosteric drugs tend to modulate enzyme activity rather than eliminating it completely.[3] Allosteric drugs do not necessarily need to bind to the target protein directly to affect the protein's function. The effect of an allosteric drug may be propagated along different proteins or receptors often by altering protein-protein interfaces.[3] A phenomena illustrated by the indirect allosteric modulation of the G-protein coupled receptor (GPCR). Ligand binding reduces the interactions between different combinations of receptors in the glucagon receptor family (GPCR class B).[3,29] An increase in the interactions between the gastric-inhibitory-peptide-receptor (GIPR) and the glucagon-like-peptide-1-receptor (GLP 1R) is observed upon binding of GLP-1 to the GLP 1R. The binding of GIP to GIPR-GLP reverses this effect. [3,29] Although this allosteric propagation may broaden the range of available therapeutic targets it may

also make it more difficult to predict the possible side effects of an allosteric drug. Moreover, it must be remembered that drug development targets a population of patients and this population may have significant variance in their metabolism and genetics due to factors such as age, ethnicity and health.[3] This variance may prevent some allosteric drugs working on individual patients due to different propagation pathways operating within the metabolism of different patients.

Another complication that may arise in the development of allosteric drugs is the difficulty to identify the allosteric binding sites of a protein. The exact effect of an effector can also be difficult to predict.[3,26] Unlike orthosteric sites, the allosteric binding sites of a protein are more likely to differ widely between organisms. Thus allosteric drugs that work in a rat model may not work in the human homologue.[3] Furthermore allosteric drugs are not immune to the development of drug resistance as observed by melanoma cells becoming resistant to B-RAF (V600E) inhibition by allosteric MEK inhibitors by up regulating receptor tyrosine kinases.[3,30]

The pursuit of allosteric drugs offers new opportunities for the development of novel drugs if the target proteins are carefully considered in an effort to mitigate the additional challenges allosteric drugs can pose. Perhaps one of the greatest potential benefits of pursuing allosteric drugs is the possibility of developing treatment plans to combat drug resistance by using a combination of allosteric and orthosteric drugs.[3]

1.2. *Mycobacterium tuberculosis*

Mycobacterium tuberculosis (*M. tuberculosis*) is a contagious airborne pathogen that is the primary causative agent of tuberculosis (Tb). In 2012, 8.3 million people contracted Tb, the infection proving fatal in 1.4 million of those cases, making Tb the second leading cause of mortality from a single infectious agent.[31,32] It is believed that Tb affects more than one third of the world's population and although incidence is reported throughout the world, prevalence is greatest in developing nations.[31]

Inadequate diagnostics and the long (6-9 month) treatment plans for Tb have lead to the emergence of multi-drug resistant Tb (MDR-Tb), which is defined as resistant to two types of the first-line anti-Tb drugs, isoniazid and rifampin.[31,33] In 2006, the World Health Organisation (WHO) and the US Centers for Disease Control and Prevention (CDC) classified a new extensively drug-resistant Tb (XDR-Tb) strain.[34] XDR-Tb is defined as resistance to flouroquinolone and at least one other second-line injectable anti-Tb drug (kanamycin, amikacin or capreomycin) in addition to isoniazid and rifampin.[33-36] Incidences of MDR- or XDR-Tb have been reported worldwide and treatment for both requires the use of less effective and more expensive second-line drugs for at least 20 months.[31,33,34,36]

Alarmingly in 2009 a new strain of totally drug-resistant Tb (TDR-Tb) was announced, possibly resistant to all first- and second-line anti-Tb drugs.[37] WHO is yet to recognise the emergence of TDR-Tb, mainly due to ambiguity in defining and testing the antibiotic resistance of all first and second-line drugs.[38] Several countries (Iran, India, South Africa and Italy) have reported incidents of TDR-Tb, making the possibility of potentially untreatable Tb outbreaks increasingly likely.[37,39,40 41] To counter the threat that MDR-, XDR- and potentially TDR-Tb pose to global health there is a need to develop new and novel anti-Tb drugs.

1.3. The shikimate pathway and aromatic amino acid biosynthesis

Ideal targets for novel drug development are biosynthetic pathways present in the target pathogen, such as *M. tuberculosis*, but absent in the human host. The shikimate pathway, ultimately responsible for aromatic amino acid biosynthesis, is only found in bacteria, plants and apicomplexan parasites (Figure 1.6).[42-44] Furthermore gene disruption studies have shown the operation of the shikimate pathway is essential for the viability of *M. tuberculosis*.[45] Thus the enzymes of this pathway are ideal candidates for exploration as a potential anti-Tb drug targets.

The shikimate pathway is responsible for the conversion of D-erythrose 4-phosphate (E4P) and phosphoenolpyruvate (PEP) to chorismate via a set of seven enzyme-catalysed reactions. Chorismate

can either then be directed toward the formation of Tryptophan (Trp) by anthranilate synthase or toward the biosynthesis of Phenylalanine (Phe) and Tyrosine (Tyr) via chorismate mutase. Chorismate is also a precursor for other essential metabolites including vitamins E and K, folic acid and various quinones.[46]

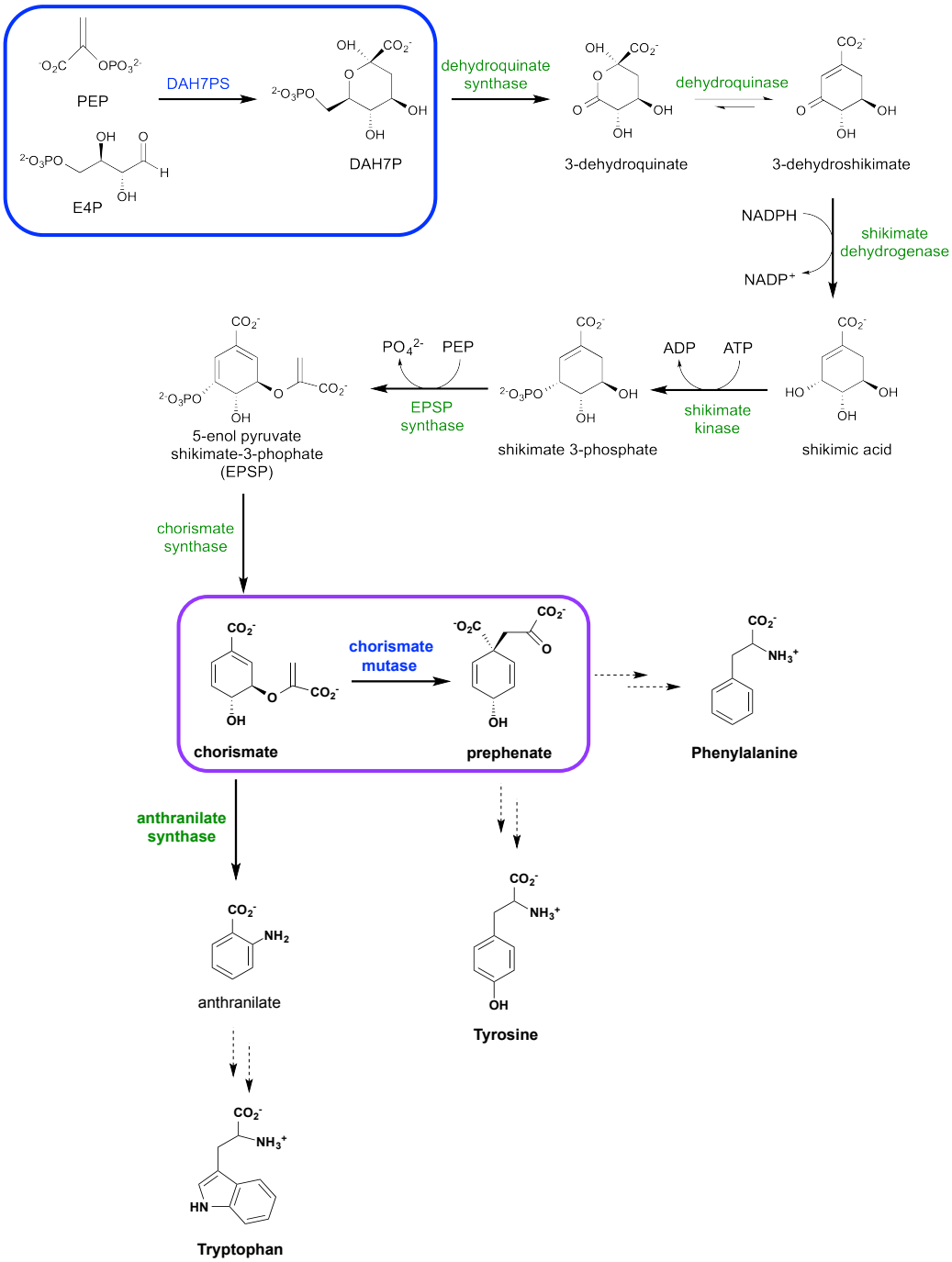

Figure 1.6 The seven enzyme-catalysed reactions of the shikimate pathway leading to the formation of chorismate. Chorismate is then directed toward the aromatic amino acid biosynthesis by either anthranilate synthase or chorismate mutase. The reactions catalysed by DAH7PS and chorismate mutase are highlighted in blue and purple respectively.

1.4. 3-Deoxy-D-*arabino*-heptulosonate 7-phosphate synthase (DAH7PS)

The first committed step of the shikimate pathway is the aldol-like condensation of E4P and PEP to produce the seven-carbon sugar 3-deoxy-D-*arabino*-heptulosonate 7-phosphate (DAH7P). This reaction is catalysed by 3-deoxy-D-*arabino*-heptulosonate 7-phosphate synthase (DAH7PS). DAH7PS enzymes, located at the start of the shikimate pathway, have been found to be tightly feedback regulated in many organisms due to the need to control the entry of metabolites into the pathway. [47-51]

DAH7PS enzymes have been classified into two types based primarily on molecular mass.[52] Type I DAH7PS enzymes are less than 40 kDa in mass whilst Type II DAH7PS enzymes typically have a mass of about 54 kDa.[53,54] Type I DAH7PS enzymes have been very well characterised structurally and functionally, and have been further divided into two sub-families, Type Iα and Type Iβ, based mainly on sequence similarity. Type Iβ share less than 18 % sequence identity with the Type Iα DAH7PS enzymes and are more closely related to 3-deoxy-D-*manno*-octulosonate 8-phosphate synthase (KDO8PS).[55] KDO8PS enzymes catalyse the aldol-like condensation of PEP and arabinose 5-phosphate to produce the eight-carbon sugar 3-deoxy-D-*manno*-octulosonate 8-phosphate.[54] Type II DAH7PS enzymes share less than 10% sequence similarity with Type I DAH7PS enzymes and have been less well characterised.[53]

All available crystal structures of DAH7PS enzymes to date show Type Iα, Type Iβ and Type II share the same core structure (Figure 1.7); a $(\beta/\alpha)_8$ barrel fold with the active site located at the C-terminal end of the barrel.[47-49,51,56-65] Variation amongst DAH7PS enzymes generally arises due to extensions and additions to the core barrel structure sometimes referred to as decorations to the barrel. The more extensive decorations often contribute to the formation of the allosteric sites responsible for the feedback regulation of DAH7PS enzymes.[47-51] The unregulated *Pyrococcus furiosus* and *Aeropyrum pernix* enzymes possess only small additions to the N-terminus of the core $(\beta/\alpha)_8$ barrel.[60,65] The Type 1α DAH7PS enzymes from *Escherichia coli, Saccharomyces cerevisiae* and *Neissseria meningitidis* all

possess similar structures and are all feedback regulated by selected aromatic amino acids.[49,51,59] The N-terminal extension and the inserted β-sheets both contribute to the formation of their allosteric sites and no significant changes in structure are observed on effector binding. The N-terminal extension to the core structure of the DAH7PS from *Thermotoga maritima* (*Tma*DAH7PS) is more elaborate and includes an ferredoxin-like domain which shares structural homology with known ACT domains.[62,66] This ferredoxin-like domain has been shown to be involved in formation of the allosteric binding sites responsible for the feedback regulation of *Tma*DAH7PS by undergoing a detectable conformational change that effectively blocks the active site.[47] DAH7PS enzymes from other organisms such as *Listeria monocytogenes, Bacillus subtilis* and *Porphyromonas gingivalis* possess N- or C-terminal extensions which contain a functional chorismate mutase-like domain, are also responsible for the regulation of DAH7PS activity by binding chorismate or prephenate.[61,67,68]

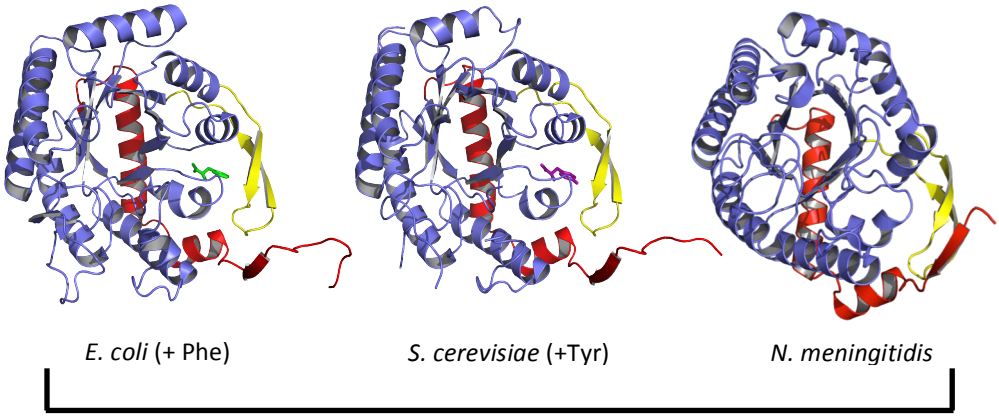

E. coli (+ Phe) *S. cerevisiae* (+Tyr) *N. meningitidis*

Type Iα

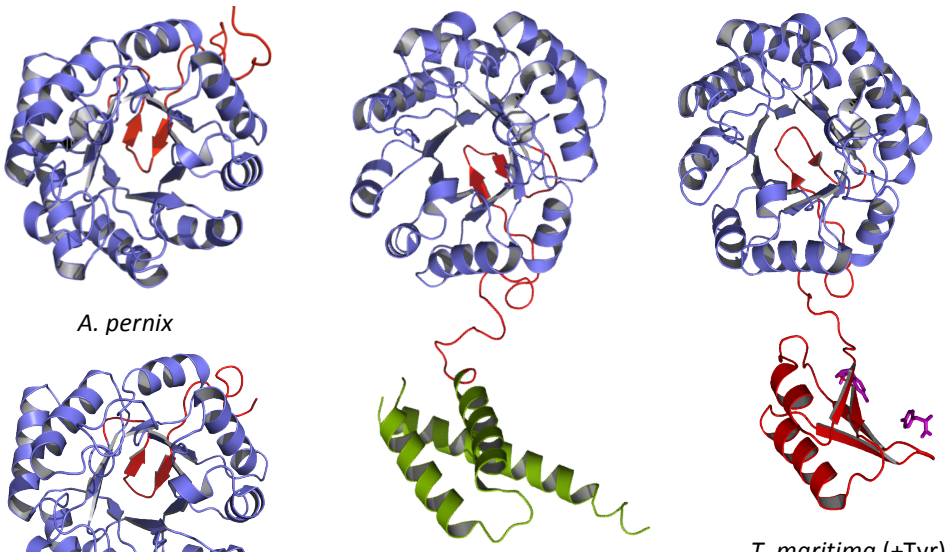

A. pernix *L. monocytogenes* *T. maritima* (+Tyr)

P. furiosus

Type Iβ

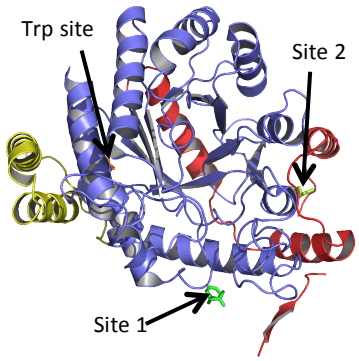

M. tuberculosis (+Trp +Phe)

Type II

Figure 1.7 Cartoon depiction of the subunits of the Type Iα DAH7PSs from *Escherichia coli* (PDB code: 1KFL), *Saccharomyces cerevisiae* (1OF6) and *Neisseria meningitidis* (4HSN); the Type Iβ DAH7PSs from *Aeropyrum pernix* (1VS1) *Pyrococcus furiosus* (1ZCO), *Listeria monocytogenes* (3NVT) and *Thermotoga maritima* (3PG9) and the Type II DAH7PS *Mycobacterium tuberculosis* (3KGF). The core $(\beta/\alpha)_8$ barrel structure is coloured blue, N-terminal additions are coloured red and insertions to the core structure are coloured yellow. The functional chorismate mutase domain of *L. monomcytogenes* DAH7PS is coloured olive. Allosteric ligands Trp, Phe and Tyr have been shown in green, orange and purple sticks respectively. The allosteric binding sites of *Mtu*DAH7PS have been highlighted.

1.4.1. *M. tuberculosis* DAH7PS

The *M. tuberculosis* genome encodes for a single DAH7PS classified as a type II DAH7PS. The DAH7PS from *M. tuberculosis* (*Mtu*DAH7PS) is the only structurally characterised Type II DAH7PS to date. *Mtu*DAH7PS subunits have the same $(\beta/\alpha)_8$ barrel core structure and are decorated by two major additions (Figure 1.7).[69,70] A β-strand and three helices form an N-terminal extension to the barrel, whilst two α-helices have been inserted between the α2-helix and β3-sheet of the barrel. *Mtu*DAH7PS has been shown to be synergistically feedback regulated by Trp in combination with either Phe or Tyr, whereas no single aromatic amino acid elicits a significant inhibitory response.[48,69] The decorations to the core barrel structure of *Mtu*DAH7PS contribute to the formation of the allosteric binding sites of the aromatic amino acids and the structure does not undergo any significant structural change on ligand binding.[48,71] Three allosteric binding sites have been identified (Figure 1.7). One site has been observed to bind Trp primarily and designated the Trp site. The remaining two sites have been designated as sites 1 and 2 and have both been observed to bind both Phe and Tyr. The allosteric binding sites are discussed in greater detail in the relevant chapters (Sections 3.1 and 6.1).

1.5. Chorismate mutase (CM)

Chorismate mutase (CM) catalyses the Claisen rearrangement of chorismate to prephenate and is a rare example of an enzyme-catalysed pericyclic reaction.[72] The reaction catalysed by CM is the first committed step toward the biosynthesis of Phe and Tyr.[72,73]

CM enzymes have also been divided into distinct unrelated families, AroH (or Type I) and AroQ (or Type II).[74] The AroH class are characterised by their trimeric pseudo α/β-barrel structure, exemplified by the monofunctional *B. subtilis* CM (*Bsu*CM) and is relatively rare (Figure 1.8).[75] The AroQ class are

generally characterised by CM enzymes with a dimeric α-helical structure and often accompanied by another enzyme for optimal activity.[76,77]

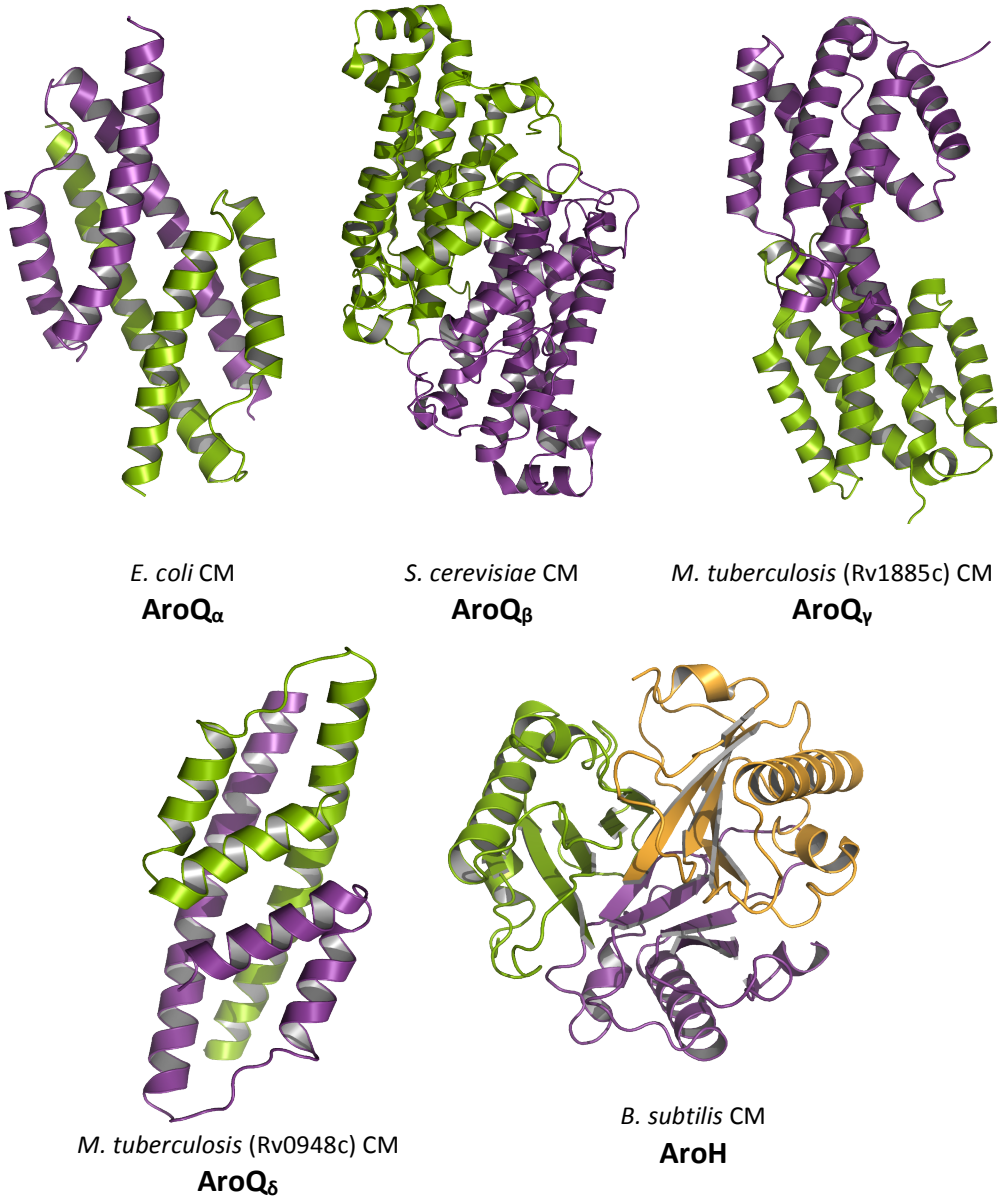

Figure 1.8 Cartoon depiction of the dimeric or trimeric chorismate mutase structures of *E. coli, S.cerevisiae, M. tuberculosis* encoded by the open reading frames Rv1885c and Rv0948c and *B. subtilis*. The structures show each subunit as olive and purple for all dimeric CMS and olive, purple and orange for the trimeric *Bsu*CM.

The AroQ class has been further divided into four subfamilies $AroQ_{\alpha}$-$AroQ_{\delta}$ The $AroQ_{\alpha}$ subclass of CM enzymes is exemplified by the structure of *E. coli* CM (*Eco*CM). The *Eco*CM subunit consists of three α-helices folded to resemble the number 4 (Figure 1.8).[76] Two active sites are created on formation of the *Eco*CM dimer with residues contributed by both subunits.[78] Most bacterial CM enzymes fit into the $AroQ_{\alpha}$ subclass including those belonging to bifunctional or fusion enzymes. These CM fusion

enzymes are also grouped into subfamilies based on the fusion partner; $AroQ_p$ have CM enzymes fused to prephenate dehydratase; $AroQ_t$ have CMs fused to prephenate dehydrogenase and $AroQ_d$ have CMs fused to DAH7PSs.[78-80]

The structure of *S. cerevisiae* CM (*Sce*CM) is representative of the subclass $AroQ_\beta$. The $AroQ_\beta$ subclass typically includes the CM enzymes from most eukaryotes and usually has a regulatory domain.[78] *Sce*CM has a more complicated subunit structure with 12 helices and the topology of the fold said to resemble the antiparallel α domain of Greek key helix bundles (Figure 1.8).[78,81] The active site is fully contained within the subunit.[78] The *Sce*CM protomer consists of a catalytic domain very similar to *Eco*CM and a regulatory domain responsible for the formation of allosteric binding sites for Trp or Tyr.[78,82]

1.5.1. *M. tuberculosis* CM

The genome for *M. tuberculosis* encodes reading frames for two CM with novel AroQ folds. One highly active CM is secreted by *M. tuberculosis* and is encoded by the open reading frame Rv1885c (**Mtu*CM).[78,83] The subunit structure of **Mtu*CM is similar to *Eco*CM, but with some key differences leading to it being assigned to a new $AroQ_\gamma$ subclass (Figure 1.8).[78] The subunit of **Mtu*CM consists of three α-helices, the first much shorter than the one found in *Eco*CM, and like *Sce*CM the active site is fully contained within each subunit.[78] All CMs known to date belong to the $AroQ_\gamma$ subclass are all exported CMs.[84]

The second intracellular CM from *M. tuberculosis* (*Mtu*CM) encoded by the open reading frame Rv0948c and was originally found to have very poor activity.[78,83,85-87] *Mtu*CM also has a novel topology not seen in other AroQ subclasses and was assigned the new $AroQ_\delta$ subclass.[78] The subunit structure of *Mtu*CM contains six α-helices and forms a dimeric quaternary structure with a active site located in each subunit (Figure 1.8).[85,86] So far the CM enzymes belonging to the $AroQ_\delta$ subclass have only been found in Gram-positive genera.[78,83,84]

Interestingly *Mtu*CM was shown to form a non-covalent complex with *Mtu*DAH7PS, boosting *Mtu*CM activity by over a 100-fold and endowing the *Mtu*CM with regulatory sensitivity to Phe and Tyr.[85] Sasso *et al.* showed the activity boost in *Mtu*CM was due to the rearrangement of *Mtu*CM active site residues on formation of the non-covalent complex.[85] The interaction between *Mtu*CM and *Mtu*DAH7PS is discussed in greater detail in chapter 4.

In 2013 kinetic analysis by Li *et al.* discovered the CM of *Corynebacterium glutamicum* (*Cgl*CM) alters the properties of DAH7PS of *C. glutamicum* (*Cgl*DAH7PS), this in combination with homology modelling lead the authors to propose the two enzymes form a non-covalent complex similar to *Mtu*CM and *Mtu*DAH7PS.[88] Complex formation had no effect on *Cgl*CM activity but instead significantly enhanced the activity of *Cgl*DAH7PS.[88,89] *Cgl*DAH7PS alone shows only slight sensitivity and to Trp and is insensitive to Tyr and Phe, in the presence of CM, *Cgl*DAH7PS activity is regulated by prephenate.[88,90] This endowed regulatory sensitivity to prephenate draws parallels to the DAH7PS from *B. subtilis*, which is regulated by chorismate and prephenate via a fused CM domain.[67] Evidence of the complex formation between *Cgl*CM and *Cgl*DAH7PS has relied on biophysical and kinetic characterisation and as yet there is no structural characterisation available of the non-covalent complex for structural comparison to the complex formed between *Mtu*DAH7PS and *Mtu*CM or other CM enzymes covalently fused to DAH7PS enzymes.

1.6. Outline of this thesis

The primary goal of this thesis is to carry out a detailed examination of the allosteric regulation of *Mtu*DAH7PS. A more comprehensive understanding of how *Mtu*DAH7PS regulates its own activity and the activity of *Mtu*CM may contribute to more efficient research into the development of anti-TB drugs that target *Mtu*DAH7PS and/or *Mtu*CM.

Chapter 2 presents a comprehensive kinetic, biophysical and solution structural analysis of *Mtu*DAH7PS and provides data that acts as a point of comparison for later chapters. Chapter 3 describes the investigation into the specificity of the allosteric binding sites of *Mtu*DAH7PS, sites 1

and 2, and the occupancy of these two sites required for regulation. Chapter 4 details studies that explored the interactions between *Mtu*CM and *Mtu*DAH7PS, with an emphasis on determining the mechanism by which *Mtu*DAH7PS regulates *Mtu*CM activity. Chapter 5 describes the inspection of residues believed to be part of the allosteric communication network responsible for signal transmission between the allosteric binding sites or between the allosteric binding sites and the active sites of *Mtu*DAH7PS. Chapter 6 presents work that probed the Trp binding site of *Mtu*DAH7PS to identify residues that are critical to Trp binding and the effect of disrupting Trp binding on *Mtu*DAH7PS. Chapter 7 details studies that examined the catalytic and regulatory properties of dimeric *Mtu*DAH7PS to gain insight into whether the *Mtu*DAH7PS dimer is a biologically relevant species.

2. Characterisation of *Mtu*DAH7PS

2.1. Introduction

Previous work has shown *Mtu*DAH7PS is only subject to synergistic feedback inhibition when Trp is present in combination with either Phe or Tyr.[48,69,70] Also prior to the start of this research several crystal structures of *Mtu*DAH7PS had been solved including one structure with Trp bound, one with Phe bound and one with Trp and Phe bound.[48] The Trp and Phe soaked crystal structure (PDB code: 3KGF) revealed that *Mtu*DAH7PS has three distinct allosteric binding sites present in each *Mtu*DAH7PS subunit (Figure 2.1). One molecule of Trp was observed to bind per subunit at a site designated here as the Trp site, whereas Phe was observed to bind at two different sites, designated site 1 and site 2. Site 1 is occupied by Phe in all subunits, whereas site 2 was occupied in only one of the subunits of the dimer that is in the asymmetric unit, thus in two subunits of the homotetramer. Later work demonstrated Tyr was also able to bind at site 1 and site 2.[48,91] Since there are three distinct allosteric binding sites per *Mtu*DAH7PS subunit and three aromatic amino acids, the next logical question to consider was whether all three aromatic amino acids could bind simultaneously.

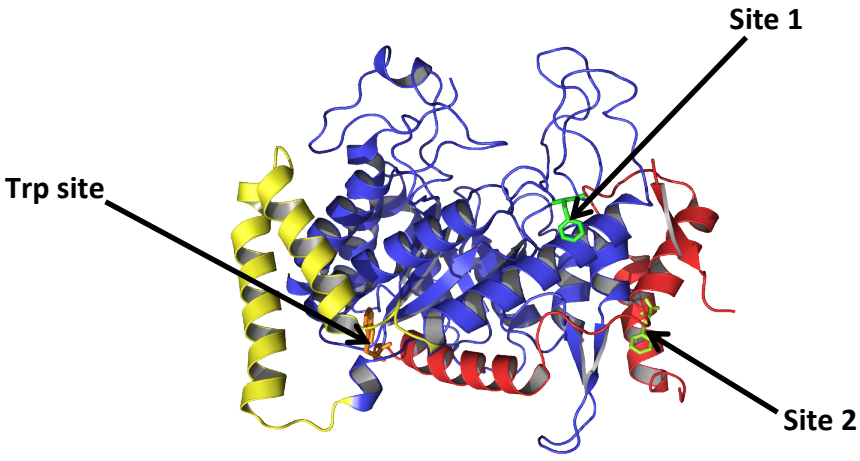

Figure 2.1 The subunit structure of *Mtu*DAH7PS soaked with Trp and Phe (PDB code: 3KGF). The core $(\beta/\alpha)_8$ barrel structure is coloured blue, the N-terminal extension is coloured red, the additional helices to the α2-β3 loop are coloured yellow and the metal ion (Mn^{2+}) is shown in purple. Trp is shown in orange bound to the Trp site. Phe bound to site 1 is shown in green and Phe bound to site 2 is shown in limon.

Previous structural characterisation of *Mtu*DAH7PS has relied heavily on crystallography, and reveals *Mtu*DAH7PS as a homotetramer in the crystalline form.[48,64,69,70] However, some proteins exist as an equilibrium of a number of oligomeric states in solution or an ensemble of various conformational states.[92-97] The position of this equilibrium is subject to any changes to the external conditions, such as temperature or concentration. As crystallisation typically occurs under conditions of high protein concentrations, these conditions may favour higher oligomeric states. Analysis of *Mtu*DAH7PS^{WT} by structural techniques that analyse proteins in solution such as small angle X-ray scattering (SAXS), analytical ultracentrifugation (AUC) and native polayacrylamide gel electrophoresis (PAGE), can be carried out at a range of protein concentrations, and can reveal alternative conformers or oligomers. By complimenting the known crystallographic data on *Mtu*DAH7PS with solution phase techniques a better understanding of the *in vivo* structure of *Mtu*DAH7PS may be developed.

Crystallographic studies also showed the binding of the aromatic amino acids to the allosteric binding sites of *Mtu*DAH7PS^{WT} did not result in any significant change in protein conformation. However, the possibility that crystal packing effects mask changes in conformation have yet to be eliminated. Furthermore the binding of the aromatic amino acids may also alter the *Mtu*DAH7PS quaternary structure equilibrium in solution. Both possibilities need to be explored through analysis of *Mtu*DAH7PS structure using range of solution phase structural techniques i.e. SAXS and AUC.

2.2. Chapter aims

The primary aim of this chapter was to establish a thorough and robust characterisation of *Mtu*DAH7PS^{WT} to serve as a point of comparison for work described in later chapters of this thesis. As a part of this goal efforts were made to expand upon previous knowledge of the allosteric regulation of *Mtu*DAH7PS by better understanding the contribution of Tyr. Studies were also conducted to establish the quaternary structure of *Mtu*DAH7PS^{WT} in solution and to determine if the aromatic amino acids caused any detectable changes.

2.3. Preparation, expression and purification

2.3.1. Construct details

Shaun Lott (University of Auckland) had previously cloned the gene for *Mtu*DAH7PS into a pProEx-HTa vector. This vector contained an ampicillin resistance gene, T7 promoter regions for the lac operon and N-terminal tobacco etch virus (TEV) protease cleavable His_6-tag. The ampicillin resistance gene allowed selection for cells that contain the plasmid, whilst the incorporation of T7 promoter permitted induction of protein expression in the presence of isopropyl-β-D-thiogalactopyranoside (IPTG). The inclusion of a TEV protease cleavable polyhistidine tag (His_6-tag) permitted the use of immobilised metal affinity chromatography (IMAC) techniques for simpler and faster purification procedures. The sequence for this tag is shown below (Figure 2.2).

MSYYHHHHHHDYDIPTTENLYFQGA

Figure 2.2 Sequence of the pProEx-HTa His_6-tag. Highlighted are the polyhistidine metal binding site (blue), the TEV protease recognition site (purple) and the residues retained at the N-terminus post cleavage (pink).

The pProEx-HTa vector containing the *Mtu*DAH7PS gene was electroporated into BL21(DE3) pGroESL cells. Contained in this cell line was a pGroESL plasmid for the production of chaperonins pGroES and pGroEL, which assist protein folding. Previous work showed these chaperonins were essential for soluble expression of *Mtu*DAH7PS.[70] The pGroESL plasmid also carried a chloramphenicol resistance gene. Consequently colonies were selected for ampicillin and chloramphenicol resistance.

2.3.2. Expression, lysis and purification

Protein expression was carried out as outlined in Section 9.5, and resulted in the overexpression of *Mtu*DAH7PS as confirmed by sodium-dodecyl sulphate polyacrylamide gel elect (SDS-PAGE). The SDS-PAGE gel showed an overexpressed protein band of ~55 kDa which matched the expected molecular mass of the His_6-tagged *Mtu*DAH7PS (Figure 2.3B). Plasmid sequencing and mass spectrometry were used to confirm there were no unintended alterations to the amino acid sequence.

Cells were lysed using either sonication or preferentially cell disruption and the resulting lysate was clarified by centrifugation to remove insoluble cell debris. The lysis of cells by cell disruption was quicker and more reliably achieved complete cell lysis than sonication, with purifications using this method frequently resulting in higher yields. The *Mtu*DAH7PS in the lysed supernatant was purified utilising IMAC and size exclusion chromatography (SEC). The procedure is outlined in Figure 2.3A and presented with an SDS-PAGE (Figure 2.3B) illustrating protein purity achieved at each step. The purification procedure is detailed in Section 9.5 and largely followed the protocol set out by Richard Hutton, who himself had improved upon the original protocol developed by Celia Webby.[48,70]

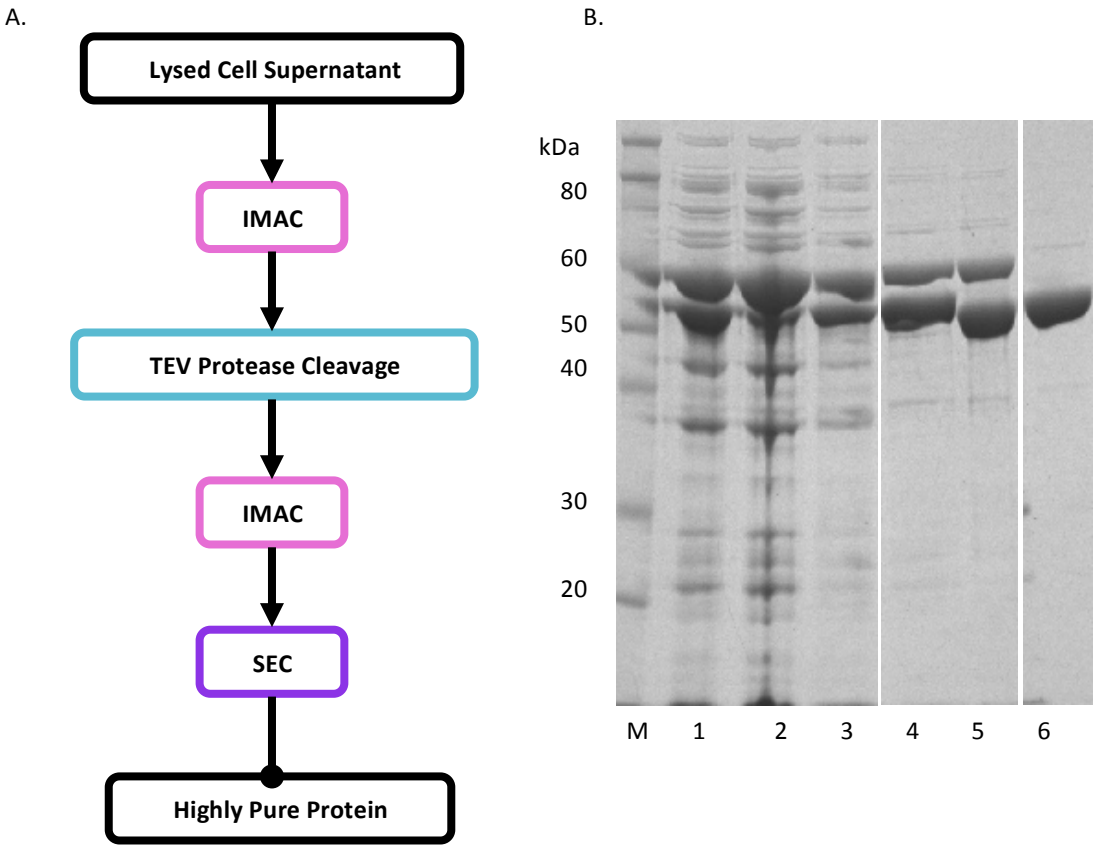

Figure 2.3 A. An outline of the standard purification protocol for *Mtu*DAH7PS. B. SDS-PAGE gel. Lane M is the molecular weight maker; lane 1 whole lysate; lane 2 soluble fraction of the cell lysate; lane 3 insoluble fraction of the cell lysate; lane 4 protein isolated from IMAC gradient; lane 5 TEV protease treated *Mtu*DAH7PS (TEV protease removed) and lane 6 pooled fractions after SEC overexpressed protein bands can be observed at ~50 kDa, ~55 kDa and ~60 kDa which correspond to *Mtu*DAH7PS^{WT}, His$_6$-tagged *Mtu*DAH7PS and the chaperonin proteins respectively.

2.4. Kinetic characterisation

2.4.1. Kinetic parameters

Previous work had established optimal conditions for the kinetic assays[69]. Assays were conducted at 37 °C in 50 mM Bis-tris propane (BTP) buffer at pH 7.5 and required a divalent metal ion (Mn^{2+}) and reducing agent tris(2-carboxyethyl)phosphine (TCEP) for efficient catalysis. The procedure is described in Section 9.9.1. The kinetic parameters of *Mtu*DAH7PS^{WT}, determined using steady-state Michaelis-Menten kinetics, were compared with previously published results (Table 2.1).[69]

Table 2.1 A comparison of kinetic parameters for *Mtu*DAH7PS^{WT} from this study and those published previously.[70] Michaelis-Menten kinetic plots supplied in Appendix I.

***Mtu*DAH7PS**	K_m^{E4P} (μM)	K_m^{PEP} (μM)	k_{cat} (s^{-1})	**Catalytic Efficiency** k_{cat}/K_m^{E4P} ($mM^{-1}s^{-1}$)	**Catalytic Efficiency** k_{cat}/K_m^{PEP} ($mM^{-1}s^{-1}$)
This study	28 ± 2	37 ± 4	4.7 ± 0.1	170 ± 20	130 ± 20
Webby[69]	25 ± 1	37 ± 3	3.1 ± 0.1	124 ± 9	80 ± 10

2.4.2. Feedback regulation by individual aromatic amino acids

Kinetic assays were conducted under standard assay conditions for *Mtu*DAH7PS, including 150 μM of E4P and PEP and are outlined in Section 9.9.3. This study found that when present at a concentration of 200 μM the individual aromatic amino acids only caused a small reduction in activity (Figure 2.4), results consistent with previous work.[48] When the aromatic amino acid concentration exceeded ~1 mM substantial inhibition of *Mtu*DAH7PS activity was observed. Phe and Tyr reduced *Mtu*DAH7PS^{WT} activity by up to ~40 % and Trp up to ~50 %.

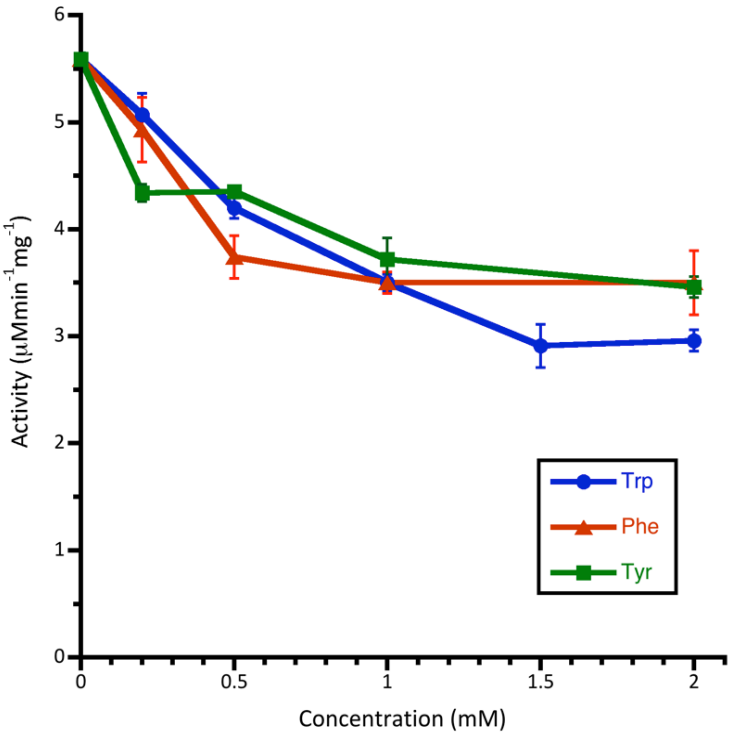

Figure 2.4 Response of *Mtu*DAH7PS^{WT} activity to increasing concentrations of individual aromatic amino acids; tryptophan (Trp)(dark blue); phenylalanine (Phe) (red) and tyrosine (Tyr) (green). E4P and PEP concentrations were held constant at 150 μM. Error bars depict the standard deviation of triplicate measurements.

2.4.3. Feedback regulation

Kinetic assays were conducted under the standard assay conditions used for all inhibition studies as outlined in Section 9.9.3. Each aromatic amino acid was added to the assay conditions to give a final concentration of 200 μM, unless stated otherwise. In agreement with previous work, Trp in combination with either Phe or Tyr dramatically reduced *Mtu*DAH7PS^{WT} activity (Figure 2.5).[48,71] The most potent binary combination was Trp and Phe, which reduced *Mtu*DAH7PS^{WT} activity to ~6 % of the observed activity of the unliganded enzyme. The inhibition achieved by the combination of Trp and either Phe or Tyr was more than the ~20-30 % inhibition expected of an additive effect for the two aromatic amino acids and clear evidence of synergy.

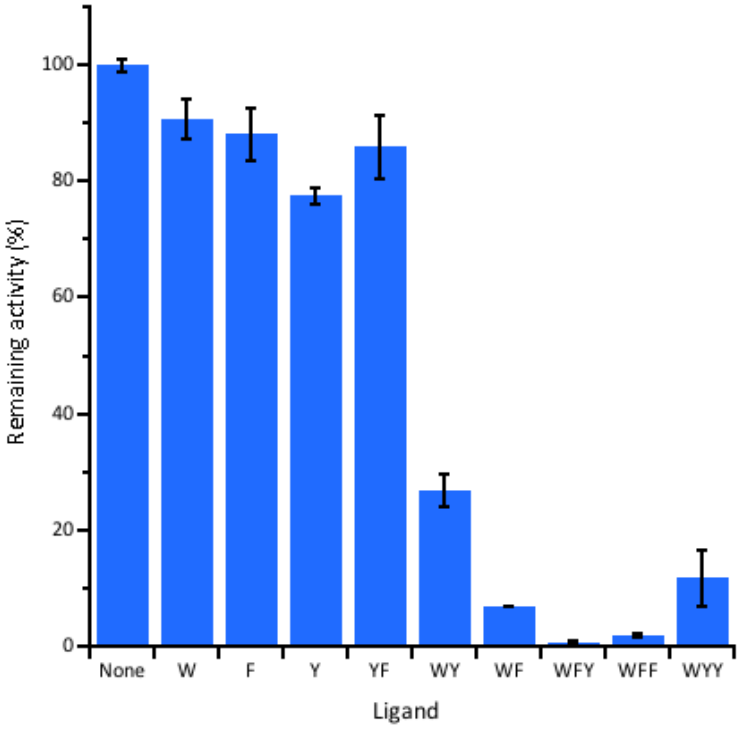

Figure 2.5 Remaining activity of *Mtu*DAH7PS^{WT} in the presence of various single, binary and ternary combinations of aromatic amino acids. The aromatic amino acids are represented by their one letter code; Trp, W; Phe, F and Tyr, Y. Each letter also represents 200 µM of the corresponding aromatic amino acid. E4P and PEP concentrations were held constant at 150 µM. Error bars depict the standard deviation of triplicate measurements. P-values provided in appendix V.

The combination of all three aromatic amino acids almost completely inhibited *Mtu*DAH7PS^{WT}, reducing enzyme activity to ~0.6 %. This was a level of inhibition that was not achieved by using an equivalent total concentration of only two aromatic amino acids (i.e. 200 µM Trp and 400 µM or either Phe or Tyr) (Figure 2.5). The inhibition of *Mtu*DAH7PS^{WT} was found to be more complex than first proposed; this study showed all three aromatic amino acids contribute to the synergistic regulation of the enzyme. Each amino acid makes a contribution that could not be compensated for by simply increasing the concentration of the alternative amino acids, making this, to the best of our knowledge, the first reported example of enzyme regulation by ternary synergy found in the literature.

2.5. Biophysical characterisation

2.5.1. Thermal stability

Differential scanning fluorimetry (DSF) is a technique commonly used to measure the thermal stability of a protein. The protein is incubated with a dye, which fluoresces upon binding hydrophobic residues of the protein. The temperature is incrementally increased causing the protein to denature and exposing more hydrophobic residues for the dye to bind, thus increasing the fluorescence. The melting temperature (T_m) reported corresponds to the maximum increase in measured fluorescence. The standard SEC buffer (10 mM BTP pH 7.5 plus 150 mM NaCl and 200 µM each of PEP, $MnSO_4$ and TCEP) was used for all DSF assays. The protocol is described in Section 9.8.1.

Ligand binding alters the thermal stability of *Mtu*DAH7PS^{WT} (Figure 2.6A). Trp has the greatest influence on the thermal stability of *Mtu*DAH7PS^{WT}. Trp (200 µM) increased the T_m by 8.6 ± 0.9 ˚C. Addition of 200 µM of Tyr or Phe caused a more modest increases in the thermal stability of *Mtu*DAH7PS^{WT} of 1 ± 0.2 ˚C and 2.6 ± 0.6 ˚C respectively. Further increases in the concentration of Trp or Phe resulted in even greater increases in thermal stability (Figure 2.6B). Trp (1000 µM) caused the greatest increase in T_m for *Mtu*DAH7PS^{WT} of 15.0 ± 0.2 ˚C. Increasing the concentration of Tyr resulted in a decrease in thermal stability.

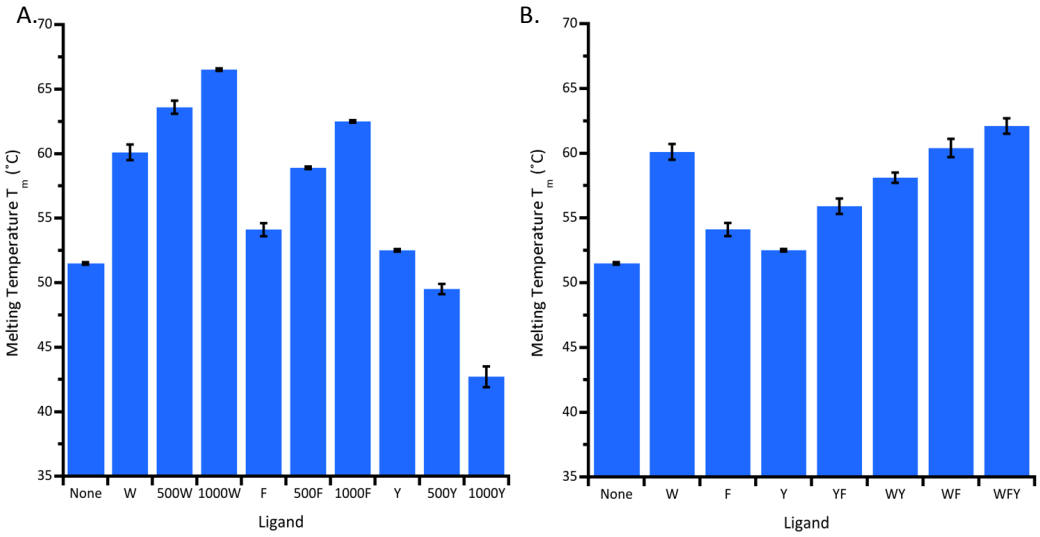

Figure 2.6 The effect of A. increasing concentrations of individual aromatic amino acids and B. individual, binary and ternary combinations on the thermal stability of *Mtu*DAH7PS^{WT}. The aromatic amino acids are represented by their one letter code; Trp, W; Phe, F and Tyr, Y. Each letter also represents 200 µM of the corresponding aromatic amino acids, except where 500, and 1000 are stated and represent their respective concentrations in µM. Assays conducted in 10 mM BTP buffer pH 7.5 in the presence of NaCl, $MnSO_4$, TCEP and PEP. Error bars depict the standard deviation of triplicate measurements. P-values provided in appendix V.

The ternary combination of Trp, Phe and Tyr caused the largest increase in the thermal stability of *Mtu*DAH7PS^{WT} observed for any ligand combination, 10.6 ± 0.7 ˚C (Figure 2.6B). The binding of each different aromatic amino acid appeared to make a separate contribution toward improving the thermal stability of *Mtu*DAH7PS^{WT}. It is possible at the higher concentrations of Trp and Phe, the amino acids start to occupy all the available binding sites, not just their preferential binding sites.

2.5.2. Binding affinities

Isothermal titration calorimetry (ITC) was used to assess the affinity *Mtu*DAH7PS displays for each aromatic amino acid under specific conditions. ITC measures the change in heat caused by a series of small injections of a ligand (in this case aromatic amino acids) into a cell containing the macromolecule (*Mtu*DAH7PS).[98-100] Origin® software then uses the resulting thermogram to iteratively fit a binding model, permitting determination of the dissociation constant (K_d), a measure of the affinity *Mtu*DAH7PS has for the ligand. The experimental protocol is described in Section 9.8.2, including the experimental setup for each experiment.

The affinity of *Mtu*DAH7PS for the individual aromatic amino acids has previously been determined.[71,91] Previous work established that pre-incubation of *Mtu*DAH7PS^{WT} with Trp improved the affinity of the protein for Phe and vice versa.[71] The intention of this study was to investigate how Tyr binding affects and is affected by the binding of Trp or Phe.

Trp binding to *Mtu*DAH7PS^{WT} became tighter when *Mtu*DAH7PS was incubated with Tyr as illustrated by the lower K_d (Figure 2.7B, Table 2.2). However, the K_d between Tyr and *Mtu*DAH7PS^{WT} was unaffected by the incubation of *Mtu*DAH7PS^{WT} with Trp prior to the titration of Tyr (Figure 2.7A, Table 2.2).

The binding of Tyr to *Mtu*DAH7PS^{WT} at either site 1 or site 2 is communicated across the protein to whichever site (or sites) Tyr binds, causing the Trp site(s) to bind Trp more tightly. The means of communication is likely a subtle change of the molecular dynamics of the enzyme, similar to that suggested for communication between the Trp and Phe sites.[71] Molecular dynamics simulations attributed the enhancement of ligand binding to the alternate allosteric binding sites to changes in local flexibility within the binding pockets, making ligand binding entropically more favourable.[71] A similar mechanism is likely responsible for the enhancement of Trp binding to *Mtu*DAH7PS once Tyr has bound.

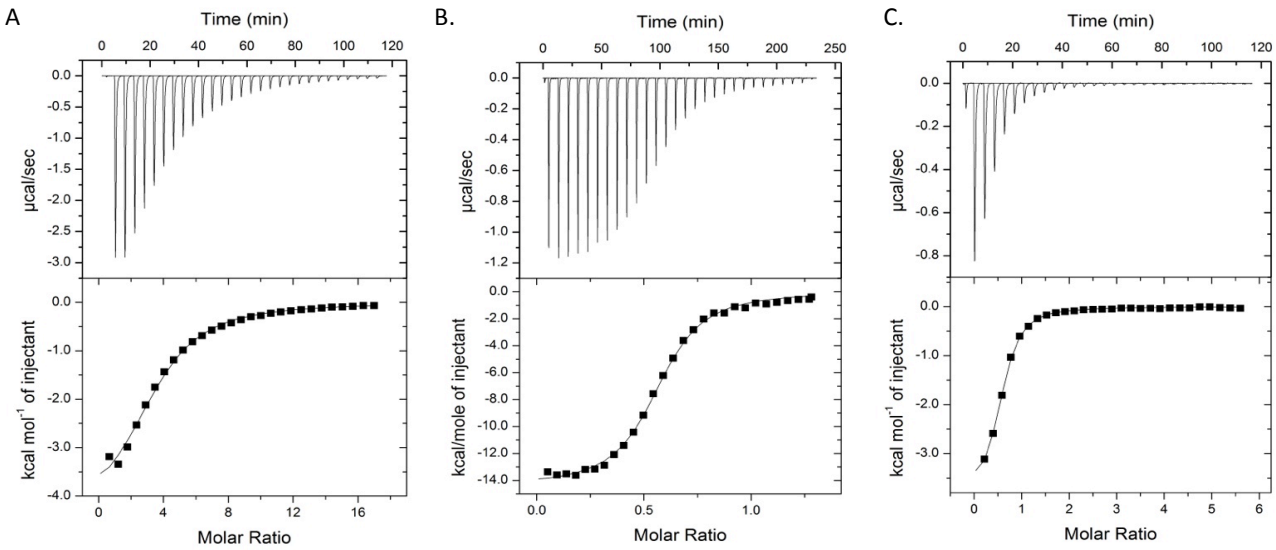

Figure 2.7 ITC data for the interaction of A. 38 µM *Mtu*DAH7PS^{WT} preincubated with 20 µM Trp and 3 mM Tyr titrant; B. 49 µM of *Mtu*DAH7PS^{WT} preincubated with 400 µM Tyr and 250 µM Trp titrant and C. 40 µM *Mtu*DAH7PS^{WT} preincubated with 400 µM Tyr and 1 mM Phe titrant.

Table 2.2 A complete list of dissociation constants determined by ITC for *Mtu*DAH7PS^{WT}. * Denotes values determined by Richard Hutton.[71,91] — Indicates no background ligand present. Values are determined from a single ITC experiment. Error represents error of curve fitting to the data set by least squares fit.

Titrated Ligand	Background Ligand	K_d (µM)
Phe	—	21 ± 1*
	Trp	5 ± 1*
	Tyr	3.2 ± 0.1
Tyr	—	39 ± 1*
	Trp	40 ± 2
	Phe	12 ± 1*
Trp	—	4.7 ± 0.1*
	Phe	1.08 ± 0.03*
	Tyr	1.0 ± 0.1

The inability of Trp to enhance Tyr binding suggests the communication pathway is only one way and is a curious result. It may suggest either, Phe and Tyr do not bind to the same binding sites or alternatively that the changes at sites 1 and/or 2 are optimised for Phe binding and not for Tyr binding. The only difference between Phe and Tyr is the hydroxyl group of the Tyr. So enhancement of Phe binding whilst leaving Tyr binding unaffected would most likely require the 'optimised' binding

site to encourage the burying of the hydrophobic phenyl group of Phe, to make Phe binding more favourable. The optimisation of the hydrophobic contacts for the phenyl group of Phe may not affect Tyr binding due to a hydrogen bond that forms between the Tyr hydroxyl group and the residues of the core barrel structure at either site 1 or site 2. This polar contact would most probably prevent the tyrosyl group from repositioning itself in the binding pocket.

This study also showed incubation of *Mtu*DAH7PS^{WT} with Tyr prior to titration of Phe resulted in tighter Phe binding (Figure 2.7C, Table 2.2). Previous work had already established a background presence of Phe decreased the K_d between *Mtu*DAH7PS^{WT} and Tyr.[48] This cooperative binding suggested a binding event at either site 1 or site 2 maybe transmitted to the other site. The enhanced binding affinity at the other site is again probably due to subtle changes in local flexibility of the binding site(s) that facilitate ligand binding. Alternatively the decrease in K_d between *Mtu*DAH7PS^{WT} and either Phe or Tyr with *Mtu*DAH7PS^{WT} pre-incubated with the other amino acid could have resulted from the elimination of weaker binding event due to the weaker binding site being occupied by the alternative amino acid. If for example site 1 binds Phe more tightly than site 2, then the K_d determined between Phe and *Mtu*DAH7PS^{WT} is an average of the two binding events. When *Mtu*DAH7PS is incubated with Tyr, Tyr occupies site 2 and only the tighter binding of Phe to site 1 is measured giving a lower K_d.

2.6. Structural characterisation

2.6.1. SAXS analysis

The quaternary structure of *Mtu*DAH7PS in solution was studied by small angle X-ray scattering (SAXS). This technique uses the elastic scattering of X-rays at low angles to discern information about a macromolecule's size and shape. The SAXS scattering profile of *Mtu*DAH7PS^{WT} was analysed with PRIMUS[101], GNOM[102], CRYSOL[103] and SAXS MoW[104] to determine the relevant SAXS parameters which are tabulated below (Table 2.3). The experimental and analytical protocols are described in Section

9.7.5 and 9.7.6. Parameters of interest include the radius of gyration (R_g), the maximum particle size (D_{max}) and the Porod volume (V_p). The R_g is defined as the root mean square distance of atoms from the centre of gravity of the macromolecule, and is an indication of the overall compactness of a molecule. D_{max} as its name implies, gives the distance of the macromolecules longest dimension. V_p is the estimated particle volume as determined by the application of Porod's Law.

The theoretical scattering patterns for both a tetramer and dimer were modelled by CRYSOL using *Mtu*DAH7PS crystal coordinates (PDB code: 3NV8). The experimental scattering profile of *Mtu*DAH7PS^{WT} fitted more closely to the theoretical scattering of an *Mtu*DAH7PS tetramer than the dimer (Figure 2.8). The fit was reflected in the χ^2 values, which is a measure of goodness of fit (Table 2.3). SAXS MoW is an online server that uses the GNOM output to calculate the molecular mass of a protein and the number of subunits present. SAXS MoW estimated at the concentration analysed (~5.6 mg/mL) *Mtu*DAH7PS^{WT} exists as a tetramer in solution. The D_{max} of 127 Å was determined from the pair wise distribution analysis performed by GNOM. A D_{max} of 122 Å was estimated from the tetrameric *Mtu*DAH7PS crystal structure (PDB code: 3NV8).

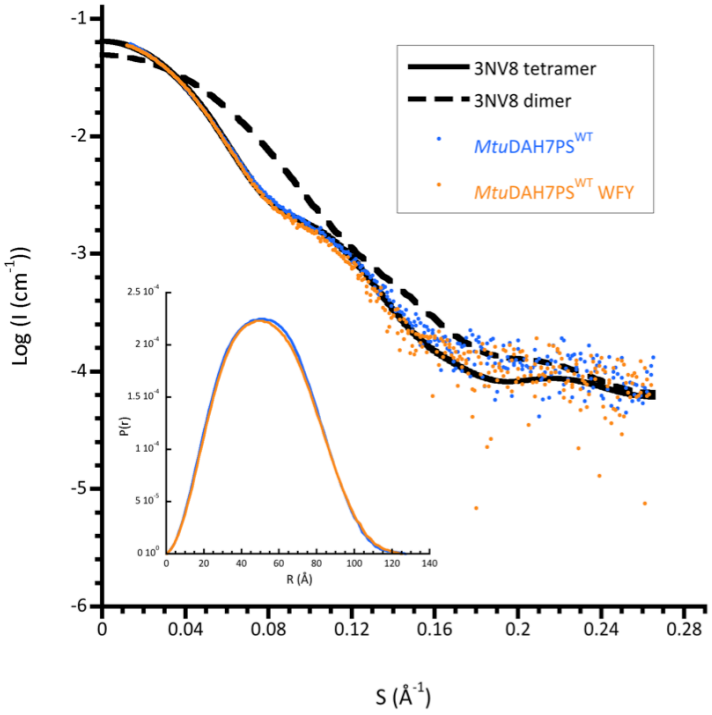

Figure 2.8 SAXS scattering profiles for *Mtu*DAH7PS^{WT} (blue) and *Mtu*DAH7PS^{WT} in the presence of Trp, Phe and Tyr (WFY) (orange) each ligand at a concentration of 200 µM. Also shown are the theoretical scattering profiles for an *Mtu*DAH7PS tetramer (solid black) and dimer (dash black) as predicted by CRYSOL using the crystal coordinates PDB code: 3NV8. Concentration of *Mtu*DAH7PS was ~5.6 mgmL^{-1}. Inset shows the pair wise distribution from analysis by GNOM.

Table 2.3 SAXS parameters from *Mtu*DAH7PS^{WT} with and without Trp, Phe and Tyr (WFY) present (each at a concentration of 200 µM). SAXS profiles were analysed with PRIMUS, GNOM, SAXS MoW and CRYSOL. Values are results from a single experminent.

***Mtu*DAH7PS**	**Wild type**	**Wild type WFY**
Guinier Analysis		
R_g (Å)	41.6 ± 0.3	41.9 ± 0.2
I (0) (cm^{-1})	0.168 ± 0.001	0.048 ± 0.001
Pair Distribution Analysis		
Real Space R_g (Å)	40.9 ± 0.2	41.0 ± 0.2
D_{max} (Å)	127	125
V_p, (Da)	282700	311707
Molecular Weight Estimates from SAXS MoW Analysis		
M_w from V_p (Da)	199 100	206 800
Nō of Subunits	4	4
CRYSOL Analysis with Tetrameric 3NV8		
R_{gE} (Å)	42.4 ± 0.2	41.3 ± 0.2
R_{gT} (Å)	40.6	41.0
χ^2	0.996	0.425

The scattering profile of *Mtu*DAH7PS^{WT} determined in the presence of 200 µM each of Trp, Phe and Tyr was almost identical to *Mtu*DAH7PS^{WT} alone (Figure 2.8). This implies that the binding of the allosteric ligands does not cause a detectable change in conformation or oligomeric state in solution, which agrees with the comparison of ligand bound and non-ligand bound *Mtu*DAH7PS^{WT} crystal structures.[48,71]

2.6.1. Native PAGE

Native polyacrylamide gel electrophoresis (PAGE) was conducted using blue native PAGE (detailed in Section 9.7.2). Blue native PAGE complexes the protein with Coomassie® G-250, making it negatively charged, so the protein will migrate toward the anode at the neutral pH of 7.5 regardless of its isoelectric point. *Mtu*DAH7PS has a predicted isoelectric point of 5.5 from ProtParam tool on the ExPASy proteomics server[105]. Results showed two oligomers were separated out at the low concentration of ~0.2 mg/mL at which *Mtu*DAH7PS was applied to the gel (Figure 2.9). One band is observed with a mass of ~50 kDa and a second with a mass of ~100 kDa consistent with the molecular mass of an *Mtu*DAH7PS^{WT} monomer and dimer respectively.

It is possible the Coomassie® G-250 dye may disrupt protein-protein interactions so caution must be taken to ensure the results of the blue native PAGE are not over interpreted. Consequently it was prudent to compliment these findings with further structural analysis of *Mtu*DAH7PS^{WT} by analytical ultracentrifugation.

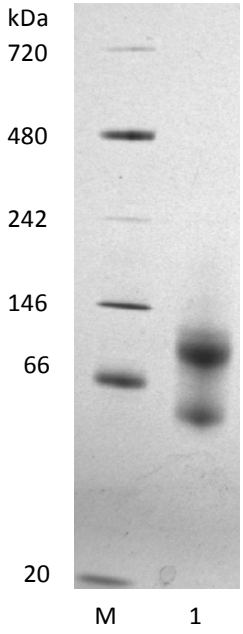

Figure 2.9 Blue native PAGE; Lane M displays the molecular weight marker and Lane 1 *Mtu*DAH7PS^{WT}.

2.6.2. Analytical ultracentrifugation (AUC) analysis

Sedimentation velocity experiments were carried out to assess the quaternary structure of *Mtu*DAH7PS^{WT} in solution. Ali Nazmi conducted the AUC experiments and assisted with the analysis of the collected data. During centrifugation a centrifugal force is applied to the samples causing the molecules to separate into layers based on their size and shape.[106-108] These layers result in boundaries and their movement can be monitored by UV absorbance. The rate of movement of the boundaries is used to calculate the sedimentation coefficient, a parameter used to define a molecule's behaviour during sedimentation.[106,107] The sedimentation coefficient (*s*) is more strictly defined as the ratio of a molecules sedimentation velocity to the force applied to it.[106] The sample preparation, experimental setup and analysis are described in Section 9.7.7.

The *Mtu*DAH7PS^{WT} data for each concentration was fitted to a continuous size distribution model to determine the sedimentation coefficients and calculated molecular mass (Figure 2.10A). At 1.0 mg/mL a single boundary was observed with a sedimentation coefficient of ~8.8 S. The calculated mass of this species was ~199 kDa, very close to the expected 204 kDa of an *Mtu*DAH7PS tetramer. At 0.4 mg/mL

the boundary had a slightly lower sedimentation coefficient of ~8.5 S, giving a mass of ~164 kDa, less than expected for an *Mtu*DAH7PS tetramer. The lowest concentration (0.2 mg/mL) data revealed two boundaries were present. The major species had a sedimentation coefficient of ~8.6 S and again most likely corresponds to a tetramer. The second boundary has a lower sedimentation coefficient of ~5.7 S with a calculated molecular mass of 81 kDa, less than 102 kDa molecular mass predicted for an *Mtu*DAH7PS dimer.

Presence of multiple boundaries in the 0.2 mg/mL sample indicated there was a mixture of dimer and tetramer in solution. If the interconversion between the dimer and tetramer is rapid relative to the time scale of the experiment the distribution of the boundaries will depend on concentration as seen here for *Mtu*DAH7PS.[109] At concentrations greater than 0.2 mg/mL the equilibrium was driven almost entirely toward the *Mtu*DAH7PS^{WT} tetramer whereas at 0.2 mg/mL and below the proportion of dimer present increased. The variation of the quaternary structure of *Mtu*DAH7PS^{WT} with concentration observed by AUC correlates well with the SAXS and native PAGE analyses previously described.

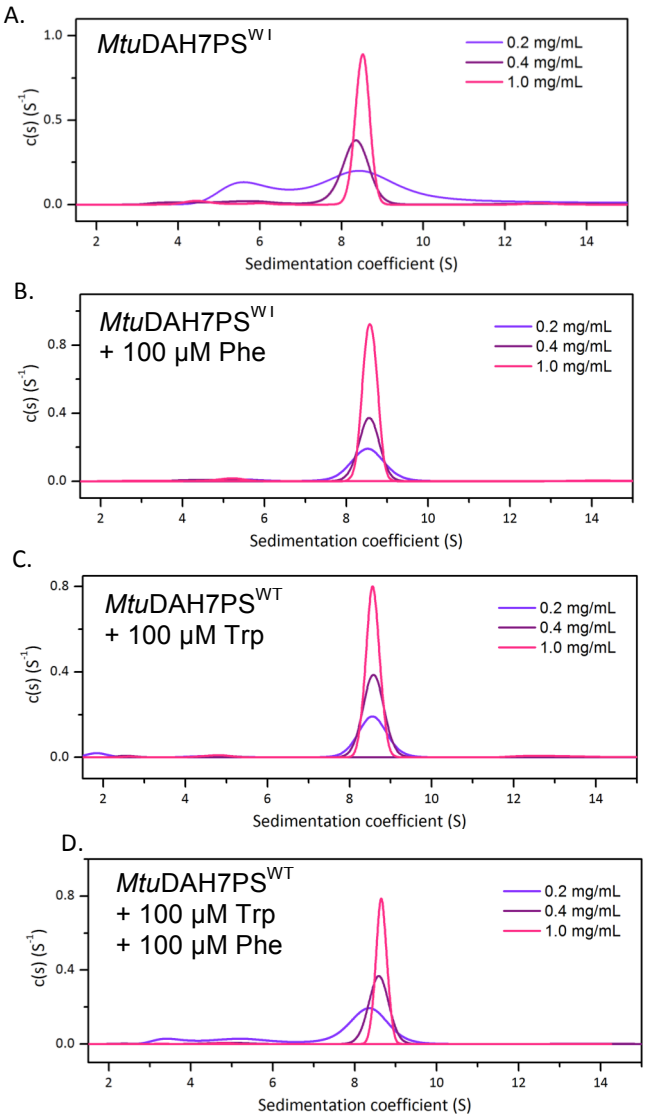

Figure 2.10 Normalised *c*(*s*) distribution functions from AUC data for *Mtu*DAH7PS^{WT} A. alone, B. plus 100 µM Phe, C. plus 100 µM Trp and D. plus 100 µM Trp and 100 µM Phe, analysed at 0.2 mg/mL (violet), 0.4 mg/mL (purple) and 1.0 mg/mL (pink). AUC data, fits and residuals are provided in Appendix II.

The most remarkable finding from the analytical ultracentrifugation (AUC) studies was how the presence of 100 µM of Trp and/or Phe resulted in single predominant species being detected at all concentrations (Figure 2.10B-D). The sedimentation coefficient for each set of experiments, with Trp, Phe or both were all ~8.6 S and gave a calculated molecular mass of ~174 kDa, the expected molecular mass of 204 kDa for the *Mtu*DAH7PS tetramer. The allosteric binding sites are all located in close proximity to either the tight dimer (sites 1 and 2) or weak dimer (Trp site) interfaces, so it is

plausible ligand binding could stabilise the *Mtu*DAH7PS^{WT} tetramer, as suggested by these findings. The *Mtu*DAH7PS tetramer may in all likelihood be the functional regulatory species.

2.7. Chapter summary

Successful expression and purification of *Mtu*DAH7PS^{WT} gave an active enzyme with kinetic parameters comparable to those previously reported.[48,70] In agreement with previous work synergistic regulation of *Mtu*DAH7PS^{WT} was also observed.[48] Addition of Trp and either Phe or Tyr to *Mtu*DAH7PS^{WT} resulted in a huge reduction in enzymatic activity, which could not be achieved by any single aromatic amino acid even at very high concentrations. For the first time this study showed the regulation of *Mtu*DAH7PS^{WT} activity was subject to ternary synergy, with the presence of all three aromatic amino acids almost completely abolishing enzymatic activity.

Biophysical characterisation by DSF indicated each aromatic amino acid makes a separate contribution to the overall thermal stability of the enzyme. ITC studies revealed the binding of Tyr to *Mtu*DAH7PS^{WT} enhances the affinity of *Mtu*DAH7PS^{WT} for Trp and Phe. Similarly Phe binding enhances *Mtu*DAH7PS^{WT} affinity for Tyr and Trp yet Trp binding will only enhance the affinity of *Mtu*DAH7PS^{WT} for Phe and not Tyr.

Evaluation of *Mtu*DAH7PS^{WT} by SAXS, AUC and native PAGE revealed the concentration dependence of the observed quaternary structure. At high concentrations AUC and SAXS showed *Mtu*DAH7PS^{WT} exists primarily as a tetramer. As the concentration was reduced, the proportion of dimer (and possibly even monomer if the native PAGE is believed) increases, indicating *Mtu*DAH7PS^{WT} exists in a dynamic equilibrium. Furthermore the addition of ligand (Trp or Phe) drives the equilibrium towards the tetrameric *Mtu*DAH7PS species as shown by AUC, suggesting the tetramer may be the functionally relevant regulatory species.

3. *Mtu*DAH7PS has a Phe-selective site and a Tyr-selective site

3.1. Introduction

*Mtu*DAH7PS is subject to a highly sophisticated feedback regulatory mechanism in which all three aromatic amino acids contribute to the total inhibition observed (Section 2.4.3) Analysis of multiple ligand bound crystal structures clearly shows the presence of three distinct allosteric binding sites.[48,71,91] These have been designated the Trp site, and sites 1 and 2. Trp has only been observed to occupy the Trp site, in the crystal structures reported to date. The binding preference of sites 1 and 2 is more ambiguous, as both sites have been observed to bind Phe and Tyr in the various liganded crystal structures.[48,71,91] The work described in this chapter has investigated the specificity and selectivity of sites 1 and 2 for Phe and Tyr in order to establish the role and function of each site. This was achieved by disrupting ligand binding at each site through site-directed mutagenesis to substitute key binding site residues. The properties of the enzyme variants and the impact of the changes on *Mtu*DAH7PS regulation were monitored by kinetic and biophysical techniques.

3.1.1. Architecture of site 1

Site 1 is located at the tight dimer interface ~23 Å from the active site and has been shown to be occupied in each chain of the homotetrameric MtuDAH7PS structure. The analysis of several ligand bound crystal structures revealed the key residues involved in binding ligands at site 1 (

Figure 3.1A).[48,71,91] Phe binds to site 1 through contacts formed between the carboxyl group of the bound amino acid with the side chains of residues Arg171, Asn175 (α2 helix) and the α-amino group

of the bound ligand hydrogen bonding to the main chain carbonyl oxygen of Phe91 (β1-α1 loop). The benzyl group of the ligand is tucked into a hydrophobic pocket created by Val51* (α0b helix), Val55*, Pro56* (α0b-α0c), Tyr173*, Ala174*, Ala174 and Ala178 (α2 helix), Residues from the β0 strand from the N-terminal extension of the adjacent chain cap the binding pocket. Asp6* forms a hydrogen bond to a water molecule which coordinates to the carbonyl of the bound ligand. Trp3* is positioned between two adjacent site 1 binding sites, one from each subunit (Phe ligands bind ~8 Å apart) and contributes to both. The architecture of site 1 is similar in all subunits.

Alignment of non-ligand bound (PDB code: 3NV8) and Trp- and Phe-bound tetrameric *Mtu*DAH7PS crystal structures (PDB code: 3KGF) gives a RMSD of 0.271 Å between equivalent C_α atoms, revealing little change in overall conformation

Figure 3.1B). Close inspection of the site 1 binding site reveals that although the critical residues retain similar positions, the cap provided by β0 strand is positioned differently in the unliganded structure, resulting in residues Trp3* to Asp6* being moved along by ~10 Å. In the absence of allosteric ligands Asp6* no longer coordinates to a water molecule (the water is not observed at all) and its side chain carboxyl group is orientated away from the binding site. Trp3* has also moved, its side chain no longer contributing to the site 1 binding site of either chain.

Alignment of the Trp and Phe ligand bound crystal structure (PDB code: 3KGF) with the crystal structure in which Phe only occupies site 1 (PDB code: 2YPO) shows the there is very little difference in the structures (C_α RMSD 0.232 Å). The Phe ligand is found in the exact same orientation in both of these structures and all residues contributing to the formation of site 1 are in identical positions (

Figure 3.1C).

Further comparison of the tetrameric Trp and Phe ligand bound structure with a Tyr soaked crystal structure (PDB code: 2YPP) shows Tyr bound at site 1, forming contacts that are remarkably similar to when Phe is bound (C_α RMSD 0.287 Å) (

Figure 3.1D). The benzyl ring of the Tyr is slightly repositioned in the hydrophobic binding pocket to allow the hydroxyl group of the side chain to coordinate via a water molecule to the main chain carbonyl oxygen of Ala174.

* Indicates residues contributed to the site by the adjacent subunit

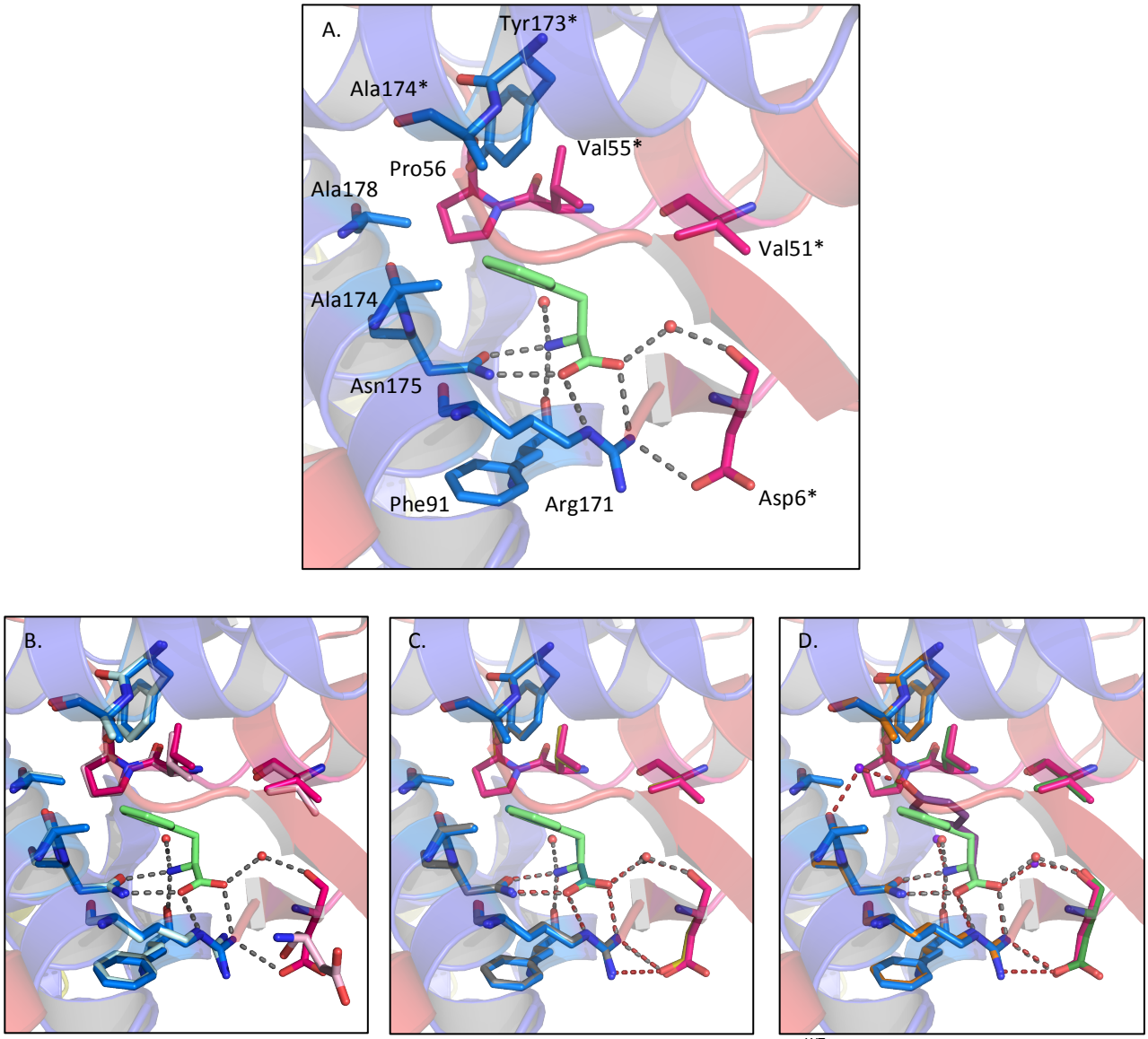

Figure 3.1 Critical residues involved in ligand binding at site 1. A. *Mtu*DAH7PS^{WT} Trp and Phe soaked crystal structure (PDB code: 3KGF, 2.00 Å resolution). Backbone carbons are shown in cartoon form with the core barrel and N-terminal extension coloured blue and red respectively and key residues shown in stick form. The carbons of the bound Phe ligand are shown in light green, coordinated waters are shown as red spheres and the dashed grey lines represent hydrogen bonding interactions. B. Alignment of A. with non-ligand bound crystal structure (PDB code: 3NV8, 2.25 Å resolution, C_α RMSD 0.271 Å). Key residues of 3NV8 are shown as sticks in light blue and light pink (coloured by core and N-terminal extension respectively). C. Alignment of A. with the low concentration Phe soaked crystal structure (PDB code: 2YP0, 2.00 Å resolution, C_α RMSD 0.232Å). Key residues of 2YP0 are shown as sticks in grey and mustard (coloured by core and N-terminal extension respectively), carbons of the Phe ligand are coloured teal and hydrogen bonds are shown in red. D. Alignment of A. with the Tyr soaked crystal structure (PDB code: 2YPP, 2.30 Å resolution, C_α RMSD 0.287Å). Key residues of 2YPP are shown as sticks in orange and dark green (coloured by core and N-terminal extension respectively), carbons of the bound Tyr ligand are coloured deep purple and hydrogen bonds are shown in red

3.1.2. Architecture of site 2

This site is located ~20 Å from site 1 and ~35 Å from the active site. Phe or Tyr has only ever been observed to occupy site 2 at one subunit of the asymmetric unit, thus two of the available four sites of

the tetrameric unit.[48,71,91] It is unclear if crystal packing restricts or alters ligand access to site 2 at the remaining unoccupied sites of the subunit. In the Tyr-bound crystal structure Tyr occupies two different allosteric binding sites (PDB code: 2YPP).[91] The first Tyr is found bound at Site 1, as described in Section 3.1.1, the second Tyr at site 2. The carboxyl group of the bound Tyr forms two hydrogen bonds to each guanidinium group of the side chains of Arg256 and Arg23 (from the α0a and α3 helices respectively) (Figure 3.2A). In addition the α-amino group of the bound Tyr hydrogen bonds to the backbone carbonyl oxygen of Arg256, the side chain of Glu53 (α0b helix) and coordinates via a water molecule to Leu259 (α3-β4 loop). The residues Leu18 (β0-α0a loop), Leu259, Leu261, and Leu271 (α3-β4 loop) form the hydrophobic pocket for the benzyl ring. The hydroxyl group of the Tyr forms a hydrogen bond to the main chain carbonyl oxygen of Leu261. The backbone amide nitrogen group of Pro16 (β0-α0a loop) coordinates directly to the hydroxyl group of the ligand.

Alignment of the tetrameric Tyr-bound structure with the non-ligand bound crystal structure (PDB code: 3NV8) reveals only small changes in the conformation of site 2 due to ligand binding (Figure 3.2B). Most notably the positions of Pro16 and Leu18 have been altered due to the movement of the β0-α0a loop to allow coordination of the amide nitrogen of Pro16 to the hydroxyl group of the bound Tyr.

The binding of Trp at the Trp site in the Trp- and Tyr-bound crystal structure (PDB code: 2YPQ) does not alter Tyr binding at site 2 (Figure 3.2C). Only minor movements in residues contributing to site 2 are observed when the Trp- and Tyr-bound tetrameric structure is compared to the Tyr soaked crystal structure (C_α RMSD 0.529 Å).

Alignment of the Trp and Phe soaked crystal structure (PDB code: 3KGF), with Phe bound at site 2, shows how Phe can not form a hydrogen bond to Pro16 leaving the β0-α0a loop in a similar position for site 2 as is observed in the absence of ligand (Figure 3.2D).

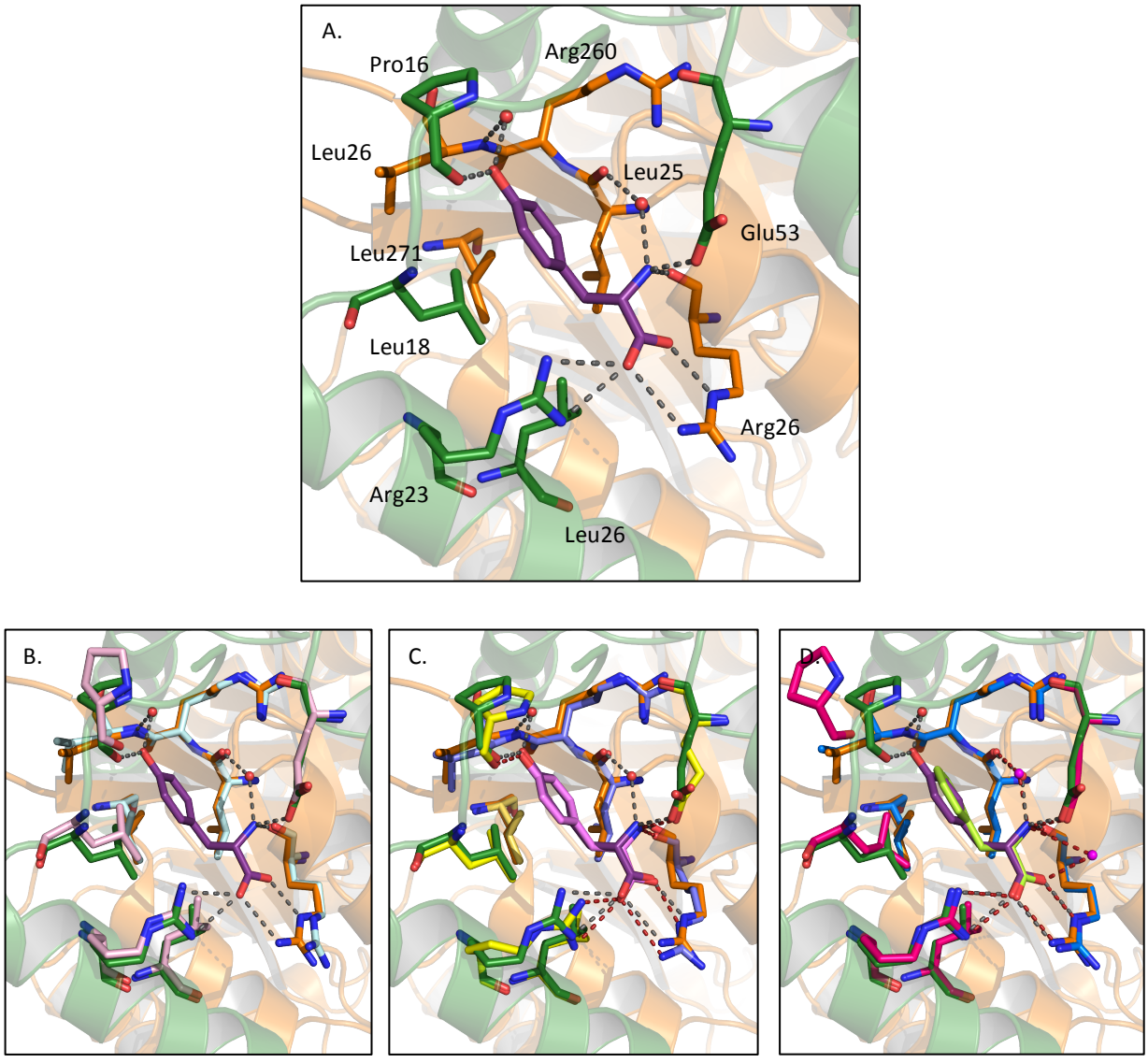

Figure 3.2 Critical residues involved in ligand binding at site 2. A. *Mtu*DAH7PS Tyr soaked crystal structure (PDB code: 2YPP, 2.30 Å resolution). Backbone carbons are shown in cartoon form with the core barrel and N-terminal extension coloured orange and dark green respectively and key residues shown in stick form. The carbons of the bound Tyr ligand are shown in deep purple, coordinated waters are shown as red spheres and the dashed grey lines represent hydrogen bonding interactions. B. Alignment of A. with unliganded crystal structure (PDB code: 3NV8, 2.25 Å resolution, C_α RMSD 0.208 Å). Key residues of 3NV8 are shown as sticks in light blue and light pink (coloured by core and N-terminal extension respectively). C. Alignment of A. with the Tyr soaked crystal structure (PDB code: 2YPQ, 2.76 Å resolution, C_α RMSD 0.529 Å). Key residues of 2YPQ are shown as sticks in yellow and light purple (coloured by core and N-terminal extension respectively), carbons of the Tyr ligand are coloured pink and hydrogen bonds are shown in red. D. Alignment of A. with the Trp and Phe soaked crystal structure (PDB code: 3KGF, 2.00 Å resolution, C_α RMSD 0.287Å). Key residues of 3KGF are shown as sticks in blue and red (coloured by core and N-terminal extension respectively), carbons of the bound Phe ligand are coloured light green and hydrogen bonds are shown in red.

3.2. Chapter aims

The aim of the work described in this chapter was to differentiate the roles that sites 1 and 2 play in the ternary synergistic inhibition observed for *Mtu*DAH7PS. Site-directed mutagenesis was used to generate two *Mtu*DAH7PS variants with ligand binding hindered at either site 1 or site 2, leaving the alternate site available for ligand binding. Theoretically these variants allow sites 1 and 2 to be investigated separately, albeit still in combination with the Trp site. This approach has enabled the investigation into the ligand preferences of each site and the relationship between the occupancy of each site and the inhibitory response.

3.3. Preparation of *Mtu*DAH7PS^{R171A} and *Mtu*DAH7PS^{R256A}

3.3.1. Selection of residues for mutagenesis

The primary goal of the site-directed mutagenesis was to generate *Mtu*DAH7PS variants incapable of binding ligands at either site 1 or site 2. To start residues were identified which make a number of stabilising contacts to the bound ligand through their side chain. Replacement of the identified residue with an Ala effectively removes the side chain and its functional group, whilst preserving the rigidity of the backbone conformation to maintain the secondary structure.

When Tyr or Phe binds to site 1 Arg171 forms two hydrogen bonds between the nitrogen's of its guanidinium group and the carboxyl of the bound ligand (

Figure 3.1A). Thus the substitution of Arg171 to Ala is an excellent candidate for mutagenesis. Similarly, the guanidinium group of Arg256 forms two hydrogen bonds to the carboxyl group of the

bound ligand (either Tyr or Phe) at site 2 (Figure 3.2A). Thus substitution of Arg256 to Ala would prevent these contacts, and so would be expected to significantly attenuate ligand binding at site 2.

3.3.2. Mutagenesis, expression and purification

SDM was performed using the QuikChange® Lightning Site-Directed Mutagenesis Kit (Stratagene). Primers were designed using the QuikChange® Primer Design tool (Agilent technologies) to incorporate the desired mutations and the pProEx-Hta vector containing the *Mtu*DAH7PS gene was used as the template for the PCR detailed in Section 9.2.

Once DNA sequencing confirmed the incorporation of the correct mutations the SDM products were electroporated into BL21(DE3) pGroESL cells. Expression and protein purification followed the methodology previously detailed for *Mtu*DAH7PS^{WT} in Section 9.5.

3.3.3. Confirmation of product

SDS-PAGE analysis of the final purified *Mtu*DAH7PS variants showed both were highly pure, producing a single protein band at ~50 kDa in agreement with the expected molecular mass of an *Mtu*DAH7PS monomer (Figure 3.3). Mass spectrometry confirmed the final purified proteins were of the correct molecular mass. Both *Mtu*DAH7PS^{R171A} and *Mtu*DAH7PS^{R256A} had experimental masses that perfectly matched their expected mass of 50,699 Da (Table 3.1).

Table 3.1 Calculated molecular masses determine from amino acid sequence and empirical molecular masses determined from mass spectroscopy for *Mtu*DAH7PS^{R171A} and *Mtu*DAH7PS^{R256A}.

Variant	Calculated M_w (kDa)	Empirical M_w (kDa)
*Mtu*DAH7PS^{R171A}	50699	50699
*Mtu*DAH7PS^{R256A}	50699	50699

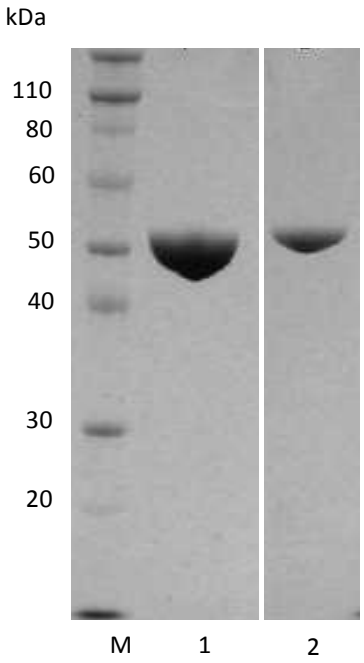

Figure 3.3 SDS-PAGE gel illustrating the size and purity of each purified *Mtu*DAH7PS variant. Lane M molecular weight marker; Lane 1 *Mtu*DAH7PS^{R171A} and Lane 2 *Mtu*DAH7PS^{R256A}.

3.4. Structural analysis

3.4.1. Comparison of secondary structure

CD spectrophotometry permits assessment of protein secondary structure by using the uneven absorption of left- and right-handed circularly polarised light to detect secondary structural elements within proteins.[110,111] The CD spectra were measured in 20 mM Tris buffer at pH 7.5, and the protocol is detailed in Section 9.7.4.

Comparison of the CD spectra of the *Mtu*DAH7PS variants with *Mtu*DAH7PS^{WT} confirmed the alteration to the amino acids sequence had not perturbed protein folding (Figure 3.4).

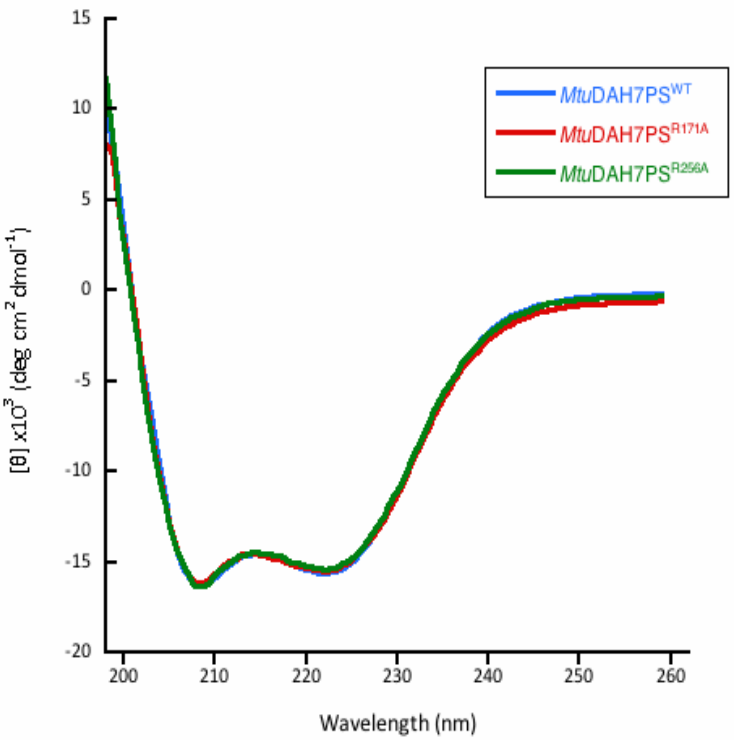

Figure 3.4 CD spectra for *Mtu*DAH7PS^{WT} (blue), *Mtu*DAH7PS^{R171A} (red) and *Mtu*DAH7PS^{R256A} (green).

3.4.2. Quaternary structure analysis in solution

The SAXS was used to assess the quaternary structure of *Mtu*DAH7PS^{R171A} and *Mtu*DAH7PS^{R256A} in solution. The experimental SAXS scattering profiles of both variant enzymes were almost identical to *Mtu*DAH7PS^{WT}, correlating well with the theoretical scattering profile predicted by CRYSOL[103] for the *Mtu*DAH7PS tetramer from the crystal coordinates PDB code: 3NV8 (Figure 3.5). Furthermore the parameters derived from the scattering profiles of *Mtu*DAH7PS^{R171A} and *Mtu*DAH7PS^{R256A} were in good agreement with the parameters of *Mtu*DAH7PS^{WT} (Figure 3.5, Table 3.2). Thus at high concentrations (>4.5 mg/mL) *Mtu*DAH7PS^{R171A} and *Mtu*DAH7PS^{R256A} adopt the same quaternary structure as *Mtu*DAH7PS^{WT} in solution.

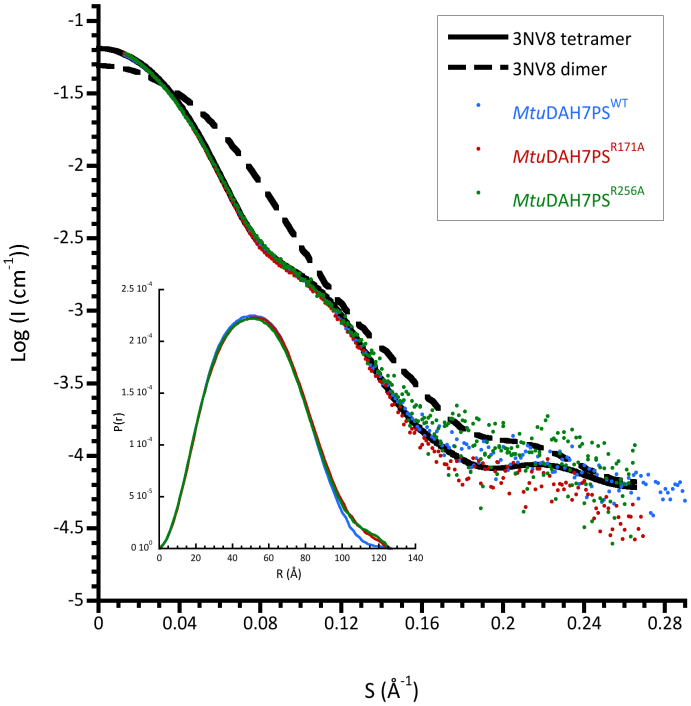

Figure 3.5 SAXS scattering profiles of *Mtu*DAH7PS^{WT} (blue), *Mtu*DAH7PS^{R171A} (red) and *Mtu*DAH7PS^{R256A} (green). Also shown is the theoretical scattering for the tetrameric (black) and dimeric (black dash) species from PDB code: 3NV8. Inset pair-wise distribution profiles.

Table 3.2 SAXS parameters determined from the SAXS scattering profile of *Mtu*DAH7PS^{WT}, *Mtu*DAH7PS^{R171A} and *Mtu*DAH7PS^{R256A}. SAXS profiles were analysed with PRIMUS, GNOM, SAXS MoW and CRYSOL. Values determined from a single SAXS experiment.

***Mtu*DAH7PS**	**Wild type**	**R171A**	**R256A**
Guinier Analysis			
R_g (Å)	41.6 ± 0.3	42.8 ± 0.2	53.2 ± 0.3
I (0) (cm^{-1})	0.168 ± 0.001	0.188 ± 0.001	0.071 ± 0.001
Pair Distribution Analysis			
Real Space R_g (Å)	40.9 ± 0.2	41.7 ± 0.2	41.80 ± 0.07
D_{max} (Å)	127	126	125
V_p, (Da)	282700	327700	291600
Molecular Weight Estimates from SAXS MoW Analysis			
M_w from V_p (Da)	199 100	204300	198700
Nō of Subunits	4	4	4
CRYSOL Analysis with Tetrameric 3NV8			
R_{gE} (Å)	42.4 ± 0.2	42.3 ± 0.2	42.4 ± 0.2
R_{gT} (Å)	40.6	40.6	40.6
χ^2	0.996	0.966	0.939

Unfortunately, due to the tendency for *Mtu*DAH7PS to aggregate, all SAXS analysis was conducted by passing the sample through a size exclusion chromatography column just prior to analysis, limiting analysis of *Mtu*DAH7PS to concentrations above 4.5 mg/mL. As an alternative means of probing the quaternary structure at very low concentrations blue native polyacrylamide electrophoresis (PAGE) was used. *Mtu*DAH7PS^{R171A} and MtuDAH7PS^{R256A} were applied to the gel at ~ 0.2 mg/mL and found to exist as two species in solution. One band at ~50 kDa, and another at ~100 kDa, consistent with expected molecular masses of the *Mtu*DAH7PS monomer and dimer respectively (Figure 3.6). The ratio of intensity between the two bands for the two *Mtu*DAH7PS variants is similar to *Mtu*DAH7PS^{WT}. The results of the blue native PAGE and SAXS imply the Arg to Ala substitution introduced into each *Mtu*DAH7PS variant has not caused any changes to the quaternary structure.

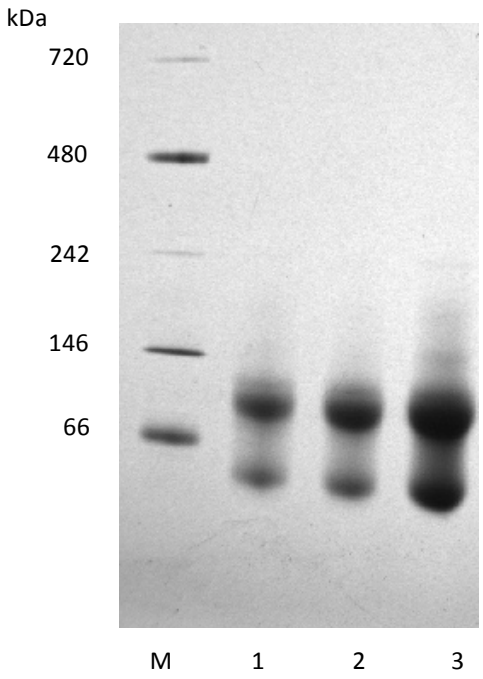

Figure 3.6 Blue native PAGE; Lane M displays the molecular weight marker; Lane 1 *Mtu*DAH7PS^{WT}; Lane 2 *Mtu*DAH7PS^{R256A} and Lane 3 *Mtu*DAH7PS^{R171A}.

3.5. Determination of kinetic parameters

The kinetic assays for *Mtu*DAH7PS^{R171A} and *Mtu*DAH7PS^{R256A} were determined under the same conditions as *Mtu*DAH7PS^{WT} (detailed in Section 9.9.1) and fitted to the Michaelis-Menten equation to derive the kinetic parameters. The kinetic parameters showed some variation to those of *Mtu*DAH7PS^{WT} (Table 3.3). These results showed the substitutions introduced to *Mtu*DAH7PS^{R171A} and *Mtu*DAH7PS^{R256A} have no significant adverse effects on the catalytic abilities of the enzymes.

Table 3.3 Comparison of kinetic parameters determined from a single set of Michaelis-Menten kinetics for *Mtu*DAH7PS^{WT}, *Mtu*DAH7PS^{R171A} and *Mtu*DAH7PS^{R256A}. For Michaelis-Menten plots refer to Appendix I. Error bars represent the error of fit of the equation to the data as determined by least squares fit.

***Mtu*DAH7PS**	K_m^{E4P} (μM)	K_m^{PEP} (μM)	k_{cat} (s^{-1})	**Catalytic Efficiency** k_{cat}/K_m^{E4P} ($s^{-1}mM^{-1}$)	**Catalytic Efficiency** k_{cat}/K_m^{PEP} ($s^{-1}mM^{-1}$)
Wild type	28 ± 2	37 ± 4	4.7 ± 0.1	170 ± 20	130 ± 20
R171A	35 ± 3	60 ± 6	7.0 ± 0.3	200 ± 30	120 ± 20
R256A	33 ± 1	16 ± 2	5.5 ± 0.1	170 ± 10	340 ± 50

3.6. Assessment of ligand binding

3.6.1. Thermal stability

DSF of *Mtu*DAH7PS^{WT} demonstrated the melting temperature (T_m) increased in the presence of the aromatic amino acids (Section 2.5.1). Thus DSF can be used as a tool to quickly evaluate whether the aromatic amino acids are likely to bind to the proteins by monitoring the increase in thermal stability of the *Mtu*DAH7PS variants. DSF assay conditions and experimental setup are described in Section 9.8.1.

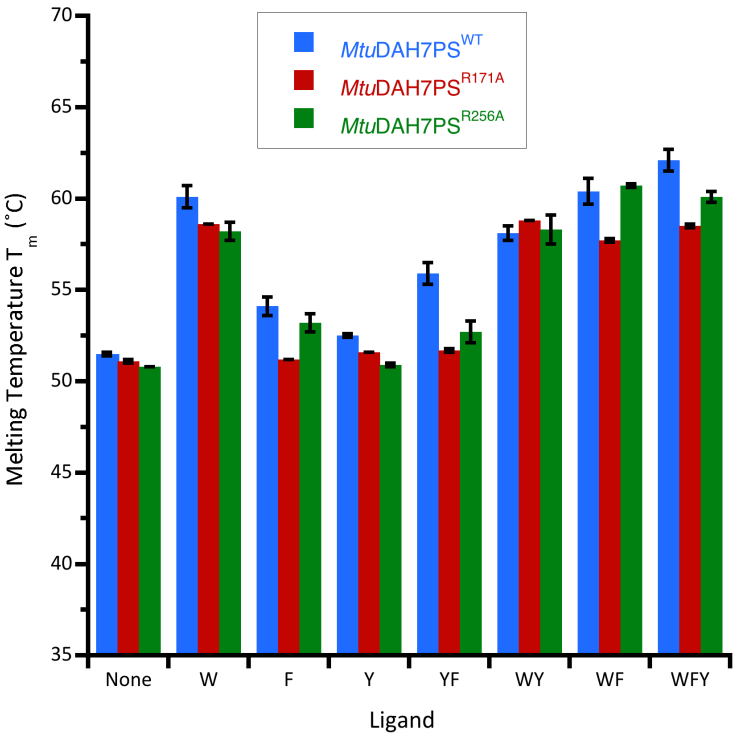

Figure 3.7 Thermal melting points determined by DSF for *Mtu*DAH7PS^{WT} (blue), *Mtu*DAH7PS^{R171A} (red) and *Mtu*DAH7PS^{R256A} (green). Error bars depict the standard deviation of triplicate measurements. P-values provided in appendix V.

Unlike wild type enzyme, *Mtu*DAH7PS^{R171A} displayed no increase in thermal stability in the presence of Phe (Figure 3.7). As the substitution of Arg171Ala is designed to disrupt ligand binding at site 1, these results offer evidence Phe must be able to bind to site 1 to improve *Mtu*DAH7PS thermal stability. Likewise the thermal stability of *Mtu*DAH7PS^{R256A} was unaffected by Tyr. Recalling *Mtu*DAH7PS^{R256A}

has been engineered to disrupt ligand binding at site 2, the inability of Tyr to stabilise *Mtu*DAH7PS^{R256A} indicates Tyr binding to site 2 plays an integral part in the stabilisation of *Mtu*DAH7PS by Tyr.

Both *Mtu*DAH7PS^{R171A} and *Mtu*DAH7PS^{R256A} were significantly stabilised by Trp in accordance with what was observed for the wild type enzyme, suggesting Trp binding does take place. Careful inspection also revealed the change in T_m for *Mtu*DAH7PS^{R171A} in the presence of Trp and Phe was equivalent to that observed for Trp alone. Similarly the presence of Trp, Phe and Tyr yielded an increase in T_m of *Mtu*DAH7PS^{R171A} equivalent to the increase observed for Trp and Tyr. Together these findings suggest the Arg171Ala substitution disrupted Phe binding at site 1.

Likewise *Mtu*DAH7PS^{R256A} displayed almost an identical increase in T_m in the presence of Trp and Tyr, but in the presence of all three aromatic acids the T_m was 0.5 ˚C less than in the presence of Trp and Phe.

Furthermore both *Mtu*DAH7PS variants demonstrated an increase in their thermal stability equal to the additive affect of each component when multiple aromatic amino acids were present. This was consistent with results for *Mtu*DAH7PS^{WT} and indicates multiple ligands are still able to bind the *Mtu*DAH7PS variants simultaneously.

3.6.2. Binding affinities

Although DSF can detect ligand binding by changes in thermal stability it does not absolutely prove a ligand has not bound simply because no change is observed. A ligand that binds to an *Mtu*DAH7PS variant but is unable to elicit an increase in thermal stability would not increase the determined melting temperature. ITC directly measures the enthalpy changes associated with ligand binding to *Mtu*DAH7PS. This provides definitive and quantitative information about the ability of each *Mtu*DAH7PS variant to bind a particular ligand. Preparation, experimental conditions and setup are

detailed in Section 9.8.2. The K_d are determined by iteratively fitting the appropriate model (either a one or two site binding model) to the ITC data using Origin® software.

The isotherm for binding of Phe to *Mtu*DAH7PS^{R171A} displayed very weak binding with a K_d in excess of 1 mM and beyond the detection limit of the VP ITC system (Figure 3.8A). Recalling the Arg171Ala substitution of *Mtu*DAH7PS^{R171A} was intended to disrupt Tyr or Phe binding at site 1, and given the K_d of ~21 µM between *Mtu*DAH7PS^{WT} and Phe this result confirmed Phe does not bind to site 2 (or the Trp site) of *Mtu*DAH7PS^{R171A} with any significant affinity. Furthermore the K_d determined for the binding of Phe to *Mtu*DAH7PS^{R256A} was very similar to *Mtu*DAH7PS^{WT} (Figure 3.8E, Table 3.4). As *Mtu*DAH7PS^{R256A} was the variant with impaired ability to bind ligands at site 2 this was further proof Phe preferentially binds to site 1.

Table 3.4 Dissociation constants determined for *Mtu*DAH7PS^{WT}, *Mtu*DAH7PS^{R171A} and *Mtu*DAH7PS^{R256A} by ITC. A background Phe concentration of 50 µM was used. * Denotes values determined by Richard Hutton.[71,91] — Indicates no background ligand is present. Values were determined from a single ITC experiment. Error represents error of curve fitting to the data set by least squares fit.

Titrated Ligand	Background Ligand	*Mtu*DAH7PS		
		Wild Type K_d (µM)	R171A K_d (µM)	R256A K_d (µM)
Phe	—	21 ± 1*	>>1000	17 ± 1
Tyr	—	39 ± 1*	19 ± 2	54 ± 4
Tyr	Phe	12 ± 1*	40 ± 3	120 ± 20
Trp	—	4.7 ± 0.1*	1 ± 8 and 1 ± 3	3.4 ± 0.4

Tyr was able to bind reasonably well to *Mtu*DAH7PS^{R256A} with a K_d higher than that observed for the wild type enzyme (Figure 3.8F, Table 3.4). Tyr has only ever been observed to concurrently occupy sites 1 and 2 crystallographically.[91] The substitution introduced to *Mtu*DAH7PS^{R256A} was designed to impair binding at site 2. Hence the K_d determined between Tyr and *Mtu*DAH7PS^{R256A} could be considered primarily a measure of how tightly Tyr binds to site 1. Interestingly, the K_d between Tyr and *Mtu*DAH7PS^{R171A} showed that Tyr binds more tightly to this variant than *Mtu*DAH7PS^{R256A} (Figure 3.8B, Table 3.4). Although Tyr can bind to both sites it binds more tightly to site 2 than site 1.

The K_d between Tyr and *Mtu*DAH7PS^{R256A} was shown to increase markedly when the variant enzyme was incubated with Phe prior to the titration of Tyr (Figure 3.8G, Table 3.4). A similar result was observed for *Mtu*DAH7PS^{R171A} preincubated with Phe (Figure 3.8C), but with a less significant increase in K_d. This suggests there may be strong competition between Tyr and Phe to occupy site 1, and despite the very weak binding of Phe to site 2, Tyr also competes with Phe somewhat to occupy site 2. In contrast the K_d between *Mtu*DAH7PS^{WT} and Tyr decreased if the enzyme was preincubated with Phe.

The K_d between Trp and *Mtu*DAH7PS^{R256A} was approximately that same as for *Mtu*DAH7PS^{WT} suggesting Trp binding is unaffected by the substitution (Figure 3.8H, Table 3.4). The ITC data for both *Mtu*DAH7PS^{WT} and *Mtu*DAH7PS^{R256A} fitted nicely to a single site binding model. On the other hand the isotherm for the titration of Trp into a cell containing *Mtu*DAH7PS^{R171A} produced an isotherm with the distinctive shape of a two site binding model (Figure 3.8D). Two separate and independent binding events for Tyr to *Mtu*DAH7PS were recorded with the same K_d but opposite enthalpies. Intriguingly, Trp binding to *Mtu*DAH7PS^{R171A} was tighter, for both binding events, than *Mtu*DAH7PS^{WT} so fortunately Trp binding has not been compromised.

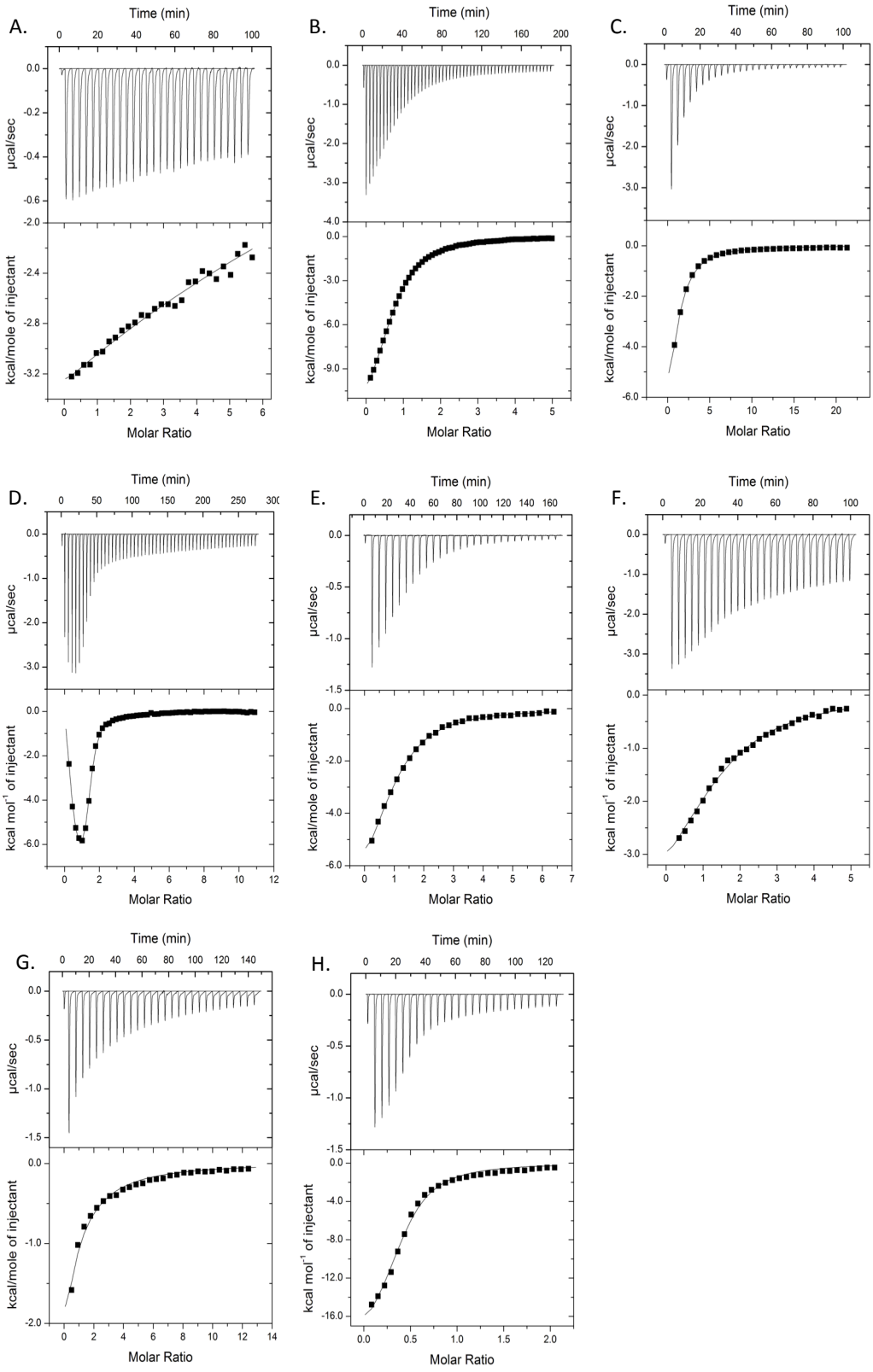

Figure 3.8 ITC data for the interaction of A. 30 µM *Mtu*DAH7PS^{R171A} with 2 mM Phe titrant, B. 30 µM of *Mtu*DAH7PS^{R171A} with 3 mM Tyr titrant; C. 30 µM *Mtu*DAH7PS^{R171A} preincubated with 50 µM Phe and 3 mM Tyr titrant; D. 70 µM *Mtu*DAH7PS^{R171A} with 3 mM Trp titrant; E. 30 µM *Mtu*DAH7PS^{R256A} with 900 µM Phe titrant, F. 60 µM *Mtu*DAH7PS^{R256A} with 2 mM Tyr titrant; G. 50 µM *Mtu*DAH7PS^{R256A} preincubated with 50 µM Phe and 3 mM Tyr titrant and H. 30 µM *Mtu*DAH7^{R256A} with 300 µM Trp titrant.

3.7. Disruption of feedback regulation

Previously inhibition studies were used to show binary and ternary combinations of the aromatic amino acids that included Trp inhibited *Mtu*DAH7PS^{WT} (Section 2.4.3). The loss of ligand binding to site 1 or site 2 should perturb this feedback regulation of *Mtu*DAH7PS if the affected site contributes to the regulatory function of *Mtu*DAH7PS. Kinetic assays were conducted under the standard inhibition assay conditions used to study the wild type enzyme detailed in Section 9.9.3.

*Mtu*DAH7PS^{R171A} displayed a huge reduction in sensitivity to the combination of Trp and Phe relative to the wild type protein, yet retained sensitivity to the combination of Trp and Tyr (Figure 3.9). In the presence of all three aromatic amino acids the level of inhibition achieved was equivalent to the inhibition achieved by Trp and Tyr. *Mtu*DAH7PS^{R171A} was designed to hinder ligand binding at site 1, thus only site 2 is available for Tyr and Phe binding. These results demonstrate Phe must occupy site 1 to elicit any inhibitory response in combination with Trp. As *Mtu*DAH7PS^{R171A} was still sensitive to Trp and Tyr, site 1 is not essential for regulatory sensitivity to Tyr, however it should be noted Trp and Tyr inhibition was ~20 % less effective than observed for *Mtu*DAH7PS^{WT}.

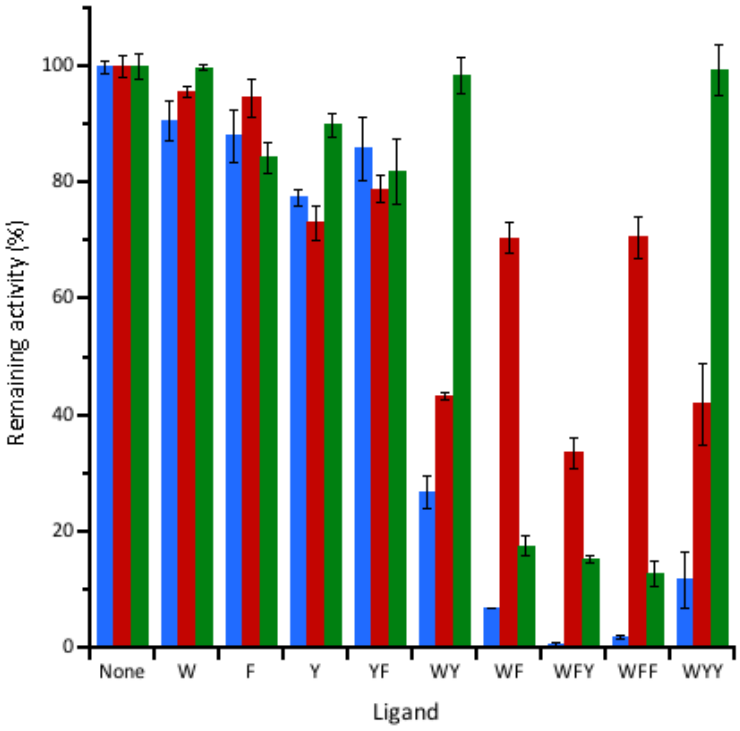

Figure 3.9 Remaining activity of *Mtu*DAH7PS^{WT} (blue), *Mtu*DAH7PS^{R171A} (red) and *Mtu*DAH7PS^{R256A} (green) in the presence of various single, binary and ternary combinations of aromatic amino acids. The aromatic amino acids are represented by their one letter code; Trp, W; Phe, F and Tyr, Y. Each letter also represents 200 µM of the corresponding aromatic amino acid. Error bars depict the standard deviation of triplicate measurements. P-values provided in appendix V.

Conversely, *Mtu*DAH7PS^{R256A} was strongly inhibited by the combination of Trp and Phe, but had lost the sensitivity to the combination of Trp and Tyr (Figure 3.9). The inhibitory response of *Mtu*DAH7PS^{R256A} in the presence of all three amino acids was equivalent to the combination of Trp and Phe. The substitution introduced to *Mtu*DAH7PS^{R256A} was intended to disrupt ligand binding at site 2, only. The sensitivity displayed to the presence of Trp and Phe by *Mtu*DAH7PS^{R256A} is evidence Phe binding at site 2 was nonessential for the regulatory response. The complete loss of sensitivity of *Mtu*DAH7PS^{R256A} to the combination of Trp and Tyr revealed Tyr binding to site 2 was essential for Tyr to inhibit *Mtu*DAH7PS activity. The combination of Trp, Phe and Tyr failed to reduce the activity of *Mtu*DAH7PS^{R171A} and *Mtu*DAH7PS^{R256A} to less than 1 % as observed for *Mtu*DAH7PS^{WT}. This indicates all three allosteric ligand binding sites must be occupied for the greatest inhibitory effect.

3.8. Chapter summary

The preparation and purification of both *Mtu*DAH7PS^{R171A} and *Mtu*DAH7PS^{R256A} was successful. Structural analysis by SAXS, native PAGE and CD showed both variants had similar structures to *Mtu*DAH7PS^{WT} in solution. Furthermore the kinetic parameters determined from the Michaelis-Menten kinetics of each *Mtu*DAH7PS variant showed no adverse affects to the catalytic efficiency of variant enzymes as a result of the introduced substitutions.

*Mtu*DAH7PS contains three distinct allosteric binding sites per subunit (Figure 3.10). Through crystallography one site has been shown to selectively bind Trp, even in the presence of Tyr or Phe.[48,69,71,91] Tyr and Phe have been shown to occupy both sites 1 and 2 in various crystal structures.[48,71,91] The introduction of the Arg171Ala substitution to site 1 of *Mtu*DAH7PS^{R171A} has prevented ligand binding to site 1, leaving only site 2 available for Phe and Tyr binding. Similarly, by mutating Arg256 to Ala ligand binding to site 2 has been prevented and Phe and Tyr can only bind to site 1. This allowed sites 1 and 2 to be investigated independently of each other. ITC and DSF studies demonstrated that Phe binds very poorly to *Mtu*DAH7PS^{R171A}. Inhibition studies of *Mtu*DAH7PS^{R171A} showed the enzyme activity was insensitive to the presence of Phe and only responded to the presence of Trp and Tyr. In conjunction with ITC and DSF, the inhibition studies illustrated that Phe does not bind readily to site 2 of *Mtu*DAH7PS.

Investigation of Phe binding to *Mtu*DAH7PS^{R256A} by ITC and DSF, showed that Phe binding to the enzyme is unaffected by the Arg256Ala substitution. Furthermore inhibition studies showed *Mtu*DAH7PS^{R256A} activity retained sensitivity to the combination of Trp and Phe. Thus Phe only needs to bind to site 1 to elicit an inhibitory response.

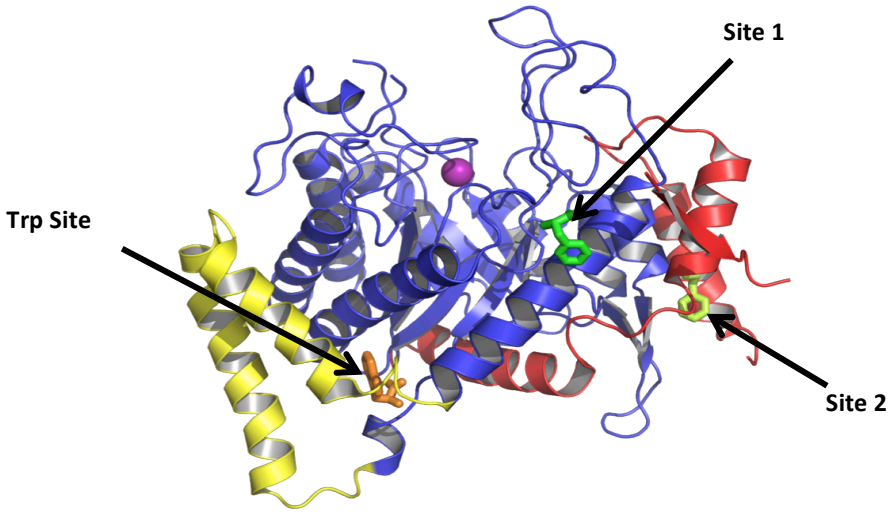

Figure 3.10 The subunit structure of *Mtu*DAH7PS soaked with Trp and Phe (PDB code: 3KGF). The core $(\beta/\alpha)_8$ barrel structure is coloured blue, the N-terminal extension is coloured red, the additional helices to the α2-β3 loop are coloured yellow and the metal ion (Mn^{2+}) is shown in purple. Trp is shown in orange bound to the Trp site. Phe bound to site 1 is shown in green and Phe bound to site 2 is shown in limon.

ITC and DSF studies showed *Mtu*DAH7PS^{R171A} was responsive to the presence of Tyr. This was further supported by the inhibition studies showing *Mtu*DAH7PS^{R171A} is inhibited by the combination of Trp and Tyr, but not quite as effectively as observed for *Mtu*DAH7PS^{WT}. These findings show Tyr is able to bind to site 2 and elicit an inhibitory response.

Remarkably ITC and DSF studies of *Mtu*DAH7PS^{R256A} revealed Tyr can bind to *Mtu*DAH7PS^{R256A} with considerable affinity, however the inhibition studies showed Trp and Tyr are ineffective at inhibiting *Mtu*DAH7PS^{R256A} activity. Overall these results suggested Tyr can also bind to site 1, although it does not provide an inhibitory response by binding in this position. How *Mtu*DAH7PS is able to distinguish between Phe and Tyr binding at site 1, given their structural similarity and similar binding modes, presents a new conundrum, worthy of further investigation.

Collectively these findings reveal site 1 can bind both Phe and Tyr. All kinetic and biophysical characterisation carried out in this chapter suggests Phe preferentially binds to site 1. Most importantly Tyr cannot regulate *Mtu*DAH7PS very well by occupying site 1 alone (in the presence of Trp) hence, site 1 is a Phe-selective site. This conclusion is in agreement with crystallographic studies

run in parallel to this research by Sebastian Reichau which show the soaking of an *Mtu*DAH7PS^{WT} crystal in a low concentration solution of Phe results in Phe only being observed to occupy site 1.[91]

Site 2 is exclusively a Tyr binding site and Tyr must bind to site 2 for an inhibitory response involving Trp to be observed. These observations indicate site 2 is a Tyr-selective site. There was little evidence to suggest Phe had a significant affinity for this site. However it should be noted, that although Tyr binding was required at site 2 for an inhibitory response involving Tyr, a greater level of inhibition was observed when Tyr was able occupy both site 1 and site 2. Curiously, all crystallographic data to date has only ever shown Tyr to occupy both sites 1 and 2.[48,71,91]

4. Interaction of *Mtu*CM with *Mtu*DAH7PS

4.1. Introduction

Early investigations of chorismate mutase (Rv0948c) from *M. tuberculosis* had reported *Mtu*CM as an unusually poor catalyst, with no known regulatory control.[78,83,84,86] In 2009 two articles were published describing the first crystal structure of a non-covalent complex between two enzymes of the shikimate pathway, *Mtu*DAH7PS and *Mtu*CM (PDB code: 2W19) (Figure 4.1A).[85,112] The authors demonstrated that the non-covalent complex between *Mtu*DAH7PS and *Mtu*CM boosted *Mtu*CM activity by two orders of magnitude, but left the *Mtu*DAH7PS activity unaffected.[85] Additionally, and most excitingly, *Mtu*CM activity developed sensitivity to the presence of Tyr or Phe on complex formation.

A.

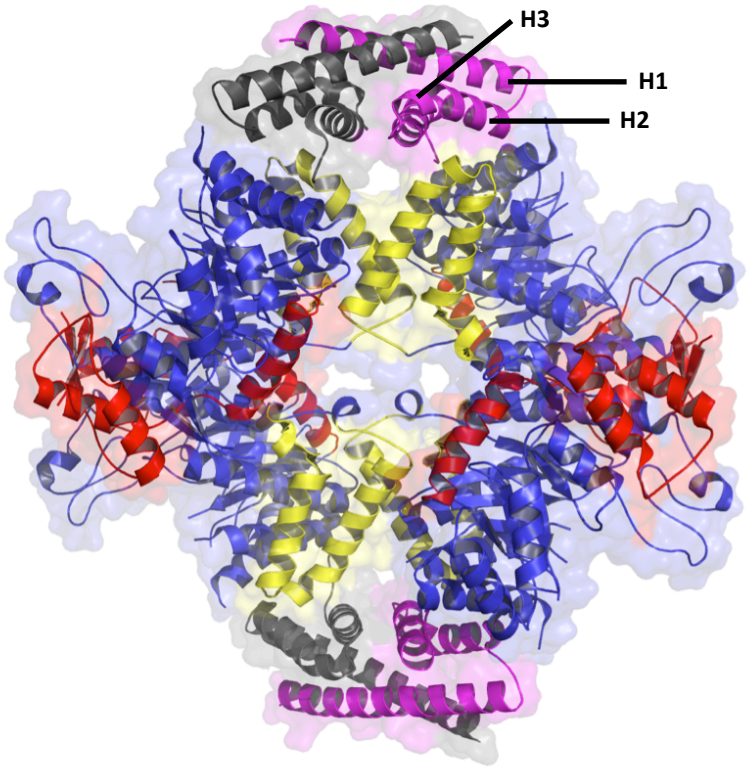

B.

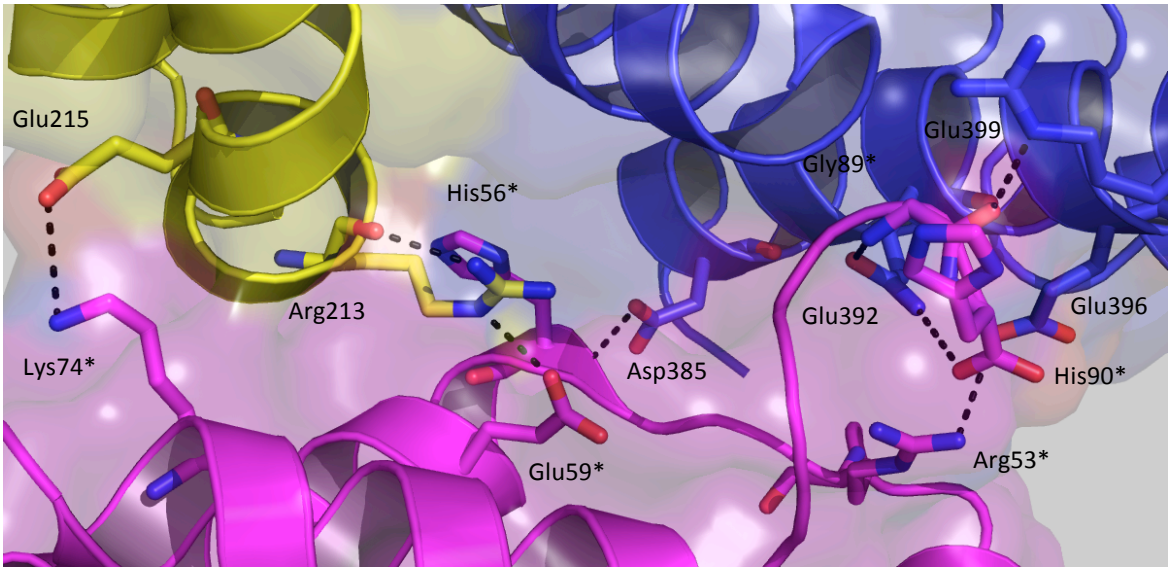

Figure 4.1 Heterooctamer structure of *Mtu*CM•*Mtu*DAH7PS complex (PDB code: 2W19, 2.15 Å resolution). A. *Mtu*DAH7PS shown with the core $(\beta/\alpha)_8$ barrel structure is coloured blue, the N-terminal extension is coloured red, the additional helices to the α2-β3 loop coloured yellow and the metal ion (Mn^{2+}) is shown in purple and *Mtu*CM with subunit A and subunit B coloured grey and magenta respectively. B. Interface between *Mtu*CM and *Mtu*DAH7PS and the dashed black lines represent hydrogen bonds.* indicate residues contributed from *Mtu*CM The H1-H3 α-helices of *Mtu*CM are labelled on one *Mtu*CM subunit.

4.1.1. Interface of the non-covalent complex

Approximately 855 Å^2 of the *Mtu*DAH7PS subunit surface area (5 % of the total subunit surface area of a single subunit) is estimated to be buried at the interface of *Mtu*CM and *Mtu*DAH7PS, formed via a combination of polar and non-polar interactions (Figure 4.1B).[85] In comparison ~10% of the surface area of each *Mtu*DAH7PS chain is buried at the dimer interface, that forms between the two subunits of the crystallographic asymmetric dimer and ~5 % of the surface area is buried by the formation of the tetramer interface. The major contributions from *Mtu*DAH7PS to form the *Mtu*CM•*Mtu*DAH7PS interface are from the inserted α2b helix and its preceding loop, and the α7 and α8 helices of the core barrel of *Mtu*DAH7PS. *Mtu*CM contributes residues from the H1-H2 loop and the H1 and H2 helices. A list of the polar and nonpolar interactions that form the *Mtu*CM•*Mtu*DAH7PS interface is provided in Appendix III. The most notable interactions are contributed by the C-terminal of *Mtu*CM are the residues Leu88*, Gly89* and His90*. These residues pack into a shallow grove on the surface of *Mtu*DAH7PS forming numerous hydrophobic interactions with the residues of the α7 and α8 helices of *Mtu*DAH7PS and with additional polar interactions forming between His90* and Glu392 (*Mtu*DAH7PS α7 helix) and also Gly89* and both Glu392 and Arg399 (*Mtu*DAH7PS α7 helix).

4.1.2. Proposed mechanism of *Mtu*CM activation

Complex formation causes the C-terminus and H1-H2 loop of *Mtu*CM to undergo substantial conformational change. Key active site residues are located along the C-terminus and H1-H2 loop, thus the conformational change of these regions repositions these key residues and this is likely to be responsible for the improved *Mtu*CM catalytic efficiency (Figure 4.2). Alignment of the *Mtu*CM dimer (PDB code: 2BQV) with the *Mtu*CM bound to *Mtu*DAH7PS (PDB code: 2W19, Cα RMSD 0.568) reveals a residue previously shown to be critical to catalysis, Arg46*, has moved considerably upon formation of the complex.[85] The guanidinium group of Arg46* is orientated for more efficient interaction with an incoming ligand. The movement of Arg46* is caused by a dramatic shift in the position of the H1-H2 loop, shifting Arg53* from coordinating to Glu59* in the unbound *Mtu*CM structure to coordinate the guanidinium group of Arg46* in the *Mtu*CM•*Mtu*DAH7PS complex structure. Furthermore residues

* Indicates residues belong to *Mtu*CM

Leu54*, Val55* and His56, also located in the H1-H2 loop, have shifted along by one residue enabling Leu54* to contact Leu88* in the *Mtu*CM•*Mtu*DAH7PS complex structure, whereas these two residues are 20 Å apart in the *Mtu*CM structure. The formation of the complex also causes a shift of the C-terminal tail of *Mtu*CM facilitating the formation of two hydrogen bonds between the guanidinium group of Arg85* and the carboxylate of Glu59*.

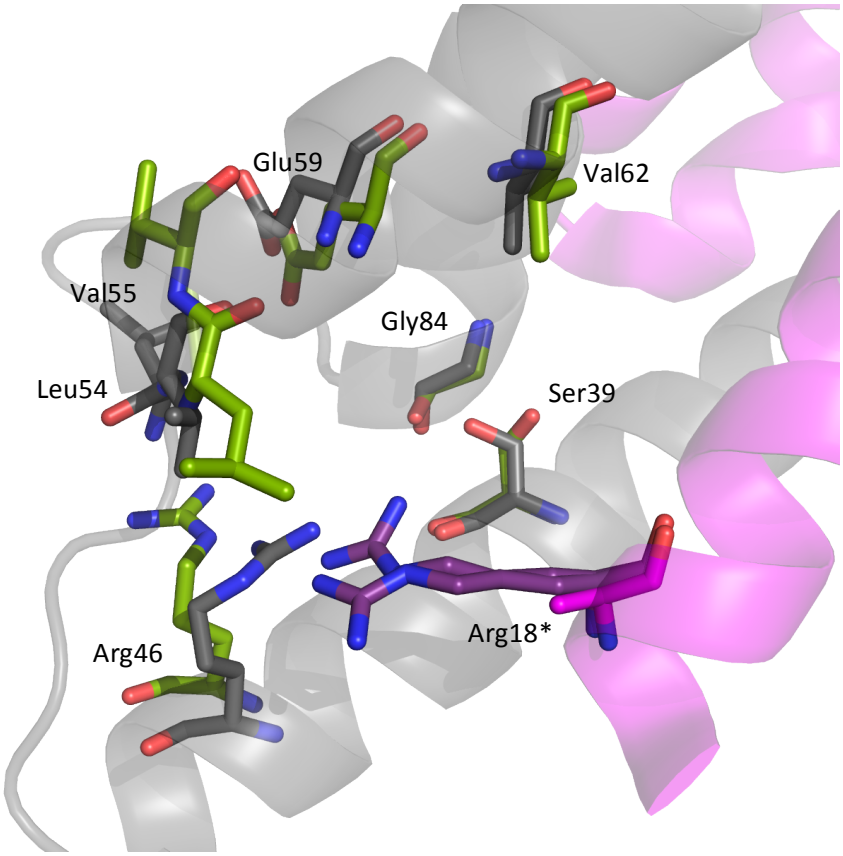

Figure 4.2 Alignment of *Mtu*CM active site residues from the non-complexed *Mtu*CM (PDB code: 2BQV, 2.00 Å resolution) and *Mtu*CM•*Mtu*DAH7PS complex (PDB code: 2W19, 2.15 Å resolution and RMSD of 0.568). Unbound *Mtu*CM shown with residues from subunit A coloured olive and subunit B deep purple. Backbone cartoon is depicted from the structure with *Mtu*CM bound to *Mtu*DAH7PS and is shown with subunit A and subunit B coloured grey and magenta respectively.

Sasso *et al.* proposed that on complex formation the residues of the H1-H2 loop and the C-terminal tail are brought into a more catalytically beneficial conformation.[85] To support their hypothesis the authors investigated the importance of the last four C-terminal residues (Arg87*, Leu88*, Gly89* and His90*) for catalysis and showed that although they are not essential for basal *Mtu*CM activity, the last four C-terminal residues are essential for activation of *Mtu*CM activity by *Mtu*DAH7PS.[85]

4.1.3. Chapter aims

One significant limitation of the work conducted to characterise the *Mtu*CM•*Mtu*DAH7PS complex by Sasso *et al.* was the use of a polyhistidine tagged *Mtu*DAH7PS (*Mtu*DAH7PS^{H6}) to conduct the kinetic characterisation. Prior work by the Parker research group has found retention of the polyhistidine tag adversely effects crystallisation of *Mtu*DAH7PS, so it may also affect other properties of the enzyme.[70] Consequently the studies described in this chapter aimed to assess the activation and regulation of the *Mtu*CM•*Mtu*DAH7PS complex when untagged *Mtu*DAH7PS^{WT} was used to form the complex. This work was complemented by a detailed investigation into the regulatory properties of *Mtu*DAH7PS^{H6} itself.

This work also aimed to prove unequivocally the allosteric sites of *Mtu*DAH7PS (site 1 and site 2) were responsible for the regulation of *Mtu*CM by utilising the binding site variants, *Mtu*DAH7PS^{R171A} and *Mtu*DAH7PS^{R256A}, generated as described in Chapter 3.

Finally, all structural evidence of complex formation between *Mtu*CM and *Mtu*DAH7PS thus far has relied on crystallography and native PAGE. This work aimed to observe the formation of the complex in solution. Formation of the complex in solution would suggest the complex may form *in vivo* and is more likely to be biologically relevant. Fortuitously by studying the complex formation in solution, these studies also permitted an insight into the mechanism of the inhibition of *Mtu*CM activity by the *Mtu*CM•*Mtu*DAH7PS complex.

4.2. Preparation of *Mtu*CM

4.2.1. Construct details

A synthetic *Mtu*CM gene optimised for *E. coli* codon usage was obtained from GeneArt. Richard Hutton transferred the synthetic gene into pDEST™ 15 vector using Gateway cloning technology (Invitrogen). The pDEST™ 15 vector allows production of a N-terminal glutathione *S*-transferase (GST)-tagged recombinant protein for purification via affinity chromatography. The GST-tag was TEV

protease cleavable. The pDEST™ 15 vector also encoded the T7 promoter regions to allow induction of protein expression by addition of IPTG and an ampicillin resistance gene to allow for selection in *E. coli.* The tag sequence is shown in Figure 4.3.

[GST]PWSNQTSLYKKAGFENLYFQGSGA

Figure 4.3 Sequence of the pDEST ™ 15 GST-tag. Highlighted are the GST fusion protein (blue), the TEV protease recognition site (purple) and the residues retained at the N-terminus post cleavage (pink).

The pDEST™ 15 vector containing the synthetic *Mtu*CM gene was transformed into BL21 Star™ (DE3) (Life technologies) and colonies bearing the plasmid were selected for ampicillin resistance.

4.2.2. Expression and lysis

Protein expression was conducted as outlined in Section 9.3. Overexpression of *Mtu*CM was confirmed by SDS-PAGE gel. Mass spectrometry and plasmid sequencing confirmed the amino acid sequence was unaltered and as expected. Cells were resuspended in 10 mM phosphate buffer pH 7.5 and lysed by sonication. The whole lysate was then clarified by centrifugation and insoluble fraction discarded.

4.2.3. Purification

The purification procedure is outlined in Figure 4.4A and detailed in Section 9.6. The progress of the purification is shown by the SDS-PAGE (Figure 4.4B). Initially the soluble crude lysate was purified by affinity chromatography using a GSTrap (GE healthcare). The GSTrap uses a reduced glutathione ligand covalently attached to the solid phase of the column to bind the GST-tag of the fusion protein. The GSTrap retains the fusion protein, and any other protein with an affinity for reduced glutathione, as all the other proteins in the crude lysate pass through the column as it is washed with phosphate

buffer. The fusion protein was eluted from the GSTrap with an increasing gradient of reduced glutathione. The fractions containing *Mtu*CM were collected and the GST-tag cleaved with TEV protease by incubation overnight at 4 °C.

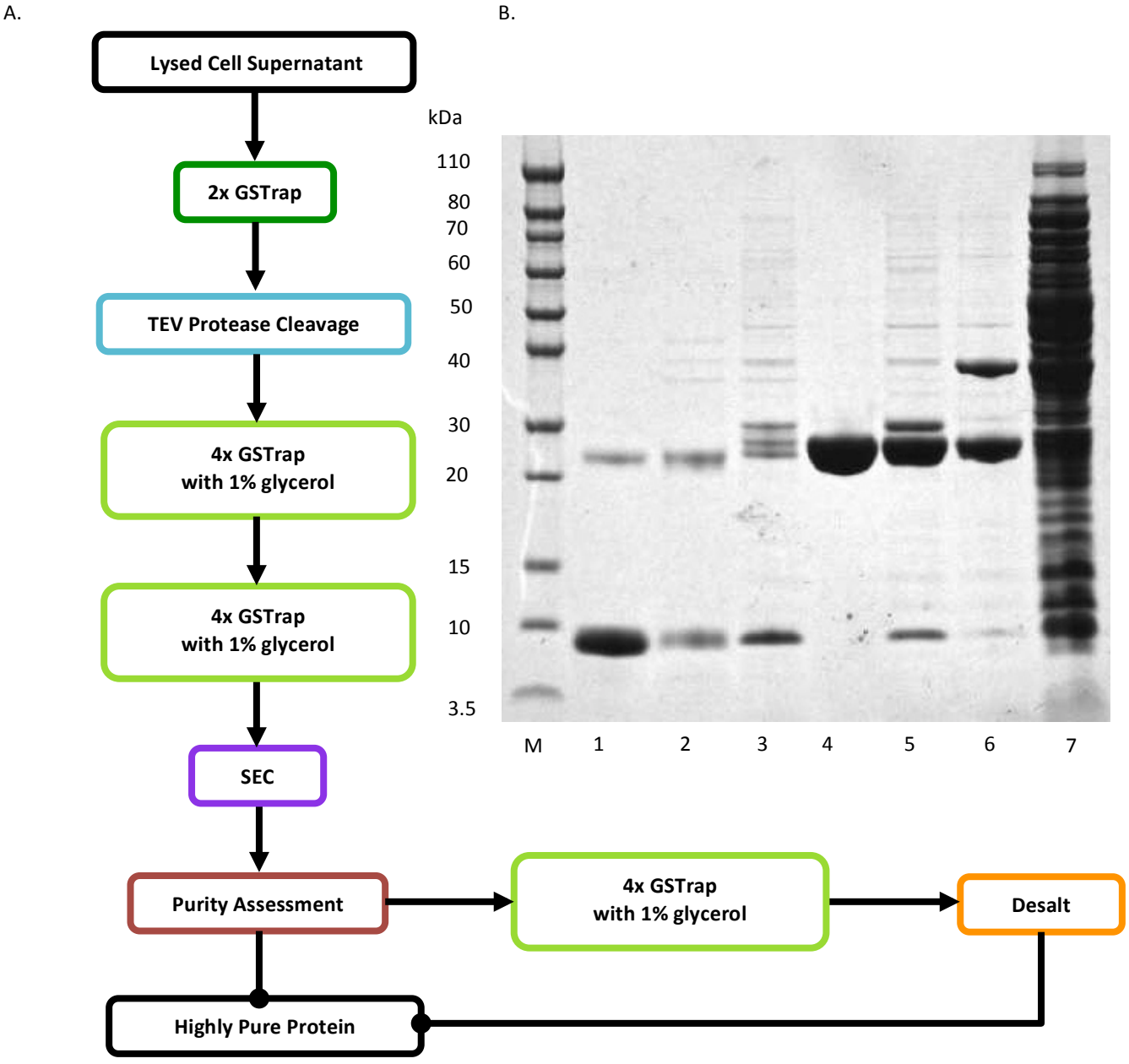

Figure 4.4 A. An outline of the standard purification protocol for *Mtu*CM. B. SDS-PAGE gel. Lane M is the molecular weight maker; lane 1 pooled *Mtu*CM post SEC; lane 2 second iteration of GST-tag removal; lane 3 first iteration of GST-tag removal; lane 4 GST-tag removed in the second iteration of GST-tag removal; lane 5 TEV protease treated *Mtu*CM; lane 6 *Mtu*CM fusion protein isolated by reduced glutathione gradient and lane 7 soluble fraction of the cell lysate. Overexpressed fusion protein band can be observed at ~35 kDa, the GST-tag at ~26 kDa and *Mtu*CM at ~10 kDa.

Usually passing the TEV protease treated protein back through a GSTrap would be expected to separate the GST-tag from the cleaved protein. Unfortunately, *Mtu*CM had significant affinity for the cleaved GST-tag. Although a good portion of the GST-tag bound the GSTrap, a significant proportion was eluted in the flow-through with the *Mtu*CM. The collected *Mtu*CM fractions were iteratively applied to four GSTraps in series in an effort to quickly separate the GST-tag. After each application to the four columns in series the eluted *Mtu*CM was assessed by SDS-PAGE gel. Once the *Mtu*CM was shown to be pure and/or a significant portion of *Mtu*CM was starting to be lost with the eluted the GST-tag the *Mtu*CM fractions were collected pooled and concentrated. *Mtu*CM has a low extinction coefficient (1490 cm^{-1} mol^{-1}), making it difficult to monitor the purification process by UV absorption at 280 nm. Consequently SDS-PAGE gels were essential for monitoring and evaluating each purification step post GST-tag cleavage.

The initial purification required more than eight applications of the *Mtu*CM to the series of four GSTrap columns to remove enough GST-tag to continue with SEC and the entire purification took up to five days to complete. To reduce the affinity between *Mtu*CM and the GST-tag glycerol (1 %) was added to the binding buffer after TEV protease cleavage. The glycerol was added to discourage protein-protein interactions. It has been proposed glycerol stabilises proteins in solution through the preferential interaction of glycerol with the hydrophobic surface regions of the protein.[113] When the purification was repeated using glycerol only two to three passes through the four GSTraps were required, allowing the purification to be completed in two to three days. Unfortunately glycerol interfered with the kinetic assays and had to be completely removed by either SEC or by application to a desalting column before the purified *Mtu*CM could be used.

The *Mtu*CM was concentrated and applied to a SEC column to separate any remaining GST-tag and any other contaminants including any glycerol present. Fractions were collected either to maximise purity or yield depending on the intended use. Fractions identified as pure by SDS-PAGE were pooled, concentrated and flash frozen in small aliquots (~50 µL). In order maximise yield, fractions that contained GST-tag contamination were reapplied to the four GSTraps in series to remove as much GST-tag as possible. Generally most batches of purified *Mtu*CM were contaminated by a small amount

of GST-tag, but the amount of contamination varied between batches. The glycerol introduced during this final step was removed by a PD10 desalting column before the protein was flash frozen and stored at -80 ˚C.

4.2.4. Determination of concentration

*Mtu*CM contains only a single Tyr residue and accordingly has a very low extinction coefficient of 1490 cm^{-1} mol^{-1} at 280 nm. Thus measurement of concentration by direct spectrophotometry was imprecise. Concentration determination was further complicated by the presence of any remaining GST-tag that gave misleading results when either directs protein spectrophotometry or Bradford assays were used to determine concentration. Fortunately a highly pure batch of *Mtu*CM was purified. Bradford assay was used to determine the concentration of this highly pure *Mtu*CM and its kinetic activity, with and without *Mtu*DAH7PS was recorded. This highly pure *Mtu*CM was used as a standard for determining the concentration and purity of every other batch of *Mtu*CM purified. Even if *Mtu*CM batches were contaminated by a small amount of GST-tag only active and available *Mtu*CM could contribute to the activity determined. This method does assume that the GST-tag does not significantly affect to the overall CM activity of the protein sample. Thus based on the total protein concentration determined through Bradford assay and the relative activity of each batch compared to the standard a consistent and reproducible method of *Mtu*CM concentration determination was developed.

4.2.5. Confirmation of product

SDS-PAGE gel displayed a band just under 10 kDa and this size is comparable with the predicted 10.4 kDa molecular mass of *Mtu*CM monomer (Figure 4.5). Analysis by mass spectrometry yielded a mass of 10361 Da in close agreement with the expected molecular mass of 10362 Da for *Mtu*CM.

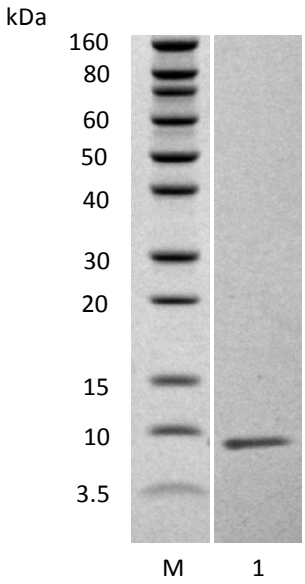

Figure 4.5 SDS-PAGE gel of Lane M the molecular weight maker and lane 1 purified *Mtu*CM.

4.3. Basic characterisation of *Mtu*CM

4.3.1. Kinetic parameters

The activity of *Mtu*CM was assessed under conditions similar to *Mtu*DAH7PS and is described in Section 9.9.1. Assays were conducted at 30 °C in BTP buffer pH 7.5. Assays were also conducted in the presence of a divalent metal ion (Mn^{2+}), reducing agent (TCEP) and PEP, which would later be required to stabilise *Mtu*DAH7PS, as the *Mtu*CM activity of the *Mtu*CM•*Mtu*DAH7PS complex was assessed. Kinetic assays monitored the loss of chorismic acid at 274 nm. Kinetic parameters were determined using continuous steady-state Michaelis-Menten kinetics. *Mtu*CM was found to have poor activity, and has been compared with previously published results (Table 4.1).[78,83-86] The *Mtu*CM from this study has four additional residues at the N-terminus (GlySerGlyAla), whereas Sasso *et al.* did not utilise an affinity tag to purify *Mtu*CM, consequently their protein had no additional residues at the N-terminus.[85] The purification by Kim *et al.* purified *Mtu*CM via a subtilisin-prodomain fusion protein that does not leave any remaining residues at the N-terminus when *Mtu*CM is cleaved.[86]

Table 4.1 Comparison of *Mtu*CM Kinetic parameters determined from a single set of Michaelis-Menten kinetics compared to previously published results. Chorismic acid is abbreviated to CA. For Michaelis-Menten plot refer to Appendix I. Error bars represent the error of fit of the equation to the data as determined by least squares fit.

***Mtu*CM**	**K_m^{CA} (μM)**	**k_{cat} (s^{-1})**	**Catalytic efficiency (M^{-1} s^{-1})**
This study	500 ± 30	0.42 ± 0.02	840 ± 90
Sasso[85]	1140 ± 20	2.0 ± 0.1	1750 ± 90
Kim[86]	1500 ± 100	5.5 ± 0.2	3700 ± 400

4.3.2. Absence of feedback regulation

Inhibition studies carried out on *Mtu*CM showed the addition of any single, binary or ternary combination of the three aromatic amino acids, Trp, Phe or Tyr had no effect on *Mtu*CM activity (Figure 4.6). Assays were conducted in the standard assay conditions used to determine the Michaelis-Menten kinetics of *Mtu*CM and initiated with 150 μM of chorismic acid (detailed Section 9.9.3). Each amino acid was added at a concentration of 200 μM.

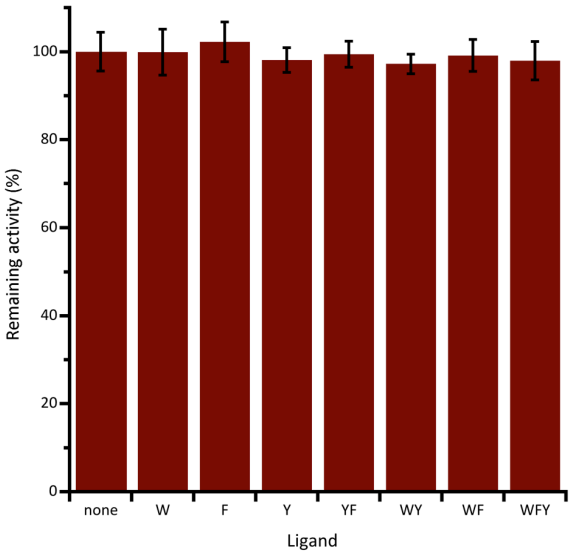

Figure 4.6 Remaining activity of *Mtu*CM in the presence of various single, binary and ternary combinations of aromatic amino acids. The aromatic amino acids are represented by their one letter code; Trp, W; Phe, F and Tyr, Y. Each letter also represents 200 μM of the corresponding aromatic amino acids. Assays conducted in the presence of 150 μM chorismic acid. Error bars depict the standard deviation of duplicate measurements. P-values provided in appendix V.

4.3.3. Thermal stability

Although the aromatic amino acids did not affect *Mtu*CM activity, DSF showed the amino acids had a measurable influence on the thermal stability of *Mtu*CM. DSF Assays were conducted under the same conditions as *Mtu*DAH7PS^{WT} and are described in Section 9.8.1.

The greatest difference in the recorded T_m of *Mtu*CM was a ~6 ˚C drop caused by the addition of 200 µM Tyr (Figure 4.7). Trp and Phe (200 µM each) caused smaller losses in *Mtu*CM thermal stability of ~ 2.7 ˚C. These findings suggest despite the ligands generating no inhibitory effect on *Mtu*CM activity they are still able to interact with *Mtu*CM. Interestingly the loss in thermal stability caused by the addition of Tyr could be partially recovered by adding Phe or Trp and Phe.

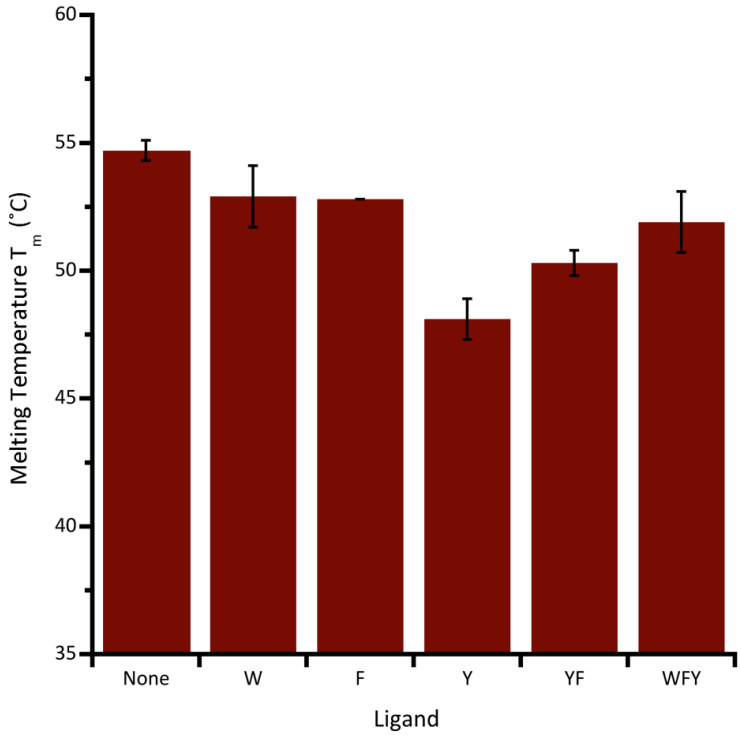

Figure 4.7 Effect of individual, binary and ternary combinations of allosteric amino acids on thermal melting temperature. The aromatic amino acids are represented by their one letter code; Trp, W; Phe, F and Tyr, Y. Each letter also represents 200 µM of the corresponding aromatic amino acids. Error bars depict the standard deviation of triplicate measurements. P-values provided in appendix V.

4.4. Activation of *Mtu*CM activity by *Mtu*DAH7PS^{WT}

4.4.1. Kinetic assay development

Initial work sought to develop the kinetic assay conditions to be used for monitoring *Mtu*CM activity of the *Mtu*CM•*Mtu*DAH7PS complex. More specifically the ratio of *Mtu*CM to *Mtu*DAH7PS to be used for the assays had to be determined.

Assays were conducted under the standard assay conditions for measuring *Mtu*CM activity and were initiated by the addition of 150 µM *Mtu*CM. The concentration of *Mtu*CM was held constant at 10 nM and the concentration of *Mtu*DAH7PS was varied between 0 and 8 µM. In the absence of *Mtu*DAH7PS the concentration of *Mtu*CM was adjusted to 90 nM and normalised in order to detect the very low *Mtu*CM activity.

As may have been intuitively expected, increasing the molar concentration of *Mtu*DAH7PS^{WT} in the presence of a constant amount of *Mtu*CM increased *Mtu*CM activity. This increase in activity was hyperbolic; initially displaying a rapid boost in activation of *Mtu*CM activity with increasing *Mtu*DAH7PS concentration, and plateauing as the concentration of *Mtu*DAH7PS exceeded 2 µM (a 200-fold molar excess of *Mtu*DAH7PS) (Figure 4.8A). The maximum *Mtu*CM activity of 103 ± 3 µMmin^{-1}mg^{-1} was found when 8 µM *Mtu*DAH7PS was present which was a 142 ± 3 -fold activation of *Mtu*CM activity compared to *Mtu*CM alone (0.73 µMmin^{-1}mg^{-1}).

Given these finding a molar ratio of 1:10 *Mtu*CM:*Mtu*DAH7PS^{WT} was chosen for all further characterisation of the *Mtu*CM•*Mtu*DAH7PS^{WT} complex. The *Mtu*CM activity of this ratio allowed changes in the affinity between the two enzymes that may result in increases or decreases in activity. An important consideration in choosing the molar ratio of 1:10 *Mtu*CM:*Mtu*DAH7PS^{WT} was that the amount of enzyme consumed in each kinetic assay was economical, and would not quickly exhaust proteins stocks. The ratio of 1:10 (*Mtu*CM:*Mtu*DAH7PS^{WT}) was an economical choice, which would permit a concise investigation of any *Mtu*DAH7PS variant required.

The interface of the *Mtu*CM•*Mtu*DAH7PS complex is formed through a considerable number of hydrophobic interactions. To study if these hydrophobic interactions were primarily responsible for the interaction between *Mtu*CM and *Mtu*DAH7PS the effect of increasing NaCl concentration on *Mtu*CM activity was monitored. Assays were conducted under standard assay conditions outlined in Section 9.9.1, using a molar ratio of 1:10 *Mtu*CM:*Mtu*DAH7PS^{WT}, a concentration of 10 nM *Mtu*CM and 150 µM chorismic acid.

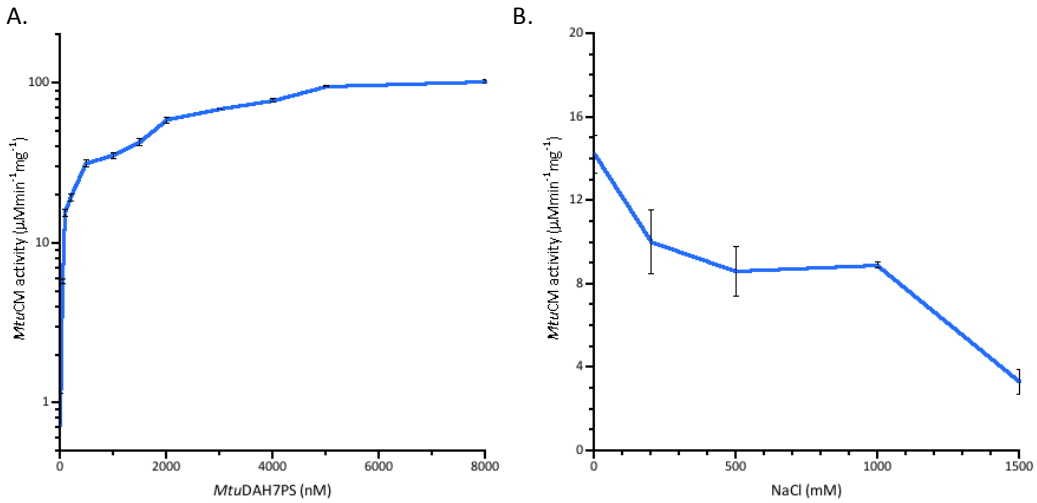

Figure 4.8 Change in *Mtu*CM activity caused by A. the increased molar concentration of *Mtu*DAH7PS or B. increasing concentration of NaCl. For A. assays were conducted under standard *Mtu*CM assay conditions, with 10 nM *Mtu*CM except in the absence of *Mtu*DAH7PS^{WT} where 90 nM of *Mtu*CM was used and the activity normalised. For B. assays conducted under standard *Mtu*CM assay conditions with 10 nM of *Mtu*CM and 100 nM of *Mtu*DAH7PS^{WT}. Reactions for both A and B were initiated with 150 µM chorismic acid.

Addition of the NaCl to the assay conditions increases the ionic strength of the buffer and encourages the association of hydrophobic (or non-polar) areas between proteins. If this strengthened the interaction between *Mtu*CM and *Mtu*DAH7PS it should be reflected in an increase in *Mtu*CM activity, but this was not observed. Instead the addition of salt appeared to be detrimental to *Mtu*CM activity (Figure 4.8B). The reduced activity is either a result of the NaCl affecting the *Mtu*CM directly or it may hint the hydrophobic contacts between *Mtu*CM and *Mtu*DAH7PS are not the most significant contributions to the interface. The activity of *Mtu*CM alone in the presence of a NaCl (> 1mM) needs to be determined to identify if *Mtu*CM activity is directly harmed.

4.4.2. *Mtu*CM•*Mtu*DAH7PS^{WT} kinetic parameters

The Michaelis-Menten kinetics for the *Mtu*CM activity of the complex was determined under the same experimental conditions as for *Mtu*CM alone but with the addition of a ten-fold molar excess of *Mtu*DAH7PS as described in Section 9.9.1. For all assays the *Mtu*CM and *Mtu*DAH7PS were added to the assay condition and allowed to incubate together for 10 min at 30 °C prior to initiation of the reaction with chorismic acid. This data was used for comparison with *Mtu*DAH7PS variants in later work. To obtain data comparable to previously published work by Sasso *et al.* a second set of Michaelis-Menten kinetics was obtained with a 200-fold molar excess of *Mtu*DAH7PS and using a concentration of 10 nM *Mtu*CM.

Table 4.2 Comparison of *Mtu*CM Kinetic parameters determined from a single set of kinetic data with and without *Mtu*DAH7PS^{WT} by Michaelis-Menten kinetics with previously published results[85]. *Activation factor determined by the ratio of the k_{cat}/K_m with and without *Mtu*DAH7PS^{WT},– indicates not applicable. Chorismic acid is abbreviated to CA, *Mtu*CM to CM and *Mtu*DAH7PS to D. For this study the concentration of *Mtu*CM used for assays with a ten-fold molar excess of *Mtu*DAH7PS was 30nM, and 10 nM *Mtu*CM for assays with 200-fold molar excess of *Mtu*DAH7PS. For work by Sasso *et al*. *Mtu*CM activity was determined with 2 µM *Mtu*DAH7PS^{H6} and 10 nM *Mtu*CM. For Michaelis-Menten plots refer to Appendix I. Error represents the fit of the data to the model as determined by a least squares fit.

Protein	Ratio (CM:D)	K_m^{CA} (µM)	k_{cat} (s^{-1})	k_{cat}/K_m^{CA} ($mM^{-1}s^{-1}$)	Activation factor*
This study					
*Mtu*CM	1:0	500 ± 30	0.42 ± 0.02	0.84 ± 0.09	–
*Mtu*CM•*Mtu*DAH7PS^{WT}	1:10	52 ± 4	5.4 ± 0.1	104 ± 9	120 ± 20
*Mtu*CM•*Mtu*DAH7PS^{WT}	1:200	38 ± 6	10.5 ± 0.4	280 ± 50	330 ± 90
Sasso et al.[85]					
*Mtu*CM	1:0	1140 ± 20	2.0 ± 0.1	1.75 ± 0.09	–
*Mtu*CM•*Mtu*DAH7PS^{H6}	1:200	34 ± 3	8 ± 2	240 ± 60	140 ± 40

A ten-fold molar excess of *Mtu*DAH7PS^{WT} enhanced the catalytic efficiency of *Mtu*CM from less than 1 to over 100 $mM^{-1}s^{-1}$, a 120-fold increase (Table 4.2). A 200-fold molar excess of *Mtu*DAH7PS^{WT} enhanced the catalytic efficiency of *Mtu*CM by ~330-fold. Both sets of data displayed a huge drop in the Michaelis constant for chorismic acid (K_m^{CA}) and an increase in the turnover number (k_{cat}), which contributed to the enhanced catalytic efficiency of *Mtu*CM in presence of *Mtu*DAH7PS^{WT}. This enhancement in the catalytic efficiency is most likely attributed to the rearrangement of the *Mtu*CM

active site residues on formation of the *Mtu*CM•*Mtu*DAH7PS^{WT} complex.[85] Rearrangement of the *Mtu*CM active site may better facilitate interaction with the substrate whilst also optimising the residues to perform catalysis.

The kinetic parameters for *Mtu*CM activity determined in the presence of a 200-fold molar excess of *Mtu*DAH7PS were consistent with those previously reported by Sasso *et al*.[85] using polyhistidine tagged *Mtu*DAH7PS. However, the calculated activation of *Mtu*CM activity by *Mtu*DAH7PS^{WT} was found to be about three times higher than previously reported; yet the catalytic efficiency for both studies was in good agreement. The similar catalytic efficiency was because the activation of *Mtu*CM is calculated using the catalytic efficiency of *Mtu*CM alone, and this varied for each study. Furthermore no investigation has previously been made to assess if the polyhistidine tag of *Mtu*DAH7PS affects the interaction between *Mtu*CM and *Mtu*DAH7PS. Hence no conclusion could definitively be drawn with regard to whether the reduced activation of *Mtu*CM activity was due to the use of polyhistidine tagged *Mtu*DAH7PS by Sasso *et al*. or simply due to variation in the purification and analysis of *Mtu*CM.

4.5. Evidence of *Mtu*CM•*Mtu*DAH7PS^{WT} complex in solution

Numerous techniques were trialled in an attempt to obtain unequivocal evidence of the formation of the *Mtu*CM•*Mtu*DAH7PS complex in solution. Efforts were continually hampered by the low yield and instability of the *Mtu*CM protein or its poor extinction coefficient at 280 nM (1490 $cm^{-1}mol^{-1}$). SAXS, light scattering techniques and analytical SEC were attempted without success. Eventually AUC proved to be the only technique to enable visualisation of the complex formation between *Mtu*DAH7PS^{WT} and *Mtu*CM at a range of concentrations in solution.

Sedimentation velocity experiments were carried out under the same conditions used to analyse *Mtu*DAH7PS^{WT} and these conditions are described in Section 9.7.7. AUC experiments were carried out by Ali Nazmi. The proteins were combined at the stated molar ratio (either 4:1, 1:1 or 1:2;

*Mtu*CM:*Mtu*DAH7PS^{WT}) and dialysed for 2-3 hours prior to being analysed by AUC. Analysis was carried out at three *Mtu*DAH7PS^{WT} concentrations 0.2, 0.4 and 0.6 mg/mL. AUC was attempted on *Mtu*CM alone, but was unsuccessful due to the instability of *Mtu*CM over the time course of the analysis, and the analysis of these experiments was further hampered by the low extinction coefficient of the enzyme.

The sedimentation coefficient (*s*) determined in the presence for a 4:1 *Mtu*CM:*Mtu*DAH7PS^{WT} mixture was ~9.3 S at all three *Mtu*DAH7PS^{WT} concentrations and corresponded to a molecular mass of ~220 kDa (Figure 4.9A). The expected molecular mass of the heterooctameric complex between *Mtu*CM and *Mtu*DAH7PS is ~244 kDa. This was ~1 S greater than sedimentation coefficient of *Mtu*DAH7PS alone (~8.4 S) (Figure 4.9D).

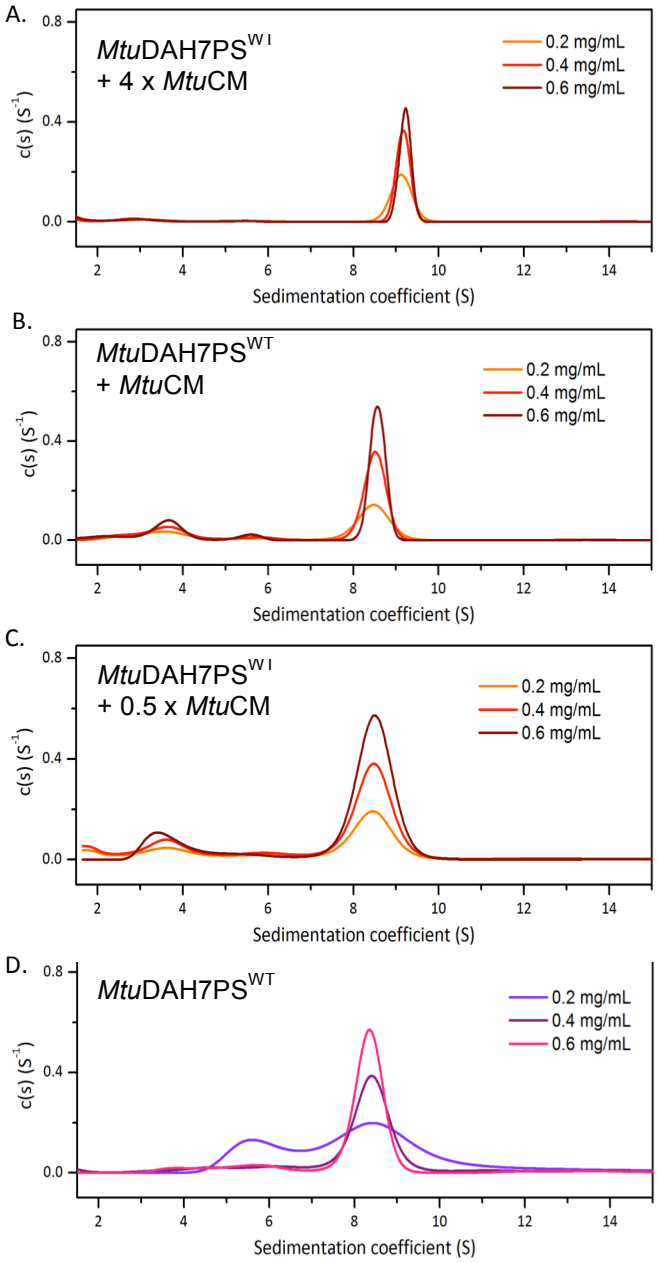

Figure 4.9 Normalised continuous size *c*(*s*) distribution of sedimentation velocity data: A. *Mtu*DAH7PS and a four-fold molar excess of *Mtu*CM; B. *Mtu*DAH7PS^{WT} and equal molar amount of *Mtu*CM; C. *Mtu*DAH7PS^{WT} and half the molar concentration of *Mtu*CM and D. *Mtu*DAH7PS^{WT} alone. Analyses conducted at *Mtu*DAH7PS^{WT} concentrations of 0.2 mg/mL, 0.4 mg/mL or 0.6 mg/mL coloured mustard, red and wine respectively for mixtures of *Mtu*CM and *Mtu*DAH7PS^{WT} and violet, purple and pink for *Mtu*DAH7PS alone. Note that the molar extinction coefficient of *Mtu*CM is 1490 $cm^{-1}mol^{-1}$, whereas that of *Mtu*DAH7PS^{WT} is 41160 $cm^{-1}mol^{-1}$ at a wavelength of 280 nm. AUC data and fits shown in Appendix II.

Analysis of the 1:1 and 0.5:1 mixtures of *Mtu*CM and *Mtu*DAH7PS^{WT} revealed a single peak at each concentration with a sedimentation coefficient of ~ 8.8 S and ~8.5 S respectively (Figure 4.9B-C). As the molar ratio of *Mtu*CM to *Mtu*DAH7PS decreased, the sedimentation coefficient tended toward that of *Mtu*DAH7PS alone, whilst the peaks of the continuous size distribution model became broader. The broadened peaks indicated the boundary layers were less defined and were most probably a result of a broader range of molecular weight species being present in solution, such as the *Mtu*DAH7PS tetramer with a single *Mtu*CM dimer bound.

The 1:1 and 0.5:1 mixtures of *Mtu*CM and *Mtu*DAH7PS were conducted with *Mtu*CM with a small amount of GST-tag contamination. Consequently there is a small peak at ~3.6 S corresponding to a molecular mass of ~41 kDa. The expected mass for a GST dimer is ~52 kDa. Due to the very low extinction coefficient of *Mtu*CM at 280 nm (1490 $cm^{-1}mol^{-1}$) a peak for *Mtu*CM is not clearly observed at the wavelength of analysis. Note the *Mtu*CM extinction coefficient is much smaller than that of *Mtu*DAH7PS (41160 $cm^{-1}mol^{-1}$).

Another striking observation from the sedimentation velocity experiments was the quaternary structure equilibrium of *Mtu*DAH7PS shifted in the presence of *Mtu*CM toward the formation of the tetramer (Figure 4.9A-C). Even at a ratio of 0.5:1 *Mtu*CM:*Mtu*DAH7PS there was no hint of a dimer peak at 0.2 mg/mL unlike *Mtu*DAH7PS^{WT} which shows a sizeable peak at ~ 5.7 S.

4.6. Regulation of the *Mtu*CM•*Mtu*DAH7PS^{WT} complex

4.6.1. Feedback regulation

Inhibition studies were carried out using a ten-fold molar excess of *Mtu*DAH7PS relative to the concentration of *Mtu*CM (30 nM), and the two components were incubated for 10 min in the assay conditions prior to initiation with substrate. Assays for the inhibition studies were conducted under the standard assay conditions used to determine the Michaelis-Menten kinetics of *Mtu*CM and are described in Section 9.9.3. Each amino acid was added at a concentration of 200 µM.

The addition of *Mtu*DAH7PS^{WT} to the *Mtu*CM inhibition assays resulted in the regulation of *Mtu*CM activity by the aromatic amino acids. The effectiveness of the inhibition was shown to be dependent on substrate concentration, with *Mtu*CM activity at lower chorismic acid concentrations being more responsive to the addition of the aromatic amino acids (Figure 4.10). In agreement with previous work, Phe was found to be the most potent inhibitor, followed by Tyr reducing *Mtu*CM activity by ~85 % and ~40 % respectively, in the presence of 25 µM chorismic acid.[85] The addition of Trp had no effect on the *Mtu*CM activity even in the presence of *Mtu*DAH7PS^{WT}.

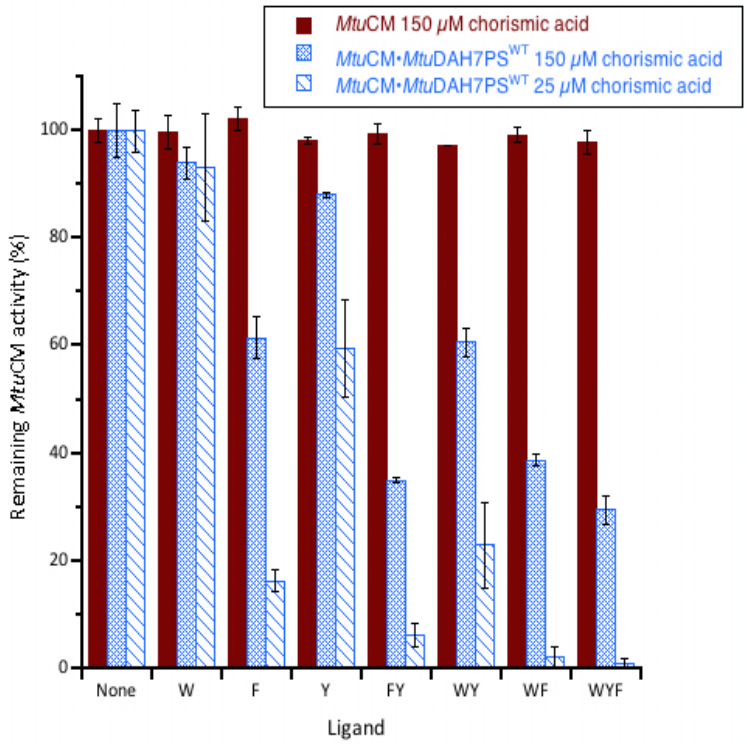

Figure 4.10 Remaining *Mtu*CM activity in the presence of various single, binary and ternary combinations of aromatic amino acids for *Mtu*CM alone (burgundy) or with a ten-fold excess of *Mtu*DAH7PS^{WT} initiated by either 150 µM (blue hash) or 25 µM (blue stripe) chorismic acid. The aromatic amino acids are represented by their one letter code; Trp, W; Phe, F and Tyr, Y. Each letter also represents 200 µM of the corresponding aromatic amino acids. Assays conducted in the presence of 150 µM chorismic acid unless otherwise stated. Error bars depict the standard deviation of at least duplicate measurements. *Mtu*CM concentrations was 3 µM or 60 nM for *Mtu*CM alone or in combination with *Mtu*DAH7PS respectively. P-values provided in appendix V.

Previous work stated Phe and Tyr synergistically inhibit *Mtu*CM activity in the presence of *Mtu*DAH7PS.[85] This study found the remaining activity determined in the presence of Phe and Tyr was ~6 %, and it is not clear whether Tyr and Phe act synergistically or additively to inhibit *Mtu*CM activity. However, synergistic inhibition of *Mtu*CM activity (in the presence of *Mtu*DAH7PS) was observed

when Trp was added in combination with either Phe or Tyr. The combination of Trp with either Tyr or Phe reduced the remaining *Mtu*CM activity to ~25% or ~2 %, making the Trp and Phe combination more potent than Phe and Tyr. The combination of all three aromatic amino acids reduced *Mtu*CM activity slightly more the combination of Trp and Phe. The activity loss with combinations including Trp has not previously been observed.[85]

The observed pattern of synergistic inhibition of *Mtu*CM activity in the presence of *Mtu*DAH7PS was reminiscent of the synergistic inhibition reported for *Mtu*DAH7PS^{WT} itself in response to the aromatic amino acids. Hence, it is highly plausible the allosteric binding sites of the *Mtu*DAH7PS are also responsible for the regulation of *Mtu*CM activity.

4.6.2. Effect of Phe and Tyr on kinetic parameters of *Mtu*CM•*Mtu*DAH7PS^{WT}

The determination of the Michaelis-Menten kinetic parameters for *Mtu*CM activity was conducted under standard assay conditions, with a ten-fold excess of *Mtu*DAH7PS^{WT} and addition of either Phe, Tyr or both ligands at either 100 µM or 200 µM. The experimental protocol is detailed in Section 9.9.1.

The addition of Phe and or Tyr altered the kinetic parameters determined for *Mtu*CM activity in the presence of *Mtu*DAH7PS^{WT} (Table 4.3). In the presence of either Tyr or Phe the Michaelis constant determined for chorismic acid (K_m^{CA}) increased, whilst the k_{cat} remained relatively unaffected (Table 4.3). Therefore a higher concentration of chorismic acid was required for effective catalysis in the presence of either Phe or Tyr. Thus Phe and Tyr act primarily to reduce the affinity of *Mtu*CM for its substrate, chorismic acid, making them K-type inhibitors. Although Tyr was a less effective inhibitor than Phe, Tyr significantly augments the inhibitory response to Phe resulting in a greater overall inhibition of *Mtu*CM than either amino acid alone.

Table 4.3 Kinetic parameters determined from the Michaelis-Menten kinetics for a single set of *Mtu*CM in the presence of ten-fold excess of *Mtu*DAH7PS^{WT} and ligand as indicated. Michaelis-Menten plots are shown in Appendix I. Error represents error of curve fitting to the data set by least squares fit.

Inhibitor (concentration)	K_m^{CA} (μM)	k_{cat} (s^{-1})	k_{cat}/K_m^{CA} ($mM^{-1}s^{-1}$)	Relative activity (%)
none	52 ± 4	5.4 ± 0.1	104 ± 9	100 ± 20
Phe(200 μM)	220 ± 20	6.3 ± 0.2	29 ± 3	28 ± 5
Phe(100 μM) Tyr(100 μM)	340 ± 30	6.0 ± 0.3	18 ± 2	17 ± 4
Phe(200 μM) Tyr(200 μM)	480 ± 40	8.0 ± 0.3	17 ± 5	16 ± 7
Tyr(200 μM)	84 ± 5	5.0 ± 0.1	60 ± 5	58 ± 9

4.7. Determination of the apparent dissociation constant between *Mtu*CM and *Mtu*DAH7PS

The dissociation constant of *Mtu*CM and *Mtu*DAH7PS^{WT} could not be measured directly by ITC due to the instability of *Mtu*CM and high concentration of protein that this technique demands. As an alternative, kinetic analysis was used to estimate the apparent dissociation constant ($K_{d,app}$) between *Mtu*CM and *Mtu*DAH7PS^{WT}.

This method has been previously established and is detailed in Section 9.9.4 and assumes the physical association of *Mtu*CM and *Mtu*DAH7PS^{WT} is correlated to the enhancement in the *Mtu*CM specificity constant.[85] Duplicate independent *Mtu*CM Michaelis-Menten kinetics were determined for each concentration of *Mtu*DAH7PS^{WT}. The concentration of *Mtu*CM was kept at 10 nM *Mtu*CM, except in the absence of *Mtu*DAH7PS^{WT} where 90 nM was used and the data normalised. The *Mtu*CM catalytic efficiencies were calculated from these data and plotted against *Mtu*DAH7PS^{WT} concentration to derive the $K_{d,app}$ between *Mtu*CM and *Mtu*DAH7PS^{WT} (Figure 4.11). Equation 4.1 was fitted to the data, using the catalytic efficiency of the complex ($\upsilon_{CM\bullet DS}$) and $K_{d,app}$ as the fitting parameters, by the iterative curve fitting software KaleidaGraph (Synergy Software). Sasso *et al.* adapted work by Taira

and Benkovic to derive this equation allowing the determination of the apparent *Mtu*CM•*Mtu*DAH7PS^{WT} dissociation constant for a 1:1 stoichiometry.[114]

$$\upsilon = \upsilon_{CM} + \left([CM]_0 + [DS]_0 + K_{d,app} - \sqrt{([CM]_0 + [DS]_0 + K_{d,app})^2 - 4[CM]_0[DS]_0}\right) \bullet \frac{\upsilon_{CM \bullet DS} - \upsilon_{CM}}{2[CM]_0}$$

Equation 4.1 υ, υ_{CM} and $\upsilon_{CM \bullet DS}$ are the corresponding catalytic efficiencies, $[CM]_0$ and $[DS]_0$ are the total concentrations of *Mtu*CM and *Mtu*DAH7PS^{WT} respectively. $K_{d,app}$ is the apparent dissociation constant of the complex.

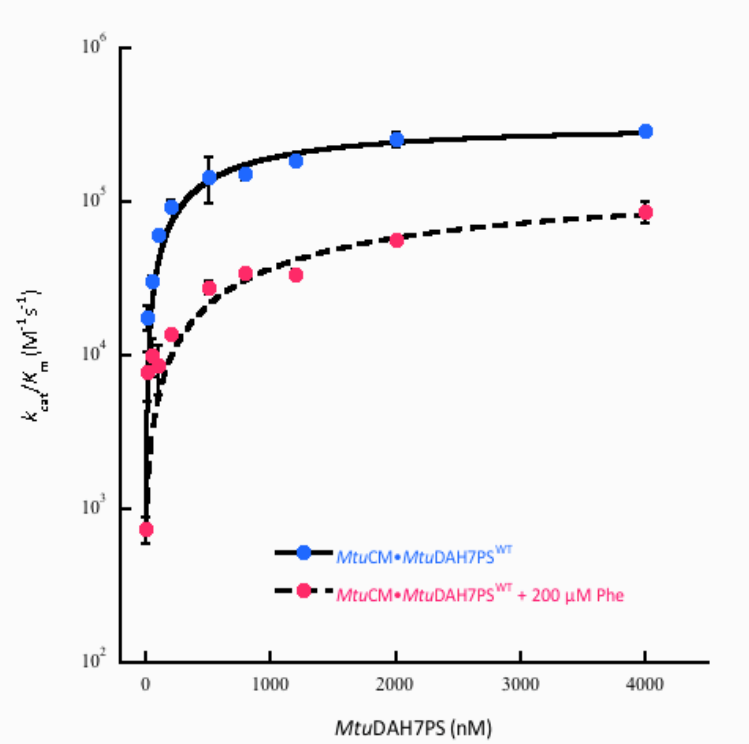

Figure 4.11 Response of *Mtu*CM catalytic efficiency (k_{cat}/K_m) to increasing concentrations of *Mtu*DAH7PS^{WT} in the absence (blue dot) and presence (pink dot) of 200 µM Phe. All assays conducted with 10 nM *Mtu*CM. Error bars represent the standard deviation of duplicate independent Michaelis-Menten measurements with at least seven points.

The $K_{d,app}$ between *Mtu*CM and *Mtu*DAH7PS^{WT} was found to be 700 ± 200 nM greater than the value of 140 ± 30 nM determined by previously under similar conditions (Figure 4.11).[85] The difference between the values is in part due to the difficulty of accurately determining the catalytic efficiencies of the lower ratios of *Mtu*CM and *Mtu*DAH7PS^{WT}, which help define the shape at the start of the curve. Both studies give $K_{d,app}$s in the nM range and indicate a moderate affinity between the two proteins.

The $K_{d,app}$ between *Mtu*CM and *Mtu*DAH7PS^{WT} was also determined in the presence of 200 µM Phe. Phe reduced the maximum activation of *Mtu*CM activity by ~68 % (Figure 4.11). The $K_{d,app}$ was determined to be 3.0 ± 0.9 µM and indicated Phe had reduced the affinity between the two proteins by more than three-fold.

Molecular dynamic simulations that modelled Phe binding to *Mtu*DAH7PS^{WT} found the β7-α7 and β8-α8 loops of *Mtu*DAH7PS became highly flexible upon ligand binding.[71] This increased flexibility of these loops may reflect a subtle change in conformation or molecular dynamics in the local area, including the interface between *Mtu*DAH7PS^{WT} and *Mtu*CM. Any changes at the interface are likely to negatively affect the contacts between the *Mtu*CM and *Mtu*DAH7PS^{WT}, reducing the affinity between the two proteins. The binding of Phe to *Mtu*DAH7PS may shift the average species of the population ensemble of the protein toward a species that has a lower affinity for *Mtu*CM and/or is less suited to activating *Mtu*CM activity. By changing the affinity of the *Mtu*DAH7PS population ensemble for *Mtu*CM it is possible the rates at which the enzymes associate and dissociate has also changed and could be responsible for the change in the apparent $K_{d,app}$.

4.8. Evidence of complex dissociation in solution

4.8.1. Native PAGE

Native PAGE to observe the formation of the complex between *Mtu*CM and *Mtu*DAH7PS was conducted using horizontal Amersham ECL 12% gels with a Tris-Alanine running buffer at pH 9.2 (detailed in Section 9.7.3). Samples are loaded at an *Mtu*DAH7PS^{WT} concentration of ~6 µM. Initial attempts were conducted under the blue native PAGE conditions used to analyse the *Mtu*DAH7PS^{WT} in Section 9.7.2 but were unsuccessful. It was thought the coomassie® G250 dye used to negatively charge the protein interfered with or blocked the interface preventing *Mtu*CM from binding.

The sample of *Mtu*DAH7PS^{WT} analysed by native PAGE under the Tris-Alanine conditions yielded a single band, with a molecular mass of ~240 kDa. The expected mass of the *Mtu*DAH7PS tetramer is

204 kDa (Figure 4.12A). This differs from the results reported for *Mtu*DAH7PS^{WT} analysed by blue native PAGE in Section 2.6.1, which showed a mixture of monomer and dimer were present. The discrepancy in results is most likely due to the difference in pH of the two running buffers. The blue native PAGE buffer is neutral and the Tris-Alanine buffer is basic. However, more thorough investigation is required to before it can be assumed the quaternary structure of *Mtu*DAH7PS^{WT} is pH dependent.

The *Mtu*DAH7PS^{WT} sample analysed in the presence of a four-fold molar excess of *Mtu*CM displayed a second higher molecular weight band (~300 kDa). The expected mass of the heterooctameric complex is 244 kDa. The difference in mass between the two bands is ~60 kDa, similar to the change in mass expected on the formation of the heterooctameric complex of ~40 kDa. Thus the second band is believed to correspond to the formation of *Mtu*CM•*Mtu*DAH7PS^{WT} complex. *Mtu*CM alone, with an expected molecular mass of ~10 kDa, does not migrate toward the anode under these native PAGE conditions.

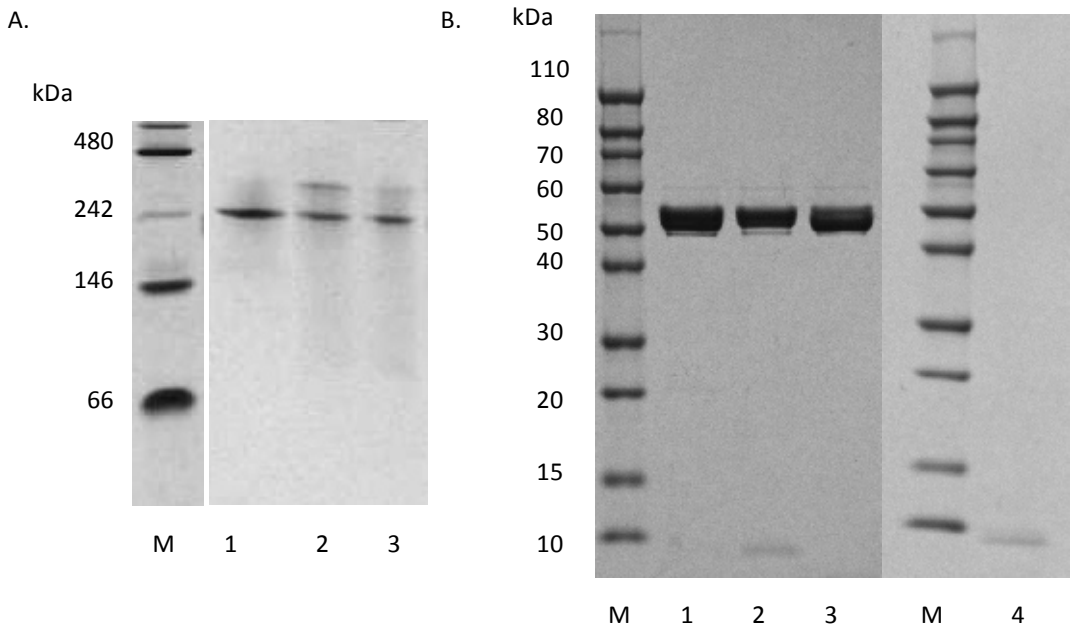

Figure 4.12 A. Native PAGE of *Mtu*DAH7PS alone (Lane 1), with four-fold molar excess of *Mtu*CM (Lane 2) and with four-fold molar excess of *Mtu*CM and 1 mM Phe (Lane 3). Lane M native molecular mass marker. B. SDS-PAGE gel of fractions eluted with elution buffer from IMAC. Lane M molecular mass marker; Lane 1 *Mtu*DAH7PS^{H6}; Lane 2 *Mtu*DAH7PS^{H6} with a four-fold molar excess of *Mtu*CM; Lane 3 *Mtu*DAH7PS^{H6} with a four-fold molar excess of *Mtu*CM and 1 mM Phe and Lane 4 *Mtu*CM prior to injection onto IMAC.

More excitingly, the second higher molecular weight band present for a sample containing a mixture of *Mtu*CM and *Mtu*DAH7PS^{WT} diminished with the addition of 1 mM Phe to the sample. This result suggested the addition of Phe prevented the formation of the heterooctameric *Mtu*CM•*Mtu*DAH7PS^{WT} complex; supporting the hypothesis Phe binding to *Mtu*DAH7PS weakens the association of the two proteins.

4.8.2. IMAC pull down assay

Although exciting, the evidence of *Mtu*CM•*Mtu*DAH7PS complex formation and dissociation obtained from the Tris-Alanine native PAGE required such precise conditions the results needed further corroboration, preferably at a more biologically relevant pH. To this end a pull down assay utilising the His_6-tagged *Mtu*DAH7PSs (*Mtu*DAH7PS^{H6}) inherent affinity for the IMAC column was developed, Section 9.7.8.

To enable *Mtu*DAH7PS to bind an IMAC column the protein was purified retaining the polyhistidine tag (*Mtu*DAH7PS-H_6). *Mtu*CM was purified as previously stated, and has no inherent affinity for an IMAC column. The proteins were applied to an IMAC column and the column washed with wash buffer to remove all unbound protein. Any bound protein was then eluted from the column using elution buffer. SDS-PAGE of the protein containing fractions showed *Mtu*DAH7PS^{H6} eluted as a single band of ~55 kDa in agreement with its expected monomeric mass (Figure 4.12B). After incubation of *Mtu*DAH7PS^{H6} with a four-fold molar excess of *Mtu*CM for 5 min, SDS-PAGE revealed two bands were present in the protein bound fraction, one at ~ 55kDa corresponding to *Mtu*DAH7PS^{H6} and a second at ~10 kDa, the expected monomeric mass of *Mtu*CM. Finally the preincubation of *Mtu*DAH7PS^{H6} with both *Mtu*CM and 1 mM Phe (and addition of 1 mM Phe to the buffers), resulted in a single band at ~ 55 kDa corresponding to the presence of *Mtu*DAH7PS^{H6}.

The coelution of *Mtu*CM in the protein bound fraction with *Mtu*DAH7PS^{H6} indicates the association between the two proteins was great enough to prevent the *Mtu*CM from being washed off the IMAC column with the wash buffer. The addition of Phe directly to the mixture of *Mtu*CM and

*Mtu*DAH7PS^{H6} resulted in the elution of *Mtu*DAH7PS^{H6} in the bound fraction alone. This result indicates Phe sufficiently weakened the association between *Mtu*DAH7PS^{H6} and *Mtu*CM to allow the *Mtu*CM to be washed off the column by the wash buffer.

4.8.3. AUC analysis

Sedimentation velocity experiments were carried out under the same conditions used to analyse *Mtu*DAH7PS^{WT} and are described in Section 9.7.7. Ali Nazmi carried out the AUC experiments and assisted with the analysis. The proteins were combined in the stated molar ratio (either 4:1 or 1:1; *Mtu*CM:*Mtu*DAH7PS^{WT}) and dialysed for 2-3 hours. Just prior to AUC analysis samples (and the reference buffer) were spiked by 100 µM Phe. Analysis was carried out at three concentrations of *Mtu*DAH7PS^{WT} 0.2, 0.4 and 0.6 mg/mL.

In Section 4.5 AUC of samples containing a mixture of *Mtu*DAH7PS^{WT} and *Mtu*CM identified the formation of the heteroctameric *Mtu*CM•*Mtu*DAH7PS^{WT} complex in solution. Formation of the complex was identified by an increase in the sedimentation coefficient in the presence of *Mtu*CM (Figure 4.13A-C).

A four-fold molar excess of *Mtu*CM resulted in a sedimentation coefficient (*s*) of ~9.2 S, and gave a calculated molecular mass of 220 kDa (Figure 4.13A). For *Mtu*DAH7PS in the presence of 100 µM Phe and a four-fold molar excess of *Mtu*CM s decreased to ~8.8 S, and gave a calculated molecular mass of ~190 kDa, in good agreement with the expected tetrameric mass of *Mtu*DAH7PS of ~204 kDa. The change in calculated mass of ~30 kDa is similar to the expected change in mass caused by the loss of four *Mtu*CM monomers (~40 kDa) and strongly supports a dissociative mechanism of inhibition for the *Mtu*CM•*Mtu*DAH7PS complex.

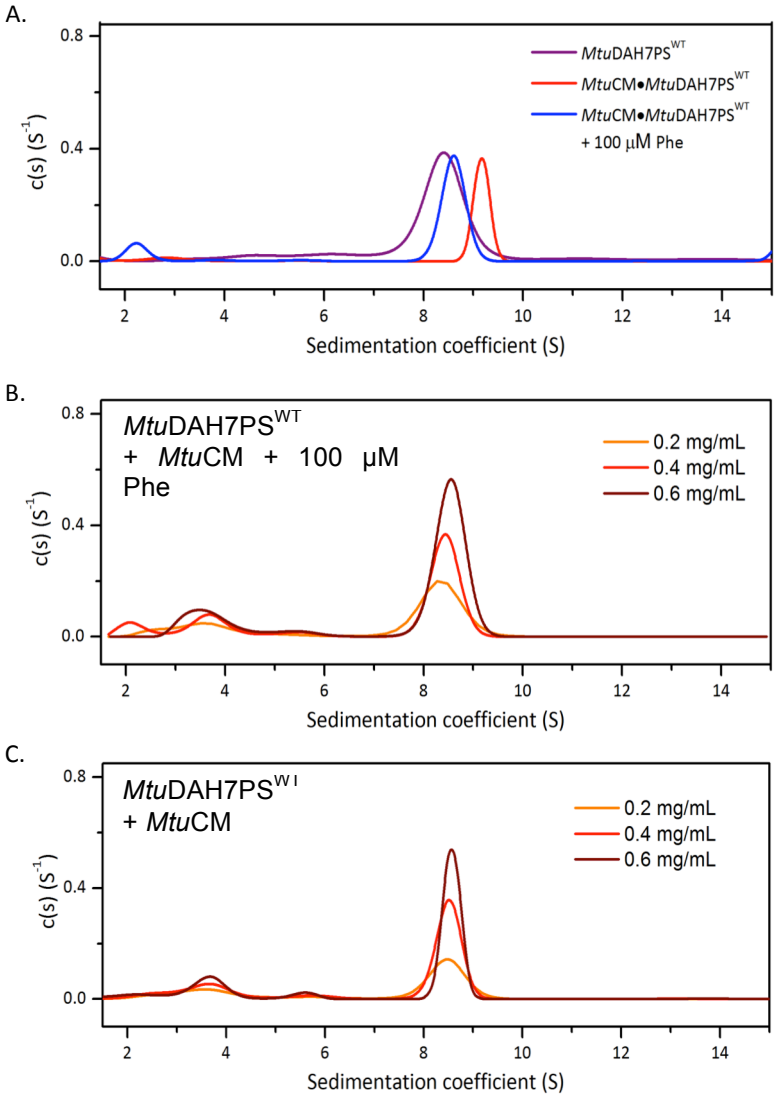

Figure 4.13 Continuous size *c*(*s*) distribution plots from sedimentation velocity experiments of A. *Mtu*DAH7PS^{WT} alone (purple), with a four-fold molar excess of *Mtu*CM (red) and four fold-molar excess of *Mtu*CM plus 100 µM Phe (blue) all analysed at an *Mtu*DAH7PS^{WT} concentration of 0.4 mg/mL; B. An equimolar mixture of *Mtu*DAH7PS^{WT} in the presence of 100 µM Phe analysed at *Mtu*DAH7PS^{WT} concentrations of 0.2 (orange), 0.4 (red) and 0.6 mg/mL (wine) and for comparison C. An equimolar mixture of *Mtu*DAH7PS^{WT} analysed at *Mtu*DAH7PS^{WT} concentrations of 0.2 (orange), 0.4 (red) and 0.6 mg/mL (wine). Experimental data and fits are shown in Appendix II.

An equimolar concentration of *Mtu*CM gave an *s* value of ~8.6 S, in the presence of 100 µM Phe *s* value was ~8.5 S, but the peaks of the distribution plot have become much broader (Figure 4.13B-C). A lower *s* value is an indication of a lower average molecular mass of the proteins in solution. The broadening of the continuous size distribution peaks indicated the sedimentation boundaries were less well defined and a greater range of molecular masses being sampled by the proteins in solution. Thus the broadening of the peaks is likely due to a larger proportion of unbound *Mtu*DAH7PS and *Mtu*CM in solution.

These results showed the addition of Phe shifted the determined sedimentation coefficient for a mixture of *Mtu*CM and *Mtu*DAH7PS toward that of *Mtu*DAH7PS^{WT} alone. This would indicate the peak represents two or more close boundaries due to a mixture of *Mtu*DAH7PS^{WT} and *Mtu*CM•*Mtu*DAH7PS^{WT} complex being present in solution. The addition of Phe promoted the dissociation of the complex, which in turn increased the proportion of lower molecular weight *Mtu*DAH7PS^{WT} in solution and resulted in the observed decrease in sedimentation coefficient and broadening of the distribution peaks.

4.9. Effect of complex formation on *Mtu*DAH7PS

4.9.1. Effect on kinetic parameters

The activity of *Mtu*DAH7PS^{WT} (60 nM) in the presence of a ten-fold molar excess of *Mtu*CM was determined using the steady-state kinetic assays developed for *Mtu*DAH7PS^{WT} and are detailed in Section 9.9.1. The data was fitted to the Michaelis-Menten equation to derive the kinetic parameters.

The presence of *Mtu*CM increased the k_{cat} and decreased the Michaelis constants for both PEP and E4P resulting in the catalytic efficiency of both substrates improving compared to *Mtu*DAH7PS^{WT} alone (Table 4.4). The modest increase in catalytic efficiency of *Mtu*DAH7PS^{WT} indicates the interaction of *Mtu*CM and *Mtu*DAH7PS has favourable effect on both enzymes, albeit overall the interaction is far more beneficial to *Mtu*CM.

Table 4.4 Kinetic parameters determined from a single set of Michaelis-Menten kinetic data for *Mtu*DAH7PS^{WT} with and without the presence of a ten-fold excess of *Mtu*CM. Michaelis-Menten plots are shown in Appendix I. Stated errors determined by least squares fit of the data to the model.

Protein(s)	K_m^{E4P} (μM)	K_m^{PEP} (μM)	k_{cat} (s^{-1})	Catalytic efficiency k_{cat}/K_m^{E4P} ($s^{-1}mM^{-1}$)	Catalytic efficiency k_{cat}/K_m^{PEP} ($s^{-1}mM^{-1}$)
*Mtu*DAH7PS^{WT}	28 ± 2	37 ± 4	4.7 ± 0.1	170 ± 20	130 ± 20
*Mtu*CM• *Mtu*DAH7PS^{WT}	20 ± 2	27 ± 2	7.1 ± 0.1	360 ± 40	260 ± 20

4.9.2. Effect of *Mtu*CM on *Mtu*DAH7PS^{WT} regulation

Inhibition of *Mtu*DAH7PS activity in the presence of a ten-fold molar excess of *Mtu*CM was investigated using the standard kinetic assays for the inhibition studies of *Mtu*DAH7PS^{WT}, except *Mtu*DAH7PS^{WT} (40 nM) and *Mtu*CM were allowed to incubate for 10 min prior to initiation with E4P. The experimental procedure is detailed in Section 9.9.3.

There were marked changes in the regulatory profile of *Mtu*DAH7PS^{WT} in the presence of a ten-fold molar excess of *Mtu*CM. Most notably the addition of Phe, Tyr or Trp activated *Mtu*DAH7PS activity in the presence of *Mtu*CM (Figure 4.14). Trp increased *Mtu*DAH7PS^{WT} activity to ~225 %, relative to the *Mtu*DAH7PS activity in the presence of just *Mtu*CM. *Mtu*DAH7PS^{WT} in the presence of *Mtu*CM displayed slightly better activity than *Mtu*DAH7PS^{WT} alone as supported by the kinetic parameters determined in 4.9.1. Thus Trp genuinely activated *Mtu*DAH7PS activity in the presence of *Mtu*CM.

It seems contradictory that the presence of Phe or Tyr was able to activate *Mtu*DAH7PS activity of a mixture of *Mtu*DAH7PS^{WT} and *Mtu*CM given the proposed mechanism of Phe binding to *Mtu*DAH7PS^{WT} weakening the association between *Mtu*DAH7PS^{WT} and *Mtu*CM. However, the inhibition studies were conducted using a ten-fold molar excess of *Mtu*CM present in this experiment, whereas AUC and native PAGE used to show the dissociation of the complex were conducted at a four-fold molar excess of *Mtu*CM. Also Phe was shown to be the least activating of the three aromatic amino acids, increasing activity to ~140 %.

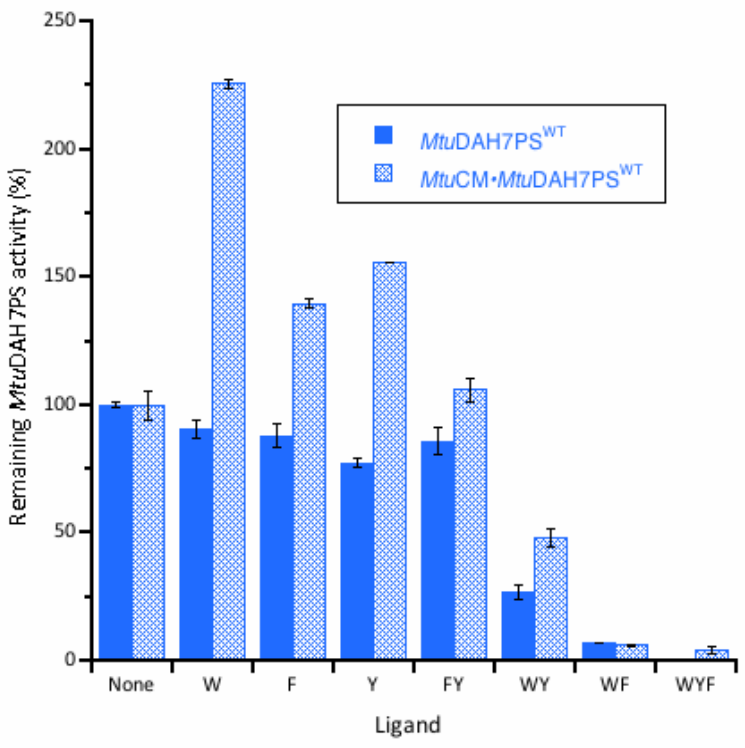

Figure 4.14 Remaining *Mtu*DAH7PS activity for *Mtu*DAH7PS^{WT} (blue) and *Mtu*DAH7PS^{WT} with a ten-fold molar excess of *Mtu*CM (blue hash) in the presence of various single, binary and ternary combinations of aromatic amino acids. The aromatic amino acids are represented by their one letter code; Trp, W; Phe, F and Tyr, Y. Each letter also represents 200 µM of the corresponding aromatic amino acid. Assays conducted in the presence of 150 µM E4P and PEP. Error bars depict the standard deviation of triplicate measurements. P-values provided in appendix V.

The activation of *Mtu*DAH7PS by Phe and Tyr indicates the dissociation of *Mtu*CM from *Mtu*DAH7PS is not straightforward. In chapter 2 AUC showed *Mtu*DAH7PS consists of a mixture of oligomeric states in solution, but the addition of Trp and/or Phe stabilise the tetramer species (Section 2.6.2). As the *Mtu*CM•*Mtu*DAH7PS interface is located across the *Mtu*DAH7PS tetramer interface it would be logical to assume that the *Mtu*DAH7PS tetramer would have a stronger interaction with *Mtu*CM than a lower oligomeric state. Thus the aromatic amino acids probably activate *Mtu*DAH7PS activity primarily by stabilising the *Mtu*DAH7PS tetramer. The binding of Phe and Tyr to *Mtu*DAH7PS may shift the position of the *Mtu*DAH7PS population ensemble toward a tetramer species that has a lower affinity for *Mtu*CM. When the complex does form between Phe-bound *Mtu*DAH7PS and *Mtu*CM it is beneficial to *Mtu*DAH7PS activity.

The activation of *Mtu*DAH7PS (in the presence of *Mtu*CM) activity by a single ligand is practically eliminated in the presence of multiple aromatic amino acids. The addition of multiple aromatic amino acids to the mixture of *Mtu*DAH7PS^{WT} and *Mtu*CM resulted in similar inhibitory behaviour as *Mtu*DAH7PS^{WT} alone (Figure 4.14). This result shows that the association between *Mtu*DAH7PS and *Mtu*CM does not adversely affect the synergistic regulatory network of *Mtu*DAH7PS.

In the absence of *Mtu*CM a single ligand cannot activate *Mtu*DAH7PS. AUC demonstrated that when *Mtu*CM or an aromatic amino acid binds to *Mtu*DAH7PS the quaternary structure equilibrium of *Mtu*DAH7PS is shifted in favour of the tetramer (Section 4.5). It is likely the tetramer is both the regulated *Mtu*DAH7PS species and the species that interacts with *Mtu*CM. The single aromatic amino acids appear to enhance *Mtu*DAH7PS activity in the presence of *Mtu*CM. *Mtu*DAH7PS activity in the presence of *Mtu*CM remained subject to synergistic inhibition by binary or ternary combinations of aromatic amino acids that included Trp were present.

4.10. Allosteric sites of *Mtu*DAH7PS regulate *Mtu*CM activity

To demonstrate that the binding sites of *Mtu*DAH7PS were responsible for allosteric regulation of *Mtu*CM inhibition studies were conducted utilising the *Mtu*DAH7PS variants described in Chapter 3. The two variants *Mtu*DAH7PS^{R171A} and *Mtu*DAH7PS^{R256A} were shown to have impaired binding at the site of the substitution, site 1 and site 2 respectively.

4.10.1. Activation of *Mtu*CM activity in the presence of *Mtu*DAH7PS^{R171A} or *Mtu*DAH7PS^{R256A}

The standard kinetic assays used to measure *Mtu*CM activity in the presence of a ten-fold molar excess of *Mtu*DAH7PS^{WT} were also used to determine the kinetic parameters of *Mtu*CM activity in the

presence of a ten-fold molar excess of *Mtu*DAH7PS^{R171A} or *Mtu*DAH7PS^{R256A}. The concentration of *Mtu*CM was held constant at 30 nM. The experimental methodology is detailed in Section 9.9.1.

The kinetic parameters for *Mtu*CM activity derived from the Michaelis-Menten kinetics for *Mtu*CM in the presence of either *Mtu*DAH7PS^{R171A} or *Mtu*DAH7PS^{R256A} were compared to those for *Mtu*CM activity in the presence of *Mtu*DAH7PS^{WT} (Table 4.5). *Mtu*DAH7PS^{WT} and the *Mtu*DAH7PS variants were all able to activate *Mtu*CM activity by ~120-fold. Based on the determined kinetic parameters the substitutions introduced to the allosteric biding sites of *Mtu*DAH7PS did not adversely affect the ability of the *Mtu*DAH7PS variants to activate *Mtu*CM activity.

Table 4.5 Kinetic parameters for *Mtu*CM activity determined from a single set of Michaelis-Menten kinetic data of *Mtu*CM with or without a ten-fold excess of variant *Mtu*DAH7PS. – indicates not applicable. * activation factor determined as the ratio of the *Mtu*CM•*Mtu*DAH7PS^{variant} catalytic efficiency to *Mtu*CM catalytic efficiency. The Michaelis-Menten plots are shown in Appendix I. Errors represent the error of fit of the data to the model as determine by a least squares fit.

Protein	K_m^{CA} **(μM)**	k_{cat} **(s^{-1})**	k_{cat}/K_m^{CA} **($mM^{-1}s^{-1}$)**	**Activation factor***
*Mtu*CM	500 ± 30	0.42 ± 0.02	0.84 ± 0.09	–
*Mtu*CM•*Mtu*DAH7PS^{WT}	52 ± 4	5.4 ± 0.1	104 ± 9	120 ± 20
*Mtu*CM•*Mtu*DAH7PS^{R171A}	64 ± 6	6.5 ± 0.2	100 ± 1	120 ± 20
*Mtu*CM•*Mtu*DAH7PS^{R256A}	53 ± 4	5.5 ± 0.1	104 ± 9	120 ± 20

To gain more insight into the ability of the *Mtu*DAH7PS variants to activate *Mtu*CM the activity of *Mtu*CM was determined with three different ratios of *Mtu*CM to *Mtu*DAH7PS: 1:1, 1:10 or 1:200. Assays were conducted using the standard assay conditions previously used for measuring *Mtu*CM activity in the presence of *Mtu*DAH7PS and is detailed in Section 9.9.1. Assays were initiated with 150 μM chorismic acid.

The activation profile of *Mtu*CM activity with increasing *Mtu*DAH7PS^{R171A} concentration was nearly identical to *Mtu*DAH7PS^{WT} (Figure 4.15). Although this study found the activation profile with

increasing *Mtu*DAH7PS^{R256A} concentration was similar to *Mtu*DAH7PS^{WT}, *Mtu*DAH7PS^{R256A} was able to better enhance *Mtu*CM activity when present at a 200-fold excess. Further investigation is required to verify the result, but if confirmed it suggests the Arg256Ala substitution may have slightly improved the interaction between the two proteins.

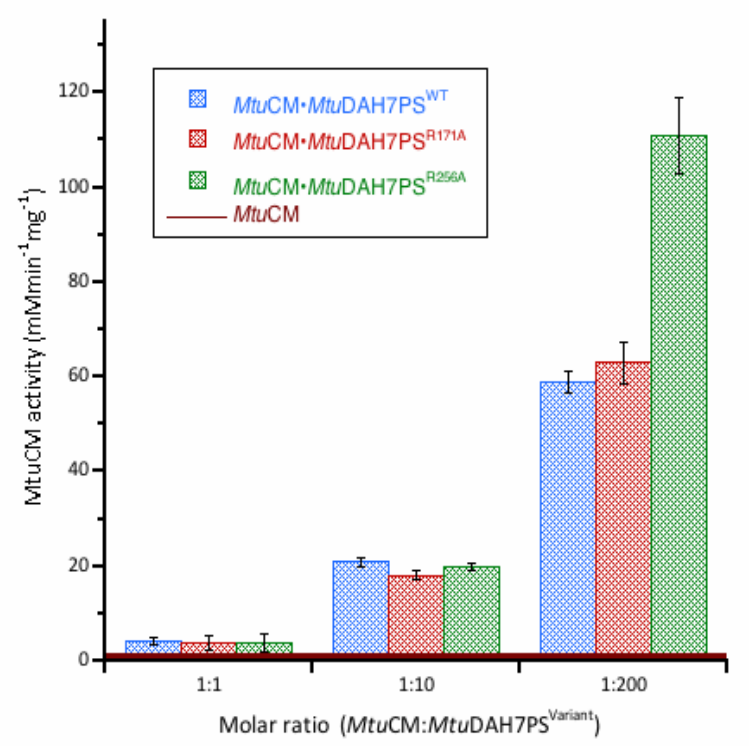

Figure 4.15 Three point activation profile for the activation of *Mtu*CM activity by *Mtu*DAH7PS^{WT} (blue hash) *Mtu*DAH7PS^{R171A} (red hash) and *Mtu*DAH7PS^{R256A} (green hash). Error bars depict the standard deviation of duplicate measurements.

4.10.2. Regulation of *Mtu*CM activity by *Mtu*DAH7PS^{R171A} and *Mtu*DAH7PS^{R256A}

*Mtu*DAH7PS^{R171A} or *Mtu*DAH7PS^{R256A} were added to the assay conditions in a ten-fold excess of the molar concentration of *Mtu*CM (60 nM). Assays for *Mtu*CM activity were conducted as previously stated for *Mtu*CM and *Mtu*DAH7PS^{WT} and detailed in Section 9.9.3. Assays were initiated with 25 µm chorismic acid to observe the maximum inhibition possible.

The *Mtu*CM activity of a mixture of *Mtu*DAH7PS^{R171A} and *Mtu*CM was insensitive to the addition of any single or multiple combinations of aromatic amino acids (Figure 4.16). The substitution of *Mtu*DAH7PS^{R171A} was introduced to disrupt binding at site 1, the Phe-selective binding site (Section 3). The inability of *Mtu*DAH7PS^{R171A} to regulate *Mtu*CM activity suggests site 1 plays a vital role in both the Phe and Tyr regulation of *Mtu*CM activity.

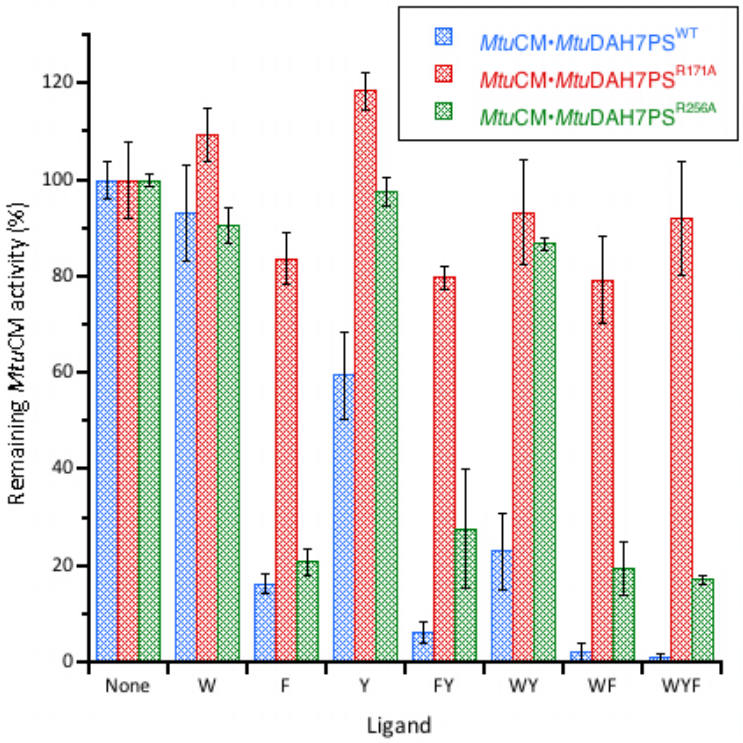

Figure 4.16 Remaining *Mtu*CM activity in the presence of various single, binary and ternary combinations of aromatic amino acids for *Mtu*CM with a ten-fold excess of *Mtu*DAH7PS^{WT} (blue hash) *Mtu*DAH7PS^{R171A} (red hash) or *Mtu*DAH7PS^{R256A} (green hash). The aromatic amino acids are represented by their one letter code; Trp, W; Phe, F and Tyr, Y. Each letter also represents 200 µM of the corresponding aromatic amino acids. Assays conducted with 25 µM chorismic acid and 60 nM *Mtu*CM. Error bars depict the standard deviation of at least duplicate measurements. P-values provided in appendix V.

The activity of *Mtu*CM with a ten-fold molar excess of *Mtu*DAH7PS^{R256A} was insensitive to Tyr but retained sensitivity to Phe. *Mtu*CM activity was also insensitive to the combination of Trp and Phe in the presence of *Mtu*DAH7PS^{R256A}. Remember, the Arg256Ala substitution was introduced to disrupt binding at site 2, the Tyr-selective binding site. Hence, Phe only needs to bind to site 1 of *Mtu*DAH7PS to inhibit *Mtu*CM activity. On the other hand Tyr must bind to both site 1 and site 2 of *Mtu*DAH7PS to inhibit *Mtu*CM activity. Like *Mtu*DAH7PS^{WT}, *Mtu*DAH7PS^{R256A} was able to synergistically regulate *Mtu*CM activity in the presence of Trp and Phe or Trp, Phe and Tyr.

Native PAGE analysis was also conducted on both *Mtu*DAH7PS variants under the same conditions as *Mtu*DAH7PS^{WT} (as outlined in Section 9.7.3) in order to observe formation of the *Mtu*CM•*Mtu*DAH7PS variant complexes. Samples were prepared with ~6-10 µM *Mtu*DAH7PS and In the presence of a four-fold molar excess of *Mtu*CM. Samples of *Mtu*DAH7PS^{R171A} and *Mtu*DAH7PS^{R256A} ran on the gel as a single band of ~240 kDa as seen previously for the wild type enzyme (Figure 4.17). Both *Mtu*DAH7PS variants formed two bands in the presence of *Mtu*CM, the first at ~240 kDa and the second at higher molecular mass of ~300 kDa. This indicated both *Mtu*DAH7PS variants are able to form a complex with *Mtu*CM.

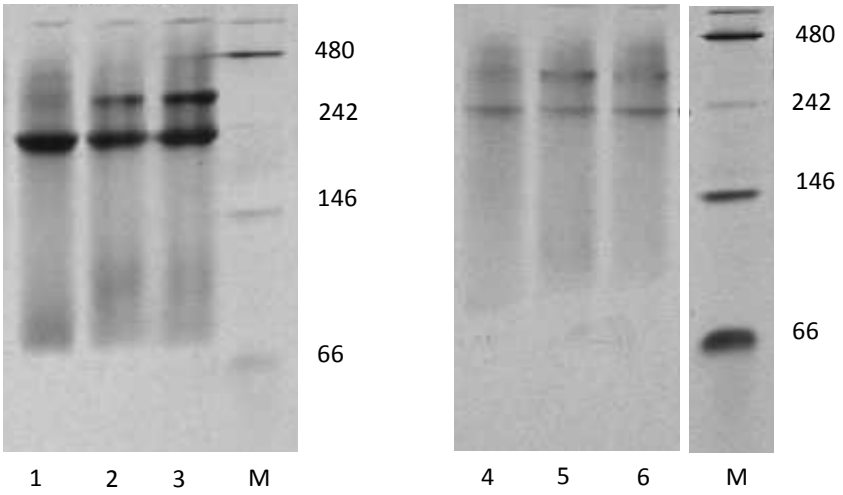

Figure 4.17 Native PAGE of *Mtu*DAH7PS^{R171A} alone (Lane 1), with four-fold molar excess of *Mtu*CM (Lane 2) and with four-fold molar excess of *Mtu*CM and 1 mM Phe (Lane 3) and *Mtu*DAH7PS^{R256A} alone (Lane 4), with four-fold molar excess of *Mtu*CM (Lane 5) and with four-fold molar excess of *Mtu*CM and 1 mM Phe (Lane 6). Lane M native molecular mass marker.

The addition of 1 mM Phe to a mixture of *Mtu*DAH7PS^{R256A} and *Mtu*CM diminish the intensity of the higher molecular mass band as seen previously for *Mtu*DAH7PS^{WT}. The loss of the higher molecular mass band suggests the *Mtu*CM•*Mtu*DAH7PS^{R256A} complex is able to dissociate in the presence of Phe. This finding is consistent with the previous inhibition studies that showed *Mtu*CM•*Mtu*DAH7PS^{R256A} was sensitive to Phe (Section 4.10.2). Of greater interest, was the failure of 1 mM Phe to diminish the second higher molecular mass band in the presence of a mixture *Mtu*DAH7PS^{R171A} and *Mtu*CM. This observation is also consistent with the inhibition studies, as the addition of Phe to *Mtu*CM•*Mtu*DAH7PS^{R171A} does not appear to affect the *Mtu*CM activity of the complex. Overall, these results reveal the addition of Phe changes the nature of the interaction

between *Mtu*DAH7PS and *Mtu*CM, causing dissociation under the right conditions. This change may be a very important part of the regulatory mechanism.

Both the inhibition studies and native PAGE conducted with *Mtu*DAH7PS^{R171A} and *Mtu*DAH7PS^{R256A} indisputably showed the allosteric binding sites of *Mtu*DAH7PS were responsible for observed regulation of *Mtu*CM activity of the *Mtu*CM•*Mtu*DAH7PS complex. Site 1 of *Mtu*DAH7PS was found to be primarily responsible for the regulatory sensitivity of *Mtu*CM activity to Phe. For *Mtu*CM to show significant sensitivity to Tyr both sites 1 and 2 of *Mtu*DAH7PS had to be available for ligand binding.

4.10.3. Effect of *Mtu*CM on *Mtu*DAH7PS^{R171A} and *Mtu*DAH7PS^{R256A} kinetic parameters

The activities of *Mtu*DAH7PS^{R171A} and *Mtu*DAH7PS^{R256A} in the presence of a ten-fold molar excess of *Mtu*CM was measured using the steady-state kinetic assays developed for *Mtu*DAH7PS^{WT} and are detailed in Section 9.9.1. The concentration of *Mtu*DAH7PS was held constant at 60 nM. The data was fitted to the Michaelis-Menten equation to derive the kinetic parameters.

The kinetic parameters determined for *Mtu*DAH7PS^{R256A} in the presence of *Mtu*CM were compared to *Mtu*DAH7PS^{WT} in the presence of *Mtu*CM (Table 4.6). *Mtu*CM activated both *Mtu*DA7PS^{WT} and *Mtu*DAH7PS^{R256A} by approximately two-fold, suggesting the Arg256Ala substitution has had no adverse affect on the activation of *Mtu*DAH7PS by *Mtu*CM.

There was some variation in the kinetic parameters of *Mtu*DAH7PS^{R171A} compared to *Mtu*DAH7PS^{WT} when determined in the presence of *Mtu*CM (Table 4.6). The catalytic efficiency with respect to PEP of *Mtu*DAH7PS^{R171A} is higher. Thus the introduction of the Arg171Ala substitution into site 1 of *Mtu*DAH7PS has perturbed the interaction between *Mtu*CM and *Mtu*DAH7PS^{R171A}, but not necessarily to the disadvantage of either enzyme. Whether a change has occurred at the interface of *Mtu*CM and *Mtu*DAH7PS^{R171A} or along a signal transmission pathway is unclear. These findings do however suggest

site 1 is able to interact with both *Mtu*CM *Mtu*DAH7PS interface and the active site, in agreement with the inhibition studies.

Table 4.6 Kinetic parameters determined from a single set of Michaelis-Menten kinetics for *Mtu*DAH7PS activity of variant *Mtu*DAH7PSs with and without the presence of a ten-fold excess of *Mtu*CM. – Indicates not applicable. The Michaelis-Menten plots are shown in Appendix I. Error represents the error of curve fitting to the data set by least squares fit.

Protein(s)	K_m^{E4P} (μM)	K_m^{PEP} (μM)	k_{cat} (s^{-1})	Catalytic efficiency k_{cat}/K_m^{E4P} ($s^{-1}mM^{-1}$)	Catalytic efficiency k_{cat}/K_m^{PEP} ($s^{-1}mM^{-1}$)	Activation factors E4P	Activation factors PEP
*Mtu*DAH7PS^{WT}	28 ± 2	37 ± 4	4.7 ± 0.1	170 ± 20	130 ± 20	–	–
*Mtu*CM• *Mtu*DAH7PS^{WT}	20 ± 2	27 ± 2	7.1 ± 0.1	360 ± 40	260 ± 20	2.1 ± 0.5	2.1 ± 0.5
*Mtu*DAH7PS^{R171A}	35 ± 3	60 ± 6	7.0 ± 0.3	200 ± 30	120 ± 20	–	–
*Mtu*CM• *Mtu*DAH7PS^{R171A}	48 ± 4	15 ± 1	10.1 ± 0.2	210 ± 20	670 ± 60	1.1 ± 0.2	5 ± 1
*Mtu*DAH7PS^{R256A}	33 ± 1	16 ± 2	5.5 ± 0.1	170 ± 10	340 ± 50	–	–
*Mtu*CM• *Mtu*DAH7PS^{R256A}	23 ± 1	10 ± 1	6.4 ± 0.1	280 ± 20	640 ± 70	1.7 ± 0.2	1.9 ± 0.5

4.11. Effect of the *Mtu*DAH7PS polyhistidine tag on the interaction of *Mtu*DAH7PS and *Mtu*CM

All *Mtu*DAH7PS variants characterised in this thesis have had their polyhistidine tag removed, unless expressly stated otherwise. This was necessary to increase *Mtu*DAH7PS stability and purification yields. Previously published work appears to have been conducted using polyhistidine tagged *Mtu*DAH7PS for all kinetic analysis.[85] No studies were conducted to show if the polyhistidine tag affected the characterisation of the *Mtu*CM•*Mtu*DAH7PS complex. This section of work investigated if the retention of the *Mtu*DAH7PS polyhistidine tag (*Mtu*DAH7PS^{H6}) affects the regulation of *Mtu*DAH7PS directly or the activation and regulation of *Mtu*CM activity.

4.11.1. Feedback regulation of *Mtu*DAH7PS^{H6}

To understand the impact retention of the polyhistine tag on *Mtu*DAH7PS^{H6} has on the activation and regulation of *Mtu*CM activity the effect on the feedback regulation of *Mtu*DAH7PS itself needs to be

established. Kinetic assays were conducted under the standard inhibition assay conditions used to study the wild type enzyme detailed in Section 9.9.3.

The regulation of *Mtu*DAH7PS^{H6} was less sensitive to the presence of multiple aromatic amino acids. The addition of Trp and Phe resulted in ~15 % more activity than *Mtu*DAH7PS^{WT} (Figure 4.18). The addition of Trp and Tyr was even less effective, with a total reduction of *Mtu*DAH7PS activity of ~35 %, much less than the ~75 % achieved by *Mtu*DAH7PS^{WT}. Similarly, the ternary combination of aromatic amino acids was less effective, reducing *Mtu*DAH7PS activity to ~7 %. The regulatory behaviour of *Mtu*DAH7PS is adversely affected by the retention of the polyhistidine tag used for affinity purification.

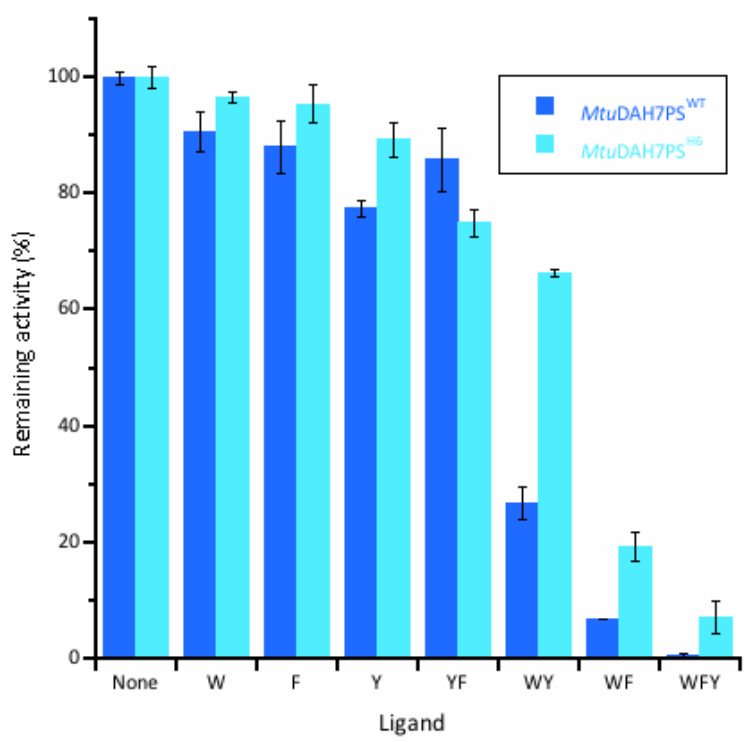

Figure 4.18 Remaining activity of *Mtu*DAH7PS^{WT} (blue), *Mtu*DAH7PS^{H6} (cyan) in the presence of various single, binary and ternary combinations of aromatic amino acids. The aromatic amino acids are represented by their one letter code; Trp, W; Phe, F and Tyr, Y. Each letter also represents 200 µM of the corresponding aromatic amino acid. Error bars depict the standard deviation of triplicate measurements. P-values provided in appendix V.

Residues Trp3 and Asp6, located on the N-terminal tail of *Mtu*DAH7PS, were shown crystallographically to contribute to the formation of site 1, and move on Phe or Tyr binding.[48,69] Therefore the addition of the polyhistidine tag at the N-terminal end of *Mtu*DAH7PS may disrupt the

interactions these residues are responsible for at site 1. Furthermore the added bulk at the end of the N-terminal extension by the polyhistidine tag may alter the flexibility of the N-terminal residues, limiting the movement of the residues involved in signalling ligand binding at site 1 to other allosteric binding sites. Alternatively the steric bulk created by the additional residues of the polyhistidine tag may physically block either or both site 1 or site 2, preventing ligand access.

4.11.2. Activation of *Mtu*CM by *Mtu*DAH7PS^{H6}

A three point activation profile to quickly determine how well *Mtu*DAH7PS^{H6} can activate *Mtu*CM activity in comparison to *Mtu*DAH7PS^{WT} was carried out as detailed in Section 9.9.1. The *Mtu*CM activity was determined for 1:1, 1:10 and 1:200 (*Mtu*CM:*Mtu*DAH7PS) mixtures of the two proteins and initiated with 150 µM chorismic acid. *Mtu*DAH7PS^{H6} was found to activate *Mtu*CM slightly less effectively than the wild type enzyme when *Mtu*DAH7PS was present in a ten-fold molar excess or more (Figure 4.19).

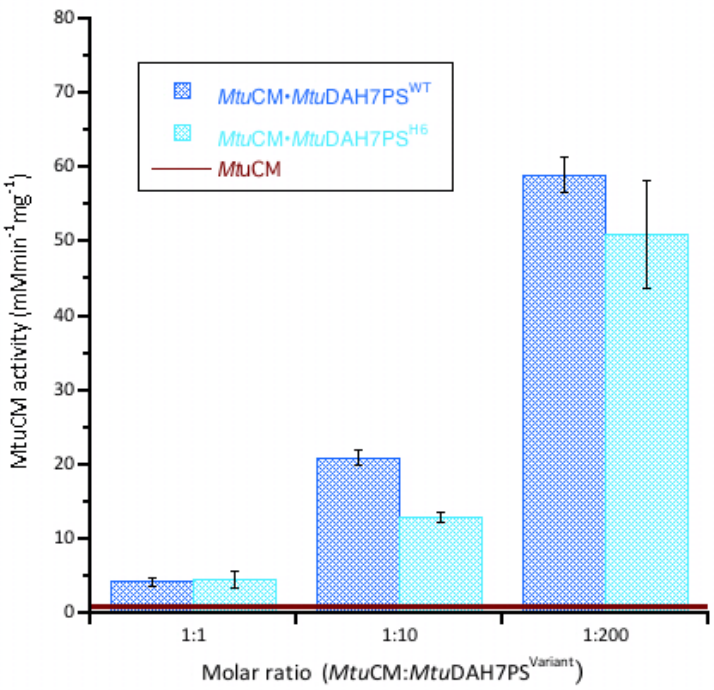

Figure 4.19 The activation of *Mtu*CM activity in the presence of with either an equimolar, ten-fold or 200-fold excess of *Mtu*DAH7PS^{WT} (blue hash) or *Mtu*DAH7PS^{H6} (cyan hash). The burgundy line indicates the activity of *Mtu*CM alone. Assays conducted with 150 µM chorismic acid and 60 nM *Mtu*CM except for reactions requiring a 200-fold excess of *Mtu*DAH7PS where 10 nM of *Mtu*CM and *Mtu*CM alone where 90 nM were used and the results normalised. Error bars depict the standard deviation of duplicate measurements

4.11.3. Feedback regulation of the *Mtu*CM activity

Inhibition studies were conducted to determine the regulatory sensitivity of *Mtu*CM activity in the presence of ten-fold excess of *Mtu*DAH7PS^{H6}. Assays were conducted as detailed in Section 9.9.3.

*Mtu*CM activity retained similar sensitivity to Phe or Tyr in the presence of either *Mtu*DAH7PS^{WT} or *Mtu*DAH7PS^{H6}. Nevertheless, there were striking differences in the feedback inhibition of *Mtu*CM activity in the presence of excess *Mtu*DAH7PS^{WT} compared to *Mtu*DAH7PS^{H6}. The *Mtu*CM activity of a mixture of *Mtu*CM and *Mtu*DAH7PS^{H6} was sensitive to the addition of Trp, reducing activity to ~50 % (Figure 4.20). Intriguingly, despite the increased sensitivity to Trp, the addition of Trp and Phe resulted in less effective inhibition of *Mtu*CM activity in the presence of *Mtu*DAH7PS^{H6}. The acquired sensitivity of *Mtu*CM activity to Trp was unexpected and had not previously been reported[85]. *Mtu*CM activity to combinations of Trp and Tyr or Trp, Phe and Tyr, were slightly more sensitive in the presence of *Mtu*DAH7PS^{H6}. This work demonstrated the polyhistidine tag of the *Mtu*DAH7PS does alter the regulatory sensitivity conveyed to its non-covalent partner *Mtu*CM.

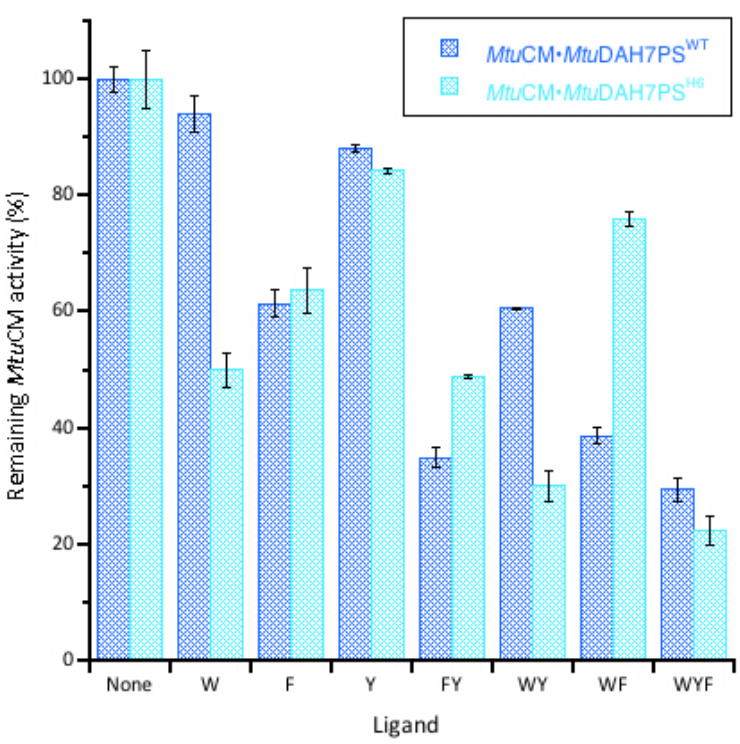

Figure 4.20 Remaining *Mtu*CM activity in the presence of various single, binary and ternary combinations of aromatic amino acids for *Mtu*CM with a ten-fold excess of *Mtu*DAH7PS^{WT} (blue hash) or *Mtu*DAH7PS^{H6} (cyan hash). The aromatic amino acids are represented by their one letter code; Trp, W; Phe, F and Tyr, Y. Each letter also represents 200 µM of the corresponding aromatic amino acids. Assays conducted in the presence of 150 µM chorismic acid and 60 nM *Mtu*CM. Error bars depict the standard deviation of at least duplicate measurements. P-values provided in appendix V.

Prior work has shown the Trp and Phe site are intimately connected through subtle changes in molecular dynamics.[71,115] Movement of the N-terminal residues (Trp 3 through to Asp 6) are the only crystallographically detectable changes that occur upon ligand binding to site 1.[48,69] The inhibition studies of *Mtu*DAH7PS^{H6} hinted the polyhistidine tail had affected the ability of site 1 to bind or signal binding to other allosteric binding sites and the active site. It has also been shown Phe must bind to site 1 of *Mtu*DAH7PS in order to elicit a regulatory response from both *Mtu*DAH7PS activity (in combination with Trp) and *Mtu*CM activity. As the regulation of *Mtu*CM activity for Phe alone is unaffected by the polyhistidine tag of *Mtu*DAH7PS^{H6}, site 1 cannot be physically blocked by the tag. Instead it suggests that the polyhistidine tag of *Mtu*DAH7PS^{H6} disrupts the binding contacts and or the changes in flexibility that signal to the Trp site ligand binding has occurred at site 1. The acquired sensitivity of *Mtu*CM activity to Trp binding and decreased sensitivity to the combination of Trp and

Phe also support disruption of the communication network between the Trp site and site 1 of *Mtu*DAH7PS.

4.12. Chapter summary

The expression and purification protocol developed was successful, yielding *Mtu*CM of the correct molecular mass and with comparable kinetic properties to previous studies[85,86]. *Mtu*CM showed no regulatory sensitivity to any combination of aromatic amino acids, but DSF studies showed the amino acids affected the thermal stability of *Mtu*CM.

The formation of the *Mtu*CM•*Mtu*DAH7PS complex in solution was identified by AUC. The sedimentation coefficient of *Mtu*DAH7PS increased in the presence of a four-fold molar excess of *Mtu*CM to ~9.4 S and corresponded to a molecular mass ~ 220 kDa, in the close agreement with the expected 244 kDa molecular mass of the heterooctameric *Mtu*CM•*Mtu*DAH7PS complex. AUC also showed the amount of the *Mtu*CM•*Mtu*DAH7PS complex formed in solution was proportional to the ratio of the two components. For a fixed concentrations of *Mtu*DAH7PS, as the molar excess of *Mtu*CM was increased so too did the amount of *Mtu*CM•*Mtu*DAH7PS complex formed.

*Mtu*DAH7PS was modestly activated (two-fold activation) by the presence of a ten-fold excess of *Mtu*CM. As previously reported *Mtu*DAH7PS greatly enhances *Mtu*CM activity; this study found a ten-fold molar excess enhanced catalytic efficiency by ~120-fold.[85] *Mtu*CM catalytic efficiency showed a hyperbolic response to increasing *Mtu*DAH7PS^{WT} concentration, plateauing when the molar excess of *Mtu*DAH7PS^{WT} exceeded 200-fold. The increase in *Mtu*CM catalytic efficiency in the presence of *Mtu*DAH7PS^{WT} was attributed to a huge decrease in the Michaelis constant of chorismic acid and a large increase in the turnover number. Comparison of crystal coordinates of *Mtu*CM with and without *Mtu*DAH7PS bound revealed significant rearrangement of the H1-H2 loop and C-terminal tail of *Mtu*CM.[85] These changes were accompanied by significant rearrangement of the *Mtu*CM active site, arguably better positioning the residues for interaction with the substrate. These conformational

adjustments may account for the improved kinetic parameters when *Mtu*CM is in the presence of *Mtu*DAH7PS^{WT}.

Most surprisingly the presence of any single aromatic amino acids was found to activate *Mtu*DAH7PS activity in the presence of a ten-fold molar excess of *Mtu*CM. However, combinations of aromatic amino acids including Trp were found to synergistically regulate *Mtu*DAH7PS activity, as seen for *Mtu*DAH7PS alone. In *E. coli* cells the concentration of Trp, Phe and Tyr have been reported to be 12, 18 and 29 μM respectively.[116] Intriguingly, these relative cellular concentrations of the aromatic amino acids correlate with their ability to activate the *Mtu*DAH7PS activity in the presence of *Mtu*CM.

At the end of the shikimate pathway chorismate is either directed toward the synthesis of Trp by anthranilate synthase or toward the synthesis of Phe and Tyr via chorismate mutase. When *Mtu*DAH7PS was in the presence of two aromatic amino acids (the end products of the pathway), one from each branch of the aromatic amino acid biosynthetic pathway (i.e. Trp in combination with either Phe or Tyr), *Mtu*DAH7PS activity was inhibited whether or not *Mtu*CM was present. Thus excess product from a single branch of the aromatic amino acid biosynthetic pathway will not prevent synthesis of the end products of another branch, until the cellular requirements of both branches are met. Thus the regulation of *Mtu*DAH7PS is incredibly sophisticated and highly efficient allowing aromatic amino acid biosynthesis to be finely tuned to meet cellular demands.

Furthermore the addition of *Mtu*DAH7PS^{WT} endows *Mtu*CM not only with sensitivity to Phe and Tyr as first reported by Sasso *et al.* but also showed for the first time *Mtu*CM activity became synergistically regulated by the binary and ternary combinations including Trp.[85] Examination of the *Mtu*CM Michaelis-Menten kinetics of a mixture of *Mtu*CM and *Mtu*DAH7PS^{WT} with the addition of Phe and or Tyr revealed the ligands act primarily as K-type inhibitors, radically increasing the K_m of chorismic acid. The complex synergistic regulation of *Mtu*CM activity was reminiscent of the regulation of *Mtu*DAH7PS^{WT} itself. Thus it seems logical the allosteric binding sites of *Mtu*DAH7PS may be responsible for conveying regulation to *Mtu*CM.

To establish if the allosteric binding sites were responsible for regulating *Mtu*CM activity, the two allosteric binding site *Mtu*DAH7PS variants described in chapter 3 were used. *Mtu*DAH7PS^{R171A} was designed to eliminate ligand binding at site 1, leaving site 2 available for Phe and Tyr binding. *Mtu*DAH7PS^{R256A} was designed to eliminate binding at site 2, leaving site 1 available for Phe and Tyr binding. Inhibition studies showed *Mtu*CM activity in the presence of excess of *Mtu*DAH7PS^{R171A} was insensitive to Phe and Tyr, whereas inhibition studies conducted with excess *Mtu*DAH7PS^{R256A} showed *Mtu*CM activity was insensitive to Tyr but had retained sensitivity to Phe. Phe must bind to site 1 of *Mtu*DAH7PS to inhibit *Mtu*CM activity. Tyr must bind to both site 1 and site 2. Thus the allosteric binding sites of *Mtu*DAH7PS are essential to the allosteric regulation of *Mtu*CM activity.

In an effort to understand the mechanism by which the *Mtu*CM activity of the *Mtu*CM•*Mtu*DAH7PS complex was regulated the apparent dissociation constant between *Mtu*CM and *Mtu*DAH7PS were kinetically determined in the presence and absence of Phe. The $K_{d,app}$ between *Mtu*CM and *Mtu*DAH7PS was ~720 nM, but in the presence of 200 μM Phe this increased by approximately four-fold to 3 μM. Therefore the binding of Phe to the *Mtu*CM•*Mtu*DAH7PS complex weakens the interaction between the two proteins. AUC supplemented with additional evidence from native PAGE and a pull down assay provided additional proof Phe sufficiently weakened the interaction between the two proteins to cause dissociation of the *Mtu*CM•*Mtu*DAH7PS complex under these conditions. Molecular dynamic studies show the β7-α7 and β8-α8 loops near the *Mtu*CM•*Mtu*DAH7PS interface are expected to become more flexible on Phe binding.[71] The change in the molecular dynamics of *Mtu*DAH7PS due to ligand binding implies ligand binding changes the average amplitude of the molecular dynamic fluctuations about a mean conformation of the *Mtu*DAH7PS population ensemble. If the *Mtu*CM•*Mtu*DAH7PS interface were to become more flexible on Phe binding the association between the two proteins may become entropically unfavourable and encourage dissociation. Unfortunately molecular modelling does not predict the same change in flexibility of the *Mtu*CM•*Mtu*DAH7PS interface region when Trp and Phe are bound which does cast some doubt on this mechanism of action.

An alternative theory for the dissociation which is far more difficult to prove, is the possibility that on binding an aromatic amino acid at any of the allosteric binding sites *Mtu*DAH7PS undergoes a subtle twist across the weak dimer interface effectively changing the average conformation of the *Mtu*DAH7PS population ensemble. At the dimer interface the β0-strand of one subunit forms antiparallel β-sheet with the β0-strand of adjacent subunit (Figure 4.21A). In the absence of ligand, Trp3 is located on the N-terminal tail just prior to the start of the β0-strand in both subunits (Figure 4.21B-C). When Phe binds, Trp3 of one subunit moves to towards the Phe binding site and is located in the middle of the β0-strand. The Trp3 located on the adjacent subunit has not moved and is located on the N-terminal tail just prior to the β0-strand. This movement of the residues belonging to one β0-strand relative to the other may cause a slight twist in the plane of the tetramer. This twist is not enough to cause an obvious change in the shape of the protein, and could be masked by crystal packing, but it may be enough to alter the interactions between *Mtu*CM and *Mtu*DAH7PS. This change to the interactions may result in an *Mtu*DAH7PS species that poorly activates *Mtu*CM and/or lowers the affinity of *Mtu*DAH7PS for *Mtu*CM. The stabilisation of loops via site directed mutagenesis and molecular dynamic simulations have been shown to increase the propensity of a neuraminidase from the influenza virus and the photoswitching Dronpa from *Pectinidae* to form higher order olgiomers.[117,118]

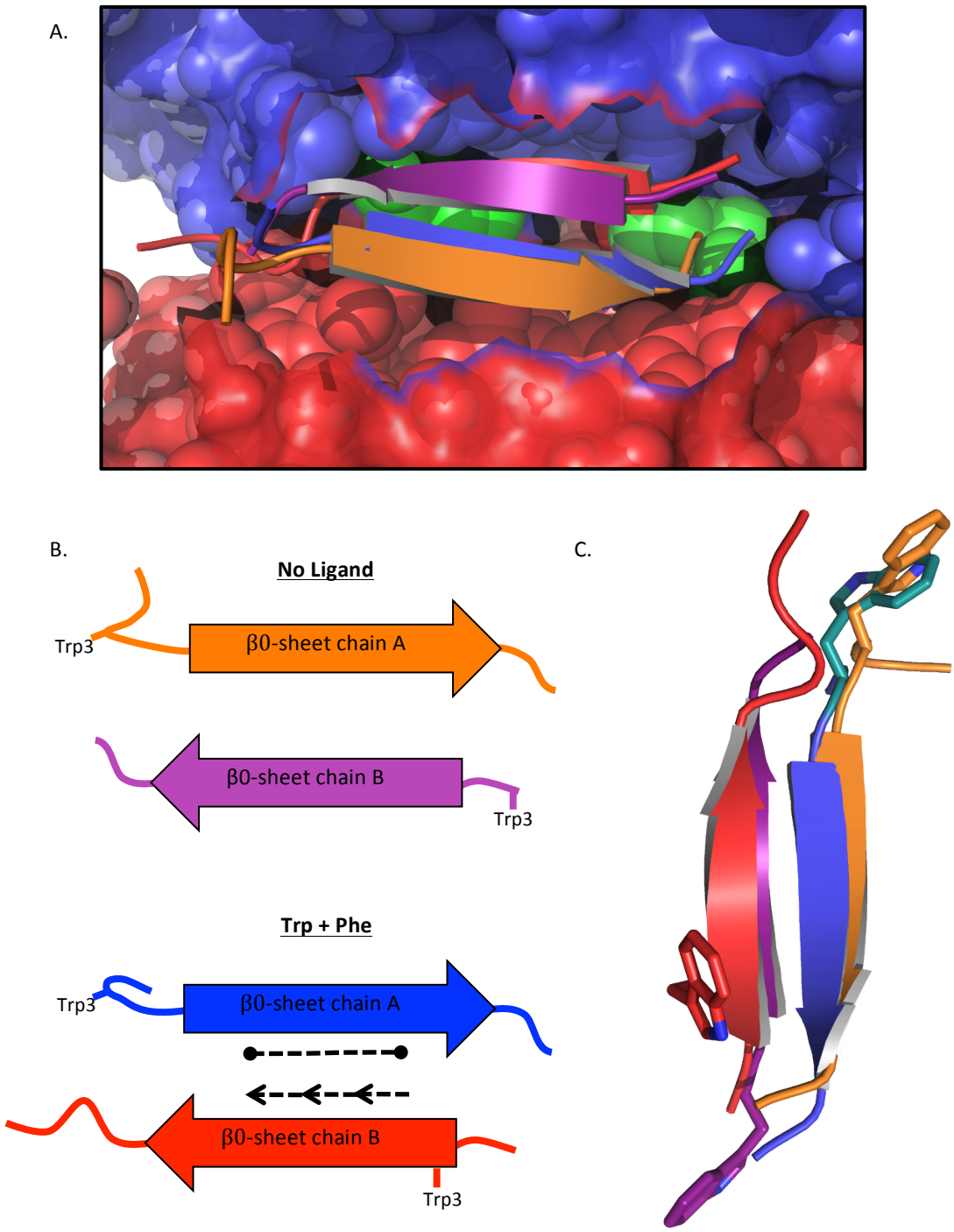

Figure 4.21 The interaction of the β0-strand of adjacent subunits at the dimer interface, located between subunits of the crystallographic asymmetric unit. The unliganded *Mtu*DAH7PS crystal structure (PDB code: 3NV8) is shown with one subunit shown in blue and the second subunit shown in red. The Trp- and Phe-bound *Mtu*DAH7PS crystal structure (PDB code: 3KGF) is shown with one subunit colour orange and the other coloured purple. A. Close-**u**p of the *Mtu*DAH7PS dimer interface with the β0-strands of the unliganded and the Trp- and Phe-bound *Mtu*DAH7PS crystal structures structure aligned. B. Schematic of the β0-strands that form the antiparallel β-sheet at the dimer interface showing the relative position of Trp3 on each strand. C. An alignment of the antiparallel β-sheet from the unliganded and Trp- and Phe-bound *Mtu*DAH7PS crystal structures shown in cartoon form with the Trp3 shown as sticks. The functional group of Trp3 on the blue subunit, shown in teal, was unrefined in the 3NV8 crystal structure and has been modelled in by PyMol.

Previous kinetic studies conducted by Sasso *et al.* used polyhistidine tagged *Mtu*DAH7PS, but no investigation had been made into whether the polyhistidine tag affected the activation or regulation of *Mtu*CM.[85] A brief investigation found there was no reason to suspect the polyhistidine tag was detrimental the ability of *Mtu*DAH7PS to activate *Mtu*CM activity. The polyhistidine tag did alter the regulatory sensitivity of *Mtu*DAH7PS. *Mtu*DAH7PS activity was less sensitive to combinations of aromatic amino acids. The polyhistidine tag also adversely affected the synergistic regulation of *Mtu*CM activity in the presence of excess *Mtu*DAH7PS^{H6}. Trp alone was able to inhibit *Mtu*CM activity, yet when Trp was combined with Phe inhibition was less effective. Crystal coordinates with Phe and Tyr bound showed the N-terminal tail of *Mtu*DAH7PS is repositioned on Phe or Tyr binding. Trp3 moves to cap site 1 when ligand is bound, and Asp 6 coordinates to the ligand via a water molecule. The addition of the polyhistidine tag to the N-terminus of *Mtu*DAH7PS would likely reduce the flexibility of the N-terminal region, which interacts with site 1, preventing or at least hampering the capping of the binding site. The movement of the N-terminal tail may be an important part of the signalling pathway between allosteric sites, hampering the movement of the N-terminal tail may then result in the observed disruption of synergistic regulation.

In summary, *Mtu*CM and *Mtu*DAH7PS have a synergistic relationship where the activity of both enzymes is improved on formation of the non-covalent heterooctameric complex. *Mtu*CM activity was found to have a similarly sophisticated synergistic feedback regulation as *Mtu*DAH7PS. Thus it was unsurprising to find the allosteric binding sites of *Mtu*DAH7PS were directly responsible for the regulation of *Mtu*CM. The binding of the aromatic amino acids of *Mtu*DAH7PS change either the average *Mtu*DAH7PS tetramer conformation or the amplitude or frequency of the dynamic fluctuations of the tetramer conformation about the mean tetramer conformation resulting in a tetramer species that displays a lower affinity for *Mtu*CM and poorly activates *Mtu*CM activity.

5. Residues potentially pivotal to the allosteric regulation of *Mtu*DAH7PS

5.1. Introduction

Allosteric regulation is when an effector molecule binds to a protein at a site remote from the active site and alters the functionality of the protein. The effector molecule may alter the functionality of the protein by changing the average conformation of a protein ensemble or by changing the amplitude or frequency of fluctuations from the average conformation of a protein ensemble. Allosteric regulation has most frequently been characterised in enzymes that undergo detectable conformational changes associated with ligand binding such as haemoglobin, *E. coli* aspartase transcarbomoylase and even examples amongst the DAH7PS family, including *T. maritima* DAH7PS.[3,47,119,120] More recently, enzymes that undergo very subtle changes to their flexibility or molecular dynamics due to effector binding have been uncovered, such as the catabolite activator protein and PDZ domains.[8,25,121] Allostery mediated by larger conformational changes is largely considered to be enthalpy driven, whereas fluctuations about a mean conformation mediated by protein dynamics delivers primarily entropically driven allostery.[22] Computational techniques such as statistical coupling analysis (SCA) and molecular dynamic (MD) simulations are more frequently being used to investigate systems that do not undergo major conformational change in an effort to understand signal transmission between binding sites.[25,115,122-124]

Kinetic and biophysical studies provide clear evidence that Trp, Phe and Tyr regulate *Mtu*DAH7PS synergistically.[48,91] However, comparison of *Mtu*DAH7PS structure with ligands bound at the allosteric binding sites with the structure of the non-liganded protein provides no evidence of significant structural change.[48,91] A detailed investigation into the synergistic regulation of *Mtu*DAH7PS using a combination of MD simulations and SCA was used to illuminate the role of protein dynamics in *Mtu*DAH7PS regulation.[115] SCA is used to measure coupling between positions on a multiple sequence alignment of a protein family.[125] A cluster of 39 residues was identified, which, may be involved in

signal transmission between active sites of *Mtu*DAH7PS.[71,115] The MD simulations predict the flexibility of residues in the presence and absence of allosteric ligands and can identify residues that display either correlated or anticorrelated movements. The residues identified by SCA were weighted by the MD analysis, effectively correlating the motion from the MD simulations with the evolutionary conservation of the type II DAH7PS family determined from SCA in order to identify the 29 residues of greatest interest for experimental investigation from the cluster of 39 residues originally identified.

5.1.1. Residues chosen for investigation

The focus of this study was to identify residues critical to communication between the allosteric binding sites and the active site. Of the 29 potential residues identified as important, eight were considered for analysis in this chapter (Table 5.1). Residues located directly at the active site or subunit interfaces were not investigated here, as they were likely to directly disrupt catalysis, substrate binding or quaternary structure. Residues that make contacts through their peptide functionality were also eliminated due to the difficulty in finding an appropriate substitution to disrupt the interactions. SDM was attempted on all eight residues, however for only four, soluble protein was successfully produced without disruption to the quaternary structure. These variants are discussed within this chapter.

Table 5.1 List of residues considered as targets for mutagenesis.

Residue	Location	Substitution	Comments
Thr114	Trp site	Thr114Val	Disrupted quaternary structure, not pursued due similarity to other variants
Gly190	2nd shell Trp site	Gly190Pro	Successful, discussed Chapter 5
Gly232	2nd shell Trp site	Gly232Pro	Disrupted quaternary structure, discussed Chapter 7
Asn175	Site 1	Asn171Ala	Successful, discussed Chapter 5
Tyr131	2nd shell site 1	Tyr131Ala	Successful, discussed Chapter 5
Asn94	2nd shell site 1	Asn94Ala	Difficulty solubilising, abandoned
Val103	2nd shell Trp site	Val103Ala	Successful, discussed Chapter 5
Thr240	Near Tetramer interface	Thr240Ala	Difficulty solubilising, abandoned

5.1.2. *Mtu*DAH7PS SCA variants

The four variants, which were successfully purified without disruption to the quaternary structure, were *Mtu*DAH7PS Gly190Pro, Tyr131Ala, Val103Ala and Asn175Ala. Gly190 is positioned along the loop between α2 and α2a helices (

Figure 5.1B). The flexibility of α2-α2a loop allows the loop to bend permitting the formation of a hydrogen bond between the Trp ligand the backbone carbonyl Ala192. Interestingly another residue considered for substitution was Gly232 (Chapter 7), also located on the α2b-β3 loop on the succeeding the α2a and α2b helices. These Gly residues afford these helices greater movement than other secondary structure elements within the tetramer. SCA identified several residues along the α2a and α2b helices, plus MD simulations showed the flexibility of the loops changed on ligand binding.[71,115] Thus the flexibility of the inserted α2a and α2b helices may play a critical role in signal transmission between binding sites. Gly is unique as it allows the peptide backbone greater flexibility than other residues due to the side chain being a hydrogen atom. Pro consists of a pyrrollidine ring which includes the β carbon of the amide linkage enforcing a dihedral backbone angle of ~60˚ and therefore rigidity on the protein backbone. In order to probe the importance of the flexibility of the α2-α2a loop, Gly190 was targeted for substitution to Pro.

Asn175 is located at site 1 and makes direct contacts with the carbonyl group of the bound ligand via its amide side chain (

Figure 5.1A). Asn175 also makes polar contacts to Asn94 and Arg171 a residue shown to be essential for strong ligand binding (Chapter 3). Multiple sequence alignment conducted as part of the SCA identified this position to be occupied by either Asn or Gln, conserving the side chain functionality.[115] Despite Asn175 being located at site 1 and interacting with the bound ligand, it was chosen for investigation as it had also been highlighted as a critical residue in previous work.[126] It was shown both D- and L-Phe were able to bind in site 1, but only the presence of the L-amino acid was communicated to other allosteric sites and the active site. Crystallographic studies revealed the only notable difference between the binding modes of the D- and L-Phe was the hydrogen bond formed between Asn175 and L-Phe. Asn175 was substituted for Ala to remove the side chain functionality

without compromising the integrity of the secondary structure. This variant would allow the importance of the amide side chain for allosteric communication to be investigated.

Tyr131 is in close proximity but does not make any polar contacts to Phe91 or Asn175, both of which make direct contacts with the bound ligand at site 1 (

Figure 5.1C). Tyr 131 is ~13 Å from site 1. SCA on multiple sequences, found the position was usually occupied by either Tyr or Phe, both aromatic amino acids.[115] Substitution of Tyr131 to Ala would effectively remove the aromatic side chain, whilst causing the least disruption to the secondary structure. This would allow the importance of the aromatic side chain of Tyr131 to allosteric regulation to be investigated.

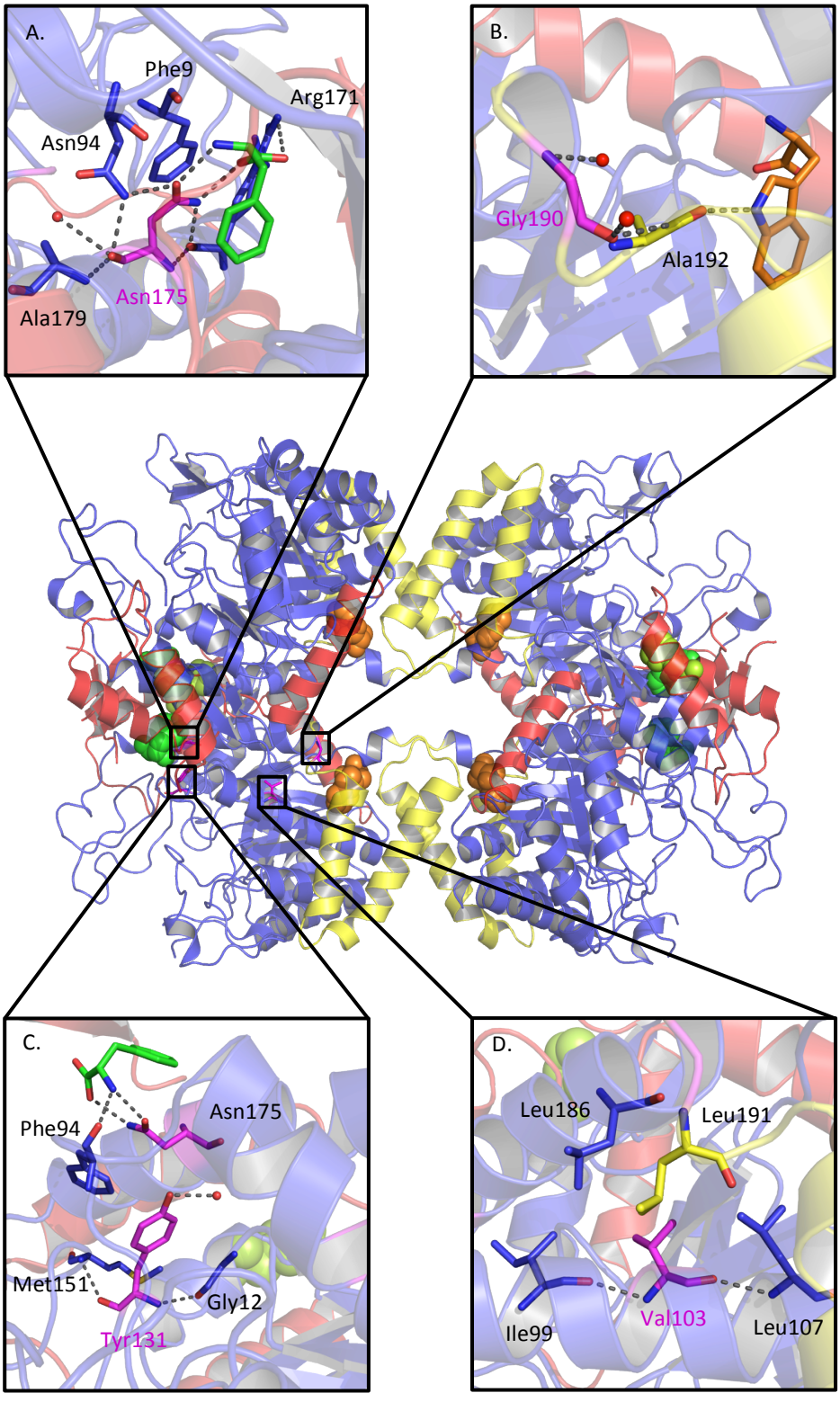

Figure 5.1 Structure of tetrameric *Mtu*DAH7PS soaked with Trp and Phe (PDB code: 3KGF). The core $(\beta/\alpha)_8$ barrel structure is coloured blue, the N-terminal extension is coloured red, the additional helices to the α2-β3 loop are coloured yellow Trp is shown in orange bound to the Trp site. Phe bound to site 1 is shown in green and Phe bound to site 2 is shown in limon. Residues of interest as identified by SCA and MD simulations shown in magenta. Close up view to show the interactions of A. Asn175; B. Gly190; C. Tyr131 and D. Val103. Hydrogen bonds shown by dashed grey lines and water by red spheres.

Val103 is in close proximity to the Trp site (~14 Å), and forms hydrophobic interactions with the surrounding hydrophobic residues Ile99, Leu186, Leu191 and most importantly Leu107, which helps to form the hydrophobic pocket for Trp binding (

Figure 5.1D). Substitution of Val103 to a polar or charged side chain would risk disrupting the local secondary structure, as it may rearrange to move the polar residue into a position where it could be stabilised by making polar contacts. Instead Val103 was mutated to Ala to remove the branched carbon side chain and allow the interactions of the branched side chain with the surrounding hydrophobic residues to be investigated.

5.1.3. Chapter aims

The combination of SCA and MD simulations identified a network of residues that may be involved in the signal transmission between allosteric binding sites and to the active site, but as yet there has been no experimental work to support these findings. The main aim of the studies described in this chapter was to experimentally validate the findings from the SCA and MD analyses and show whether the substitutions at the positions identified would disrupt or alter the allosteric regulation of *Mtu*DAH7PS.

5.2. Preparation of *Mtu*DAH7PS variants

5.2.1. Mutagenesis, expression and purification

SDM was performed using the QuikChange® Lightning Site-Directed Mutagenesis Kit (Stratagene). The QuikChange® Primer Design tool (Agilent technologies) was used to design the primers incorporating the desired mutations. Protocols are detailed in Section 9.2.

DNA sequencing confirmed the incorporation of the correct mutations before the SDM products were electroporated into BL21(DE3) PGroESL cells. Expression and protein purification followed the procedures outlined for *Mtu*DAH7PS^{WT}, Section 9.5.

5.2.2. Confirmation of product

The purification products for each *Mtu*DAH7PS variant were analysed by SDS-PAGE gel (Figure 5.2). Each variant was shown to be pure and their bands matched the expected monomeric molecular mass of ~50 kDa. Molecular masses determined by mass spectrometry were consistent with the expected mass of each variant (Table 5.2).

Table 5.2 Comparison of the calculated and empirical molecular weight (M_w) for *Mtu*DAH7PS variants.

Variant	Calculated M_w (kDa)	Empirical M_w (kDa)
*Mtu*DAH7PS^{G190P}	50825	50823
*Mtu*DAH7PS^{V103A}	50756	50756
*Mtu*DAH7PS^{Y131A}	50692	50690
*Mtu*DAH7PS^{N175A}	50741	50742

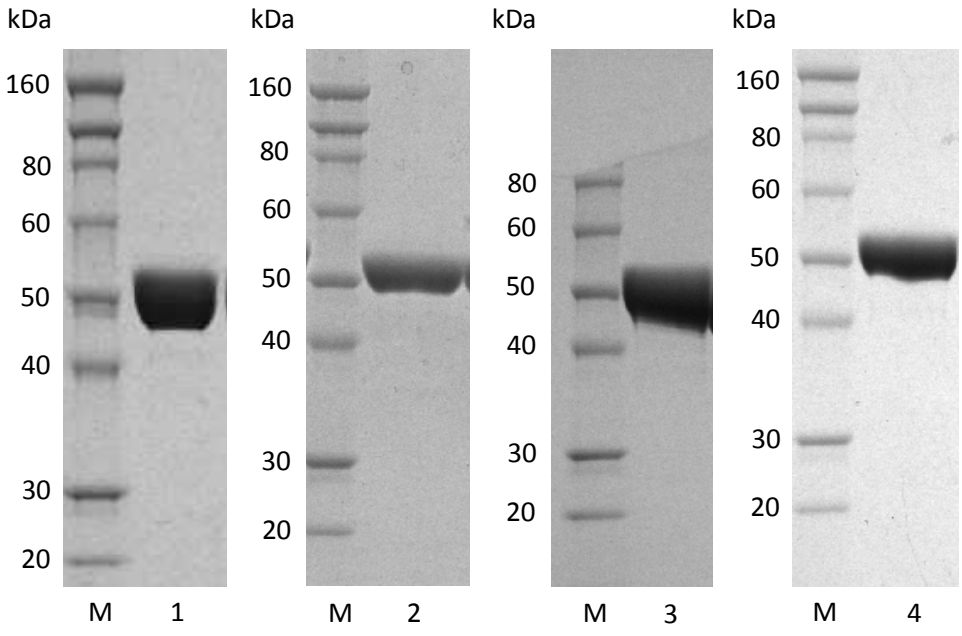

Figure 5.2 SDS-PAGE gel illustrating the size and purity of each purified *Mtu*DAH7PS variant. Lane M molecular weight marker; Lane 1 *Mtu*DAH7PS^{G190P}; Lane 2 *Mtu*DAH7PS^{V103A}; Lane 3 *Mtu*DAH7PS^{Y131A} and Lane 4 *Mtu*DAH7PS^{N175A}.

5.3. Structural analysis

5.3.1. Comparison of secondary structure

The secondary structure of each *Mtu*DAH7PS variant was inspected by CD as described previously (Section 9.7.4). Overlay of the CD spectra with *Mtu*DAH7PS^{WT} indicated little variance (Figure 5.3). Therefore, it was unlikely any of the substitution caused significant alterations to the secondary structure of *Mtu*DAH7PS.

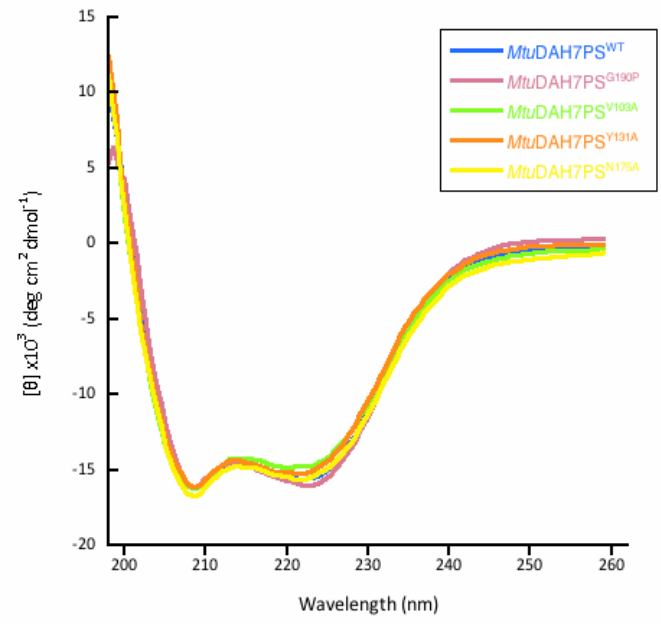

Figure 5.3 CD spectra for *Mtu*DAH7PS^{WT} (blue), *Mtu*DAH7PS^{G190P} (dusty pink), *Mtu*DAH7PS^{V103A} (lime green), *Mtu*DAH7PS^{Y131A} (orange) and *Mtu*DAH7PS^{N175A} (yellow).

5.3.2. Quaternary structure in solution

SAXS was used to determine the quaternary structure of each *Mtu*DAH7PS variant in solution as described in Section 9.7.5. Comparison of the scattering profiles and pairwise distribution curves of the *Mtu*DAH7PS variants and *Mtu*DAH7PS^{WT} show they are similar (Figure 5.4).

Inspection of the SAXS parameters of the *Mtu*DAH7PS variants determined from analyses with GNOM[102], PRIMUS[101] and CRYSOL[103] showed small variances from the parameters calculated for the wild type enzyme (Table 5.3). The χ^2, a measure of goodness of fit, for *Mtu*DAH7PS^{G190P} and *Mtu*DAH7PS^{N175A} were reasonably close to 1 and are a good fit with the theoretical scattering profile of the tetrameric *Mtu*DAH7PS crystal coordinates (PDB cod: 3NV8). However, *Mtu*DAH7PS^{V103A} and *Mtu*DAH7PS^{Y131A} gave χ^2 values of 2.6 and 3.4 respectively, an indication that the theoretical scattering of the tetrameric *Mtu*DAH7PS crystal coordinates cannot fully account for the experimental scattering of these two enzymes. This variation could suggest minor changes in the quaternary structure or conformation of *Mtu*DAH7PS^{V103A} and *Mtu*DAH7PS^{Y131A} have occurred.

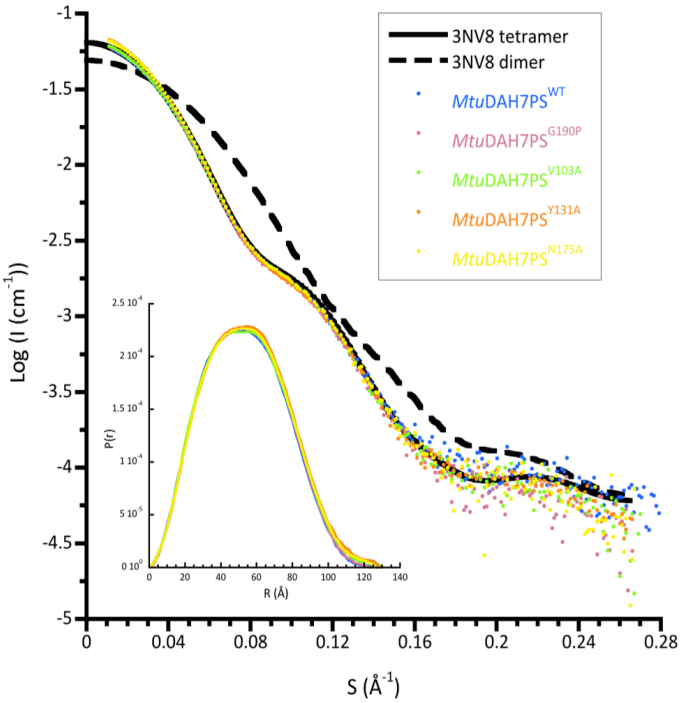

Figure 5.4 SAXS profiles of *Mtu*DAH7PS^{WT}(blue), *Mtu*DAH7PS^{G190P} (dusty pink), *Mtu*DAH7PS^{V103A} (lime green), *Mtu*DAH7PS^{Y131A} (orange) and *Mtu*DAH7PS^{N175A} (yellow). Also shown is the theoretical scattering for the tetrameric (black) and dimeric (black dash) *Mtu*DAH7PS from PDB code 3NV8. Inset pair-wise distribution profiles.

Table 5.3 SAXS parameters determined from a single sample analysis of the scattering profiles of *Mtu*DAH7PS variants using PRIMUS, GNOM, MoW, and CRYSOL.

***Mtu*DAH7PS**	**Wild type**	**G190P**	**V103A**	**Y131A**	**N175A**
Guinier analysis					
R_g (Å)	41.6 ± 0.3	41.5 ± 0.1	42.3 ± 0.3	42.8 ± 0.2	42.3 ± 0.3
I (0) (cm^{-1})	0.168 ± 0.001	0.065 ± 0.001	0.138 ± 0.001	0.188 ± 0.001	0.138 ± 0.001
Pair distribution analysis					
Real Space R_g (Å)	40.9 ± 0.2	41.07 ± 0.06	42.09 ± 0.2	41.7 ± 0.2	42.09 ± 0.2
D_{max} (Å)	127	124	126	126	126
V_p, (Da)	282700	303800	338300	327700	338300
Molecular weight estimates from SAXS MoW analysis					
M_w from V_p (Da)	199 100	203800	200900	214800	208300
Nō of Subunits	4	4	4	4	4
CRYSOL analysis with tetrameric 3NV8					
R_{gE} (Å)	42.4 ± 0.2	41.5 ± 0.2	41.9 ± 0.2	42.2 ± 0.2	42.2 ± 0.2
R_{gT} (Å)	40.6	41.2	40.9	41.4	40.6
χ^2	0.996	0.446	2.58	3.37	0.612

The quaternary structures of *Mtu*DAH7PS variants were also analysed at low protein concentrations (6-10 μM) by blue native PAGE, as described in Section 9.7.2. The native PAGE showed two bands were produced by *Mtu*DAH7PS^{N175A} one at ~50 kDa and a second at ~100 kDa and are in good agreement with the expected monomeric and dimeric *Mtu*DAH7PS molecular masses respectively (Figure 5.5). Furthermore *Mtu*DAH7PS^{WT} produced two bands of the same molecular weight and intensities as *Mtu*DAH7PS^{N175A}, providing further evidence *Mtu*DAH7PS^{N175A} has a very similar quaternary structure to *Mtu*DAH7PS^{WT}. *Mtu*DAH7PS^{V103A} generated one strong protein band at ~100 kDa and only a faint band at ~50 kDa suggesting the distribution of *Mtu*DAH7PS^{V103A} monomer and dimer has been altered to favour the dimer. The native PAGE showed *Mtu*DAH7PS^{G190P} produced a strong band at ~200 kDa and consistent with the molecular mass of an *Mtu*DAH7PS tetramer, and only faint bands at ~100 and ~50 kDa suggesting *Mtu*DAH7PS^{G190P} exists primarily as a tetramer even at low concentrations. The bands produced by *Mtu*DAH7PS^{Y131A} were quite faint. There was a band at ~100 kDa and a weaker band at ~200 kDa which suggests at low concentrations *Mtu*DAH7PS^{Y131A} may exist primarily as a mixture of dimer and tetramer as opposed to the mixture of monomer and dimer observed for *Mtu*DAH7PS^{WT}.

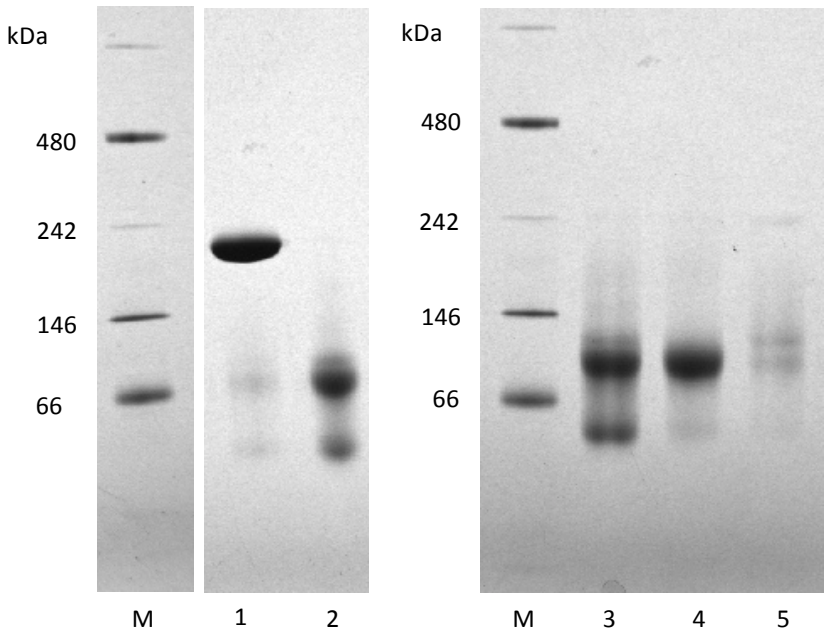

Figure 5.5 Blue native PAGE; Lane M displays the molecular weight marker; Lane 1 *Mtu*DAH7PS^{G190P}; Lane2 *Mtu*DAH7PS^{N175A}; Lane 3 *Mtu*DAH7PS^{WT}; Lane 4 *Mtu*DAH7PS^{V103A} and Lane 5 *Mtu*DAH7PS^{Y131A}.

The sedimentation velocity experiments for *Mtu*DAH7PS^{G190P} were conducted at concentrations of 0.1, 0.25 and 1 mg/mL and the experimental conditions are detailed in Section 9.7.7. Ali Nazmi ran the AUC experiments and assisted in with data analysis. At all concentrations the AUC data fitted to the continuous size distribution model determined a sedimentation coefficient (s) of ~8.3 S for *Mtu*DAH7PS^{G190P} and gives a calculated molecular mass of ~185 kDa (Figure 5.6A). The expected mass of tetrameric *Mtu*DAH7PS is 204 kDa. There is no evidence of a significant amount of monomeric or dimeric *Mtu*DAH7PS^{G190P} being present even at the lowest concentration of 0.1 mg/mL. These results are in agreement with the results of the native PAGE, which suggests the *Mtu*DAH7S^{G190P} is primarily present as a tetramer in solution at all assessable concentrations (>0.1 mg/mL).

The AUC data for *Mtu*DAH7PS^{V103A} was collected at concentrations of 0.1, 0.3 and 1 mg/mL. Unfortunately the *Mtu*DAH7PS^{V103A} was unstable and aggregated throughout the sedimentation velocity experiments resulting in data that did not fit well to the model (AUC data displayed in Appendix II). The AUC data for *Mtu*DAH7PS^{V103A} revealed that there are two oligomers present in solution at all concentrations, one with a sedimentation coefficient of ~8.3 S, representing the tetramer and one at ~5 S representing the dimer (Figure 5.6B). Notwithstanding the less than ideal quality of data, the sedimentation velocity experiments were able to reveal the quaternary structure equilibrium of *Mtu*DAH7PS^{V103A} has shifted to include a greater portion of *Mtu*DAH7PS dimer than the wild type enzyme.

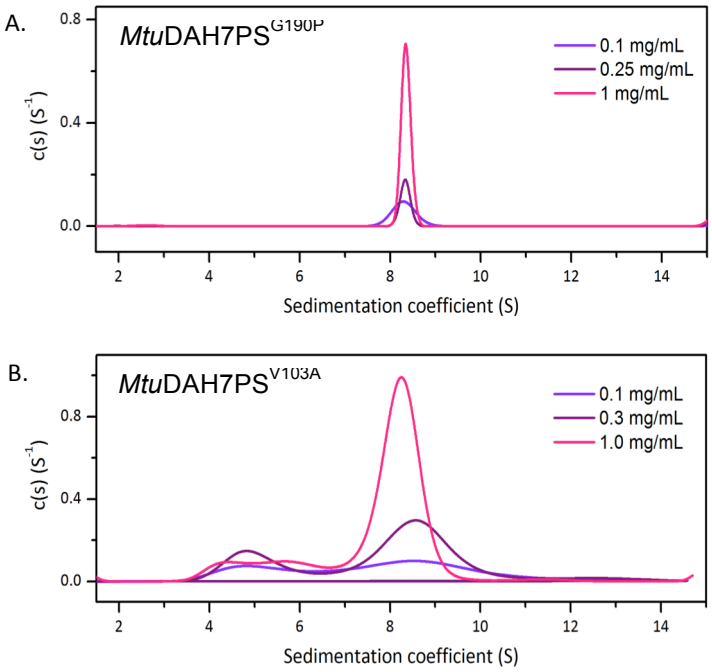

Figure 5.6 Normalised *c*(*s*) distribution functions from AUC data for A. *Mtu*DAH7PS^{G190P}, analysed at 0.1 mg/mL (violet), 0.25 mg/mL (purple) and 1.0 mg/mL (pink). And B. *Mtu*DAH7PS^{V103A}, analysed at 0.1 mg/mL (violet), 0.3 mg/mL (purple) and 1.0 mg/mL (pink). AUC data, fits and residuals are provided in Appendix II.

Overall, the results from the native gel electrophoresis and SAXS experiments indicate the quaternary structure of *Mtu*DAH7PS^{N175A} is unaffected by the introduced substitution. For *Mtu*DAH7PS^{V103A} and *Mtu*DAH7PS^{Y131A} both the SAXS analysis and native gels suggest the quaternary structure equilibrium varies slightly compared to *Mtu*DAH7PS^{WT}. For *Mtu*DAH7PS^{V103A} AUC data confirms the Val103Ala substitution has perturbed the quaternary structure equilibrium, resulting in a greater portion of dimer present at all concentrations. Any variance in quaternary structure equilibrium of the *Mtu*DAH7PS^{Y131A} compared to the wild type enzyme could be verified by AUC. At high concentrations SAXS showed *Mtu*DAH7PS^{G190P} had a tetrameric structure very similar to the *Mtu*DAH7PS^{WT} but native PAGE and AUC showed *Mtu*DAH7PS^{G190P} was almost solely tetrameric in solution at low concentrations. Thus the substitution of Gly190 for Pro has stabilised or trapped the tetrameric form of *Mtu*DAH7PS^{G190P}.

5.4. The flexibility of Gly190 is essential to communicating allosteric regulation

5.4.1. Kinetic parameters

Kinetic analysis was conducted under standard conditions as outlined in Section 9.9.1. The conversion of Gly190 to a Pro had an unexpected positive effect on the variant catalytic ability of the enzyme. The k_{cat} of *Mtu*DAH7PS^{G190P} is almost double that of *Mtu*DAH7PS^{WT} and there are some change to the determined K_m for both substrates. The overall result is the catalytic efficiency for both E4P and PEP has increased compared to the wild type enzyme (Table 5.4). This effect on the kinetic parameters is even more surprising given the distance, ~29 Å, of the site of substitution from the active site (as measured between the C_α of Gly190 and the Mn^{2+} ion at the active site).

Table 5.4 Kinetic parameters determined from a single set of Michaelis-Menten kinetics for *Mtu*DAH7PS^{G190P}. Michaelis-Menten plots are displayed in Appendix I. Error represents error of curve fitting to the data set by least squares fit.

***Mtu*DAH7PS**	K_m^{E4P} (μM)	K_m^{PEP} (μM)	k_{cat} (s^{-1})	**Catalytic Efficiency** k_{cat}/K_m^{E4P} ($s^{-1}mM^{-1}$)	**Catalytic Efficiency** k_{cat}/K_m^{PEP} ($s^{-1}mM^{-1}$)
Wild type	28 ± 2	37 ± 4	4.7 ± 0.1	170 ± 20	130 ± 20
G190P	35 ± 2	47 ± 3	9.0 ± 0.1	260 ± 20	190 ± 10

5.4.2. Disruption of feedback regulation

Inhibition studies of *Mtu*DAH7PS^{G190P} were conducted under standard assay conditions detailed in Section 9.9.3. The presence of 200 μM of any single, binary or ternary combination of aromatic amino acids had little effect on the activity of *Mtu*DAH7PS^{G190P} (Figure 5.7). Astonishingly the single residue substitution of Gly190Pro appears to disable communication between the allosteric binding sites and the active site, preventing inhibition.

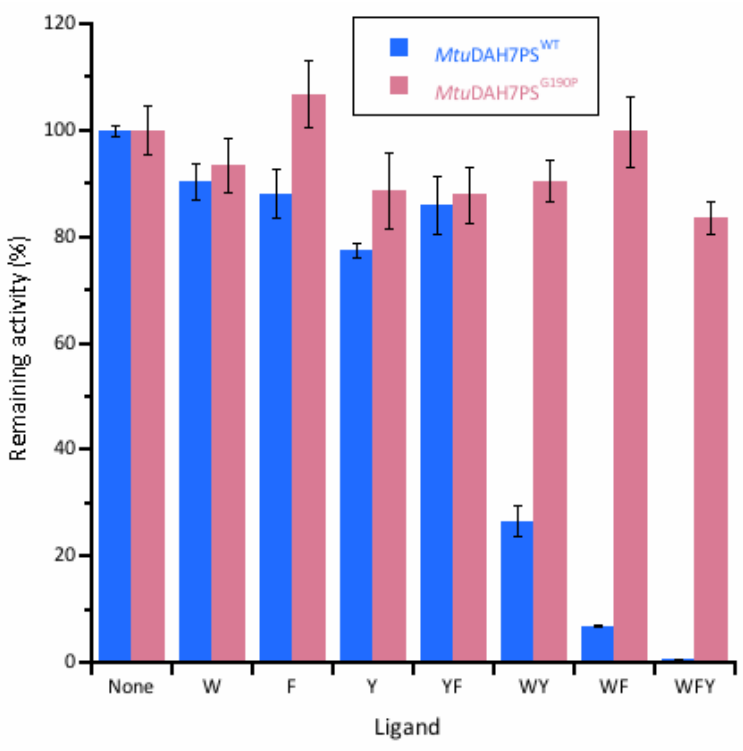

Figure 5.7 Remaining activity of *Mtu*DAH7PS^{WT} (blue) *Mtu*DAH7PS^{G190P} (dusky pink) in the presence of various single, binary and ternary combinations of aromatic amino acids. The aromatic amino acids are represented by their one letter code; Trp, W; Phe, F and Tyr, Y. Each letter also represents 200 µM of the corresponding aromatic amino acids. Assays conducted in the presence of 150 µM E4P and PEP. Error bars depict the standard deviation of triplicate measurements. P-values provided in appendix V.

5.4.3. Thermal stability

Having established that the addition of any combination of Trp, Phe or Tyr to *Mtu*DAH7PS^{G190P} could not elicit any significant inhibitory response observable in kinetic assays, the next question to be addressed was whether the ligands were still able to bind at the allosteric binding sites. The *Mtu*DAH7PS^{WT} thermal melting temperature (T_m) was shown to increase in the presence of Trp and to a lesser extent Phe (Section 9.8.1). Consequently DSF was used as an initial probe to assess binding of aromatic amino acids to the *Mtu*DAH7PS variants.

The melting temperatures determined for *Mtu*DAH7PS^{G190P} largely follow the trend observed for *Mtu*DAH7PS^{WT} (Figure 5.8). This observation indicates that all three aromatic amino acids are still able to bind at the allosteric binding sites of *Mtu*DAH7PS^{G190P}. It should also be noted that the T_m of

*Mtu*DAH7PS^{G190P} in the absence of ligand is ~ 1 ˚C greater than *Mtu*DAH7PS^{WT}, hinting that *Mtu*DAH7PS^{G190P} may be slightly more stable than the wild type enzyme. The change in T_m for *Mtu*DAH7PS^{G190P} in the presence of 200 µM Trp was ~4 ˚C lower than that observed for *Mtu*DAH7PS^{WT}. When the concentration of Trp was increased to over 500 µM the changes in T_m for *Mtu*DAH7PS^{G190P} and *Mtu*DAH7PS^{WT} were much more similar. The similarity of the T_m values suggests that at sufficiently high concentrations Trp is able to bind effectively to *Mtu*DAH7PS^{G190P} and induce similar changes in the thermal stability of *Mtu*DAH7PS^{G190P} as observed for *Mtu*DAH7PS^{WT}.

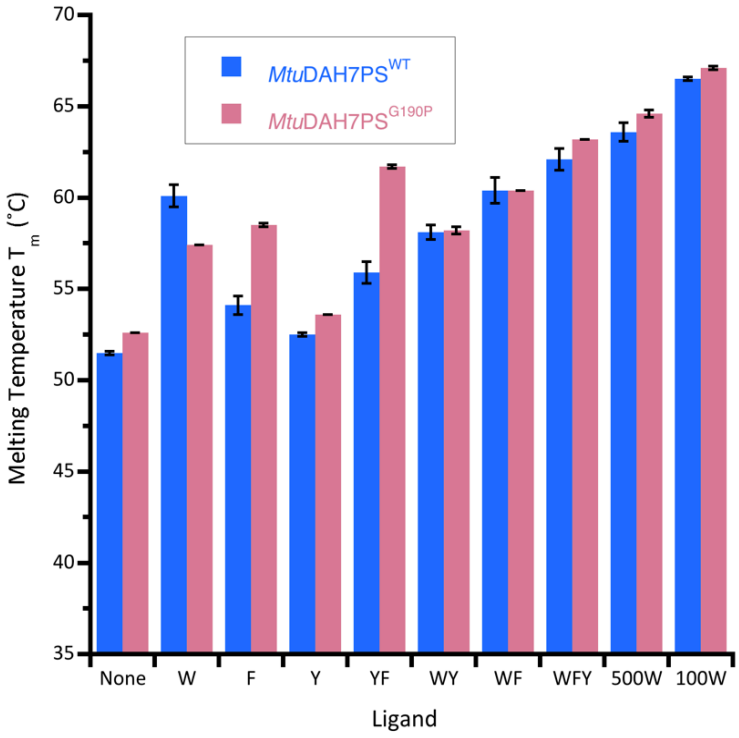

Figure 5.8 The effect of individual, binary and ternary combinations of aromatic amino acids on the thermal stability of *Mtu*DAH7PS^{WT} (blue) and *Mtu*DAH7PS^{G190P} (dusky pink). The aromatic amino acids are represented by their one letter code; Trp, W; Phe, F and Tyr, Y. Each letter also represents 200 µM of the corresponding aromatic amino acids, except where 500, and 1000 are stated and represent their respective concentrations in µM. Error bars depict the standard deviation of triplicate measurements. P-values provided in appendix V.

The change in T_m for *Mtu*DAH7PS^{G190P} in the presence of Phe was ~5.9 ˚C, which is ~3.3 ˚C greater than observed for *Mtu*DAH7PS^{WT}. The addition of Phe and Tyr also produced a large increase in the T_m for *Mtu*DAH7PS^{G190P} of ~9 ˚C, 5 ˚C greater than *Mtu*DAH7PS^{WT}. Yet the addition of combinations of aromatic amino acids that included Trp to *Mtu*DAH7PS^{G190P} resulted in similar increases in the T_m for

*Mtu*DAH7PS^{G190P} as observed for *Mtu*DAH7PS^{WT}. The dramatic increases in T_m only in the absence of Trp hint the Gly190Pro substitution has partially mimicked Trp binding, possibly signalling Trp binding to site 1, the Phe-selective site. Signal transmission to site 1 might result in tighter Phe binding and hence greater thermal stability as a greater portion of enzyme is bound with Phe.

5.4.4. Binding affinities

ITC was used to quantify the binding affinity of *Mtu*DAH7PS^{G190P} for Trp and Phe. ITC experiments were conducted under similar conditions as for *Mtu*DAH7PS^{WT}, as detailed in the methods Section 9.8.2.

There is a remarkable difference between the interactions *Mtu*DAH7PS^{G190P} and *Mtu*DAH7PS^{WT} with Trp. Titration of *Mtu*DAH7PS^{WT} with Trp displays a single tight binding event with Trp.[48] The interaction of *Mtu*DAH7PS^{G190P} with Trp, with or without the pre-incubation of the protein with Phe, results in a distinctive isotherm that fits a two site binding model (Figure 5.9A and C). The two-site binding site model assumes the two binding events are independent. The first binding event is endothermic and the second is exothermic, as each binding event has an opposite enthalpy change it allows the two binding events to be distinguished despite having similar K_d values (Table 5.5). One binding event has a K_d of ~20 µM whilst the second binding event has a K_d of ~10 µM.

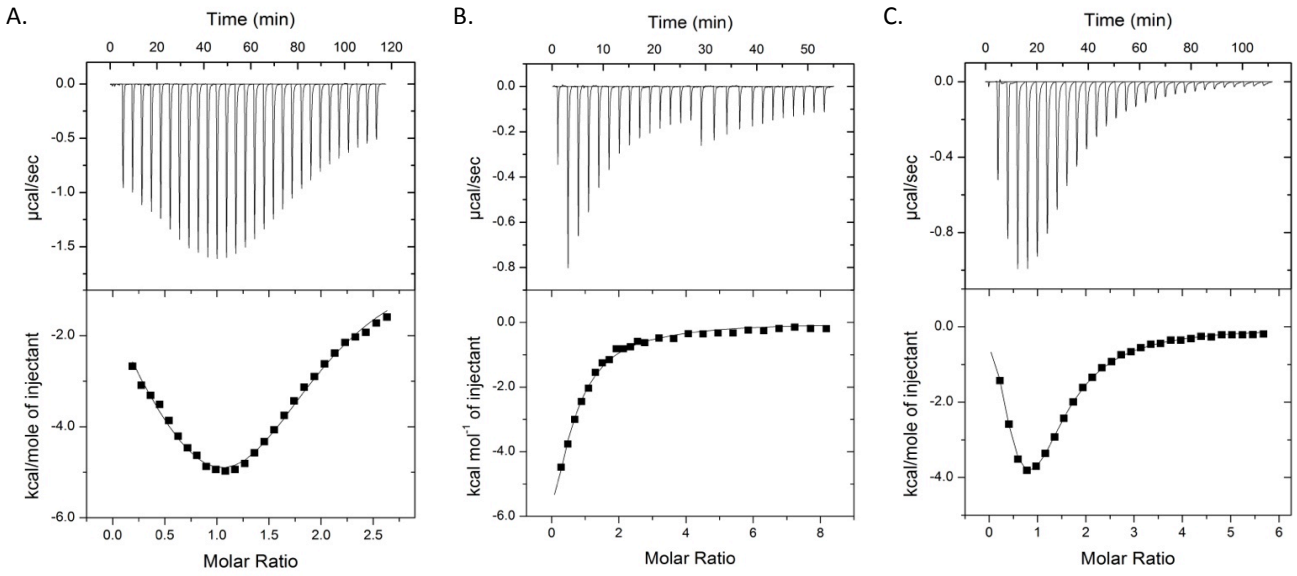

Figure 5.9 ITC data for the interaction of A. 81 µM *Mtu*DAH7PS^{G190P} with 1 mM Trp titrant; B. 49 µM of *Mtu*DAH7PS^{G190P} with 2mM Phe titrant and C. 38 µM *Mtu*DAH7PS^{G190P} and a background of 100 µM Phe present in the cell with a 1 mM Trp titrant

Table 5.5 Dissociation constants determined by ITC for *Mtu*DAH7PS^{G190P}. * Indicates results determined previously by Richard Hutton and — Indicates no background ligand present. Values are determined from a single ITC experiment. Error represents error of curve fitting to the data set as determined by a least squares fit.

Titrated ligand	Background ligand	*Mtu*DAH7PS	
		Wild type K_d (µM)	G190P K_d (µM)
Trp	—	4.7 ± 0.1*	20 ± 80 and 10 ± 10
Phe	—	21 ± 1*	47 ± 6
Trp	Phe	1.08 ± 0.03*	14.8 ± 0.8 and 3 ± 1

The K_d values between Trp and *Mtu*DAH7PS^{G190P} appear to be lower in the presence of Phe, but the high error associated with the determined K_d values in the presence of Trp mean no conclusion can be drawn until the error is reduced (Table 5.5). The K_d determined between *Mtu*DAH7PS^{G190P} and Phe was more than twice the value determined for *Mtu*DAH7PS^{WT} (Table 5.5, Figure 5.9B), indicating *Mtu*DAH7PS^{G190P} has a poorer affinity for Phe than *Mtu*DAH7PS^{WT}.

Overall the binding affinities determined for *Mtu*DAH7PS^{G190P} indicate the substitution of Gly190 for Pro does not prevent communication of ligand binding between the Trp site and site 1. However, the

substitution has correlated with a decrease in the binding affinity of *Mtu*DAH7PS^{G190P} for Trp and Phe. The Gly190Pro substitution was intended to reduce the flexibility of the α2-α2a loop. A loss in flexibility of the α2-α2a loop may explain the changes in allosteric communication by preventing the molecular dynamic changes from being transmitted between allosteric binding sites and between the allosteric binding sites and the active site.

5.4.5. Activation of *Mtu*CM by *Mtu*DAH7PS^{G190P}

Assays were conducted under standard conditions and initiated with 150 µM chorismic acid as described in Section 9.9.1. *Mtu*DAH7PS^{G190P} adequately boosts *Mtu*CM activity, but is less effective than *Mtu*DAH7PS^{WT} at molar excess ≥ ten-fold (Figure 5.10). The reduced activation of *Mtu*CM by *Mtu*DAH7PS^{G190P} at 200 fold excess *Mtu*DAH7PS^{G190P} concentrations suggests the interaction between *Mtu*DAH7PS^{G190P} with *Mtu*CM is weaker than *Mtu*DAH7PS^{WT}. The less effective activation of *Mtu*CM activity may be due to a less favourable arrangement of residues in the vicinity of the interface between *Mtu*DAH7PS^{G190P} and *Mtu*CM.

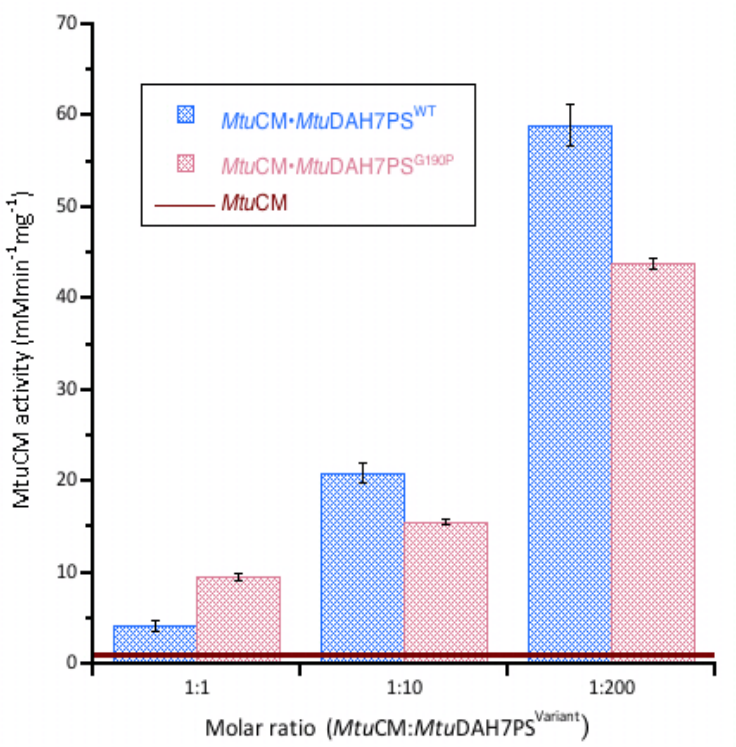

Figure 5.10 Activation of *Mtu*CM activity in the presence of either equimolar, ten-fold or 200-fold molar excess of *Mtu*DAH7PS^{WT} (blue hash) and *Mtu*DAH7PS^{G190P} (dusky pink hash). The burgundy line indicates the activity of *Mtu*CM alone. Assays conducted with 150 µM chorismic acid and 60 nM *Mtu*CM except for reactions requiring a 200-fold excess of *Mtu*DAH7PS where 10 nM of *Mtu*CM and *Mtu*CM alone where 90 nM were used and the results normalised. Error bars depict the standard deviation of duplicate measurements.

5.4.1. Regulation of *Mtu*CM by *Mtu*DAH7PS^{G190P}

The interaction of *Mtu*CM with *Mtu*DAH7PS was used to probe whether ligand binding to *Mtu*DAH7PS^{G190P} was communicated effectively to *Mtu*CM. Assays were conducted under the standard conditions and initiated with 25 µM chorismic acid as outlined in Section 9.9.3. The addition of Phe or a combination of Phe and Tyr to a mixture of *Mtu*DAH7PS^{G190P} and *Mtu*CM inhibited the *Mtu*CM activity and caused a similar reduction in the *Mtu*CM activity as was observed for *Mtu*DAH7PS^{WT} (Figure 5.11). The inhibition of *Mtu*CM activity in a mixture of *Mtu*CM and *Mtu*DAH7PS^{G190P} by the addition of Tyr was less effective compared to a mixture of *Mtu*CM and *Mtu*DAH7PS^{WT}.

The similar inhibition of *Mtu*CM activity by Phe in the presence of either *Mtu*DAH7PS^{G190P} or *Mtu*DAH7PS^{WT} indicates that the substitution of Gly190 for Pro has not affected the communication of Phe binding at site 1, the Phe-selective site, to the *Mtu*CM•*Mtu*DAH7PS interface. The Gly190Pro substitution has resulted in the relatively poor inhibition of *Mtu*CM activity by Tyr. This suggests Gly190 plays a role in the signalling of Tyr binding to the *Mtu*CM•*Mtu*DAH7PS interface. However, a dramatic reduction in the affinity of *Mtu*DAH7PS^{G190P} for Tyr could also explain this result, and no quantitative assessment has yet been made of the affinity between *Mtu*DAH7PS^{G190P} and Tyr.

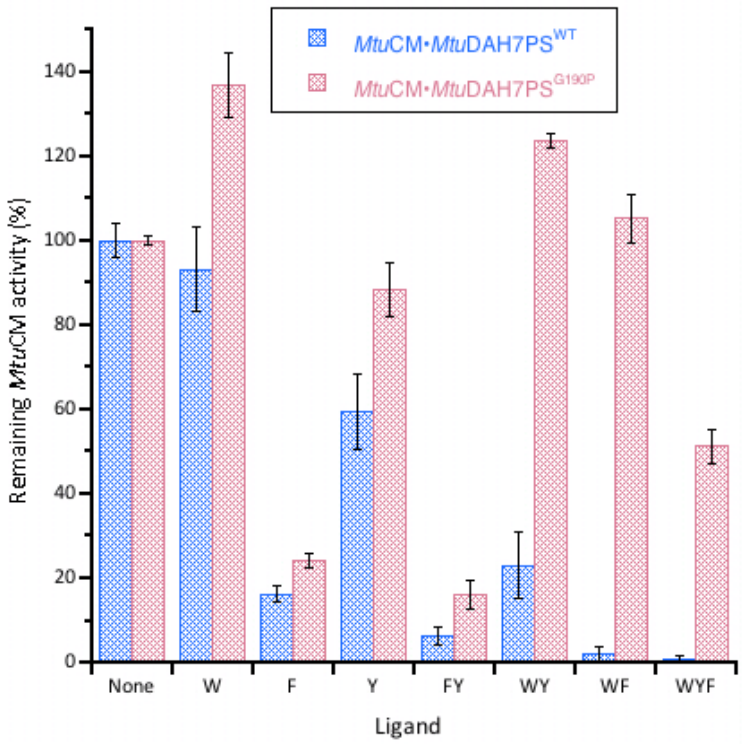

Figure 5.11 Remaining *Mtu*CM activity in the presence of various single, binary and ternary combinations of aromatic amino acids and a ten-fold excess of *Mtu*DAH7PS^{WT} (blue hash) or *Mtu*DAH7PS^{G190P} (dusky pink hash). The aromatic amino acids are represented by their one letter code; Trp, W; Phe, F and Tyr, Y. Each letter also represents 200 µM of the corresponding aromatic amino acids. Assays conducted in the presence of 150 µM chorismic acid and 60 nM *Mtu*CM. Error bars depict the standard deviation of at least duplicate measurements. P-values provided in appendix V.

The most remarkable finding from the inhibition studies was the observation that *Mtu*DAH7PS^{G190P} in the presence of Trp activated *Mtu*CM activity. The absolute *Mtu*CM activity in the presence of Trp and *Mtu*DAH7PS^{G190P} (10.8 ± 0.7 µMmin^{-1}mg^{-1}) was greater than that determined for *Mtu*CM in the presence of Trp and *Mtu*DAH7PS^{WT} (7.9 ± 0.6 µMmin^{-1}mg^{-1}). The difference in absolute *Mtu*CM

activity indicates that Trp binding has improved *Mtu*CM activation beyond what can be achieved by the wild type enzyme. Furthermore Phe or Tyr did not effectively supress this activation and even the ternary combination of aromatic amino acids failed to reduce *Mtu*CM activity below 50 %. These findings suggest that Trp may shift the *Mtu*DAH7PS^{G190P} protein ensemble further toward a species that favours the interaction and more importantly activation of *Mtu*CM.

Native PAGE provides further evidence that *Mtu*DAH7PS^{G190P} can form a complex with *Mtu*CM. As seen for a mixture of *Mtu*DAH7PS^{WT} and *Mtu*CM (Section 9.7.3) the native PAGE gel shows two bands for a mixture of *Mtu*DAH7PS^{G190P} and *Mtu*CM. One band is at ~240 kDa (according to the molecular mass marker) and corresponds to the presence of tetrameric *Mtu*DAH7PS. The second band is of a higher molecular mass ~300 kDa and is evidence of the formation of the *Mtu*CM•*Mtu*DAH7PS complex (Figure 5.12). More importantly the native PAGE showed the band at ~300 kDa becomes much weaker if 1 mM Phe was added to the mixture of *Mtu*CM and *Mtu*DAH7PS^{G190P}. The results from the Native PAGE suggest that Phe alters the affinity of *Mtu*DAH7PS^{G190P} for *Mtu*CM.

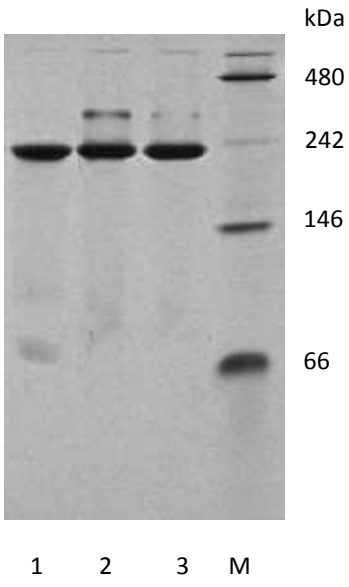

Figure 5.12 Amersham ECL native PAGE with 50 mM Tris- 175 mM Alanine running buffer pH 9.2; Lane M molecular weight marker; Lane 1 *Mtu*DAH7PS^{G190P}; Lane 2 *Mtu*DAH7PS^{G190P}with *Mtu*CM and Lane 3 *Mtu*DAH7PS^{G190P} with *Mtu*CM and 1 mM Phe. The concentration of *Mtu*CM is at an approximate four-fold molar excess of *Mtu*DAH7PS.

5.4.2. Summary of findings for *Mtu*DAH7PS^{G190P}

The quaternary structure of *Mtu*DAH7PS^{G190P} was shown to favour the tetrameric form at all concentrations analysed. Gly190 is located on the α2-α2a loop, just before the first inserted helix (α2a) and near the weak dimer interface (

Figure 5.1). The Gly190Pro substitution was intended to reduce the flexibility of the α2-α2a loop and possibly the inserted helices at the dimer interface. Such a reduction in flexibility may stabilise the formation of the tetramer. Interestingly *Mtu*DAH7PS^{G190P} was also more active than *Mtu*DAH7PS^{WT}. Whether the increased catalytic efficiency is due to the stabilisation of the tetrameric form of *Mtu*DAH7PS or the Gly190Pro substitution directly is unclear.

The inhibition studies revealed *Mtu*DAH7PS^{G190P} was no longer susceptible to inhibition by any combination of aromatic amino acids. ITC results showed that Trp and Phe can bind *Mtu*DAH7PS^{G190P} thus; the loss of feedback regulation of *Mtu*DAH7PS^{G190P} must be attributed to the Gly190Pro substitution. If this substitution restricted the flexibility of the inserted helical region as intended, it would imply the flexibility of the region is required for allosteric signal transfer between the allosteric sites and the active site. Alternatively, the substitution of Gly190 for Pro may restrict the accessible conformations of the α2-α2a loop preventing the nearby Ala192 from interacting with the bound Trp ligand. This interaction of Ala192 may be a critical contact for the transmission of the allosteric signal from the Trp site to the active site and other allosteric binding sites. Furthermore the inhibition of *Mtu*CM activity by Phe-bound *Mtu*DAH7P^{G190P} shows that allosteric communication from site 1, the Phe-selective binding site, has not been adversely affected by the Gly190Pro substitution.

*Mtu*DAH7PS^{G190P} retained the ability to regulate *Mtu*CM activity. Phe and Tyr inhibited *Mtu*CM activity for a mixture of *Mtu*DAH7PS^{G190P} and *Mtu*CM almost as effectively as for a mixture of *Mtu*CM and *Mtu*DAH7PS^{WT}. Thus the Gly190Pro substitution has not disrupted the allosteric communication network and/or mechanism that operate between *Mtu*CM and site 1 of *Mtu*DAH7PS. The response of a mixture of *Mtu*DAH7PS^{G190P} and *Mtu*CM to Trp was more peculiar, resulting in even greater activation of *Mtu*CM activity. It is highly likely that Trp binding shifts the average species of the

*Mtu*DAH7PS^{G190P} population ensemble to favour a species that optimises the interactions between *Mtu*CM and *Mtu*DAH7PS. This improved interaction between the two enzymes results in greater activation of *Mtu*CM activity and/or a higher affinity of *Mtu*DAH7PS^{G190P} for *Mtu*CM. Moreover, Trp binding to *Mtu*DAH7PS^{G190P} has also prevented effective inhibition by Phe and Tyr. This impaired inhibition of *Mtu*CM activity may be due to the Gly190Pro substitution disrupting the allosteric communication network between the allosteric binding sites of *Mtu*DAH7PS^{G190P}.

Overall structural characterisation carried out on *Mtu*DAH7PS^{G190P} showed the Gly190Pro substitution has shifted the quaternary structure equilibrium of *Mtu*DAH7PS, stabilising tetramer formation. Kinetic analysis showed *Mtu*DAH7PS^{G190P} was unregulated and thereby suggests that Gly190 is critical for signal transmission from the Trp site to the active site of *Mtu*DAH7PS. ITC studies showed Gly190 was not critical for proper signal transmission from site 1, the Phe-selective site, to the Trp site. However the impaired synergistic regulation of *Mtu*CM suggests the communication network between the Trp site and the other allosteric binding sites may not be completely intact

5.5. Investigating the role of Val103

5.5.1. Kinetic parameters

Michaelis-Menten kinetic assays were conducted under standard conditions (Section 9.9.1) for the determination of the kinetic parameters of *Mtu*DAH7PS^{V103A}. The change in the K_m for PEP was the most notable difference between *Mtu*DAH7PS^{V103A} and *Mtu*DAH7PS^{WT} (Table 5.6). Although *Mtu*DAH7PS^{V103} displayed a reduced affinity for PEP this was not of great detriment to the ability of the enzyme to catalyse the formation of DAH7P due to the accompanying increase in the k_{cat}. The K_m for E4P was similar for both *Mtu*DAH7PS^{V103A} and *Mtu*DAH7PS^{WT}. The catalytic efficiency of *Mtu*DAH7PS^{V103A} was not greatly altered by the introduction of the Val103Ala change.

Table 5.6 Kinetic parameters determined from a single set of Michaelis-Menten kinetics of *Mtu*DAH7PS^{V103A}. Michaelis-Menten plots are located in Appendix I. Error represents error of curve fitting to the data set by least squares fit.

***Mtu*DAH7PS**	K_m^{E4P} (μM)	K_m^{PEP} (μM)	k_{cat} (s^{-1})	**Catalytic Efficiency** k_{cat}/K_m^{E4P} ($s^{-1}mM^{-1}$)	k_{cat}/K_m^{PEP} ($s^{-1}mM^{-1}$)
Wild type	28 ± 2	37 ± 4	4.7 ± 0.1	170 ± 20	130 ± 20
V103A	26 ± 4	80 ± 5	6.5 ± 0.1	290 ± 50	96 ± 8

5.5.2. Disruption of feedback regulation

Inhibition studies were conducted under the standard conditions outlined in Section 9.9.3. *Mtu*DAH7PS^{V103A} showed no sensitivity to Tyr alone and only slight sensitivity with the addition of both Tyr and Trp (activity was reduced to ~80 %) (Figure 5.13). The combinations of Trp and Phe or Trp, Phe and Tyr reduced *Mtu*DAH7PS^{V103A} activity to ~20 % and ~5 % respectively, but this reduction in activity was less effective than observed for the wild type enzyme.

The loss of sensitivity of *Mtu*DAH7PS^{V103A} activity to the combination of Trp and Tyr means the hydrophobic contacts provided by Val103 may be important for signal transmission of ligand binding between the Trp site and site 2, the Tyr-selective site, or perhaps between the site 2 and the active site. The former option seems most likely as Val103 forms hydrophobic contacts with residues that contribute to the formation of the Trp binding site. As *Mtu*DAH7PS^{V103A} maintained a good level of sensitivity to the combination of Trp and Phe, Val103 probably does not play a direct role in the allosteric network that communicates Phe binding at Site 1, the Phe-selective site, or Trp binding at the Trp site to the active site. ITC could be used to verify whether Phe and Trp binding (and the synergistic binding between them) has been affected by the substitution of Val103. Use of an E4P analogue may also allow ITC to be used to probe the effect ligand binding has on the affinity of *Mtu*DAH7PS for its substrate.

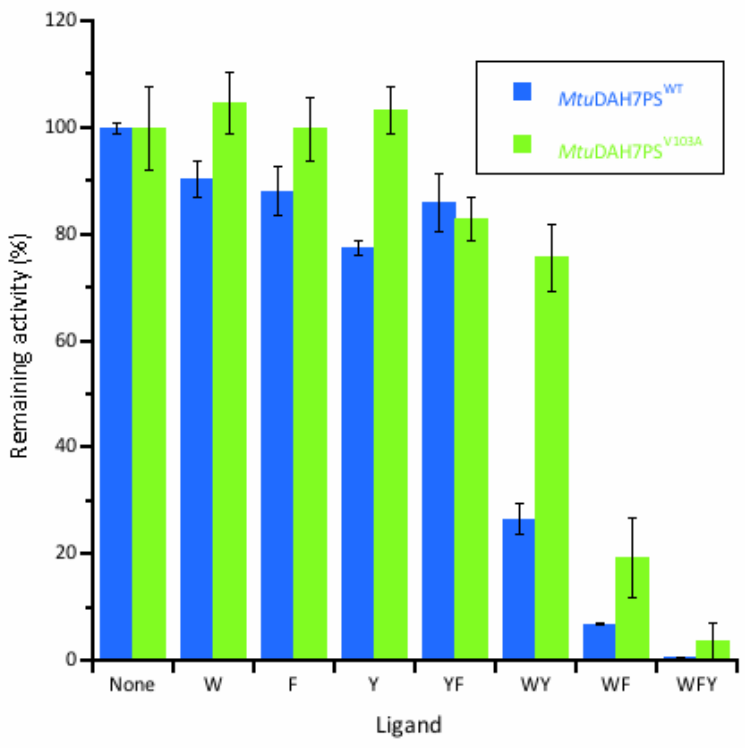

Figure 5.13 Remaining activity of *Mtu*DAH7PS^{WT} (blue) *Mtu*DAH7PS^{V103A} (lime green) in the presence of various single, binary and ternary combinations of aromatic amino acids. The aromatic amino acids are represented by their one letter code; Trp, W; Phe, F and Tyr, Y. Each letter also represents 200 µM of the corresponding aromatic amino acids. Assays conducted in the presence of 150 µM E4P and PEP. Error bars depict the standard deviation of triplicate measurements. P-values provided in appendix V.

5.5.3. Thermal stability

Due to constraints on time and protein availability it was not practical to determine the ligand binding dissociation constants of every *Mtu*DAH7PS variant by isothermal titration calorimetry. As an alternative DSF was used to gauge if ligands could bind the *Mtu*DAH7PS variants by monitoring whether the addition of ligand altered the T_m. An unfortunate limitation of this technique is ligand binding must induce a change in thermal stability to be detected. The DSF assays of all *Mtu*DAH7PS were conducted under equivalent conditions as outlined in Section 9.8.1.

The substitution of Val103Ala showed decreased thermal stability of the enzyme, as reflected by the ~11 ˚C drop in T_m for *Mtu*DAH7PS^{V103A} compared to *Mtu*DAH7PS^{WT} (Figure 5.14). The T_m of *Mtu*DAH7PS^{V103A} increased by ~11 ˚C and ~4 ˚C respectively, in the presence of Trp or Phe. The addition of Trp or Phe caused similar changes in thermal stability for both *Mtu*DAH7PS^{V103A} and

*Mtu*DAH7PS^{WT}. Tyr causes an ~8 ˚C increase in the T_m of *Mtu*DAH7PS^{V103A}, an increase ~7 ˚C greater than observed for *Mtu*DAH7PS^{WT}. Thus Tyr must be able to bind to *Mtu*DAH7PS^{V103A}. In accordance with the findings for *Mtu*DAH7PS^{WT} the addition of multiple aromatic amino acids results in greater increases in the T_m of *Mtu*DAH7PS^{V103A}. Therefore each ligand must make a separate contribution to the overall thermal stabilisation of *Mtu*DAH7PS^{V103A}. These findings showed all three aromatic amino acids are still able to bind to *Mtu*DAH7PS^{V103A}.

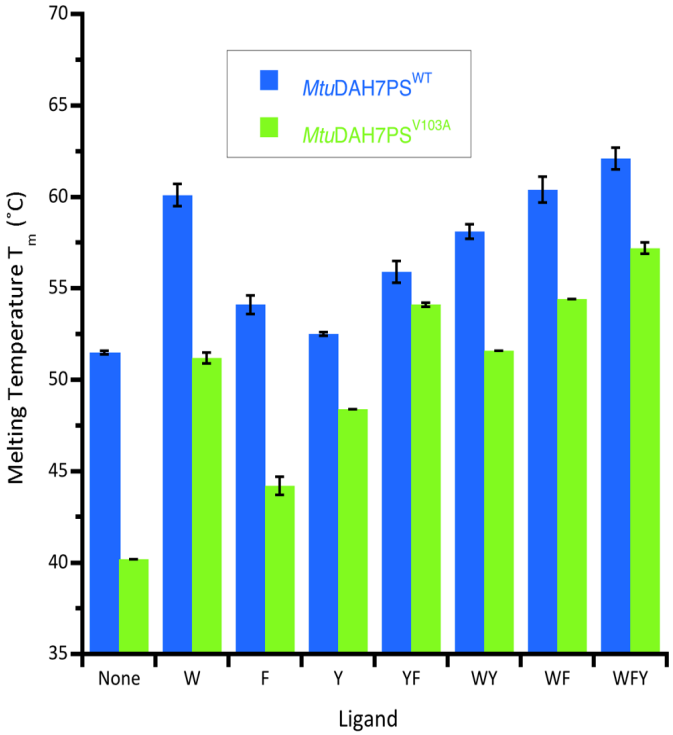

Figure 5.14 The effect of individual, binary and ternary combinations of aromatic amino acids on the thermal stability of *Mtu*DAH7PS^{WT} (blue) and *Mtu*DAH7PS^{V103A} (lime green). The aromatic amino acids are represented by their one letter code; Trp, W; Phe, F and Tyr, Y. Each letter also represents 200 µM of the corresponding aromatic amino acids. Error bars depict the standard deviation of triplicate measurements. P-values provided in appendix V.

5.5.4. Activation of *Mtu*CM

Kinetic assays conducted to determine the activation of *Mtu*CM activity in the presence of *Mtu*DAH7PS^{V103A} were carried out under the standard conditions defined in Section 9.9.1. The activation profile of *Mtu*CM activity by *Mtu*DAH7PS^{V103A} increased with excess *Mtu*DAH7PS

concentration in a similar fashion to *Mtu*DAH7PS^{WT} (Figure 5.15). However, the maximal activity achieved with a 200-fold molar excess of *Mtu*DAH7PS^{V103A}, ~90 mMmin^{-1}mg^{-1}, was better than the activation achieved by *Mtu*DAH7PS^{WT}. Overall the substitution of Val103 for Ala may have improved the activation of *Mtu*CM possibly by optimising the interactions across the *Mtu*DAH7PS•*Mtu*CM interface *Mtu*CM catalysis.

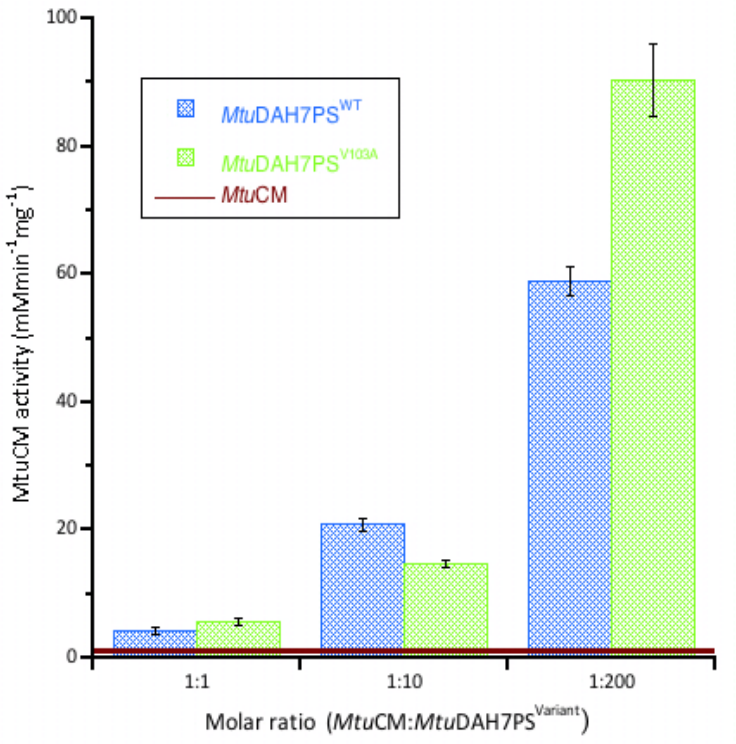

Figure 5.15 Activation of *Mtu*CM activity in the presence of either equimolar, ten-fold or 200-fold molar excess of *Mtu*DAH7PS^{WT} (blue hash) and *Mtu*DAH7PS^{V103A} (lime green hash). The burgundy line indicates the activity of *Mtu*CM alone. Assays conducted with 150 µM chorismic acid and 60 nM *Mtu*CM except for reactions requiring a 200-fold excess of *Mtu*DAH7PS where 10 nM of *Mtu*CM and *Mtu*CM alone where 90 nM were used and the results normalised. Error bars depict the standard deviation of duplicate measurements.

5.5.5. Regulation of *Mtu*CM by *Mtu*DAH7PS^{V103A}

Kinetic assays were conducted under the standard conditions detailed in Section 9.9.3. The *Mtu*CM activity of a mixture of *Mtu*CM and *Mtu*DAH7PS^{V103A} was insensitive to Tyr. Phe inhibited *Mtu*CM activity in the presence of *Mtu*DAH7PS^{V103A} but this inhibition was less effective than observed for *Mtu*DAH7PS^{WT} (Figure 5.16). The *Mtu*CM activity in the presence of *Mtu*DAH7PS^{V103A} was less responsive to the presence of Tyr and Phe, retaining approximately 30 % more activity than *Mtu*CM in

the presence of *Mtu*DAH7PS^{WT}. This loss in sensitivity to Phe and Tyr may imply Val103 plays an important part in signalling the binding of Phe or Tyr at sites 1 and/or 2 to the interface of *Mtu*CM•*Mtu*DAH7PS and across to the associated *Mtu*CM. Interestingly, Phe and Tyr appeared to synergistically inhibit *Mtu*CM activity when added together to a mixture of *Mtu*CM and *Mtu*DAH7PS^{V103A}. The inhibition achieved by adding double the concentration of Phe or Tyr (400 μM) also needs to be measured to confirm the inhibition in the presence of Phe and Tyr is not simply a response to an increase in the total concentration of Phe and Tyr.

Trp did not inhibit *Mtu*CM activity in the presence of *Mtu*DAH7PS^{V103A}. The combination of Trp and Phe did not synergistically inhibit the *Mtu*CM activity of a mixture of *Mtu*CM and *Mtu*DAH7PS^{V103A}. It is interesting to note that the *Mtu*DAH7PS^{V103A} activity was synergistically inhibited by the combination of Trp and Tyr (Section 5.5.2). These observations suggest that the substitution of Val103 for Ala has not seriously disrupted the allosteric communication network between site 1, the Trp site and the *Mtu*DAH7PS active site, but some change has occurred that prevents this regulatory signal from being transmitted to *Mtu*CM.

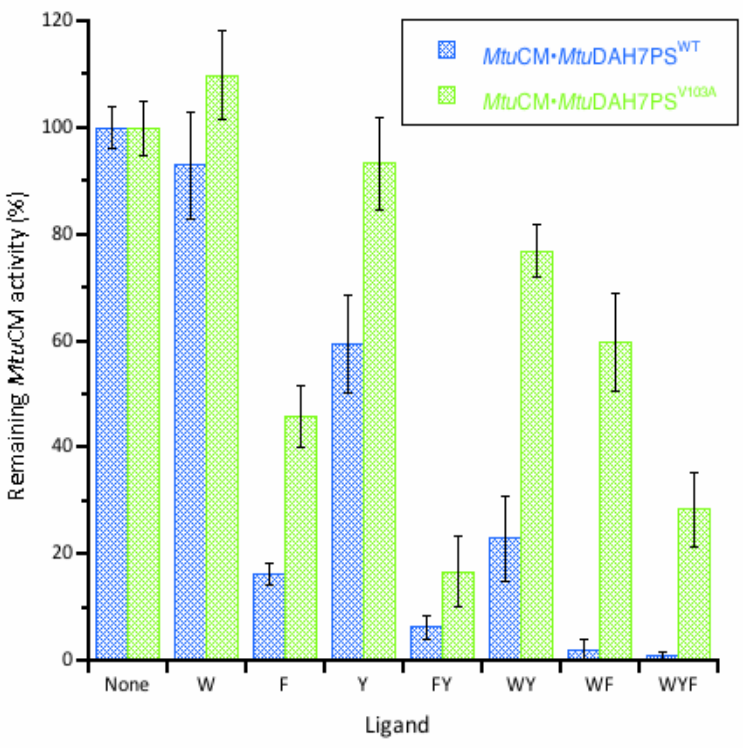

Figure 5.16 Remaining *Mtu*CM activity in the presence of various single, binary and ternary combinations of aromatic amino acids and a ten-fold excess of *Mtu*DAH7PS^{WT} (blue hash) or *Mtu*DAH7PS^{V103A} (lime green hash). The aromatic amino acids are represented by their one letter code; Trp, W; Phe, F and Tyr, Y. Each letter also represents 200 µM of the corresponding aromatic amino acids. Assays conducted in the presence of 150 µM chorismic acid and 60 nM *Mtu*CM. Error bars depict the standard deviation of at least duplicate measurements. P-values provided in appendix V.

5.5.1. Summary of findings for *Mtu*DAH7PS^{V103A}

AUC and native PAGE (Section 5.3.2) showed the quaternary structure equilibrium of *Mtu*DAH7PS^{V103A} has shifted permitting a greater proportion of dimeric *Mtu*DAH7PS^{V103A} to be present at concentrations up to 1 mg/mL. SAXS showed the tetramer formed at very high concentrations (>5 mg/mL) (Section 5.3.2), but also that its structure in solution may not be identical to *Mtu*DAH7PS^{WT}. The introduced substitution has not seriously affected the activity of *Mtu*DAH7PS^{V103A} or the ability of the enzyme to boost the activity of *Mtu*CM.

Analysis by DSF showed all three aromatic amino acids could bind *Mtu*DAH7PS^{V103A}, as they all increased the thermal stability of the enzyme. Hence the substitution of Val103 for Ala did not prevent Trp, Phe or Tyr from binding *Mtu*DAH7PS^{V103A}. Somewhat surprisingly the loss of the branched side chain of Val103 disrupted the synergistic inhibition by Trp and Tyr of *Mtu*DH7PS^{V103A}.

*Mtu*DAH7PS^{V103A} maintained sensitivity to Trp and Phe. Similarly, *Mtu*DAH7PS^{V103A} is able to inhibit *Mtu*CM activity in the presence of Phe but not Tyr. Synergistic inhibition of *Mtu*CM activity by *Mtu*DAH7PS^{V103A} by Trp in combination with Phe or Tyr has also been adversely affected.

In chapter 3 it was shown Tyr (in combination with Trp binding at the Trp site) must bind to site 2 to inhibit *Mtu*DAH7PS activity, but better inhibition is achieved when Tyr occupies both sites 1 and 2. Chapter 3 also showed site 1 was a Phe-selective site. As both *Mtu*DAH7PS^{V103A} activity and *Mtu*CM activity (in the presence of *Mtu*DAH7PS^{V103A}) remain sensitive to the presence of Phe, Val103 is most likely responsible for communication of Tyr binding from site 2 of *Mtu*DAH7PS to the active site and the Trp site. The less effective synergistic inhibition of *Mtu*CM activity by *Mtu*DAH7PS^{V103A} suggests Val103 may also play a role in communicating Trp binding from the Trp site to the other allosteric binding sites and to *Mtu*CM.

The branched side chain of Val103 fits into a hydrophobic pocket, forming hydrophobic contacts with the surrounding residues and must impose some restriction of the molecular motion of the α1 helix on which it is located (

Figure 5.1D). The loss of hydrophobic contacts with the surrounding residues may impede transmission of changes in molecular motion upon Tyr binding to other allosteric binding sites, the active site and the *Mtu*CM•*Mtu*DAH7PS interface. Val103 forms hydrophobic interactions with Leu107, which is part of the Trp site. The loss of this interaction may contribute to the disruption of the communication between the Trp site and the other allosteric sites and to *Mtu*CM. Val103 may also help to position residues of the α2-α2a loop via hydrophobic interactions with Leu191, thus also controlling the molecular dynamics of the loop to some extent. The loss of the branched side chain of Val103 by substitution for Ala probably reduces the number of hydrophobic contacts made by Leu191 and may allow the α2 α2a loop a greater range of movement. Ala192 is also located on the α2-α2a loop and form a hydrogen bond with the bound Trp ligand, thus changes to the loop flexibility may also cause disrupt an allosteric signal being transmitted to or from the Trp site.

5.6. Investigating the role of Tyr131

5.6.1. Kinetic parameters

The standard assay conditions described in Section 9.9.1 were used to carry out the Michaelis-Menten kinetics of *Mtu*DAH7PS^{Y131A}. The removal of the tyrosyl side chain has negatively impacted on the catalytic turnover of *Mtu*DAH7PS^{Y131A} reducing k_{cat} to ~1.6 s^{-1} (Table 5.7). In addition the *Mtu*DAH7PS^{Y131A} K_m for PEP also increased, signifying *Mtu*DAH7PS^{Y131A} has a decreased affinity for PEP. The consequence is a drop in PEP catalytic efficiency of the enzyme to ~ 18 $s^{-1}mM^{-1}$. The decrease in the E4P K_m helped to mitigate the affect of the low k_{cat} resulting in an E4P catalytic efficiency of ~130. Overall the Tyr131Ala substitution has harmed the catalytic efficiency of the enzyme especially with respect to PEP.

Table 5.7 Kinetic parameters determined from a single set of Michaelis-Menten kinetic data from *Mtu*DAH7PS^{Y131A}. Michaelis-Menten plots are displayed in Appendix I. Error represents error of curve fitting to the data set by least squares fit.

***Mtu*DAH7PS**	K_m^{E4P}	K_m^{PEP}	k_{cat}	**Catalytic Efficiency** k_{cat}/K_m^{E4P}	k_{cat}/K_m^{PEP}

	(μM)	(μM)	(s^{-1})	($s^{-1}mM^{-1}$)	($s^{-1}mM^{-1}$)
Wild type	28 ± 2	37 ± 4	4.7 ± 0.1	170 ± 20	130 ± 20
Y131A	13.0 ± 0.9	91 ± 4	1.63 ± 0.03	130 ± 10	18 ± 1

5.6.2. Disruption of feedback regulation

Inhibition studies were conducted under the standard experimental conditions detailed in Section 9.9.3. The final *Mtu*DAH7PS concentration used for the inhibition studies was kept between 0.01 and 0.02 mg/mL for all *Mtu*DAH7PS variants. Similarly all inhibition assays were conducted with 150 μM E4P and PEP. As a consequence of keeping both the concentration of enzyme and substrate constant for all kinetic assays, the poor catalytic efficiency of *Mtu*DAH7PS^{Y131A} gave a low baseline activity, approximately one third of *Mtu*DAH7PS^{WT} under the same conditions.

The most prominent observation from the feedback inhibition studies of *Mtu*DAH7PS^{Y131A} was the ~70 % increase in activity caused by Phe (Figure 5.17). The combination of Phe and Tyr caused the greatest increase in *Mtu*DAH7PS^{Y131A} of ~95 %. Since the absolute activity of *Mtu*DAH7PS^{Y131A} (1.7 ± 0.1 $\mu Mmin^{-1}mg^{-1}$) was less than *Mtu*DAH7PS^{WT} (5.6 ± 0.1 $\mu Mmin^{-1}mg^{-1}$), Phe and Tyr (and to a lesser extent Trp), binding may mitigate or even restore the loss of activity due to the Tyr131Ala substitution.

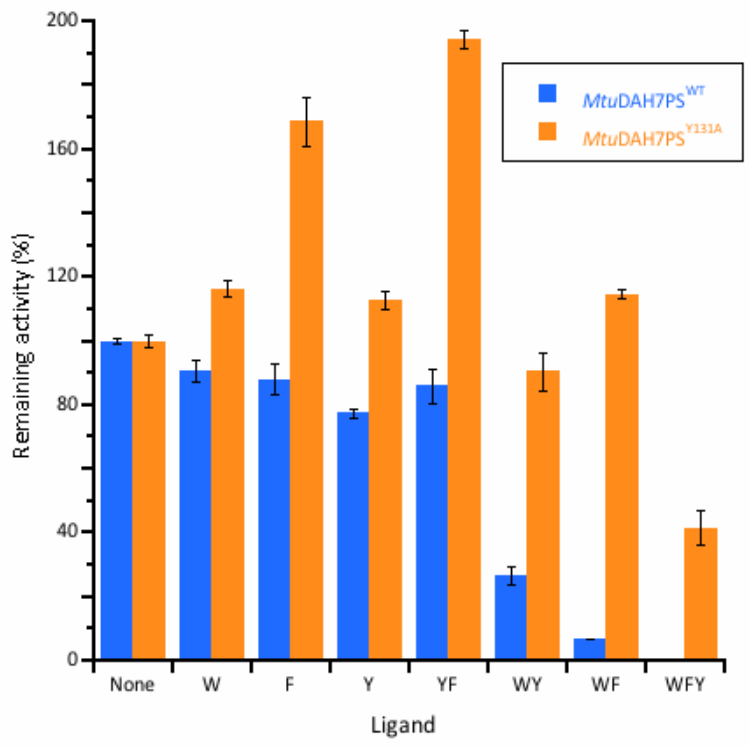

Figure 5.17 Remaining activity of *Mtu*DAH7PS^{WT} (blue) *Mtu*DAH7PS^{Y131A} (orange) in the presence of various single, binary and ternary combinations of aromatic amino acids. The aromatic amino acids are represented by their one letter code; Trp, W; Phe, F and Tyr, Y. Each letter also represents 200 µM of the corresponding aromatic amino acids. Assays conducted in the presence of 150 µM E4P and PEP. Error bars depict the standard deviation of triplicate measurements. P-values provided in appendix V.

*Mtu*DAH7PS^{Y131A} does not exhibit significant inhibitory sensitivity to any individual or binary combination of aromatic amino acids. The presence of all three aromatic amino acids, Trp, Phe and Tyr, reduced *Mtu*DAH7PS^{Y131A} activity to ~42 %. Without the tyrosyl group of Tyr131 there was no effective inhibitory response to any binary combination of aromatic amino acids and a poor response to the presence of all three aromatic amino acids. It is likely the tyrosyl side chain of Tyr131 contributes to the signalling pathway between the allosteric binding sites and the active sites.

5.6.3. Thermal stability

The thermal stability of *Mtu*DAH7PS^{Y131A} was measured by DSF under the standard experimental conditions detailed in Section 9.8.1. The T_m of *Mtu*DAH7PS^{Y131A} was ~6.5 ˚C less than *Mtu*DAH7PS^{WT}, indicating the introduction of the Tyr131Ala substitution decreased the thermal stability of the protein (Figure 5.18). The T_m determined in the presence of either Trp or Tyr (and combinations which

included Trp or Tyr) had higher T_m values. Like *Mtu*DAH7PS^{V103A} the addition of Tyr to *Mtu*DAH7PS^{Y131A} caused a big increase of ~4.5 ˚C in the T_m compared to the ~1 ˚C increase for *Mtu*DAH7PS^{WT}. The increases in T_m suggest *Mtu*DAH7PS^{Y131A} was able to bind both Trp and Tyr and gain thermal stability from doing so.

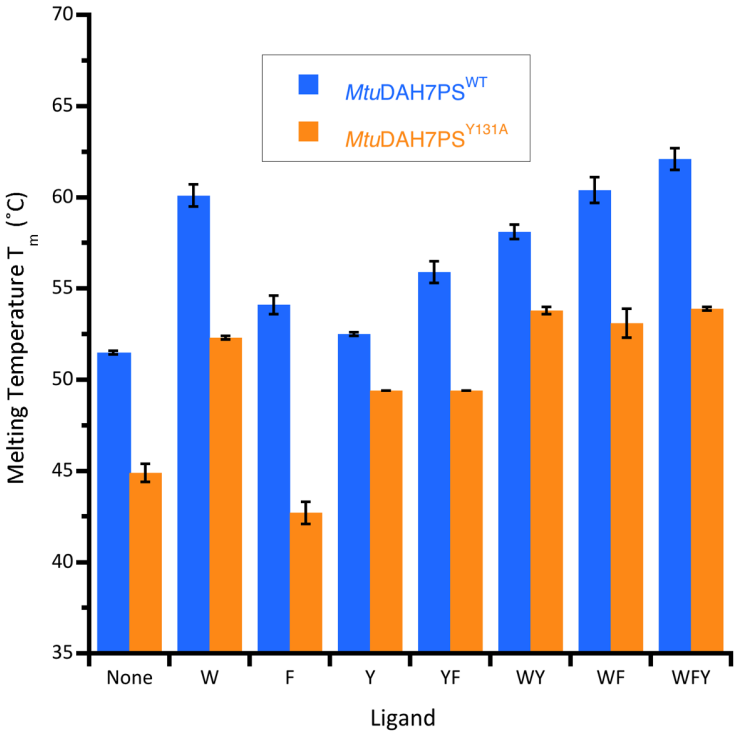

Figure 5.18 The effect of individual, binary and ternary combinations of aromatic amino acids on the thermal stability of *Mtu*DAH7PS^{WT} (blue) and *Mtu*DAH7PS^{Y131A} (orange). The aromatic amino acids are represented by their one letter code; Trp, W; Phe, F and Tyr, Y. Each letter also represents 200 µM of the corresponding aromatic amino acids. P-values provided in appendix V.

Phe does not cause a positive thermal shift, instead a slight decrease of ~2 ˚C is observed for the T_m determined when Phe is added to the conditions. As a change in stability is observed it is likely Phe does bind to *Mtu*DAH7PS^{Y131A}, but this was better confirmed with ITC (Section 5.6.4). This loss in stability shows Phe does not act to stabilise the protein as previously observed for *Mtu*DAH7PS^{WT}. Trp or Tyr binding appeared to counteract the destabilising effect of Phe binding. When Phe was added in combination with Trp or Tyr to *Mtu*DAH7PS^{Y131A} the calculated T_m.

Overall the DSF results indicate the tyrosyl group of Tyr131 is instrumental for *Mtu*DAH7PS to acquire an increase in thermal stability upon Phe binding. As site 1 was shown to be the Phe-selective site in Chapter 3, Tyr131 is most probably involved in signal transmission between site 1 and the other allosteric binding sites and the active site.

5.6.4. Binding affinities

ITC was used to quantify the binding affinity of *Mtu*DAH7PS^{Y131A} for Trp and Phe. ITC experiments were conducted under similar conditions as *Mtu*DAH7PS^{WT}, with protein and ligand concentrations optimised for each experiment as detailed Section 9.8.2.

The K_d between Phe and *Mtu*DAH7PS^{Y131A} was found to be ~50 µM, more than double the K_d between *Mtu*DAH7PS^{WT} and Phe (Figure 5.19B, Table 5.8). Thus the loss of the tyrosyl group of Tyr131 has had a detrimental affect on the affinity of *Mtu*DAH7PS^{Y131A} for Phe, but does not prevent Phe binding.

As seen previously for *Mtu*DAH7PS^{R171A} and *Mtu*DAH7PS^{G190P} the ITC thermogram for Trp binding to *Mtu*DAH7PS^{Y131A} displayed two binding events of opposite enthalpy change (Figure 5.19C). The K_d values (of 5.5 and 0.5 µM) determined for each binding event revealed Trp bound tightly to *Mtu*DAH7PS^{Y131A} (Figure 5.19A). Furthermore the observed K_d between Trp and *Mtu*DAH7PS^{Y131A} decreased by five-fold when *Mtu*DAH7PS^{Y131A} was incubated with Phe. A similar five-fold decrease in the K_d between Trp and *Mtu*DAH7PS^{WT} was observed when *Mtu*DAH7PS^{WT} was incubated with Phe. The loss of the tyrosyl group of Tyr131 has not prevented Trp binding. However, the substitution may have altered communication between the Trp sites of each monomeric unit resulting in the identification of two Trp binding events.

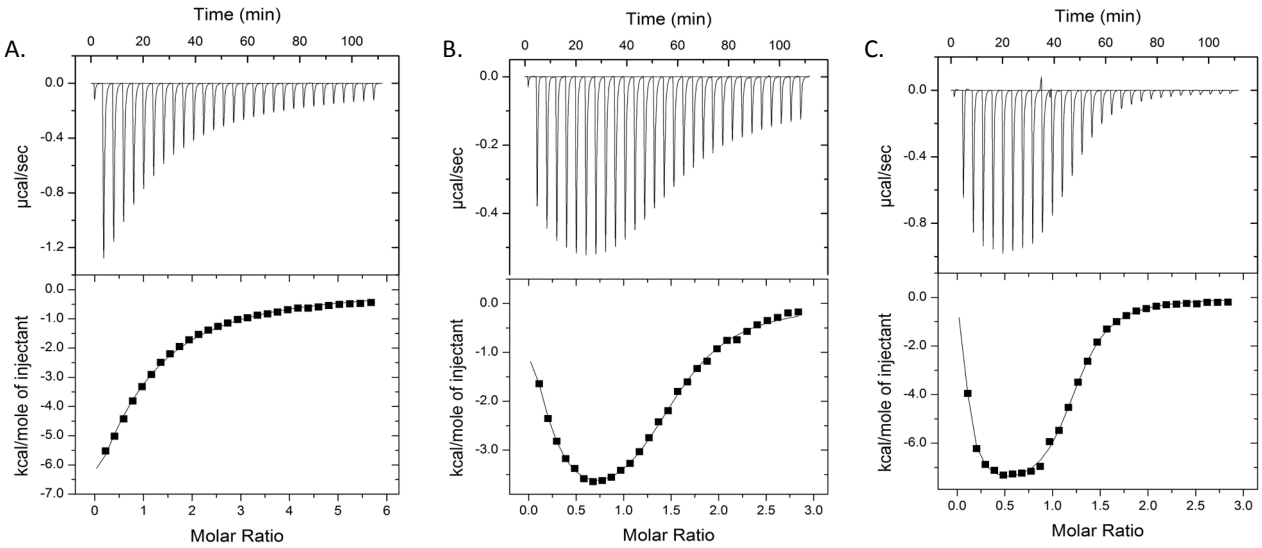

Figure 5.19 ITC data for the interaction of A. 38 µM *Mtu*DAH7PS^{Y131A} with 0.5 mM Trp titrant; B. 38 µM of *Mtu*DAH7PS^{Y131A} with 1 mM Phe titrant and C. 38 µM *Mtu*DAH7PS^{Y131A} and a background of 100 µM Phe present in the cell with a 0.5 mM Trp titrant.

Table 5.8 Dissociation constants determined by ITC for *Mtu*DAH7PS^{Y131A}. * Indicates results determined previously by Richard Hutton and — Indicates no background ligand present. Values are from a single ITC experiment. Error represents error of curve fitting to the data set by least squares fit.

Titrated ligand	Background ligand	*Mtu*DAH7PS	
		Wild type K_d (µM)	Y131A K_d (µM)
Trp	—	4.7 ± 0.1*	5.5 ± 0.2 and 0.5 ± 0.3
Phe	—	21 ± 1*	52 ± 3
Trp	Phe	1.08 ± 0.03*	1.1 ± 0.1 and 0.12 ± 0.09

5.6.5. Activation of *Mtu*CM

An activation profile of *Mtu*CM activity by *Mtu*DAH7PS^{Y131A} was obtained to gain insight into whether the interaction between the two enzymes had been compromised by the Tyr131Ala substitution. Kinetic assays were conducted under the standard conditions outlined in Section 9.9.1.

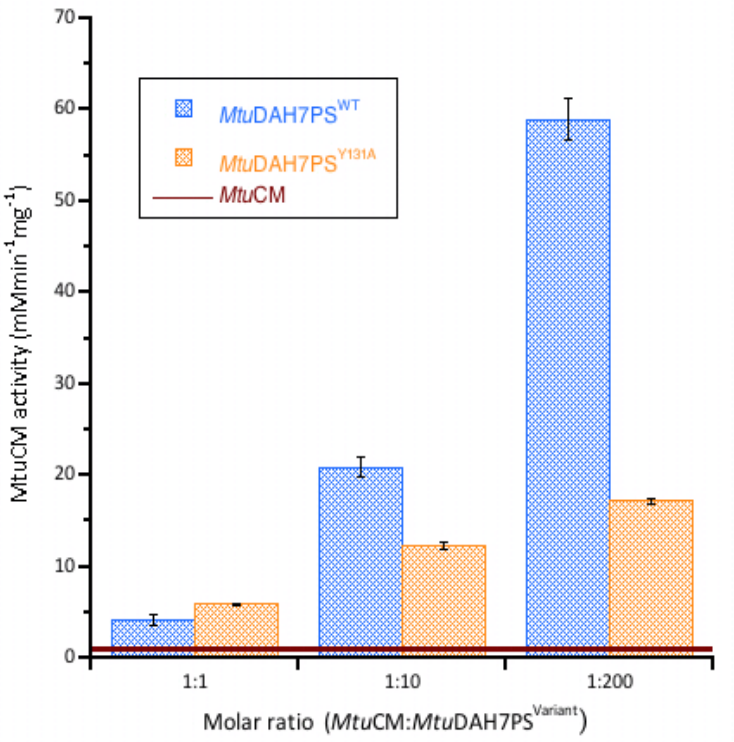

Figure 5.20 Activation of *Mtu*CM activity in the presence of either equimolar, ten-fold or 200-fold molar excess of *Mtu*DAH7PS^{WT} (blue hash) and *Mtu*DAH7PS^{Y131A} (orange hash). The burgundy line indicates the activity of *Mtu*CM alone. Assays conducted with 150 µM chorismic acid and 60 nM *Mtu*CM except for reactions requiring a 200-fold excess of *Mtu*DAH7PS where 10 nM of *Mtu*CM and *Mtu*CM alone where 90 nM were used and the results normalised. Error bars depict the standard deviation of duplicate measurements.

*Mtu*DAH7PS^{Y131A} is able to enhance the activity of *Mtu*CM. The level of enhancement achieved by *Mtu*DAH7PS^{Y131A} is abysmal in comparison with *Mtu*DAH7PS^{WT} (Figure 5.20). This indicates one of two things; either *Mtu*DAH7PS^{Y131A} has a reduced affinity for *Mtu*CM and a smaller proportion of complex is formed, or on the formation of the complex *Mtu*DAH7PS^{Y131A} is unable to cause the same rearrangement of the *Mtu*CM active site essential for the observed activity boost. Both hypotheses could account for the reduced enhancement of *Mtu*CM activity observed for *Mtu*DAH7PS^{Y131A}.

5.6.6. Regulation of *Mtu*CM by *Mtu*DAH7PS^{Y131A}

Kinetic assays for the inhibition studies of *Mtu*CM in the presence of a ten-molar excess of *Mtu*DAH7PS^{Y131A} were conducted under the standard conditions outlined in Section 9.9.3. The inhibition studies showed the *Mtu*CM activity of a mixture of *Mtu*CM and *Mtu*DAH7PS^{Y131A} was insensitive to Phe, yet sensitivity to Tyr was preserved (Figure 5.21). These results offer further

support that Tyr131 is critical to signal transmission of Phe binding, without side chain of Tyr131 the binding of Phe is not adequately communicated to *Mtu*CM and consequently does not significantly affect *Mtu*CM activity.

Synergistic inhibition of *Mtu*CM activity by *Mtu*DAH7PS^{Y131A} was observed in the presence of Phe and Tyr and suggests both Phe and Tyr can bind simultaneously to their preferred sites. The synergistic inhibition of *Mtu*CM by *Mtu*DAH7PS^{Y131A} was poor for combinations of Trp with either Phe or Tyr. The Tyr131Ala substitution may have disrupted the communication of Trp binding to sites 1 and 2 and to the *Mtu*CM•*Mtu*DAH7PS interface preventing synergistic regulation from occurring. Curiously, the combination of Phe, Tyr and Trp was resulted in the greatest reduction in activity. Thus, Tyr and Phe binding may help to re-establish the communication pathways between the allosteric binding sites and the *Mtu*CM•*Mtu*DAH7PS interface allowing *Mtu*CM activity to be regulated. Alternatively Trp binding may shift the *Mtu*DAH7PS^{Y131A} population ensemble toward a species that exhibits a greater affinity and ability to activate *Mtu*CM than unliganded *Mtu*DAH7PS^{Y131}.

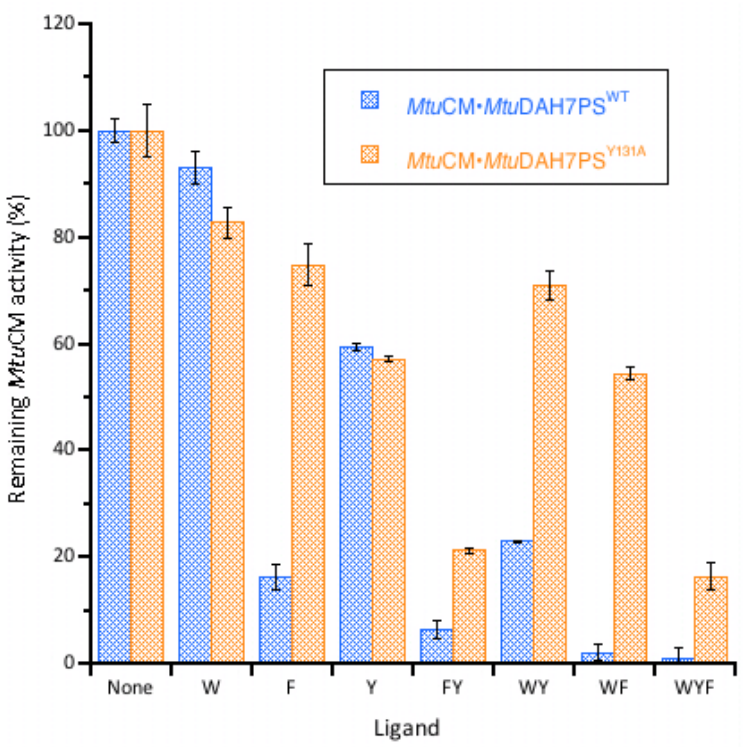

Figure 5.21 Remaining *Mtu*CM activity in the presence of various single, binary and ternary combinations of aromatic amino acids and a ten-fold excess of *Mtu*DAH7PS^{WT} (blue hash) or *Mtu*DAH7PS^{Y131A} (orange hash). The aromatic amino acids are represented by their one letter code; Trp, W; Phe, F and Tyr, Y. Each letter also represents 200 µM of the corresponding aromatic amino acids. Assays conducted in the presence of 150 µM chorismic acid and 60 nM *Mtu*CM. Error bars depict the standard deviation of at least duplicate measurements. P-values provided in appendix V.

Native PAGE also illustrated the failure of Phe binding to *Mtu*DAH7PS^{Y131A} to inhibit *Mtu*CM activity. A protein band observed on the native gel at ~300 kDa when *Mtu*DAH7PS^{Y131A} and *Mtu*CM were both present confirms *Mtu*DAH7PS^{Y131A} can form a complex with *Mtu*CM Figure 5.22). This higher molecular weight band associated with the formation of the complex *Mtu*CM•*Mtu*DAH7PS^{Y131A} is just as strong, if not stronger in the presence of Phe. The retention of the *Mtu*CM•*Mtu*DAH7PS^{Y131A} complex band in the presence of Phe is further evidence *Mtu*DAH7PS^{Y131A} can not effectively communicate Phe binding to the *Mtu*CM•*Mtu*DAH7PS^{Y131A} interface without Tyr.

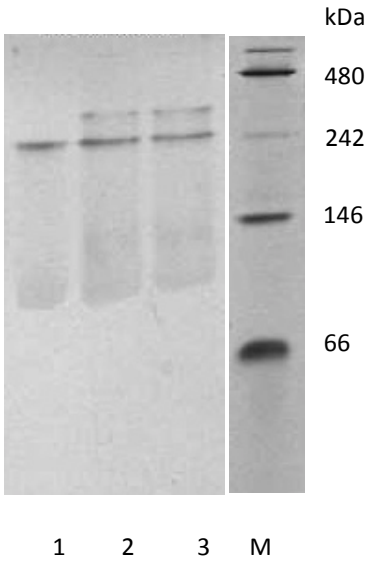

Figure 5.22 Amersham ECL Native PAGE with 50 mM Tris- 175 mM Alanine running buffer pH 9.2; Lane M molecular weight marker; Lane 1 *Mtu*DAH7PS^{Y131A}; Lane 2 *Mtu*DAH7PS^{Y131A}with *Mtu*CM and Lane 3 *Mtu*DAH7PS^{Y131A} with *Mtu*CM and 1 mM Phe. The concentration of *Mtu*CM is approximately four-fold molar excess of *Mtu*DAH7PS.

5.6.7. Summary of findings for *Mtu*DAH7PS^{Y131A}

The SAXS parameters determined for *Mtu*DAH7PS^{Y131A} suggest that although *Mtu*DAH7PS^{Y131A} was tetrameric it may not be identical to *Mtu*DAH7PS^{WT}. Native PAGE also showed the quaternary structure equilibrium of *Mtu*DAH7PS^{Y131A} had changed in comparison with *Mtu*DAH7PS^{WT}, the gel showing *Mtu*DAH7PS^{Y131A} existed mainly as a mixture of dimer and tetramer. Structural characterisation of *Mtu*DAH7PS^{G190P} and *Mtu*DAH7PS^{V103A} also suggested these proteins may adopt a different quaternary structure conformation than *Mtu*DAH7PS^{WT}. The catalytic ability of *Mtu*DAH7PS^{G190P}, *Mtu*DAH7PS^{V103A} and *Mtu*DAH7PS^{N237A} are comparable to *Mtu*DAH7PS^{WT} and their interaction with *Mtu*CM has not been significantly impaired. Conversely the catalytic efficiency of *Mtu*DAH7PS^{Y131A} has been impaired, especially with respect to PEP, and the activation of *Mtu*CM activity by *Mtu*DAH7PS^{Y131A} was also quite poor. Hence *Mtu*DAH7PS^{Y131A} has probably adopted a different conformation to the wild type enzyme and forms weaker interactions with *Mtu*CM resulting in poor activation of *Mtu*CM activity. However, it is unclear whether it is the possible change in the

conformation of *Mtu*DAH7PS^{Y131A} or the substitution of Tyr131, which is responsible for the poor activity of *Mtu*DAH7PS^{Y131A}.

DSF and ITC confirmed Trp, Phe and Tyr were all able to bind *Mtu*DAH7PS^{Y131A}. It should also be noted that Phe binding reduced the thermal stability of *Mtu*DAH7PS^{Y131A} and may be linked to any change in conformation or quaternary structure. ITC also provided evidence that Phe binding enhanced the affinity of *Mtu*DAH7PS^{Y131A} for Trp. Nonetheless the loss of the tyrosyl group of Tyr131 has severely disrupted the synergistic regulation of *Mtu*DAH7PS^{WT}. Phe, Tyr and Trp activated *Mtu*DAH7PS^{Y131A} activity and only the addition of all three aromatic amino acids could elicit a synergistic inhibitory response that was still much less effective than the ternary inhibition of *Mtu*DAH7PS^{WT}. The Tyr131Ala substitution may have led to *Mtu*DAH7PS^{Y131A} adopting a slightly different conformation to *Mtu*DAH7PS^{WT} with an inferior catalytic ability. If this is true then the activation of *Mtu*DAH7PS^{Y131A} activity on binding any of the aromatic amino acids may be due to the occupancy of the allosteric binding sites partially restoring the *Mtu*DAH7PS^{WT} conformation.

*Mtu*DAH7PS^{Y131A} endowed *Mtu*CM activity with regulatory sensitivity to Tyr, but not Phe, as shown by the *Mtu*CM inhibition studies and native PAGE. *Mtu*DAH7PS^{Y131A} did not significantly synergistically regulate *Mtu*CM activity in the presence of Trp with either Phe or Tyr, but the combination of Phe, Trp and Tyr showed evidence for synergy. The loss in synergy suggests Tyr131 may play a role in communicating Trp binding between all three allosteric bindings sites.

It is unclear from the available crystallographic coordinates of the *Mtu*DAH7PS^{WT} how the loss of Tyr131 had such a dramatic impact on *Mtu*DAH7PS activity. An aromatic amino acid residue, either Phe or Tyr, typically occupies the position of Tyr131 as shown by the multiple sequence alignment conducted as part of the SCA analysis.[115] Hence the hydrophobic interaction of the tyrosyl group of Tyr131 with the benzyl ring with Phe94 may be a critical interaction and may help to control the flexibility of the long β2-α2 loop (

Figure 5.1C). Substitution of Tyr131 for Ala, a residue with a much smaller side chain, may create space for water to bind and may disrupt the site of substitution and thus allosteric communication.

Comprehensive crystallographic studies may be conducted to determine if *Mtu*DAH7PS^{Y131A} has adopted a different conformation, providing crystal packing effects do not hide any small changes in conformation. Obtaining crystal structures of *Mtu*DAH7PS^{Y131A} with and without the aromatic amino acids present may provide insight into how the ligands are causing activation of *Mtu*DAH7PS^{Y131A} activity. Crystal coordinates of *Mtu*DAH7PS^{Y131A} may also help to clarify the role of the tyrosyl group of Tyr131 in controlling the flexibility or conformation of the β2-α2 loop and whether this is linked to the changes in *Mtu*DAH7PS conformation. Alternatively MD simulations can be used to gain insight into how the Tyr131Ala substitution may have affected the molecular motion and conformation of *Mtu*DAH7PS^{Y131A}.

5.7. Investigating the role of Asn175

5.7.1. Kinetic parameters

The kinetic parameters of *Mtu*DAH7PS^{N175A} were derived from the Michaelis-Menten kinetics under standard assay conditions detailed in Section 9.9.1. The kinetic parameters of *Mtu*DAH7PS^{N175A} were interesting because the increase in k_{cat} was accompanied by an increase in the K_m values for both E4P and PEP ultimately resulting in only a small difference in the determined catalytic efficiency of each substrate compared to *Mtu*DAH7PS^{WT} (Table 5.9). Thus the substitution of Asn175 to Ala has not seriously harmed the catalytic efficiency of the enzyme.

Table 5.9 Kinetic parameters determined from a single set of Michaelis-Menten kinetics of *Mtu*DAH7PS^{N175A}. Michaelis-Menten plots are shown in Appendix I. Error represents error of curve fitting to the data set by least squares fit.

***Mtu*DAH7PS**	K_m^{E4P} (μM)	K_m^{PEP} (μM)	k_{cat} (s^{-1})	**Catalytic Efficiency** k_{cat}/K_m^{E4P} ($s^{-1}mM^{-1}$)	**Catalytic Efficiency** k_{cat}/K_m^{PEP} ($s^{-1}mM^{-1}$)
Wild type	28 ± 2	37 ± 4	4.7 ± 0.1	170 ± 20	130 ± 20
N175A	61 ± 8	89 ± 7	7.6 ± 0.2	150 ± 20	100 ± 10

5.7.2. Disruption of feedback regulation

Feedback inhibition studies were conducted under the standard conditions stated in Section 9.9.3. The changes in both *Mtu*DAH7PS^{R171A} and *Mtu*DAH7PS^{N175A} are located at the Phe-selective binding site, site 1. Thus it was unsurprising to find that, like *Mtu*DAH7PS^{R171A}, *Mtu*DAH7PS^{N175A} activity showed significantly reduced sensitivity to the combination of Trp and Phe (Figure 5.23). However, unlike *Mtu*DAH7PS^{R171A}, which showed reduced sensitivity to all combinations of aromatic amino acids, *Mtu*DAH7PS^{N175A} activity showed increased sensitivity to Trp and Tyr. The ternary combination of all three aromatic amino acids greatly reduced the *Mtu*DAH7PS^{N175A} activity, but the reduction was not as severe as observed for *Mtu*DAH7PS^{WT}. Asn175 appears to be critical for the signalling of Phe binding to the active site. Furthermore as *Mtu*DAH7PS^{N175A} has improved sensitivity to the combination of Trp and Tyr, this suggests Asn175 may play a role in distinguishing between Phe and Tyr binding at site 1.

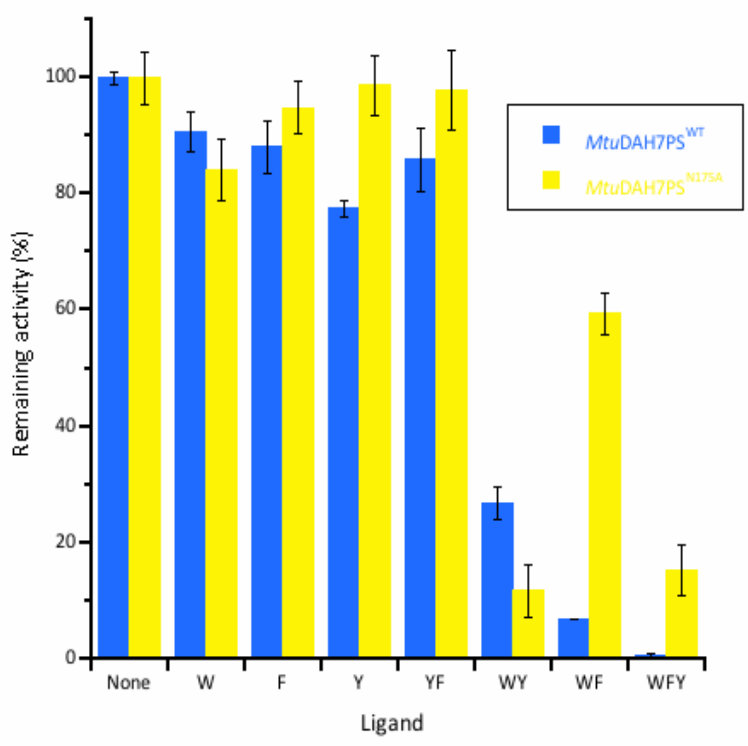

Figure 5.23 Remaining activity of *Mtu*DAH7PS^{WT} (blue) *Mtu*DAH7PS^{N175A} (yellow) in the presence of various single, binary and ternary combinations of aromatic amino acids. The aromatic amino acids are represented by their one letter code; Trp, W; Phe, F and Tyr, Y. Each letter also represents 200 µM of the corresponding aromatic amino acids. Assays conducted in the presence of 150 µM E4P and PEP. Error bars depict the standard deviation of triplicate measurements. P-values provided in appendix V.

5.7.3. Thermal stability in the presence of ligand

Unfortunately, due to limitations on time and available protein and the stability of the protein, studying ligand binding to *Mtu*DAH7PS^{N175A} by isothermal titration calorimetry was impractical. To gain some insight into whether the aromatic amino acids, particularly Phe, could bind to *Mtu*DAH7PS^{N175A} DSF was used. All assays were conducted under equivalent standard conditions outline in Section 9.8.1.

As seen for some previous *Mtu*DAH7PS variants, *Mtu*DAH7PS^{N175A} displayed an unexpected loss of thermal stability of ~6 ˚C due to the substitution of Asn175 (Figure 5.24). Trp and Tyr binding were clearly evident by the observed increases in the thermal melting temperature (T_m) when compared to the unliganded enzyme. Tyr caused a shift in the T_m of *Mtu*DAH7PS^{N175A}, of ~5 ˚C greater than the ~1 ˚C shift observed for *Mtu*DAH7PS^{WT}. The bigger increase in T_m suggests the substitution of Asn175 does not negatively impact Tyr binding and may have even improved it.

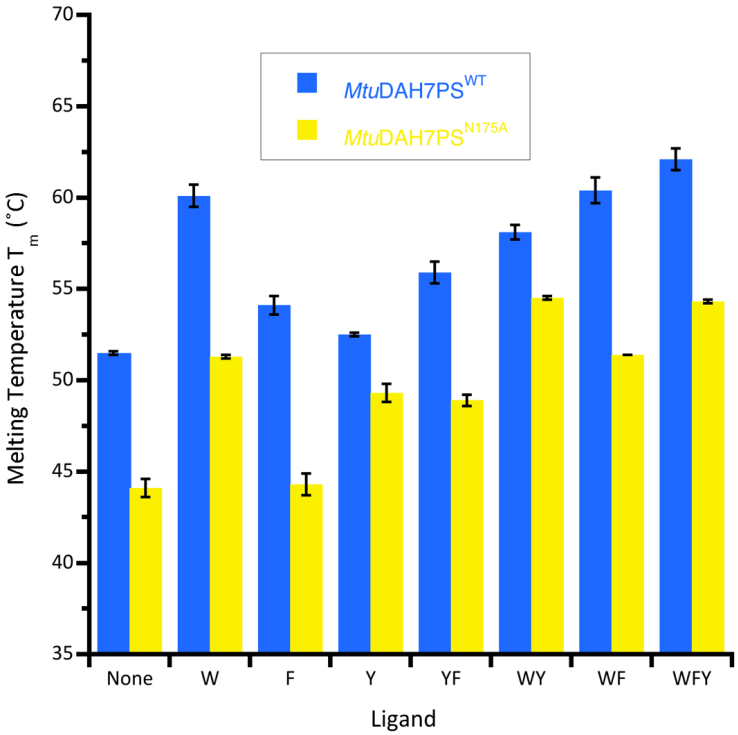

Figure 5.24 The effect of individual, binary and ternary combinations of aromatic amino acids on the thermal stability of *Mtu*DAH7PS^{WT} (blue) and *Mtu*DAH7PS^{N175A} (yellow). The aromatic amino acids are represented by their one letter code; Trp, W; Phe, F and Tyr, Y. Each letter also represents 200 µM of the corresponding aromatic amino acids. Error bars depict the standard deviation of triplicate measurements. P-values provided in appendix V.

The presence of Phe however causes little change to the thermal stability of *Mtu*DAH7PS^{N175A}, even when combined with Trp or Tyr. The lack of change in thermal stability suggests at a concentration of 200 µM Phe does not bind to *Mtu*DAH7PS^{N175A} or at least Phe binding does not offer *Mtu*DAH7PS^{N175A} any gain in thermal stability. Thus Asn175 appears to be a critical residue for either Phe binding to occur at site 1 or for signal transmission from site 1.

5.7.4. Activation of *Mtu*CM

The ability of *Mtu*DAH7PS^{N175A} to activate *Mtu*CM was very similar to *Mtu*DAH7PS^{WT} until the concentration of *Mtu*DAH7PS^{N175A} reached a 200-fold molar excess (Figure 5.25). At a 200-fold molar excess of *Mtu*DAH7PS^{N175A}, *Mtu*CM activity reached ~120 mM min^{-1} mg^{-1}, nearly double the activity boost achieved by *Mtu*DAH7PS^{WT}. The enhanced activation of *Mtu*CM by *Mtu*DAH7PS^{N175A} at high molar excess implies Asn175 may be part of the signalling pathway from site 1 to the inter-protein interface and across to the *Mtu*CM active site. The substitution of Asn175 may have unexpectedly improved the interaction between *Mtu*CM and *Mtu*DAH7PS.

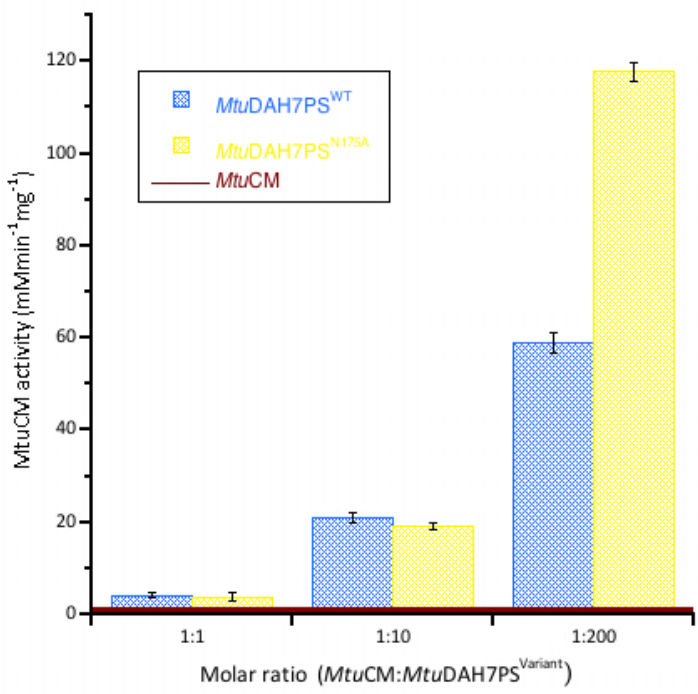

Figure 5.25 Activation of *Mtu*CM activity in the presence of either equimolar, ten-fold or 200-fold molar excess of *Mtu*DAH7PS^{WT} (blue hash) and *Mtu*DAH7PS^{N175A} (yellow hash). The burgundy line indicates the activity of *Mtu*CM alone. Assays conducted with 150 µM chorismic acid and 60 nM *Mtu*CM except for reactions requiring a 200-fold excess of *Mtu*DAH7PS where 10 nM of *Mtu*CM and *Mtu*CM alone where 90 nM were used and the results normalised. Error bars depict the standard deviation of duplicate measurements.

5.7.5. Regulation of *Mtu*CM activity by *Mtu*DAH7PS^{N237A}

To understand how the Asn175Ala substitution affected the ability of *Mtu*DAH7PS^{N175A} to regulate *Mtu*CM activity, further inhibition studies were carried out using a mixture of *Mtu*CM and *Mtu*DAH7PS^{N175A}. All the *Mtu*CM kinetic assays were conducted in accordance with the standard protocol outlined in Section 9.9.3.

*Mtu*CM activity showed a poor response to the presence of either Phe or Tyr despite the fact that Tyr (with Trp) was able to regulate *Mtu*DAH7PS^{N175A} activity (Figure 5.26). The insensitivity of *Mtu*CM activity to Tyr and Phe was also seen for *Mtu*DAH7PS^{R171A}, and confirmed site 1 of *Mtu*DAH7PS is essential for the regulation of *Mtu*CM by Tyr and Phe alone. The combination of Phe and Tyr resulted in a greater loss of *Mtu*CM activity than either amino acid could achieve on its own. The improved inhibition for the combination of Tyr and Phe suggests both amino acids are able to bind simultaneously thus it is highly probable Phe is still able to bind to site 1 of *Mtu*DAH7PS^{N175A}, as Tyr would preferentially bind to site 2, the Tyr-selective site.

The most surprising result from the inhibition studies was that Trp inhibited *Mtu*CM activity for a mixture of *Mtu*CM and *Mtu*DAH7PS^{N175A} incredibly well, reducing activity to ~5 %. The sensitivity to Trp is further evidence that site 1 is able to communicate to both the Trp site and the *Mtu*CM•*Mtu*DAH7PS interface. Curiously the addition of Trp and Tyr to the mixture of *Mtu*CM and *Mtu*DAH7PS^{N175A} resulted in less effective *Mtu*CM inhibition. Addition of Trp and Phe did not display any synergistic inhibitory effect on *Mtu*CM activity; further proof Asn175 is essential for communication between site 1 and the Trp site.

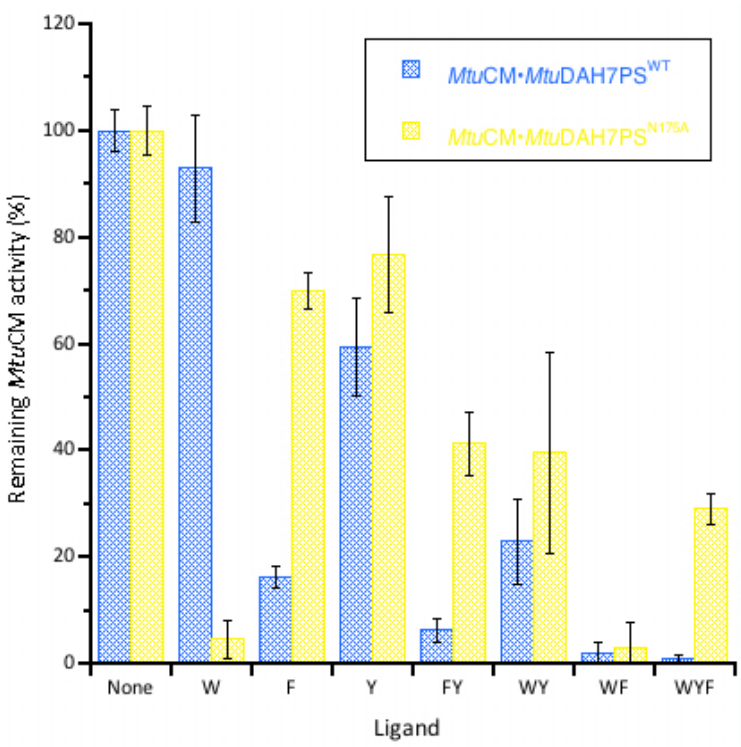

Figure 5.26 Remaining *Mtu*CM activity in the presence of various single, binary and ternary combinations of aromatic amino acids and a ten-fold excess of *Mtu*DAH7PS^{WT} (blue hash) or *Mtu*DAH7PS^{N175A} (yellow hash). The aromatic amino acids are represented by their one letter code; Trp, W; Phe, F and Tyr, Y. Each letter also represents 200 µM of the corresponding aromatic amino acids. Assays conducted in the presence of 150 µM chorismic acid and 60 nM *Mtu*CM. Error bars depict the standard deviation of at least duplicate measurements. P-values provided in appendix V.

Native PAGE confirmed the *Mtu*DAH7PS^{N175A} was less susceptible to inhibition by Phe, and is unable to cause the dissociation of *Mtu*CM•*Mtu*DAH7PS^{N175A} complex. The ~300 kDa molecular mass band observed only when both *Mtu*CM and *Mtu*DAH7PS^{N175A} are present corresponds to the formation of the *Mtu*CM•*Mtu*DAH7PS^{N175A} complex. This higher molecular mass band diminished in the presence of Phe for the wild type enzyme (Section 4.8.1) but for a mixture of *Mtu*CM and *Mtu*DAH7PS^{N175A} in the presence of Phe the ~300 kDa band remained (Figure 5.27). The native gel provides evidence Asn175 is essential for effective regulation of *Mtu*CM activity by Phe. It is clear the loss of the amide group of Asn175 is fundamental to the signalling between the allosteric binding sites of *Mtu*DAH7PS^{N175A} but also from the allosteric sites to *Mtu*CM•*Mtu*DAH7PS inter-protein interface.

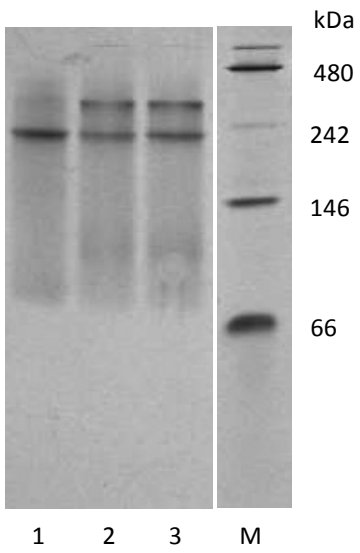

Figure 5.27 Amersham ECL Native PAGE with 50 mM Tris- 175 mM Alanine running buffer pH 9.2; Lane M molecular weight marker; Lane 1 *Mtu*DAH7PS^{Y131A}; Lane 2 *Mtu*DAH7PS^{Y131A}with *Mtu*CM and Lane 3 *Mtu*DAH7PS^{Y131A} with *Mtu*CM and 1 mM Phe. The concentration of *Mtu*CM is approximately four-fold molar excess of *Mtu*DAH7PS.

5.7.6. Summary of findings for *Mtu*DAH7PS^{N175A}

The quaternary structure of *Mtu*DAH7PS^{N175A} was shown to be unaffected by SAXS and native PAGE. The activity of *Mtu*DAH7PS^{N175A} was not notably affected by the introduced substitution. The ability of *Mtu*DAH7PS^{N175A} to activate *Mtu*CM was impressively enhanced, with a 200-fold molar excess of *Mtu*DAH7PS^{N175A} doubling the *Mtu*CM activity achieved by *Mtu*DAH7PS^{WT}. Interestingly *Mtu*DAH7PS^{R171A}, another *Mtu*DAH7PS variant with a substitution located at site 1, also roughly doubled the *Mtu*CM activity in comparison to *Mtu*DAH7PS^{WT}. The superior ability of both *Mtu*DAH7PS^{N175A} and *Mtu*DAH7PS^{R171A} to boost *Mtu*CM activity suggest site 1 is inherently linked to the *Mtu*CM•*Mtu*DAH7PS interface, about 45 Å away.

DSF showed that Trp and Tyr were able to bind *Mtu*DAH7PS^{N175A}. Phe did not cause an increase in thermal stability of *Mtu*DAH7PS^{N175A}, but ITC analysis is required to verify whether Phe is able to bind with any significant affinity to the enzyme. The sensitivity of *Mtu*DAH7PS^{N175A} activity to Trp and Tyr had improved slightly. The sensitivity of *Mtu*DAH7PS^{N175A} activity to Trp and Phe was significantly

diminished but had not been eliminated suggesting Phe may still be able to bind to the enzyme. Assuming Phe can bind with a reasonable affinity to *Mtu*DAH7PS^{N237A}, the diminished sensitivity to the combination of Trp and Phe, means Asn175 must contribute to the communication pathway between site 1 and the active site and/or between site 1 and the Trp site. ITC is needed to identify whether Phe can bind to *Mtu*DAH7PS^{N175A} and if so whether it influences or is influenced by Trp binding. This information is required to fully understand the impact the Asn175Ala substitution has had on the regulatory network of *Mtu*DAH7PS.

The interaction between the amide of Asn175 and the bound ligand at site 1 may not be absolutely essential for an inhibitory response to Trp in combination with Phe or Tyr as proposed previously.[126] Instead it appears from this study the interaction of Asn175 with the bound ligand at site 1 may allow the site to distinguish between Phe and Tyr binding. It should be noted that the amide group of Asn175 coordinates to the amine and carbonyl groups of the bound ligand, for both Tyr and Phe (

Figure 5.1A). Thus it is not obvious exactly how Asn175 may enable the enzyme to differentiate between Phe and Tyr binding. It is probable to some degree that all the residues, which contribute to the formation of Site 1, collectively distinguish between Phe and Tyr binding. ITC may be able to show if Asn175 is truly critical for distinguishing between Phe and Tyr binding.

Native PAGE and *Mtu*CM inhibition studies showed *Mtu*DAH7PS^{N175A} could not inhibit *Mtu*CM activity in the presence of Phe or Tyr very well. The loss of the amide group of Asn175 has disrupted the signal transmission of ligand binding at site 1 to the *Mtu*CM•*Mtu*DAH7PS interface. Rather unexpectedly, inhibition studies also showed *Mtu*DAH7PS^{N175A} endowed *Mtu*CM activity with sensitivity to Trp. The addition of Tyr somewhat reduced the inhibitory affect of Trp, making combinations of allosteric amino acids including Trp and Tyr less effective than Trp alone. These findings suggest the interactions of the ligand with the amide group of Asn175 are essential for the correct signal transmission between the allosteric binding sites and to the *Mtu*CM•*Mtu*DAH7PS interface.

5.8. Summary

The SCA and MD analyses of *Mtu*DAH7PS predicted a cluster of coevolved residues, believed to be inherently involved in signal transmission between both the different allosteric binding sites and to the *Mtu*DAH7PS active site. This network of residues is thought to transmit subtle changes in flexibility or molecular motion across the enzyme ultimately providing entropic control of the affinity of each binding site for its ligand.[71,115]

From the residues identified from the SCA and MD analysis, four *Mtu*DAH7PS variants were generated to verify experimentally whether the residues were readily involved in the communication network between allosteric binding sites and to the active site. These variants, *Mtu*DAH7PS^{G190P}, *Mtu*DAH7PS^{V103A}, *Mtu*DAH7PS^{Y131A} and *Mtu*DAH7PS^{N175A} were all successfully expressed and purified. CD revealed the secondary structure of all the variants to be similar to *Mtu*DAH7PS^{WT} but SAXS, AUC and native PAGE revealed more subtle changes to the quaternary structure equilibrium of some of the *Mtu*DAH7PS variants. All four variants were catalytically active, but for *Mtu*DAH7PS^{G190P} and *Mtu*DAH7PS^{Y131A} the kinetic parameters varied widely from *Mtu*DAH7PS^{WT}.

Gly190 is absolutely essential for inhibition of *Mtu*DAH7PS activity and synergy between the Trp site and sites 1 and 2 as demonstrated by the kinetic analysis of *Mtu*DAH7PS^{G190P}. This Gly190Pro substitution was intended to reduce the flexibility of α2-α2a loop, and these results therefore imply that this flexibility is essential for allosteric communication to and from the Trp site. However, the substitution may also prevent Ala192, another residue also located on the α2-α2a loop (

Figure 5.1B) from hydrogen bonding to the bound Trp ligand at the Trp site. The Ala192 contact with the bound Trp ligand may be necessary for Trp binding to be communicated to the other allosteric binding sites and the active site. Gly190 does not play a role in the communication in the inhibitory response of Phe and Tyr to *Mtu*CM.

Substitution of Val103 for Ala also disrupted the synergistic inhibition of *Mtu*DAH7PS and *Mtu*CM activities. Illustrating the SCA correctly identified Val103 as a critical member of the signal

transmission network of residues responsible for communicating ligand binding between allosteric binding sites and the active site. The hydrophobic contacts formed between Val103 and Leu194, which is also located on the α2-α2a loop, may ensure the α2-α2a loop is in the correct position for Ala192 to form a hydrogen bond to the bound Trp ligand. Val103 also forms hydrophobic contacts with Leu107, which contributes to the formation of the hydrophobic pocket for Trp binding at the Trp site. The interactions of Val103 with Leu194 and Leu107 are just two interactions that could be affected by the Val103 substitution that in turn may effect Trp binding or communication of Trp binding from the Trp site.

*Mtu*DAH7PS^{Y131A} had poor catalytic efficiency and poorly activated and regulated *Mtu*CM activity. It was proposed that the substitution of Tyr131 may result in a pseudo Phe-bound species of *Mtu*DAH7PS, which was catalytically unfavourable and weakened the interaction of *Mtu*DAH7PS^{Y131A} with *Mtu*CM. The loss of the tyrosyl side chain of Tyr131 correlated with a severe loss of inhibitory sensitivity of *Mtu*DAH7PS and *Mtu*CM activity. However, all three aromatic amino acids were able to activate *Mtu*DAH7PS activity. Tyr131 is located near the tight dimer interface on the β2-α2 loop and may influence the conformation of the dimer/tetramer as part of the mechanism of inhibition of *Mtu*DAH7PS.

Finally substitution of Asn175 at the Phe-selective binding site, site 1, unsurprisingly resulted in both *Mtu*DAH7PS and *Mtu*CM activity displaying decreased sensitivity to Phe. More interestingly *Mtu*DAH7PS^{Y131A} showed increased sensitivity to Trp and Tyr and *Mtu*CM activity maintained sensitivity to Tyr in the presence of *Mtu*DAH7PS^{N175A}. Thus Asn175 may play a significant role in distinguishing between Tyr and Phe binding at site 1. Intriguingly *Mtu*CM activity became highly sensitive to the addition of Trp in the presence of *Mtu*DAH7PS^{N175A}, but the *Mtu*CM activity was no longer synergistically inhibited. Thus the loss of the amide group of Asn175 has interfered with the signal transmission between allosteric binding sites and between allosteric binding sites and the *Mtu*CM•*Mtu*DAH7PS interface.

This work proved far more successful than first anticipated, the dramatic changes in regulatory response to the aromatic amino acids observed were not expected from single residue substitutions. All four residues identified by the SCA and MD studies were found to disrupt the synergistic inhibition of *Mtu*DAH7PS and *Mtu*CM to varying degrees. Each residue was shown to be critical to the proper signal transmission of aromatic amino acid binding across the enzyme to the other allosteric binding sites, the active site and the *Mtu*CM•*Mtu*DAH7PS interface. This work has successfully validated the SCA and MD analysis by providing evidence that four of the residues identified in the analysis were critical for effective and proper synergistic inhibition of not only *Mtu*DAH7PS activity but also *Mtu*CM activity.

6. *Mtu*DAH7PS variants used to examine Trp site residues.

6.1. Introduction

The sophisticated feedback regulation of *Mtu*DAH7PS activity is reliant on the presence of Trp in combination with either Phe or Tyr to elicit an inhibitory response. Crystallographic studies have shown the allosteric ligand binding site near the weak dimer interface is the only site Trp has been observed to occupy, and accordingly the site is identified as the Trp site.[48,70,126] As Trp binding, presumably at the Trp site, is essential for inhibition of *Mtu*DAH7PS activity there is a need for a better understanding of the interactions between Trp and *Mtu*DAH7PS.

The work described within this chapter investigated some of the critical interactions that form between *Mtu*DAH7PS and the bound Trp at the Trp site and explores how Trp binding may be communicated to the active site and the other allosteric binding sites, sites 1 and 2. SDM was used to substitute key binding site residues to prevent critical interactions between the Trp ligand and the Trp site. These variant enzymes were characterised by a range of kinetic, structural and biophysical techniques.

6.1.1. Formation of the Trp site

The Trp site is located near the weak dimer interface of *Mtu*DAH7PS (Figure 6.1A). Inspection of the Trp- and Phe-bound *Mtu*DAH7PS crystal structure (PDB code: 3NV8) reveals that Trp binds within a pocket formed between the inserted helices α2a and α2b and the core barrel. The carbonyl oxygen of Trp forms hydrogen bonds with the amine group of Lys123 (β2 beta sheet). The α-amino group of Trp forms hydrogen bonds with both Thr240 and Asn237 (α2b-β3 loop). The backbone carbonyl oxygen of Ala192 forms a polar contact to the nitrogen of the indole ring of the bound Trp molecule. Several hydrophobic residues, Val111, Leu107, Leu194, Val197 and Ala241 (α1 helix and α2a-α2b loop) contribute to the formation of a hydrophobic cavity into which the indole ring of Trp is buried.

Alignment of the tetrameric Trp-bound crystal structure (PDB code: 3NUE) with the Trp- and Phe-bound crystal structure does not reveal any significant changes to the positions of residues at the Trp site as a result of Phe binding at the site 1 and site 2 (Cα RMSD 0.189 Å) (Figure 6.1D).

Alignment of the tetrameric Trp- and Phe-bound crystal structure of *Mtu*DAH7PS (PDB code: 3KGF) with the tetrameric unliganded crystal structure (PDB code: 3NV8, Cα RMSD 0.271 Å) shows that Trp binding causes some rearrangement of the residues of the Trp site (Figure 6.1B). The α2-β3 loop has moved, most notably moving Gln239, Thr 240 and Asn237 (Cα) 6.8, 2.1 and 4.6 Å respectively toward the bound Trp ligand when Trp binds. The residues, which form the hydrophobic pocket, undergo minor repositioning on Trp binding to create more room for the indole group of the Trp ligand.

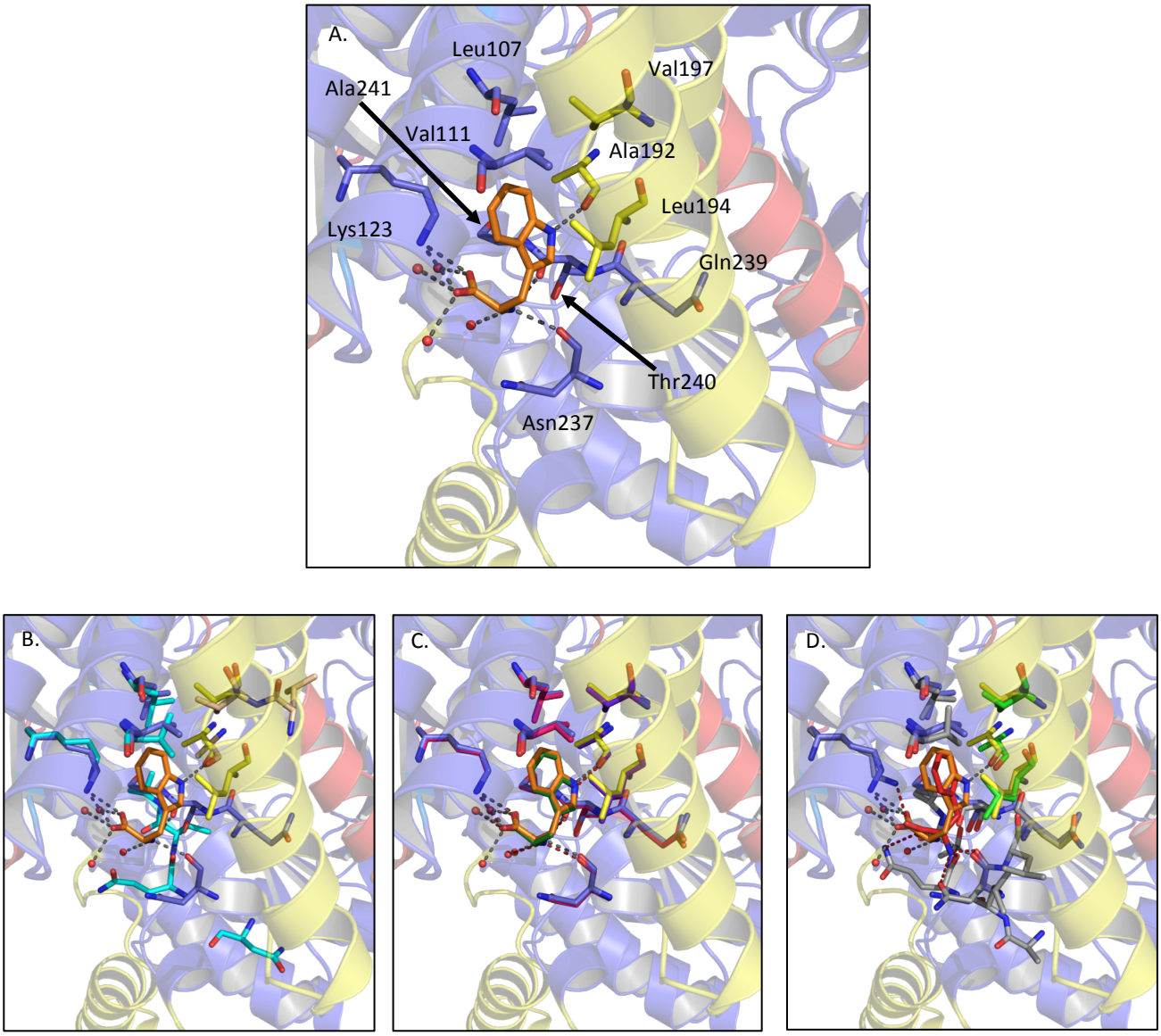

Figure 6.1 Critical residues involved in ligand binding at the Trp site. A. *Mtu*DAH7PS Trp and Phe soaked crystal structure (PDB code: 3KGF, 2.00 Å resolution). Backbone carbons are shown in cartoon form with the core barrel, inserted helices and N-terminal extension coloured blue, yellow and red respectively and key residues shown in stick form. The carbons of the bound Trp ligand are shown in orange, coordinated waters are shown as red spheres and the dashed grey lines represent hydrogen bonding interactions. B. Alignment of A. with non-liganded crystal structure (PDB code: 3NV8, 2.25 Å resolution, Cα RMSD 0.271 Å). Key residues of 3NV8 are shown as sticks in light blue and wheat (coloured by core and inserted helices respectively). C. Alignment of A. with the low concentration Trp soaked crystal structure (PDB code: 3NUE, 2.50 Å resolution, Cα RMSD 0.189 Å). Key residues of 3NUE are shown as sticks in hot pink and dark purple (coloured by core and inserted helices respectively), carbons of the Trp ligand are coloured dark green and hydrogen bonds are shown in red. D. Alignment of A. with the high concentration Phe soaked crystal structure (PDB code: 3NUD, 3.00 Å resolution, Cα RMSD 0.303 Å). Key residues of 3NUD are shown as sticks in grey and light green (coloured by core and inserted helices respectively), carbons of the bound Tyr ligand are coloured red and hydrogen bonds are shown in red.

One crystal structure of *Mtu*DAH7PS was found to have Phe bound at all the allosteric binding sites including the Trp site when the crystal was soaked at very high concentrations of Phe (>2mM) (PDB code: 3NUD). Alignment of this Phe-bound tetrameric *Mtu*DAH7PS structure with the Trp- and Phe-

bound *Mtu*DAH7PS structure (PDB code: 3KGF) (Cα RMSD 0.303 Å) revealed some minor changes in the interactions between *Mtu*DAH7PS and the bound ligand (Figure 6.1C). The phenyl group of the Phe ligand was buried in the hydrophobic pocket causing similar repositioning of the hydrophobic residues that form the pocket as observed for Trp binding. The most notable differences between Trp and Phe binding at the Trp site were changes to the polar contacts they formed with *Mtu*DAH7PS. As Phe lacks an indole ring it cannot hydrogen bond to the main chain carbonyl moiety of Ala192. The Phe-bound structure shows Lys123 is positioned so as to only form one hydrogen bond to the carboxyl group of the bound Phe ligand, compared to the two hydrogen bonds Lys123 forms to the carboxyl group of the bound Trp ligand. The amide nitrogen of Gln239 can position to form a hydrogen bond with the carboxyl group of the bound Phe ligand and was not observed for Trp binding. Asn237 is able to form two polar contacts between its amide group and the α-amino group of the bound Phe ligand. Asn237 forms only a single polar contact to the bound Trp ligand. It should be noted the side chain positions of Asn237 and Gln239 are less certain in the Phe-bound crystal coordinates (PDB code: 3NUD) with two possible rotamers existing for each.

6.1.2. Chapter aims

The work in this chapter was designed to probe key interactions between *Mtu*DAH7PS and the bound Trp ligand at the Trp site. Site directed mutagenesis was used to produce *Mtu*DAH7PS variants that lacked key interactions between specific residues (Lys123 and Asn237) and the bound Trp ligand. Generating *Mtu*DAH7PS variants that did not completely disrupt the quaternary structure and were soluble proved to be very challenging. Investigation of these two variants aimed to reveal whether Lys123 or Asn237 were critical for Trp binding or the communication of Trp binding to other allosteric binding sites (site 1 and site 2) and the active site.

6.2. Preparation of variants

6.2.1. Selection of residues for mutagenesis

Inspection of the Trp site highlighted several residues that form contacts with the bound Trp ligand, which made those residues good candidates for targeted mutagenesis (Figure 6.1A). Preventing or altering these interactions could disrupt or prevent Trp binding to the Trp site.

Residues identified for investigation were Leu194, Thr240, Lys123 and Asn237. The side chain of Leu194 reorganises upon Trp binding to help create a hydrophobic binding pocket for the indole ring. Removal of the branched side chain by substitution to Ala, or replacement of the side chain with a longer side chain with a polar or charged group (Asn or Asp) could prevent formation of the hydrophobic pocket for the indole group and discourage Trp binding. Unfortunately no change attempted to Leu194 resulted in a sufficient yield of protein for investigation. The amino group of Lys123 forms a hydrogen bond to the carbonyl group of the bound Trp ligand. Initially the substitution of Lys123 for Ala was prepared to remove the side chain of Lys123, but this protein was insoluble. The substitution of Lys123 to Met proved to be a successful alternative that replaced the positively charged amino side chain of Lys123 with a hydrophobic side chain of similar length. Substitution of Thr240 or Asn237 for Ala may prevent either residue hydrogen bonding to the α-amino group of the bound Trp ligand via their hydroxyl and amide group respectively, which would disrupt Trp binding. Attempts to generate *Mtu*DAH7PS^{T240A} were unsuccessful. *Mtu*DAH7PS^{N237A} and *Mtu*DAH7PS^{K123M} were successfully purified with reasonable yields for a thorough investigation and are discussed within this chapter.

6.2.2. Mutagenesis, expression and purification

SDM was carried out using a QiuikChange® Lightning Site-Directed Mutagenesis Kit and the QuikChange® Primer Design tool was used to design the primers required for each mutation. The recommended protocol was followed and is detailed in Section 9.2. Prior to electroporation into Bl21(DE3) PGroESL cells the DNA sequences of the SDM products were checked to ensure the desired

substitution was present and no anomalies had occurred. Following selection of colonies in the presence of ampicillin ad chloramphenicol cells were grown and purified in accordance with standard procedure for *Mtu*DAH7PS^{WT}, detailed in Section 9.5.

6.2.3. Confirmation of product

The successfully purified protein for both *Mtu*DAH7PS variants were run on SDS-PAGE gels to verify their purity and confirm their molecular weight. The gels of both *Mtu*DAH7PS^{N237A} and *Mtu*DAH7PS^{K123M} produced a single band of ~50 kDa mass, consistent with the expected molecular weight of monomeric *Mtu*DAH7PS (Figure 6.2).

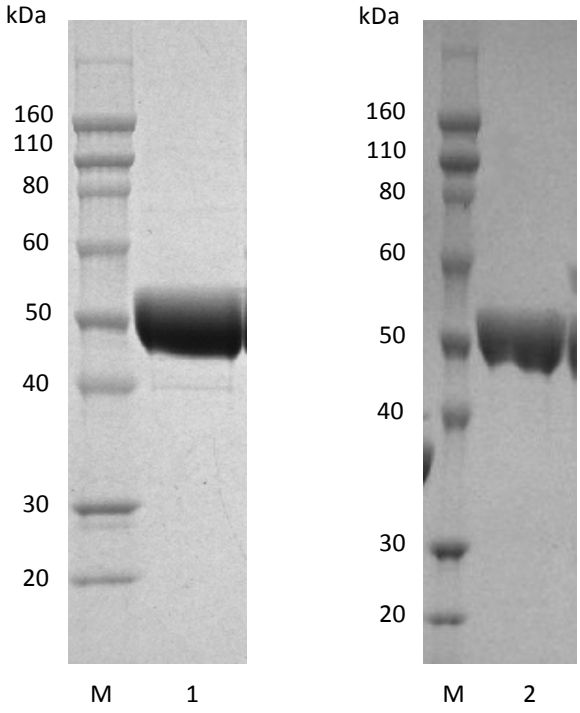

Figure 6.2 SDS-PAGE gel showing size and purity of each purified *Mtu*DAH7PS variant. Lane M molecular weight marker; Lane 1 *Mtu*DAH7PS^{N237A} and Lane 2 *Mtu*DAH7PS^{K123M}.

6.2.4. Comparison of secondary structure

CD was carried out to assess the secondary structure of the *Mtu*DAH7PS variants (experimental details are described in section 9.7.4). The CD spectra of both *Mtu*DAH7PS^{N237A} and *Mtu*DAH7PS^{K123M} are similar to the wild type enzyme (Figure 6.3).

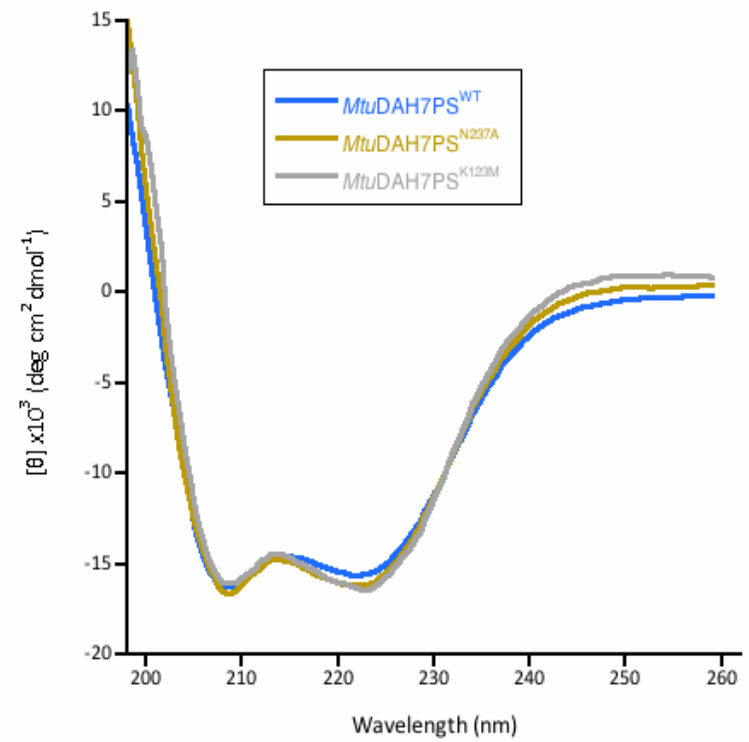

Figure 6.3 CD spectra for *Mtu*DAH7PS^{WT} (blue), *Mtu*DAH7PS^{N237A} (gold) and *Mtu*DAH7PS^{K123M} (silver).

6.3. Kinetic parameters

The introduction of the Asn237Ala or Lys123Met substitution to the Trp site has had a substantial impact on the kinetic parameters, particularly on substrate affinity (Table 6.1). Kinetic assays were carried out as detailed in Section 9.9.1. *Mtu*DAH7PS^{K123M} has an increased K_m for E4P, but the K_m value for PEP remained unchanged. This reduced affinity for E4P gives a decreased catalytic efficiency for E4P. The unchanged affinity for PEP coupled with an increase in the k_{cat} results in an improved catalytic efficiency for PEP.

The Asn237Ala substitution severely affected the enzyme kinetics of *Mtu*DAH7PS^{N237A}. The affinity for PEP was greatly reduced, as implied by the huge increase in the K_m value for PEP (Table 6.1). Intriguingly the decrease in substrate affinity has been accompanied by a significant boost in turnover number, overall resulting in a very low catalytic efficiency being determined with respect to PEP for *Mtu*DAH7PS^{N237A}.

Table 6.1 Kinetic parameters for *Mtu*DAH7PS^{N237A} and *Mtu*DAH7PS^{K123M} determined from a single set of data fitted to the Michaelis-Menten equation. ND Not determined as *Mtu*DAH7PS^{N237A} E4P data was fitted to the Hill equation. Michaelis-Menten plots are shown in Appendix I. Error represents error of curve fitting to the data set by least squares fit.

***Mtu*DAH7PS**	K_m^{E4P}	K_m^{PEP}	k_{cat}	**Catalytic Efficiency**	
				k_{cat}/K_m^{E4P}	k_{cat}/K_m^{PEP}
	(μM)	**(μM)**	**(s^{-1})**	**($s^{-1}mM^{-1}$)**	**($s^{-1}mM^{-1}$)**
Wild type	28 ± 2	37 ± 4	4.7 ± 0.1	170 ± 20	130 ± 20
N237A	ND	460 ± 50	10.0 ± 0.5	ND	22 ± 3
K123M	60 ± 4	37 ± 2	6.3 ± 0.1	105 ± 9	170 ± 10

Close inspection of the increase in *Mtu*DAH7PS^{N237A} activity with respect to E4P concentration reveals a sigmoidal curve. The data fits poorly to the Michaelis-Menten equation, but quite well to the Hill equation (Figure 6.4A and B). The $[E4P]_{0.5}$ was determined to be 116 μM from the Hill equation, which also suggests the affinity for E4P has been compromised. The Hill coefficient was found to be 1.7 ± 0.1 and means that positive cooperativity occurs when E4P binds to *Mtu*DAH7PS^{N237A}. The cooperative E4P binding observed for *Mtu*DAH7PS^{N237A} is reminiscent of the cooperative E4P binding exhibited by *Mtu*DAH7PS^{WT} in the presence of aromatic amino acid combinations including Trp.[48] The loss of the amide group of Asn237 may have resulted in an inhibited-like *Mtu*DAH7PS state, producing an enzyme with similar kinetic behaviour to the synergistically inhibited *Mtu*DAH7PS^{WT}.

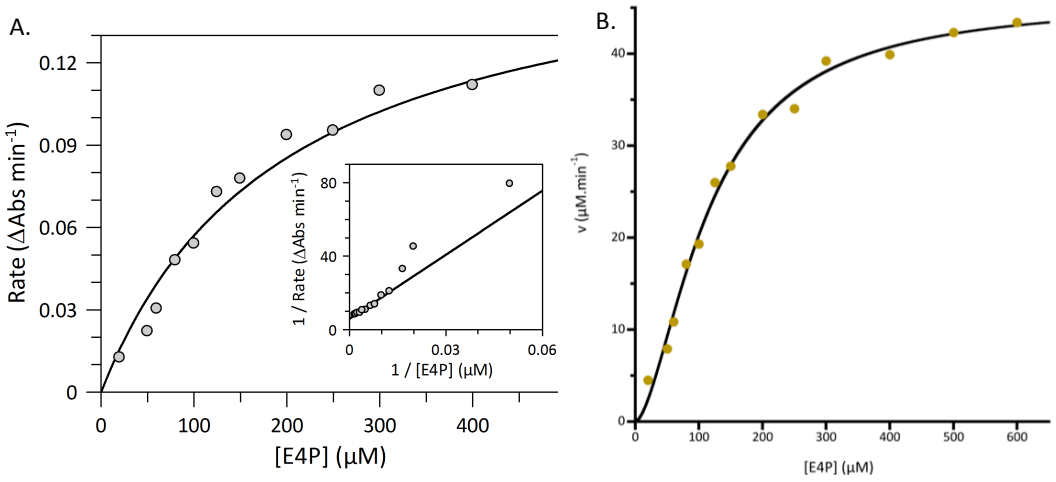

Figure 6.4 Kinetic data for *Mtu*DAH7PS^{N237A} with varying E4P concentration fitted to A. Michaelis-Menten equation with Lineweaver-Burke inset and B. the Hill equation. PEP concentration was held constant at 1 mM.

6.4. Feedback regulation

6.4.1. Disruption to feedback regulation

The inhibition studies were carried out under the standard conditions outlined in Section 9.9.3. For all assays, across all variants, the substrate concentrations were kept at 150 μM and the enzyme concentration between 0.01-0.02 mg/mL. Due to the low catalytic efficiency of *Mtu*DAH7PS^{N237A} the rates determined for the enzyme were very low which inherently resulted in greater error in their measurement. *Mtu*DAH7PS^{N237A} showed remarkable sensitivity to the presence of the aromatic amino acids (Figure 6.5). The addition of either Phe or Tyr alone caused a substantial loss (~78 % and ~61 % respectively) in *Mtu*DAH7PS^{N237A} activity. Addition of Trp did not inhibit *Mtu*DAH7PS^{N237A} activity. Nonetheless, the combination of Trp and Phe acted synergistically, further reducing *Mtu*DAH7PS^{N237A} activity to ~3 %. These results indicate that it is highly likely Trp can bind to *Mtu*DAH7PS^{N237A} and this binding can be communicated to site 1 (the Phe-selective site) and the active site. Trp does not display a synergistic effect on *Mtu*DAH7PS^{N237A} activity in combination with Tyr. The lack of synergy for Trp and Tyr suggests Asn237 may be important for the signal transmission of Trp binding to the Tyr-selective binding site, site 2.

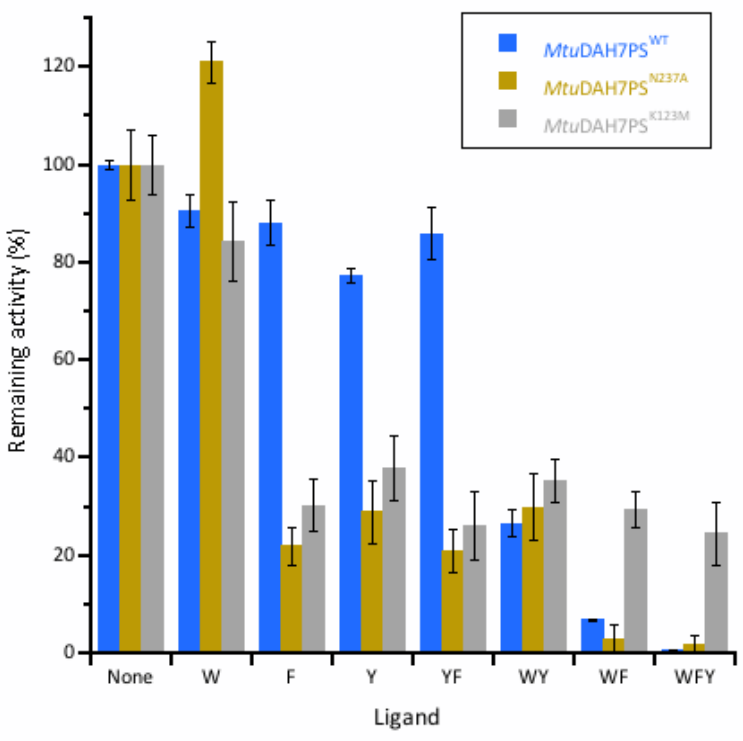

Figure 6.5 Remaining activity of *Mtu*DAH7PS^{WT} (blue), *Mtu*DAH7PS^{N237A} (gold) and *Mtu*DAH7PS^{K123M} (silver) in the presence of various single, binary and ternary combinations of aromatic amino acids. The aromatic amino acids are represented by their one letter code; Trp, W; Phe, F and Tyr, Y. Each letter also represents 200 µM of the corresponding aromatic amino acid. Error bars depict the standard deviation of triplicate measurements. P-values provided in appendix V.

Similar increases in sensitivity to Phe and Tyr alone were also observed for *Mtu*DAH7PS^{K123M}, with activity reduced to respectively 30 % and 38 % respectively (Figure 6.5). The presence of Trp has a negligible effect on *Mtu*DAH7PS^{K123M} activity. Trp in combination with Phe or Tyr causes little change in activity compared to *Mtu*DAH7PS^{K123M} activity in the presence of Phe or Tyr alone. The loss of synergy could indicate the amine group of Lys123 is essential for any synergistic mechanism to be employed by *Mtu*DAH7PS. Alternatively it may simply imply Trp does not bind very well to *Mtu*DAH7PS^{K123M}. Thus further investigation of Trp binding to *Mtu*DAH7PS^{K123M} is required.

The loss of the functional groups of Asn237 or Lys123 may have mimicked the signal that Trp has bound at the Trp site to the other allosteric bindings sites (sites 1 and 2) and the active site. This 'pseudo-Trp bound' *Mtu*DAH7PS state could explain the potent inhibition observed for *Mtu*DAH7PS^{N237A} and *Mtu*DAH7PS^{K123M} in the presence of Phe or Tyr alone. At the very least the loss

of amide of Asn237 and the amine of Lys123 has severely disrupted the synergistic inhibition mechanism that normally operates within *Mtu*DAH7PS.

6.4.2. Effect of ligand on kinetic parameters

To further ascertain the effect the inhibitors have on each variant enzyme, their E4P-dependent kinetic parameters were determined under the standard conditions detailed in Section 9.9.1, but with the addition of 200 μM of the stated ligand to the assay conditions.

For *Mtu*DAH7PS^{K123M} the kinetic parameters were determined in the presence of Phe and were fitted to Michaelis-Menten kinetics. If *Mtu*DAH7PS^{K123M} did adopt a 'pseudo-Trp bound' *Mtu*DAH7PS state then the E4P-dependent kinetics of *Mtu*DAH7PS^{K123M} in the presence of Phe should show a sigmoidal curve, evidence of cooperativity. A sigmoidal curve was observed for E4P-dependent kinetics of the wild type enzyme in the presence of Trp with either Phe or Tyr.[48,91] The E4P-dependent kinetics of *Mtu*DAH7PS^{K123M} obeyed Michaelis-Menten kinetics in the presence or absence of Phe, providing no evidence of cooperative E4P binding.

The lack of cooperative E4P binding displayed by *Mtu*DAH7PS^{K123M} suggests if a 'pseudo-Trp bound' *Mtu*DAH7PS state has been adopted by *Mtu*DAH7PS^{K123M} the substitution of Lys123 was insufficient to trigger all the changes that occur on Trp binding to the active site. To discern whether the lack of cooperative E4P binding displayed by *Mtu*DAH7PS^{K123M} is due to the cooperative mechanism being disabled by the Lys123Met substitution, the kinetic analysis needs to be repeated in the presence of both Trp and Phe. If no cooperativity is observed for *Mtu*DAH7PS^{K123M} in the presence of Trp and Phe it would suggest that the amino group of Lys123 is essential for Trp binding to be signalled to the active site and stimulate cooperative E4P binding.

The K_m for E4P increased when *Mtu*DAH7PS^{K123M} was in the presence of Phe (Table 6.2). Phe had little effect on the k_{cat} of *Mtu*DAH7PS^{K123M}. Thus Phe alone can act as a K-type inhibitor, achieving inhibition primarily by reducing the affinity of the *Mtu*DAH7PS^{K123M} for E4P. The combination of Trp with either

Phe or Tyr also acted to reduce the affinity of *Mtu*DAH7PS^{WT} for E4P. Unlike *Mtu*DAH7PS^{K123M}, the activity of the wild type enzyme displayed a sigmoidal response to increasing concentrations of E4P in the presence of Trp with either Phe or Tyr.

Table 6.2 The kinetic parameters determined for the E4P-dependent kinetics of *Mtu*DAH7PS^{N237A} and *Mtu*DAH7PS^{K123M}. Data for *Mtu*DAH7PS^{N237A} was fitted to the Hill equation and the data for *Mtu*DAH7PS^{K123M-} was fitted to the Michaelis-Menten equation. – indicates not applicable. Michaelis-Menten plots are shown in Appendix I. A single data set was collected to the appropriate kinetic equation. Error represents error of curve fitting to the data set by least squares fit.

***Mtu*DAH7PS**	K_m^{E4P} (μM)	$[E4P]_{0.5}$ (μM)	**Hill Coefficient**	k_{cat} (s^{-1})	**Catalytic Efficiency** k_{cat}/K_m^{E4P} ($s^{-1}mM^{-1}$)
Wild type	28 ± 2	–	–	4.7 ± 0.1	170 ± 20
N237A*	–	116 ± 7	1.6 ± 0.1	5.9 ± 0.2	–
N237A 200W*	–	104 ± 6	1.6 ± 0.1	7.7 ± 0.3	–
K123M	60 ± 4	–	–	6.3 ± 0.1	105 ± 9
K123M 200F	320 ± 50	–	–	7.7 ± 0.8	24 ± 6

The kinetic parameters of *Mtu*DAH7PS^{N237A} were determined in the presence of 200 μM of Trp to ascertain if the addition of Trp somehow restored more wild type-like kinetic behaviour to *Mtu*DAH7PS^{N237A}. The kinetic data for *Mtu*DAH7PS^{N237A} determined with the addition of Trp was inconsistent with Michaelis-Menten kinetics, and was better fitted to the Hill equation (Figure 6.6). The presence of Trp caused minor changes in $[E4P]_{0.5}$ and k_{cat}, resulting in a slight increase in E4P catalytic efficiency. A Hill coefficient of 1.6 was determined for *Mtu*DAH7PS^{N237A} in both the presence and absence of Trp. The lack of significant variation in kinetic parameters determined for *Mtu*DAH7PS^{N237A} makes it difficult to draw any conclusions with regards of the means by which the activation of *Mtu*DAH7PS^{N237A} occurs in the presence of Trp. The use of a higher concentration of Trp in the kinetic assays may reveal more information.

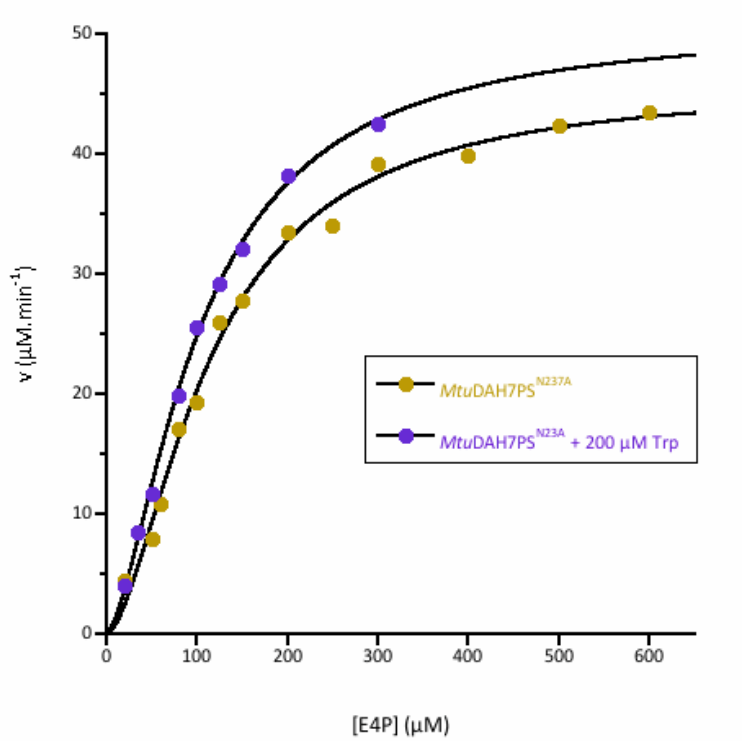

Figure 6.6 E4P-dependent kinetic data for *Mtu*DAH7PS^{N237A} with varying E4P concentration fitted to the Hill equation with (gold) and with out 200 μM Phe (purple). PEP concentration was held constant at 1 mM.

6.5. Thermal stability

The thermal stability was determined by DSF and was carried out as detailed in section 9.8.1. The thermal stability of *Mtu*DAH7PS^{N237A} in the absence of ligand is similar to wild type (Figure 6.7). Trp increased the T_m of *Mtu*DAH7PS^{N237A} by ~0.8 ˚C, much less than the marked change of ~9.2 ˚C seen for *Mtu*DAH7PS^{WT}. The small increase in T_m suggests Trp binds poorly to *Mtu*DAH7PS^{N237A}. The addition of Phe or Tyr to *Mtu*DAH7PS^{N237A} caused a large shift in the T_m, ~4 ˚C and ~5 ˚C respectively, confirming Phe and Tyr are still able to bind the variant protein. All combinations of allosteric amino acids with the exception of Phe and Tyr produce smaller shifts in T_m when compared to *Mtu*DAH7PS^{WT}.

*Mtu*DAH7PS^{K123M} has a lower thermal stability than the wild type enzyme (Figure 6.7). *Mtu*DAH7PS^{K123M} also showed no change in T_m in the presence of Trp suggesting the ligand may not be able to bind. Alternatively if the Trp can bind *Mtu*DAH7PS^{K123M} it is unable to elicit the same response from the enzyme, failing to increase the thermal stability of the enzyme. The T_m in the

presence of Tyr dropped by 1 ˚C. The presence of Phe improved the thermal stability, increasing the T_m by ~3.5 ˚C. Interestingly, combinations including Tyr and Phe resulted in increases in T_m greater than 3.5 ˚C. Thus when Phe binds to site 1 it mitigates any loss in stability caused by Tyr binding at site 2, resulting in an overall greater increase in thermal stability. The addition of Trp with Phe or Tyr showed no extra increase in thermal stability of *Mtu*DAH7PS^{K123M}.

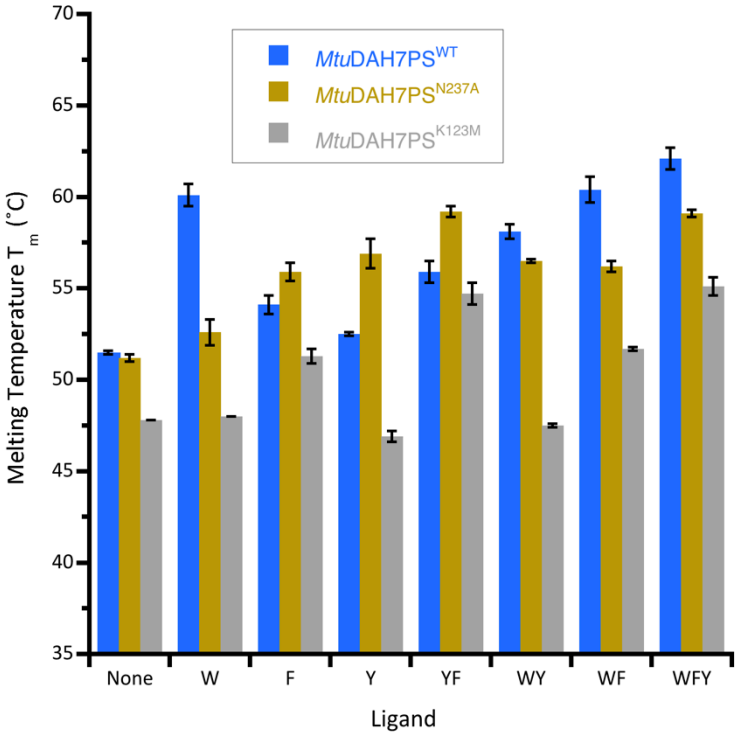

Figure 6.7 Thermal melting points determined by DSF for *Mtu*DAH7PS^{WT} (blue), *Mtu*DAH7PS^{N237A} (gold) and *Mtu*DAH7PS^{K123M} (silver). Error bars depict the standard deviation of triplicate measurements. P-values provided in appendix V.

6.6. Binding affinities

To quantify the ability of Trp to bind *Mtu*DAH7PS ITC was carried out as detailed in Section 9.8.2. Due to constraints on time and enzyme stocks, ITC was only carried out on *Mtu*DAH7PS^{N237A}. The amide functionality of Asn237 forms a hydrogen bond to the bound Trp ligand and the substitution of Asn237 for Ala was expected to prevent this bond and disrupt Trp binding. In a fascinating twist, the Asn237Ala substitution improved the affinity of *Mtu*DAH7PS for Trp. The K_d between *Mtu*DAH7PS^{N237A} and Trp was lower than that with *Mtu*DAH7PS^{WT} (Table 6.3, Figure 6.8A). The affinity of *Mtu*DAH7PS^{N237A} for Phe and Tyr has also improved compared to the wild type enzyme as illustrated

by the decrease in the K_d values determined between *Mtu*DAH7PS^{N237A} and either Phe or Tyr compared to *Mtu*DAH7PS^{WT} (Figure 6.8B-C, Table 6.3).

Crystallography has previously shown the allosteric binding sites of *Mtu*DAH7PS can be promiscuous, albeit Trp has never been observed to occupy allosteric binding site other than the Trp site.[48,63,91] Given the Asn237Ala was intended to disrupt Trp binding and the promiscuity of the allosteric binding sites there was a small possibility Trp may be able to bind sites 1 or 2 further ITC experiments were conducted to assess this possibility. Thus to investigate which allosteric binding sites Trp was binding ITC experiments were setup to identify if Trp competed with Phe to occupy site 1. *Mtu*DAH7PS^{N237A} was pre-incubated with 50 µM Phe or 20 µM Tyr in the cell prior to measuring the binding of the alternative titrated ligand (Figure 6.8D-E). Pre-incubation of *Mtu*DAH7PS^{N237A} with Phe caused a small change in the K_d determined between Trp and *Mtu*DAH7PS^{N237A} and similarly preincubation of *Mtu*DAH7PS^{N237A} with Trp caused a small change in the K_d determined between Phe and *Mtu*DAH7PS^{N237A} (Table 6.3). Neither change was great enough to confidently confirm whether competition was occurring and therefore gave no reason to believe Trp is binding to site 1. Moreover, these studies also showed Phe and Trp could not improve the binding of the other amino acid to *Mtu*DAH7PS^{N237A}, indicating cooperativity between the two sites has been disrupted.

Table 6.3 Dissociation constants determined for *Mtu*DAH7PS^{WT} and *Mtu*DAH7PS^{N237A} by ITC. A background concentrations of Phe, Trp and Tyr were 50, 20 ad 400 µM respectively. — Denotes no background ligand present. * Denotes values determined by Richard Hutton.[71,91] Values are determined from a single ITC experiment. Error represents error of curve fitting to the data set by least squares fit.

Titrated ligand	Background ligand	*Mtu*DAH7PS	
		Wild type K_d (µM)	N237A K_d (µM)
Trp	—	4.7 ± 0.1*	2.9 ± 0.2
Trp	Phe	1.08 ± 0.03*	3.6 ± 0.2
Phe	—	21 ± 1*	10 ± 2
Phe	Trp	5 ± 1*	9 ± 1
Tyr	—	39 ± 1	21.2 ± 0.7
Tyr	Trp	40 ± 2	18.1 ± 0.6

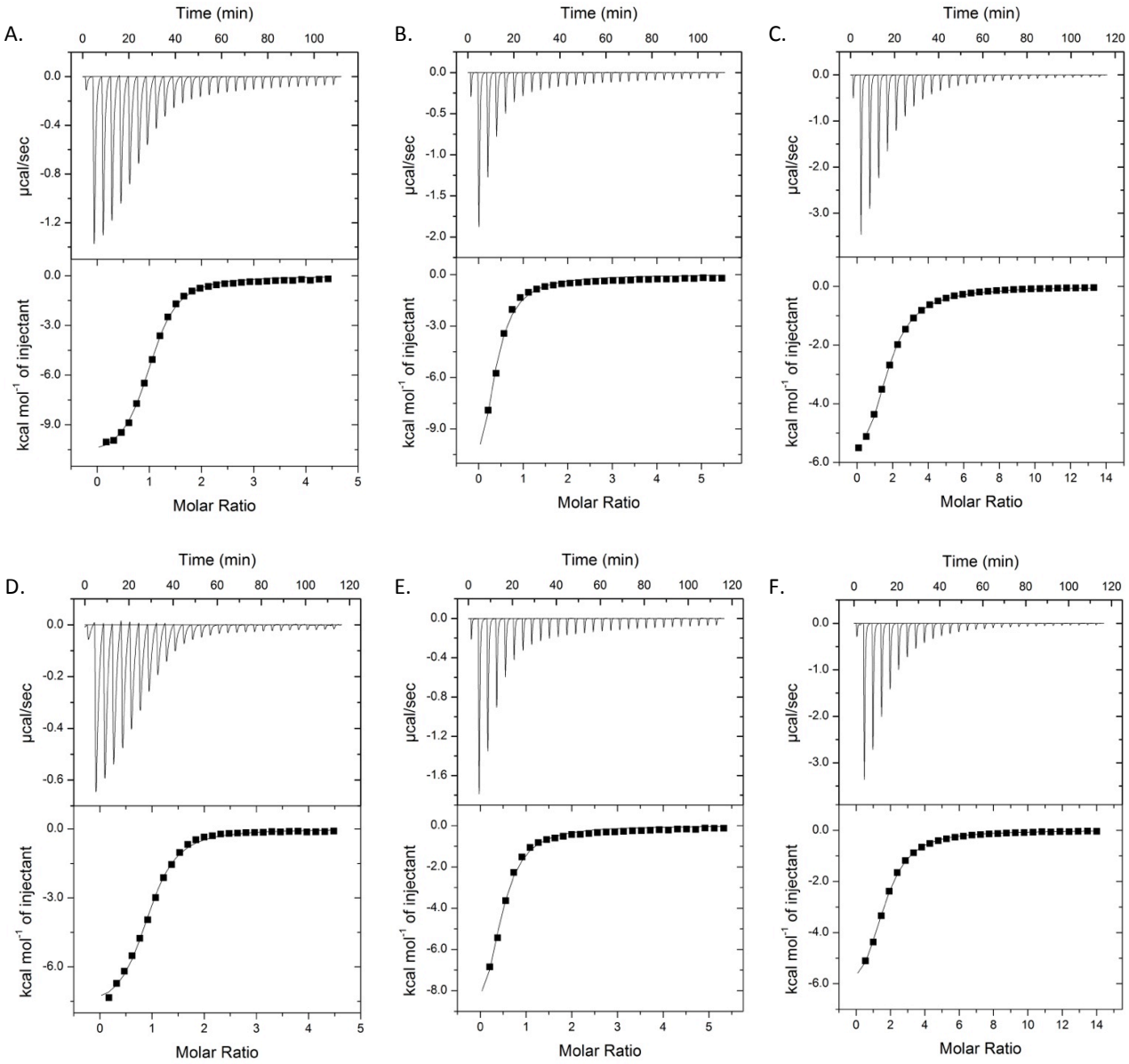

Figure 6.8 ITC data for the interaction of *Mtu*DAH7PS^{N237A} ITC data for the interaction of A. 38 µM *Mtu*DAH7PS^{N237A} with 800 µM Trp titrant; B. 41 µM of *Mtu*DAH7PS^{N237A} with 1 mM Phe titrant, C. 40µM *Mtu*DAH7PS^{N237A} with 2.5 mM Tyr titrant; D. 38 µM *Mtu*DAH7PS^{N237A} preincubated with 50 µM Phe and with 800 µM Trp titrant; E. 41 µM *Mtu*DAH7PS^{N237A} preincubated with 20 µM Trp and with 1 mM Phe titrant and F. 40 µM *Mtu*DAH7PS^{N237A} preincubated with 20 µM Trp with 2.5 mM Tyr titrant.

The K_d for Tyr binding to *Mtu*DAH7PS^{N237A} decreased to 18.1 µM by the preincubation of *Mtu*DAH7PS^{N237A} with Trp, suggesting Trp and Tyr are not competing for the same allosteric binding sites (Figure 6.8F, Table 6.3). The lack of competition between Trp and Tyr to bind *Mtu*DAH7PS^{N237A} means Trp is not binding to site 2, the Tyr-selective site.

As there is no evidence Trp competes with Tyr or Phe to bind *Mtu*DAH7PS^{N237A} it is highly likely Trp is able to bind to the Trp site of *Mtu*DAH7PS^{N237A}. This retention of Trp binding implies the hydrogen bonds formed between the amide of Asn237 and the α-amino group of the bound Trp ligand are not essential for Trp binding. The disruption to the cooperative binding between Trp and Phe suggests the substitution of Asn237 to Ala has disrupted the communication pathway between the Trp site and site 1. The loss of the polar contacts formed between the bound Trp ligand and Asn237 at the Trp site would allow the α2-β3 loop more flexibility and/or to adopt a different position, and it is likely that this change in flexibility or position of the α2-β3 loop that has disrupted the synergistic mechanism between the Trp site and site 1.

6.7. Quaternary Structure

6.7.1. SAXS analysis

The quaternary structure of both Trp site variants were analysed by SAXS and were found to differ considerably from *Mtu*DAH7PS^{WT} (Figure 6.9A-B). The experimental conditions and analysis is detailed in Sections 9.7.5 and 9.7.6. The SAXS profile of *Mtu*DAH7PS^{N237A} closely resembled the theoretical scattering profile for the tetrameric *Mtu*DAH7PS^{WT} predicted by CRYSOL using the crystal coordinates PDB code: 3NV8, except between 0.07 and 0.11 s (Figure 6.9A, Table 6.4).[69,70,103] This divergence of the scattering profile of *Mtu*DAH7PS^{N237A} from the theoretical scattering of *Mtu*DAH7PS^{WT} is an indication the shape of the protein has changed. The similarity of the D_{max} and the R_g determined for *Mtu*DAH7PS^{N237A} and *Mtu*DAH7PS^{WT} suggest a very subtle change in the average conformation of *Mtu*DAH7PS^{N237A} has occurred. The Asn237Ala substitution altered the quaternary structure of *Mtu*DAH7PS^{N237A} most probably by altering the flexibility of the α2-β3 loop where Asn237 is located.

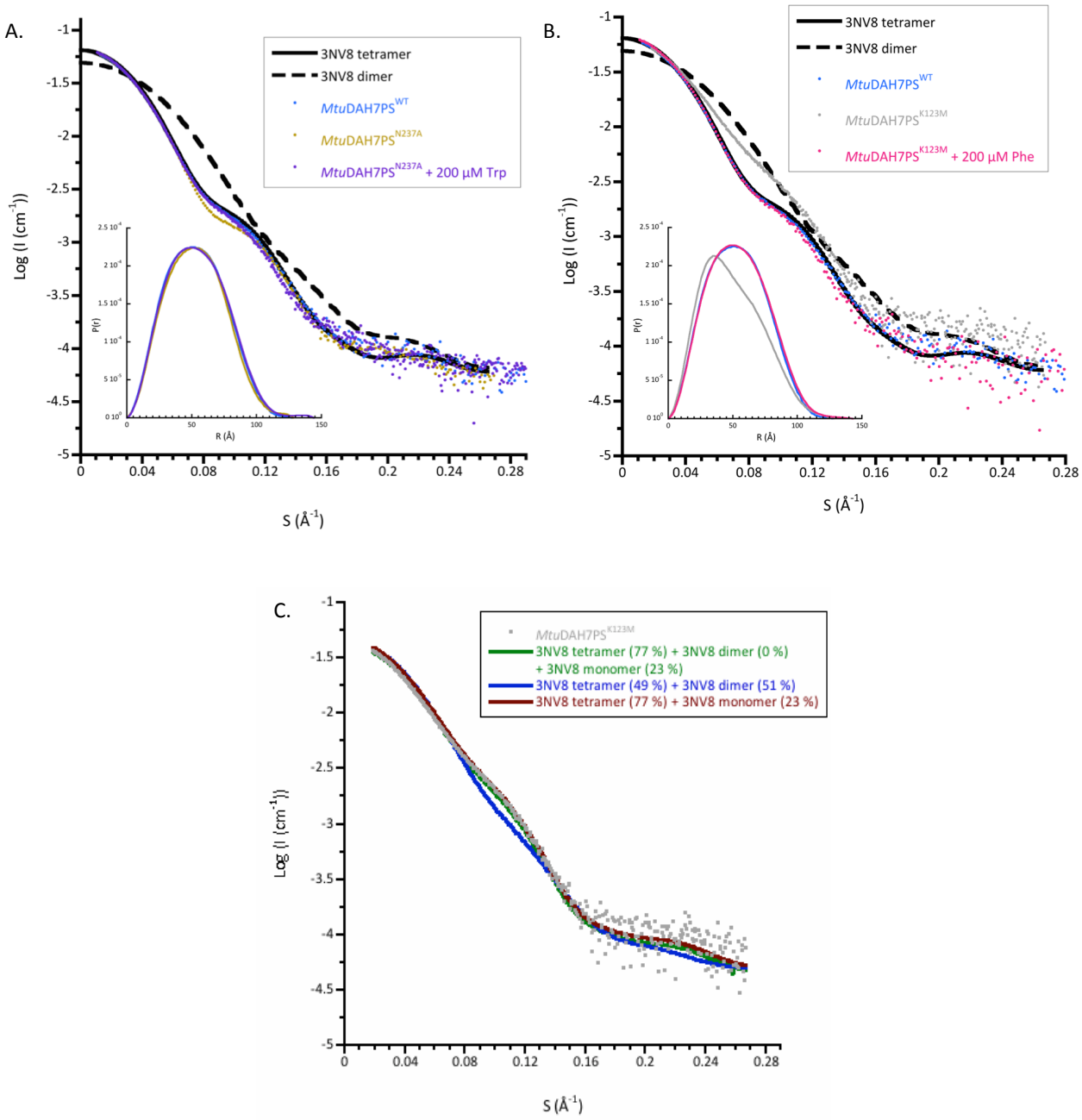

Figure 6.9 SAXS scattering profiles of *Mtu*DAH7PS^{WT} (blue dots) and A. *Mtu*DAH7PS^{N237A} with (purple dots) and with out 200 µM Trp (gold dots) and B. *Mtu*DAH7PS^{K123M} with (pink dots) and without (silver dots) 200 µM Phe. Also shown are the theoretical scattering profiles for the *Mtu*DAH7PS^{WT} tetramer (solid black line) and dimer (dashed black line) (PDB code: 3NV8) predicted by CRYSOL.[103] C. The SAXS scattering profile of *Mtu*DAH7PS^{K123M} (silver dots), and the theoretical scattering profiles *Mtu*DAH7PS consisting of a mixture of 77 % dimer and 23 % monomer (green line), a mixture of 49 % tetramer and 51 % dimer (blue line) and 77 % tetramer and 23 % monomer (burgundy line), as predicted by OLIGOMER.[101]

Table 6.4 SAXS parameters determined from PRIMUS, GNOM, CRYSOL and SAXS MoW for *Mtu*DAH7PS^{WT}, *Mtu*DAH7PS^{N237A} with and without 200 µM Trp, and *Mtu*DAH7PS^{K123M} with and without 200 µM Phe. Analysis was conducted with data from a single SAXS experiment.

***Mtu*DAH7PS**	**Wild type**	**N237A**	**N237A 200W**	**K123M**	**K123M 200F**
Guinier analysis					
R_g (Å)	41.6 ± 0.3	42.81 ± 0.05	42.0 ± 0.1	38.1 ± 0.4	41.7 ± 0.1
I (0) (cm^{-1})	0.168 ± 0.001	0.200 ± 0.001	0.178 ± 0.001	0.044 ± 0.001	0.095 ± 0.001
Pair distribution analysis					
Real Space R_g (Å)	40.9 ± 0.2	42.1 ± 0.2	41.5 ± 0.07	38.7 ± 0.1	41.6 ± 0.1
D_{max} (Å)	127	128	130	125.5	127
V_p, (Da)	282700	350000	289800	199300	338700
Molecular weight estimates from SAXS MoW analysis					
M_w from V_p (Da)	199 100	210700	200900	133900	209400
Nō of Subunits	4	4	4	3	4
CRYSOL analysis with tetrameric 3NV8					
R_{gE} (Å)	42.4 ± 0.2	41.6 ± 0.2	41.9 ± 0.2	37.2 ± 0.2	41.8 ± 0.2
R_{gT} (Å)	40.6	41.5	41.4	31.9	41.3
χ^2	0.996	8.605	1.879	3.83	0.519
CRYSOL analysis with dimeric 3NV8					
R_{gE} (Å)	41.7 ± 0.2	ND	ND	37.2 ± 0.2	41.7 ± 0.2
R_{gT} (Å)	30.7	ND	ND	31.9	31.9
χ^2	13.3	ND	ND	3.83	11.58
CRYSOL analysis with monomeric 3NV8					
R_{gE} (Å)	40.9 ± 0.2	ND	ND	36.0 ± 0.2	41.5 ± 0.2
R_{gT} (Å)	25.0	ND	ND	25.01	25.06
χ^2	22.0	ND	ND	8.89	21.32

Attempts were made to fit the SAXS scattering profile of *Mtu*DAH7PS^{N237A} to mixtures of monomer, dimer and tetramer ensembles of the *Mtu*DAH7PS^{WT} 3NV8 crystal coordinates using OLIGOMER.[101] OLIGOMER did not indicate a mixture of oligomeric species was present in solution, instead indicating the solution most likely consisted of 100% tetramer. Thus the change in the SAXS scattering profile of *Mtu*DAH7PS^{N237A} was most likely due to a subtle change in conformation of the tetramer.

The addition of 200 µM Trp to *Mtu*DAH7PS^{N237A} changed the SAXS scattering profile to better correlate with the theoretical scattering of the *Mtu*DAH7PS^{WT} tetramer (PDB code: 3NV8), as demonstrated by the decrease in the χ^2 value (Figure 6.9A, Table 6.4). Hence Trp binding caused the conformation of tetrameric *Mtu*DAH7PS^{N237A} to become more like *Mtu*DAH7PS^{WT}, possibly by restricting the flexibility or position of the α2-β3 loop. As the binding of Trp alters the conformation of the *Mtu*DAH7Ps^{N237A} tetramer it is evidence the change in tetrameric conformation due to the Asn237Ala substitution is reversible. The change in the tetramer conformation of *Mtu*DAH7PS^{N237A} due to the presence of Trp binding illustrates the interactions of the *Mtu*DAH7PS subunits are flexible and will tolerate changes in conformation, without disrupting the formation of the homotetrameric *Mtu*DAH7PS complex.

The SAXS scattering profile of *Mtu*DAH7PS^{K123M} varied extensively from the predicted dimeric and tetrameric theoretical scattering profiles for the *Mtu*DAH7PS^{WT} crystal coordinates 3NV8 predicted by CRYSOL (Figure 6.9B, Table 6.4).[103] Instead, OLIGOMER was used to assess if a combination of oligomeric states were present in solution (Figure 6.9C).[101] Theoretical scattering for various combinations of monomeric, dimeric and tetrameric *Mtu*DAH7PS^{WT} were generated from the *Mtu*DAH7PS^{WT} crystal coordinates of 3NV8 and compared to the experimental SAXS scattering profile of *Mtu*DAH7PS^{K123M}. Evaluation of the OLIGOMER results suggested *Mtu*DAH7PS^{K123M} fitted best, based on χ^2 values, to models of a solution containing 23 % *Mtu*DAH7PS monomer and 77 % *Mtu*DAH7PS tetramer (Table 6.5). The R_g determined from the Guinier plot or R_g, D_{max} and the V_p)determined from the pair wise distribution were both lower than values determined for *Mtu*DAH7PS^{WT}, and inconsistent with the presence of only tetrameric *Mtu*DAH7PS in solution (Table 6.4).

Table 6.5 SAXS parameters determined for *Mtu*DAH7PS^{K123M} by OLIGOMER calculated for; analysis 1 a mixture of *Mtu*DAH7PS tetramer and dimer; analysis 2 a mixture of *Mtu*DAH7PS tetramer and monomer and analysis 3 for a mixture of *Mtu*DAH7PS tetramer, dimer and monomer. Analysis was conducted with data from a single SAXS experiment.

	Analysis 1	**Analysis 2**	**Analysis 3**
Tetramer (%)	48.5 ± 0.8	76.6 ± 0.4	76.6 ± 0.4
Dimer (%)	51.5 ± 0.7	n/a	0.0 ± 0.0
Monomer (%)	n/a	23.4 ± 0.3	23.4 ± 0.3
M_w (Da)	132700	124900	124900
R_g (Å)	36.02	36.99	36.99
χ^2	2.45	0.76	0.76

The addition of Phe to *Mtu*DAH7PS^{K123M} gave a SAXS scattering profile that closely followed the SAXS scattering profile of *Mtu*DAH7PS^{WT} (Figure 6.9B). CRYSOL confirmed SAXS scattering profile of *Mtu*DAH7PS^{K123M} fitted very closely to the predicted theoretical scattering profile of *Mtu*DAH7PS^{WT} (PDB code: 3NV8) as indicated by χ^2 of ~0.5 (Table 6.4). The R_g, D_{max} and V_p determined for *Mtu*DAH7PS^{K123M} in the presence of Phe all increased, and became more consistent with values expected for tetrameric *Mtu*DAH7PS.

The OLIGOMER results imply *Mtu*DAH7PS^{K123M} exists as an ensemble of oligomeric states in equilibrium. The addition of Phe to *Mtu*DAH7PS^{K123M} showed the quaternary structure equilibrium of *Mtu*DAH7PS^{K123M} was dynamic, shifting to almost completely favour the formation of the *Mtu*DAH7PS^{K123M} tetramer in the presence of Phe. The substitution of Lys123 for Met has most probably altered the interactions of tight dimer interface, weakening the interactions that encourage the formation of the tight dimer and consequently displacing the quaternary structure equilibrium.

6.7.2. Native PAGE

Blue native PAGE was used to assess the oligomeric species present in a low concentration solution of *Mtu*DAH7PS and was carried out as detailed in Section 9.7.2. *Mtu*DAH7PS^{N237A} produces a single band a little over ~200 kDa in mass, the expected molecular weight of the *Mtu*DAH7PS tetramer (Figure 6.10). The presence of tetrameric *Mtu*DAH7PS^{N237A} was in agreement with the findings from the analysis of SAXS data for *Mtu*DAH7PS^{N237A} conducted at high concentrations of the enzyme (~8.8 mg/mL). The presence of a single ~200 kDa for *Mtu*DAH7PS^{N237A} contrasted with *Mtu*DAH7PS^{WT} which exhibited two bands at ~50 and ~100 kDa, representing monomeric and dimeric *Mtu*DAH7PS respectively. Therefore, the Asn237Ala substitution introduced to *Mtu*DAH7PS^{N237A} stabilises the formation of the tetramer even at very low concentrations.

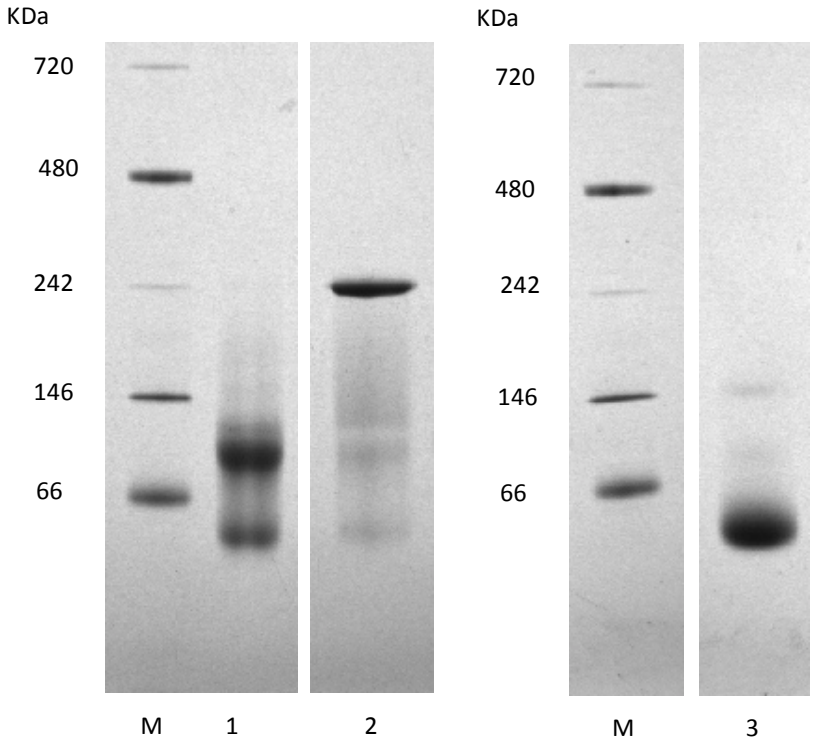

Figure 6.10 Blue native PAGE. Lane M displays the molecular weight marker; Lane 1 *Mtu*DAH7PS^{WT}; Lane 2 *Mtu*DAH7PS^{N237A} and Lane 3 *Mtu*DAH7PS^{K123M}

Conversely, *Mtu*DAH7PS^{K123M} exhibits a strong band of ~50 kDa mass, the correct mass for an *Mtu*DAH7PS monomer, and there was also evidence of a fainter higher molecular band at ~100 kDa, evidence some dimeric *Mtu*DAH7PS^{K123M} was also present at low concentrations of *Mtu*DAH7PS^{K123M}. The quaternary structures identified for a solution of low concentration of *Mtu*DAH7PS^{K123M} by native PAGE differed from the mixture of monomeric and tetrameric *Mtu*DAH7PS^{K123M} identified by SAXS of at a high concentration of *Mtu*DAH7PS^{K123M}. Thus the quaternary structure equilibrium of *Mtu*DAH7PS^{K123M} was dynamic and showed concentration dependence; at lower concentrations the *Mtu*DAH7PS^{K123M} monomer is favoured and at high concentrations the formation of the *Mtu*DAH7PS^{K123M} tetramer is favoured.

6.7.3. AUC analysis

AUC experiments were carried out on *Mtu*DAH7PS^{K123M} as described for *Mtu*DAH7PS^{WT} in Section 9.7.7. Ali Nazmi performed the AUC experiments and assisted with the data analysis. Sedimentation velocity experiments were carried out at three concentrations of *Mtu*DAH7PS^{K123M} (0.3, 0.6 and 1.0 mg/mL) and confirmed the quaternary structure equilibrium of *Mtu*DAH7PS^{K123M} was concentration dependent. In order to determine the *s* and molecular mass of *Mtu*DAH7PS^{K123M} the AUC data for *Mtu*DAH7PS^{K123M} was fitted to a continuous size *c*(*s*) distribution model. At 0.3 and 0.6 mg/mL there is a single distribution peak for *Mtu*DAH7PS^{K123M} at ~3.5 S, which gave a predicted molecular mass of 74 kDa, the expected molecular mass of an *Mtu*DAH7PS monomer is ~50 kDa (Figure 6.11). As the concentration of *Mtu*DAH7PS^{K123M} increased the tail of the distribution peak became more noticeable. At a concentration of 1.0 mg/mL *Mtu*DAH7PS^{K123M} two further peaks become more defined at ~5.7 S and 8.3 S, which corresponded to molecular masses of ~120 kDa and ~220 kDa respectively. As the concentration of *Mtu*DAH7PS^{K123M} in solution was increased from 0.3 to 1.0 mg/mL the amount of dimeric and tetrameric *Mtu*DAH7PS^{K123M} in solution also increased, but the monomeric species remained the dominant oligomeric species in solution at all three concentrations analysed. A concentration of 1 mg/mL was not enough to drive the equilibrium towards favouring the *Mtu*DAH7PS^{K123M} tetramer.

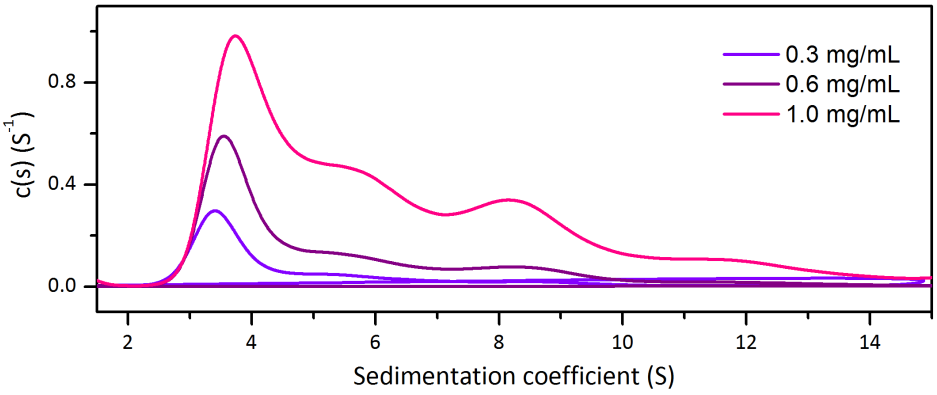

Figure 6.11 Continuous size *c*(*s*) distribution plots from sedimentation velocity experiments of *Mtu*DAH7PS^{K123M} analysed at 0.3 (violet), 0.6 (purple) and 1.0 (pink) mg/mL. AUC data and fits shown in Appendix II.

6.8. Activation of *Mtu*CM

Kinetic assays monitoring *Mtu*CM activity in the presence of the *Mtu*DAH7PS variants were carried out to determine if changes in the average quaternary structure of the variants compromised their interaction with *Mtu*CM. Assays were conducted under the conditions stated in Section 9.9.1. The ability of both variants to activate *Mtu*CM has been severely compromised compared to the *Mtu*DAH7PS^{WT} (Figure 6.12). *Mtu*DAH7PS^{N237A} achieved a 34-fold maximum enhancement of *Mtu*CM activity, and *Mtu*DAH7PS^{K123M} activated *Mtu*CM activity by 19-fold.

The change in conformation of the *Mtu*DAH7PS^{N237A} tetramer must disrupt the interface to which *Mtu*CM binds. This change at the *Mtu*CM binding face of *Mtu*DAH7PS^{N237A} either weakened the interaction between *Mtu*DAH7PS^{N237A} and *Mtu*CM or did not allow the optimal interactions to occur with the *Mtu*CM C-terminal tail that were required for the *Mtu*CM activation, resulting in the reduced ability of *Mtu*DAH7PS^{N237A} to boost *Mtu*CM activity. The poor activation of *Mtu*CM activity by *Mtu*DAH7PS^{N237A} offers evidence that a change or twist in the tetramer conformation is enough to weaken or alter the interaction between *Mtu*CM and *Mtu*DAH7PS, in turn altering the ability of *Mtu*DAH7PS to activate *Mtu*CM activity.

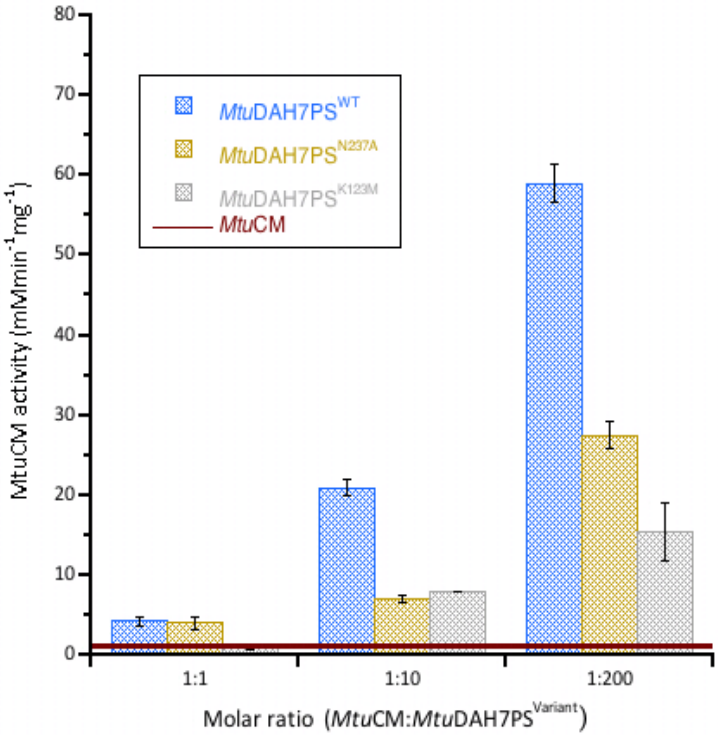

Figure 6.12 Activation of *Mtu*CM activity in the presence of either equimolar, ten-fold or 200-fold molar excess of *Mtu*DAH7PS^{WT} (blue hash), *Mtu*DAH7PS^{N237A} (gold hash) and *Mtu*DAH7PS^{K123M} (silver hash). The burgundy line indicates the activity of *Mtu*CM alone. Assays conducted with 150 µM chorismic acid and 60 nM *Mtu*CM except for reactions requiring a 200-fold excess of *Mtu*DAH7PS where 10 nM of *Mtu*CM and *Mtu*CM alone where 90 nM were used and the results normalised. Error bars depict the standard deviation of duplicate measurements.

The Lys123Met substitution has disrupted the quaternary structure equilibrium of *Mtu*DAH7PS^{K123M} to favour the monomer. The dramatically reduced ability of *Mtu*DAH7PS^{K123M} most likely reflects the much lower affinity of *Mtu*CM for the *Mtu*DAH7PS monomer compared to the *Mtu*DAH7PS tetramer. At a 200-fold molar excess of *Mtu*DAH7PS^{K123M} the quaternary structure equilibrium would shift slightly toward the formation of the *Mtu*DAH7PS^{K123M} tetramer, which is better able to activate *Mtu*CM activity.

6.9. Regulation of *Mtu*CM

Both *Mtu*DAH7PS variants were able to regulate *Mtu*CM activity, despite their changes in quaternary structure/conformation. Assays to determine *Mtu*CM activity of a mixture of *Mtu*CM and a ten-fold molar excess of variant *Mtu*DAH7PS in the presence of various aromatic amino acids were carried out

as outlined in Section 9.9.3. It should be noted the *Mtu*CM activity being measured was very low due to the poor ability of both *Mtu*DAH7PS variants to boost *Mtu*CM activity, and inherently there are greater errors associated with these measurements. The addition of Trp to a mixture of *Mtu*CM and *Mtu*DAH7PS^{N237A} dramatically boosted the activity of *Mtu*CM by ~96 % (Figure 6.13). SAXS showed the *Mtu*DAH7PS^{N237A} tetramer became more like the *Mtu*DAH7PS^{WT} tetramer when Trp was added. This change in conformation most likely strengthened or improved the interactions between *Mtu*DAH7PS^{N237A} and *Mtu*CM facilitating better activation of *Mtu*CM activity. The regulation of *Mtu*CM activity in the presence of *Mtu*DAH7PS^{N237A} showed greater sensitivity to Phe or Tyr than for a mixture of *Mtu*CM and *Mtu*DAH7PS^{WT}. The improved inhibition of *Mtu*CM activity by Phe and Tyr may be in part due to the ability of *Mtu*DAH7PS^{N237A} to bind both Phe and Tyr more tightly as shown by ITC.

Due to the very small rates measured for the inhibited *Mtu*CM activity and the large errors associated with these measurements it was difficult to determine if *Mtu*DAH7PS^{N237A} was able to synergistically inhibit *Mtu*CM activity in the presence of combinations of aromatic amino acids. The exception was the addition of Trp in combination with Tyr, which appeared to synergistically inhibit *Mtu*CM activity in the presence of *Mtu*DAH7PS^{N237A}. The synergistic inhibition of *Mtu*CM activity by Trp and Tyr in the presence of *Mtu*DAH7PS^{N237A} suggests Asn237 is not important for communicating allosteric inhibitor binding to the *Mtu*CM•*Mtu*DAH7PS interface.

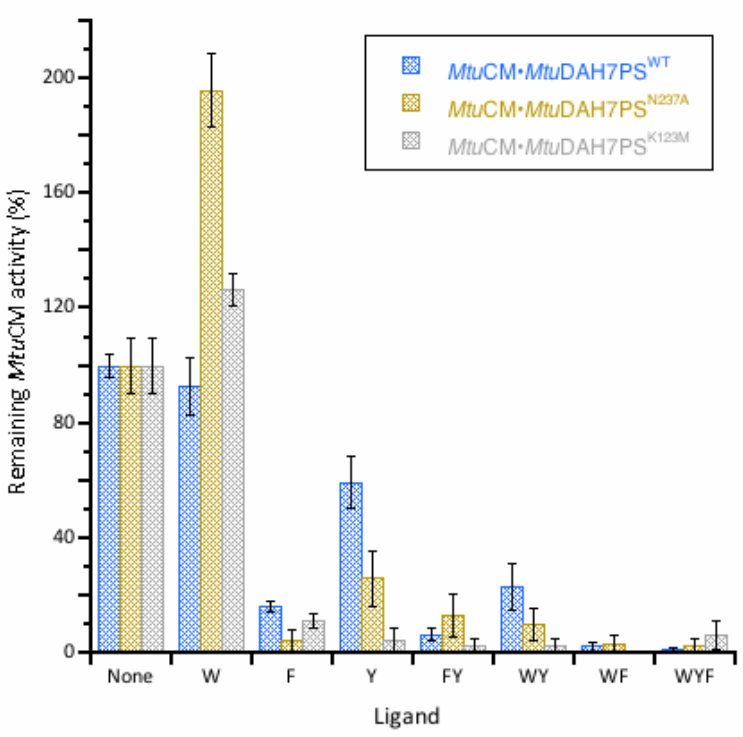

Figure 6.13 Remaining *Mtu*CM activity in the presence of various single, binary and ternary combinations of aromatic amino acids and a ten-fold excess of *Mtu*DAH7PS^{WT} (blue hash), *Mtu*DAH7PS^{N237A} (gold hash) and *Mtu*DAH7PS^{K123M} (silver hash). The aromatic amino acids are represented by their one letter code; Trp, W; Phe, F and Tyr, Y. Each letter also represents 200 µM of the corresponding aromatic amino acids. Assays conducted in the presence of 150 µM chorismic acid and 60 nM *Mtu*CM. Error bars depict the standard deviation of at least duplicate measurements. P-values provided in appendix V.

The addition of Trp to a mixture of *Mtu*CM and *Mtu*DAH7PS^{K123M} also boosts *Mtu*CM activity by ~22 % (Figure 6.13). The improved activation of *Mtu*CM activity in the presence of *Mtu*DAH7PS^{N237A} by Trp was most likely due to Trp binding shifting the quaternary structure equilibrium toward the tetramer, which in turn has a higher affinity for *Mtu*CM and results in greater enhancement of *Mtu*CM activity. The improved activation of *Mtu*CM activity in the presence of *Mtu*DAH7PS^{N237A} by Trp was also significant as this was the first evidence to indicate Trp can still bind to *Mtu*DAH7PS^{K123M}. The very low rates and their large associated errors made it difficult to identify whether synergistic inhibition was occurring. Ideally, the inhibition assays need to be repeated using a higher concentration of chorismic acid in order to increase the absolute rates of the inhibited *Mtu*CM activity. Faster rates may allow differences between the single and multiple aromatics acids combinations to be identified, and allow insight into whether synergistic inhibition of *Mtu*CM activity is occurring in the presence of these two *Mtu*DAH7PS variants. As the allosteric binding sites of *Mtu*DAH7PS are located near the dimer and tetramer interface it is highly likely the *Mtu*DAH7PS is the tetramer species is regulated species and

also the species, which regulates *Mtu*CM activity. Hence the *Mtu*DAH7PS^{K123M} tetramer is probably responsible for both the activation and any inhibition of *Mtu*CM activity.

6.10. Effect of *Mtu*CM on the E4P kinetics of *Mtu*DAH7PS^{K123M}

Evaluation of the quaternary structure of *Mtu*DAH7PS^{K123M} has shown that at low concentrations a mixture of oligomer species is present, predominately monomer. The crystal structure of the *Mtu*CM•*Mtu*DAH7PS^{WT} complex shows the dimeric *Mtu*CM binds to *Mtu*DAH7PS across the weak dimer interface.[85] The kinetics of *Mtu*DAH7PS^{K123M} were analysed in the presence of a ten-fold molar excess of *Mtu*CM as outlined in Section 9.9.1. The data was fitted to Michaelis-Menten kinetics to determine the kinetics parameters.

The addition of *Mtu*CM caused the E4P catalytic efficiency of *Mtu*DAH7PS^{K123M} to half, whereas *Mtu*DAH7PS^{WT} exhibits no catalytic penalty for being associated to *Mtu*CM (Table 6.6). It is possible *Mtu*CM encourages the association of the tetramer *Mtu*DAH7PS^{K123M} to occur, either by enabling favourable contact between subunits or by simply bringing them into close proximity. If a tetramer has been formed, it could be the tetrameric form of *Mtu*DAH7PS^{K123M} rather than the interaction with *Mtu*CM itself that is responsible for the loss in catalytic ability. The loss in E4P catalytic efficiency of *Mtu*DAH7PS^{K123M} would infer the *Mtu*DAH7PS^{K123M} tetramer was a poorer catalyst than the *Mtu*DAH7PS^{K123M} monomer.

Table 6.6 E4P-dependent kinetic parameters for *Mtu*DAH7PS^{K123M} with and without a ten-fold molar excess of *Mtu*CM. Michaelis-Menten plots are shown in Appendix I. Values were determined from a single set of kinetic data. Errors represent the error of curve fitting to the data set by least squares fit.

***Mtu*DAH7PS**	K_m^{E4P} (μM)	k_{cat} (s^{-1})	Catalytic efficiency k_{cat}/K_m^{E4P} ($s^{-1}mM^{-1}$)
K123M	60 ± 4	6.3 ± 0.1	105 ± 9
K123M-CM	67 ± 4	3.5 ± 0.1	52 ± 5

6.11. Chapter summary

Two Trp site *Mtu*DAH7PS variants, *Mtu*DAH7PS^{N237A} and *Mtu*DAH7PS^{K123M}, were prepared and purified successfully. CD showed the secondary structures of both variant enzymes were similar to *Mtu*DAH7PS^{WT}. SAXS revealed the substitution of Asn237 for Met altered the tetrameric conformation of *Mtu*DAH7PS^{N237A}. Native PAGE showed *Mtu*DAH7PS^{N237A} was tetrameric even at low concentrations, suggesting the loss of the amide of Asn237 has stabilised the *Mtu*DAH7PS^{N237A} tetramer. On the other hand, AUC, native PAGE and SAXS showed *Mtu*DAH7PS^{K123M} existed in solution as a mixture of monomer, dimer and tetramer. As expected, this equilibrium showed concentrations dependence; AUC showed at low concentrations the equilibrium favours the monomeric species, and at high concentrations the equilibrium shifted to favour the tetramer. Substitution of residues at or near the Trp site appears to correlate strongly with changes in quaternary structure.

Both *Mtu*DAH7PS^{N237A} and *Mtu*DAH7PS^{K123M} were catalytically active. The catalytic efficiency with respect to PEP of *Mtu*DAH7PS^{N237A} was severely compromised, but this catalytic efficiency of *Mtu*DAH7PS^{K123M} showed some improvement. The E4P concentration required for effective catalysis increased for both *Mtu*DAH7PS variants. Intriguingly, the kinetic data for the E4P-dependent kinetics of *Mtu*DAH7PS^{N237A} displayed cooperativity, behaviour that had only previously been observed for *Mtu*DAH7PS^{WT} in the presence of Trp and Phe.[48] Molecular modelling studies found the occupation of the allosteric binding sites of *Mtu*DAH7PS correlated with the increased flexibility of the E4P binding loop (β2-α2 loop).[71] The mechanism of *Mtu*DAH7PS inhibition proposed was that the binding of Trp and Phe to the allosteric binding sites entropically disfavoured E4P binding at the active site.[71] The change in E4P-dependent kinetics of both *Mtu*DAH7PS^{N237A} and *Mtu*DAH7PS^{K123M} is evidence the Trp site is intrinsically linked to the active site. The change in the substrate catalytic efficiencies of *Mtu*DAH7PS^{K123M} could also in part be due to the disruption of the quaternary structure. The monomer may have different catalytic properties to the tetramer. To investigate the kinetic properties of monomeric *Mtu*DAH7PS, a variant would need to be produced that disrupted the tight dimer interface sufficiently that the variant could not form higher oligomeric states.

Inhibition studies showed both *Mtu*DAH7PS^{N237A} and *Mtu*DAH7PS^{K123M} were activated by Trp. SAXS showed Phe binding drives the *Mtu*DAH7PS^{K123M} quaternary structure equilibrium towards the tetramer. It is in all likelihood Trp binding also shifts the quaternary structure equilibrium of *Mtu*DAH7PS^{K123M} toward the tetramer. If the tetramer is more catalytically active than the monomer it could explain the improvement of *Mtu*DAH7PS^{K123M} activity in the presence of Trp. SAXS also showed the conformation of the *Mtu*DAH7PS^{N237A} tetramer became more like the *Mtu*DAH7PS^{WT} tetramer in the presence of Trp, yet the E4P-dependent kinetic parameters did not reveal any significant changes. The change in *Mtu*DAH7PS^{N237A} tetramer conformation may instead improve *Mtu*DAH7PS^{N237A} activity by improving PEP catalytic efficiency. Investigation of the PEP-dependent kinetic parameters in the presence of Trp is required to determine if Trp improves PEP catalytic efficiency of *Mtu*DAH7PS^{N237A}.

The ITC of *Mtu*DAH7PS^{N237A} revealed the affinity for all three aromatic amino acids had improved compared to *Mtu*DAH7PS^{WT}. ITC did not reveal any evidence to suggest Trp was competing with Phe or Tyr to occupy sites 1 or 2, so it is highly probably Trp binds to the Trp site of *Mtu*DAH7PS^{N237A}. The loss of Asn237 was not detrimental to Trp binding to *Mtu*DAH7PS^{N237A} therefore the polar contacts between the amide of Asn237 and the α-amino group of the bound Trp ligand are not essential for the tight binding of Trp at the Trp site. ITC also showed no evidence that the presence of Trp or Phe could improve the binding of the other ligand to *Mtu*DAH7PS^{N237A}. The lack of cooperative binding between the allosteric binding sites of *Mtu*DAH7PS^{N237A} suggests the contacts formed between Asn237 and the bound Trp ligand are responsible for triggering the correct signal transmission of Trp binding to the active site and the other allosteric binding sites.

DSF and the inhibition studies with and without *Mtu*CM confirmed all three aromatic amino acids could bind to both *Mtu*DAH7PS^{N237A} and *Mtu*DAH7PS^{K123M}. The binding of Trp to *Mtu*DAH7PS^{K123M} may have been significantly weakened by substitution of Lys123 as Trp caused very little change to the thermal stability of *Mtu*DAH7PS^{K123M} and there is no synergistic regulation of *Mtu*DAH7PS^{K123M} activity. ITC of *Mtu*DAH7PS^{K123M} with a Trp titrant could identify if *Mtu*DAH7PS^{K123M} has a reduced affinity for Trp. The activity of both variant enzymes showed sensitivity to both Phe and Tyr, but did

not show strong evidence of synergistic regulation in the presence of multiple aromatic amino acids. The loss of synergistic inhibition and change in sensitivity to Phe and Tyr showed Asn237 and Lys123 are intimately involved in the signal transmission networks between the Trp site and the other allosteric binding sites and the active site. The substitution of these two residues may have falsely signalled Trp has bound to the Trp site at least partially to the other allosteric binding sites and the active site.

Both *Mtu*DAH7PS^{K123M} and *Mtu*DAH7PS^{N237A} were poor activators of *Mtu*CM activity. The *Mtu*CM activity in the presence of *Mtu*DAH7PS^{N237A} and *Mtu*DAH7PS^{K123M} also exhibited heightened sensitivity to Tyr and Phe. For *Mtu*DAH7PS^{K123M} the poor activation was most probably due to the predominance of the *Mtu*DAH7PS^{K123M} monomer in solution. Since *Mtu*CM binds across the weak dimer interface of *Mtu*DAH7PS, it is highly likely the affinity of *Mtu*CM for the *Mtu*DAH7PS monomer is very much less than the *Mtu*DAH7PS tetramer. Furthermore the monomer may not be able to form the proper contacts with the *Mtu*CM C-terminal tail, thus fail to properly activate *Mtu*CM activity. The poor activation of *Mtu*CM activity by *Mtu*DAH7PS^{N237A} is likely to be mostly due to the change in tetramer conformation, as demonstrated by the improvement of the ability of *Mtu*DAH7PS^{N237A} to activate *Mtu*CM activity in the presence of Trp. As stated previously, SAXS showed Trp binding changed the *Mtu*DAH7PS^{N237A} tetramer conformation to a conformation that was similar to the *Mtu*DAH7PS^{WT} tetramer. Therefore the change in conformation of *Mtu*DAH7PS^{N237A} must disrupt the interaction of *Mtu*DAH7PS^{N237A} with *Mtu*CM by either preventing the key interactions that facilitate the rearrangement of the *Mtu*CM active site residues or by weakening the polar and non-polar contacts required for *Mtu*CM binding to *Mtu*DAH7PS^{N237A}.

The proposed mechanism of inhibition of the *Mtu*CM•*Mtu*DAH7PS complex (Section 4.8) is that the binding of Phe causes a subtle change in the conformation of *Mtu*DAH7PS tetramer, such as a slight twist in the tetramer plane. This twist in turn disrupts the contacts at the *Mtu*CM•*Mtu*DAH7PS interface resulting in dissociation of the complex, preventing activation of *Mtu*CM activity. *Mtu*DAH7PS^{N237A} has illustrated the *Mtu*DAH7PS tetramer is flexible and can change conformation on ligand binding. Furthermore the tetramer conformation of *Mtu*DAH7PS affects the enzyme's ability to

activate *Mtu*CM. These are significant findings that give credence to the proposed mechanism of *Mtu*CM inhibition of the *Mtu*CM•*Mtu*DAH7PS complex.

In Section 2.6.2, it was shown that Trp and Phe shift the quaternary structure equilibrium of *Mtu*DAH7PS^{WT} toward the tetramer. The quaternary structure of *Mtu*DAH7PS^{N237A} was shown to be predominantly tetrameric and suggests this variant enzyme may mimic the conformation of *Mtu*DAH7PS in the presence of Trp and Phe, i.e. the inhibited state. The catalytic ability of *Mtu*DAH7PS^{N237A} was severely impaired as would be expected for an inhibited-like *Mtu*DAH7PS species. Cooperative E4P binding has previously only been described for *Mtu*DAH7PS^{WT} in the presence of Trp and Phe or Trp and Tyr.[48] Therefore the E4P binding loop of *Mtu*DAH7PS^{N237A} is most likely mimicking the changes in flexibility that occur on Trp and Phe binding to *Mtu*DAH7PS^{WT}. Like *Mtu*DAH7PS^{WT} bound with Trp and Phe or Trp and Tyr *Mtu*DAH7PS^{N237A} poorly activates *Mtu*CM activity. The dissociation constants, determined by ITC, between the aromatic amino acids and *Mtu*DAH7PS^{WT} decreased when *Mtu*DAH7PS^{WT} was preincubated with Trp (Section 2.5.2), the dissociation constants determined between the aromatic amino acids and *Mtu*DAH7PS^{N237A} were lower than for *Mtu*DAH7PS^{WT}. Phe and Tyr were only able to inhibit *Mtu*DAH7PS^{WT} when added in combination with Trp, whereas *Mtu*DAH7PS^{N237A} displayed sensitivity to the presence of Phe and Tyr alone. The improved binding of the aromatic amino acids to *Mtu*DAH7PS^{N237A} and sensitivity to Phe and Tyr are also consistent with *Mtu*DAH7PS^{N237A} adopting an inhibited-like *Mtu*DAH7PS species, which has at least partially signalled to sites 1 and 2 and the active site Trp binding has occurred.

Overall the substitutions of Asn237 and Lys123 caused remarkable changes to almost every measureable property of *Mtu*DAH7PS. The relatively small change of removing the amide side chain from Asn237 at the Trp site shifted the quaternary equilibrium, changed the tetramer conformation, decreased the enzymes catalysis, altered the regulatory sensitivity, the enzymes ability to bind the aromatic amino acids and interfered with the enzymes interaction with *Mtu*CM. Similarly switching the positively charged amino group of Lys123 to the hydrophobic thiol ether Met, shifted the quaternary structure equilibrium to favour the monomer, altering the enzyme's catalytic efficiency and regulatory sensitivity as well as impairing the ability of the enzyme to interact with and regulate

*Mtu*CM. The binding of Trp at the Trp site and the polar contacts Trp forms with Asn237 and Ly123 are an integral part of the signalling network that relays to the other allosteric binding sites and the active site. Any disruption to the residues of the Trp site involved in the signalling pathway alters almost every measurable characteristic of *Mtu*DAH7PS. The sensitivity of *Mtu*DAH7PS to substitution at the Trp site highlights the central role the Trp site plays in the allosteric regulation of *Mtu*DAH7PS.

7. The regulatory consequences of disrupting the quaternary structure of *Mtu*DAH7PS.

7.1. Introduction

The work described in chapter 2 demonstrated that *Mtu*DAH7PS^{WT} exists in solution as an ensemble of different oligomers in equilibrium (Section 2.6). This quaternary structure equilibrium moves in response to *Mtu*DAH7PS^{WT} concentration and the presence of ligand. Later work outlined in chapters 5 and 6 provided several examples which demonstrate that the substitution of a single residue could disrupt the quaternary structure equilibrium of the variant *Mtu*DAH7PS to favour a particular oligomeric state.

Based on SCA and MD simulations clusters of residues believed to be part of the communication pathways between the allosteric sites and the active site have been identified.[115] Work described in chapter 5 aimed to validate computational studies with experimental results. [115] The preparation of several variants, *Mtu*DAH7PS^{G232P,} *Mtu*DAH7PS$^{G190P/G232P}$ and *Mtu*DAH7PS^{T114V} (not covered in this thesis as the properties of *Mtu*DAH7PS^{T114V} were very similar to *Mtu*DAH7PS^{G232P} and *Mtu*DAH7PS$^{G190P/G232P}$) disrupted the quaternary structure of the variants so severely that these variant enzymes exist as dimers rather than tetramers in solution. The serendipitous formation of these dimers presented a unique opportunity to study the *Mtu*DAH7PS dimer; the findings of these studies are discussed within this chapter.

7.1.1. Subunit interfaces

Crystal coordinates of *Mtu*DAH7PS with and without ligand bound consistently identify two subunits in the asymmetric unit that interact to form a dimer. The interface of this dimer is formed principally by residues of the α2 helix from the core $(\beta/\alpha)_8$ barrel structure and the residues located on the N-

terminal extension, more specifically the α0b-α0c loop, β0 beta strand and the N-terminal tail (residues 1-3) (Figure 7.1A). The β0 strand of each subunit associates to form an inter-subunit antiparallel β-sheet. Evaluation of the dimer interface of unliganded *Mtu*DAH7PS (PDB code: 3NV8) by PDBsum[127] revealed the average buried surface area of each subunit to be 1875 Å^2. PDBsum also found a total of 170 hydrophobic contacts, 13 hydrogen bonds and 1 salt bridge between Asp10 and Arg171 (Appendix III).

The binding of Trp and Phe at the allosteric binding sites of *Mtu*DAH7PS subtly alters the interactions between the two subunits at the dimer interface (Figure 7.1B). PDBsum found 198 hydrophobic contacts and 18 hydrogen bonds were formed across the dimer interface of *Mtu*DAH7PS bound with Trp and Phe (PDB code: 3KGF), burying an average surface area of 1825 Å^2 for each subunit (Appendix III). The loss of the salt bridge between Asp10 and Arg171 is associated with the β0-α0a loop becoming disordered in the Trp and Phe bound *Mtu*DAH7PS structure.

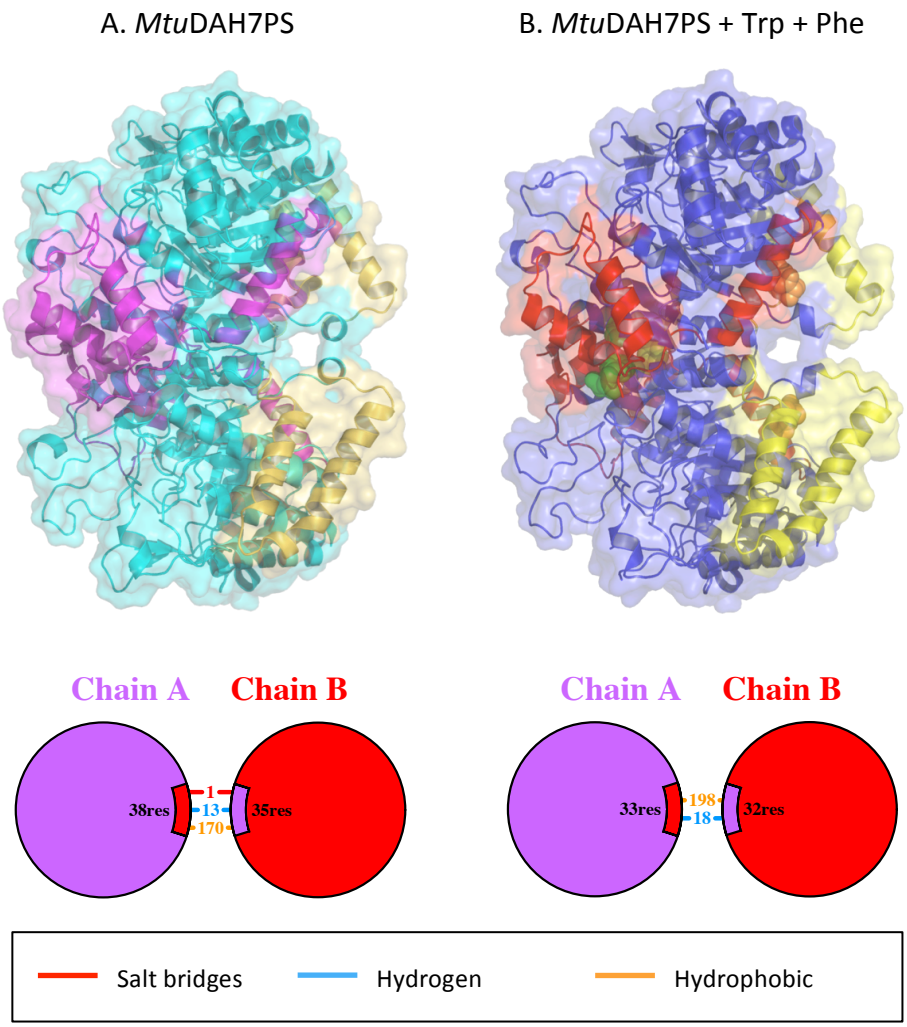

Figure 7.1 The dimer present in the crystallographic asymmetric unit, with schematic of the dimer interface interactions between the two subunits designated chain A and chain B below. A. unliganded *Mtu*DAH7PS (PDB code 3nv8) with the core $(\beta/\alpha)_8$ barrel coloured cyan, the N-terminal extension magenta and the inserted helices yellow orange, and B. Trp- and Phe-bound *Mtu*DAH7PS (PDB code: 3KGF). The core $(\beta/\alpha)_8$ barrel structure is coloured blue, the N-terminal extension is coloured red and the additional helices to the α2-β3 loop are coloured yellow.

When crystallographic symmetry is applied to the asymmetric unit, a homotetramer is generated. The interface between the two asymmetric dimers is denoted here as the tetramer interface. The residues of the inserted α2b helix, the α2-β3 loop and the α1 helix from the core $(\beta/\alpha)_8$ barrel are principally involved in forming the contacts across the tetramer interface (Figure 7.2A). The interface between two subunits across the tetramer interface was found to bury an average surface area for each subunit of 990 $Å^2$ in the unliganded *Mtu*DAH7PS crystal structure (PDB code: 3NV8) according to PDBsum. PDB sum identified 2 hydrogen bonds and 71 hydrophobic contacts between two subunits of the tetramer interface (Appendix III).

The crystal structure of Trp- and Phe-bound *Mtu*DAH7PS (PDB doe: 3KGF) revealed Trp and Phe binding to *Mtu*DAH7PS caused subtle changes at the tetramer interface of *Mtu*DAH7PS (Figure 7.2B). Evaluation of the Trp- and Phe-bound *Mtu*DAH7PS crystal structure by PDBsum revealed only a slight increase of the average buried surface of each subunit at the tetramer interface to 1055 $Å^2$. Additionally PDBsum identified 4 hydrogen bonds and 100 hydrophobic contacts between the two subunits of the tetramer interface (Appendix III). The increased number of contacts between the subunits at the tetramer interface when Trp and Phe have bound to *Mtu*DAH7PS would contribute to the stabilisation of the interface, and promote formation of the tetramer. This observation is consistent with experimental data from AUC that found Trp and Phe cause the quaternary structure equilibrium of *Mtu*DAH7PS^{WT} to shift toward the *Mtu*DAH7PS tetramer (Section 2.6.2).

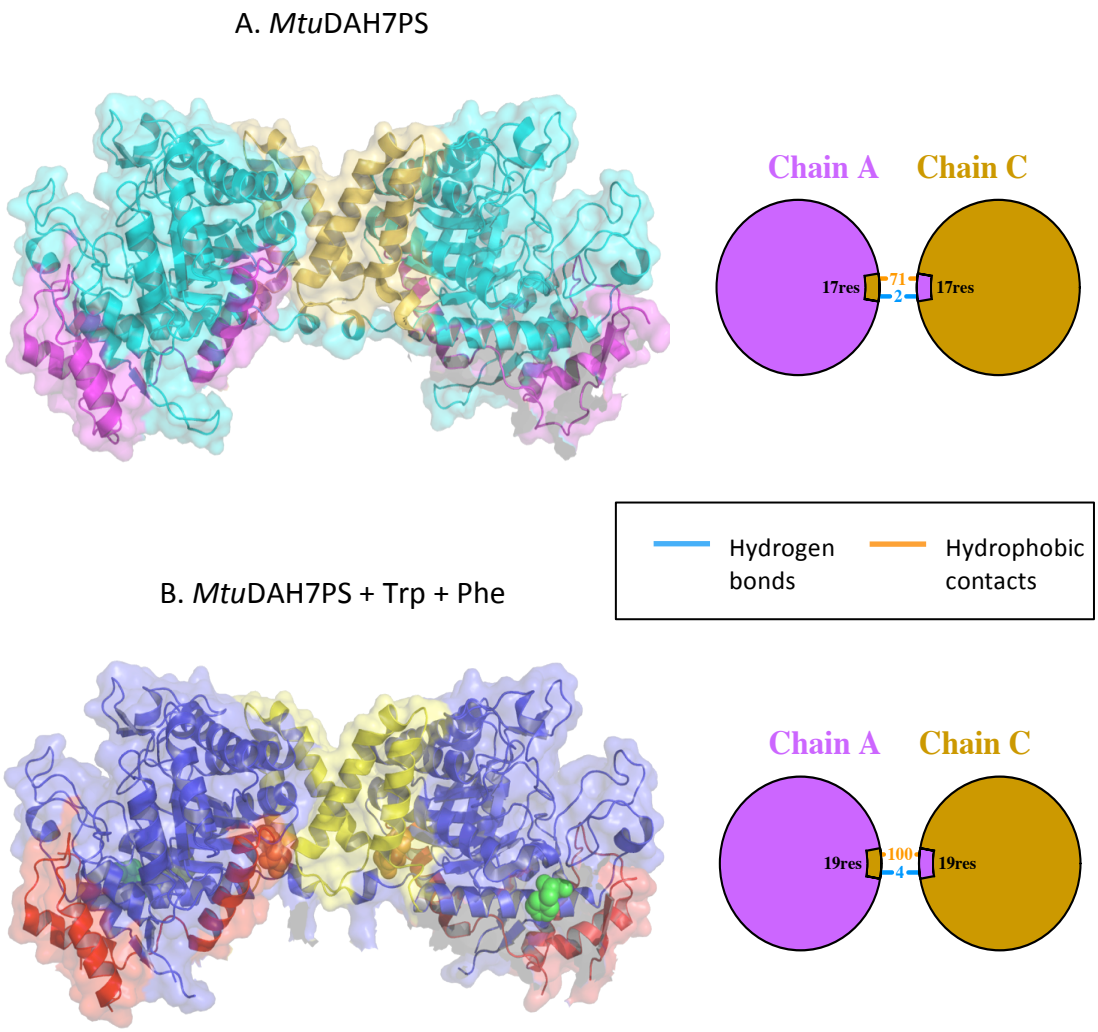

Figure 7.2 The tetramer interface formed by the interaction between chain A of the adjacent asymmetric dimers. For clarity chain A of the second dimer has been designated chain C, schematic to the right represents the interactions between chains A and C at the tetramer interface. A. unliganded *Mtu*DAH7PS (PDB code 3NV8) with the core $(\beta/\alpha)_8$ barrel coloured cyan, the N-terminal extension magenta and the inserted helices yellow orange, and B. Trp- and Phe-bound *Mtu*DAH7PS (PDB code: 3KGF). The core $(\beta/\alpha)_8$ barrel structure is coloured blue, the N-terminal extension is coloured red and the additional helices to the α2-β3 loop are coloured yellow.

7.1.2. Serendipitous dimeric *Mtu*DAH7PS variants

From the SCA and MD simulations it was proposed that restricting the flexibility of the inserted α2a and a2b helices may disrupt the regulation of *Mtu*DAH7PS by restricting fluctuations in flexibility being transmitted throughout the enzyme (previously discussed in Section 5.1). Two residues, Gly190 and Gly232, located on the loops preceding and succeeding the inserted α2a and α2b helices, were identified as potentially critical residues that control the flexibility of the α2a and α2b helices and their associated loops. Gly190, located along the α2-α2a loop, forms interactions with a water molecule and residue Ala192, whilst GlyG232 is located along the α2b-β3 loop and interacts with

residues Met228 and Ser229 of the α2a helix (Figure 7.3). The substitution of Gly190 and Gly232 for Pro enforces limitations on the backbone, reducing flexibility. The successful preparation and purification of *Mtu*DAH7PS^{G190P} showed the substitution of Gly190 for eliminated the effective synergistic regulation of *Mtu*DAH7PS activity (Section 5.4.2). Preparation and purification of *Mtu*DAH7PS^{G232P} and *Mtu*DAH7PS$^{G190P/G232P}$ were also successful, but it was immediately obvious from the size exclusion chromatography that these enzymes were not tetrameric, as they eluted ~20 mL later than typically seen for *Mtu*DAH7PS.

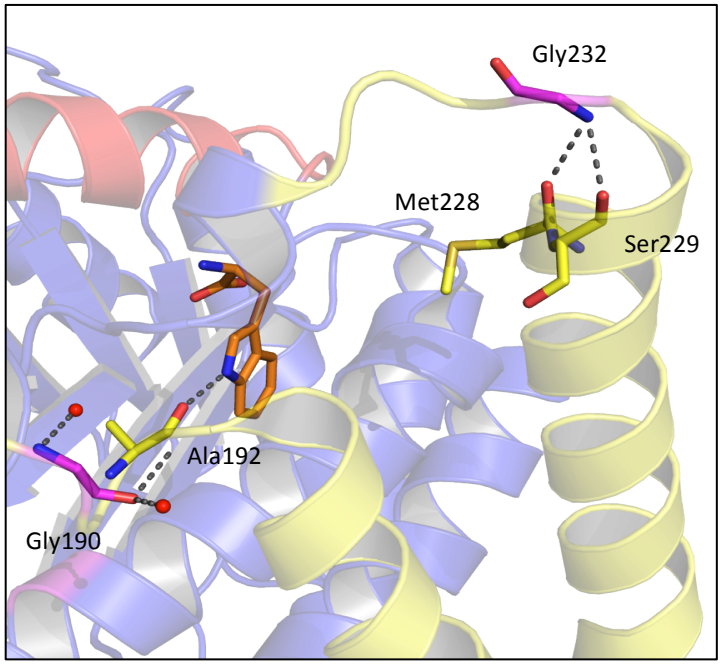

Figure 7.3 Interactions of Gly190 and Gly232 (coloured magenta and show as sticks) from the Trp- and Phe-bound *Mtu*DAH7PS crystal structure (PDB code: 3KGF). The core $(\beta/\alpha)_8$ barrel structure is coloured blue, the N-terminal extension is coloured red, the additional helices to the α2-β3 loop are coloured yellow and the bound Trp ligand is shown with carbon atoms coloured orange. Hydrogen bonds are shown a grey dashed lines and waters at red spheres.

7.1.3. Chapter aims

The primary goal of this chapter was to take full advantage of the serendipitous formation of two dimeric *Mtu*DAH7PS variants, *Mtu*DAH7PS^{G232P} and *Mtu*DAH7PS$^{G190P/G232P}$, thoroughly characterising these proteins to gain a better understanding of the role of quaternary structure in the regulation and activity of *Mtu*DAH7PS. Both Gly190Pro and Gly232Pro were changes intended to disrupt the regulation of *Mtu*DAH7PS; consequently it would be difficult to distinguish whether changes in the

properties of the variant enzymes were due to the substitution(s) or the change in quaternary structure. To address this concern, another *Mtu*DAH7PS variant was required, deliberately engineered to disrupt the tetramer interface of *Mtu*DAH7PS and prevent tetramer formation. The variant *Mtu*DAH7PS^{F227D} was successfully prepared by site directed mutagenesis and characterised alongside *Mtu*DAH7PS^{G232P} and *Mtu*DAH7PS$^{G190P/G232P}$ using a range of structural, kinetic and biophysical techniques.

7.2. Preparation of variants

7.2.1. Choice of aromatic amino acid substitution to disrupt the *Mtu*DAH7PS tetramer interface

Inspection of the tetramer interface revealed a small hydrophobic grove (Figure 7.4). Residues from the core α1 helix (Val111 and Tyr115), the α2-α2a loop (Leu194) and the inserted helices α2a (His198) and α2b (Ile221, Leu225 and Met228) form this hydrophobic grove. Phe227, located on the α2b helix of the subunit across the tetramer interface protrudes into this grove, forming hydrophobic contacts with Tyr115, Met228, and Thr114 (contacts identified by PDBsum).[127] Substitution of Phe227 for a charged residue, such as Asp, was proposed to disturb these interactions and prevent stable formation of the tetramer interface.

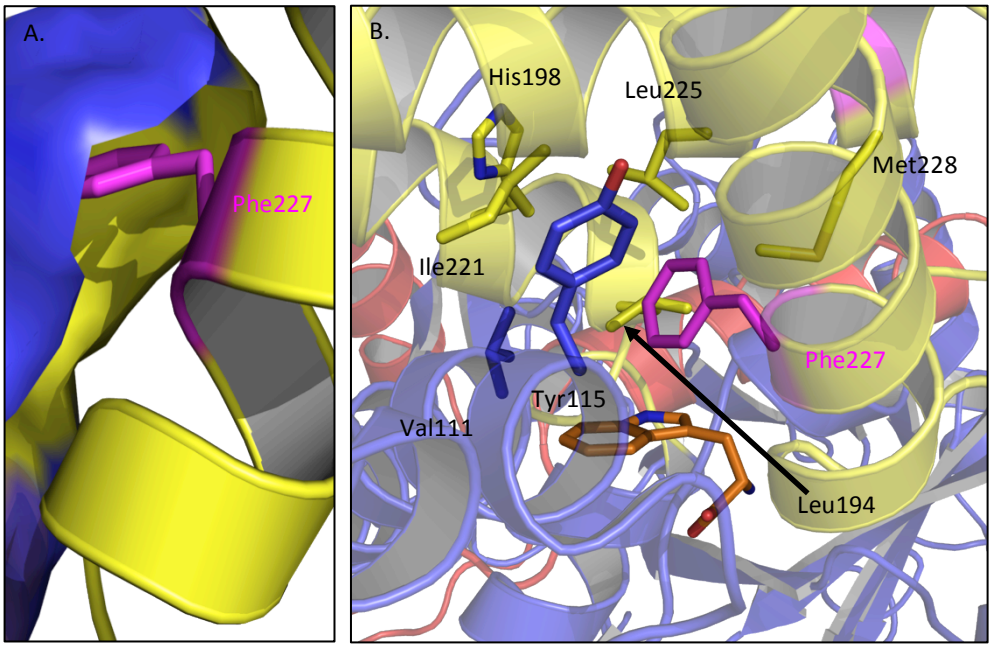

Figure 7.4 Hydrophobic grove located on tetramer interface of *Mtu*DAH7PS (PDB code: 3KGF) A. Surface representation of chain A depicting cavity created by the hydrophobic residues. Residues of the opposite chain are shown in cartoon form, and Phe227 as sticks coloured magenta. B. Diagram depicting secondary structure elements and the residues important for the formation of the grove shown as sticks. The core $(\beta/\alpha)_8$ barrel structure is coloured blue, the N-terminal extension is coloured red, the additional helices to the α2-β3 loop are coloured yellow, Phe227 as sticks coloured magenta, and the bound ligand Trp as sticks coloured orange.

7.2.2. Preparation, expression and purification

SDM was performed using the QuikChange® Lightning Site-Directed Mutagenesis Kit (Stratagene), as described in Section 9.2. All primers were designed to incorporate the desired mutations using the QuikChange® Primer Design tool (Agilent technologies). To generate the vector for *Mtu*DAH7PS$^{G190P/G232P}$ two rounds of SDM were required. The SDM product for *Mtu*DAH7PS^{G190P} was formed in the first round, sequence verified and used as the template in the second round. The second round of SDM followed the same protocol as the first but used the primers to introduce the substitution of Gly232Pro. DNA sequencing of all SDM products confirmed the correct incorporation of the desired mutations. SDM products were electroporated into BL21(DE3) PGroESL cells, expressed and purified as described for *Mtu*DAH7PS^{WT} in Section 9.5.

7.2.3. Confirmation of product

SDS-PAGE was used to assess enzyme purity and molecular mass. Analysis of the purified *Mtu*DAH7PS variants by SDS-PAGE showed all three variants produce a strong band at ~50 kDa (Figure 7.5). This mass is in agreement with the expected monomeric mass of *Mtu*DAH7PS of ~51 kDa. *Mtu*DAH7PS^{F227D} and *Mtu*DAH7PS^{G232P} are highly pure. There is a small amount of contamination present in the *Mtu*DAH7PS$^{G190P/G232P}$ sample, but this is relatively insignificant compared to the amount of *Mtu*DAH7PS$^{G190P/G232P}$ present.

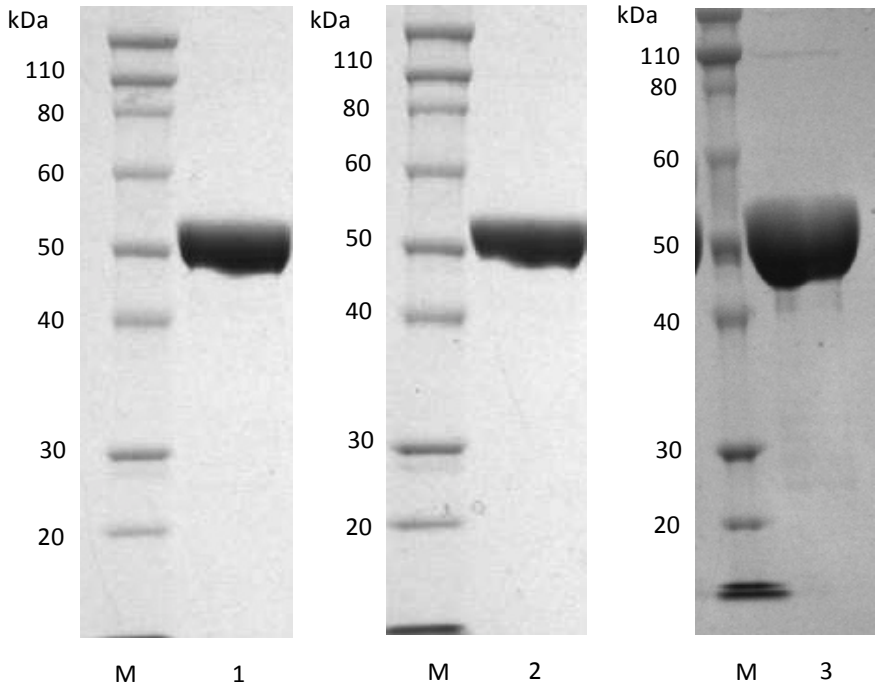

Figure 7.5 SDS-PAGE gel illustrating the size and purity of each *Mtu*DAH7PS variant. Lane M molecular weight marker; Lane 1 *Mtu*DAH7PS^{F227D}; Lane 2 *Mtu*DAH7PS^{G232P} and Lane 3 *Mtu*DAH7PS$^{G190P/G232P}$.

7.3. Comparison of secondary structure

The secondary structure of all purified *Mtu*DAH7PS variants was assessed by CD to detect if the variation to their aromatic amino acid sequence due to the substitution(s) has caused a change in their secondary structure. Assays were carried out as detailed in Section 9.7.4. Comparison of the *Mtu*DAH7PS^{WT} CD spectrum with the spectra of the *Mtu*DAH7PS^{G1232P}, *Mtu*DAH7PS$^{G190P/G232P}$ and

*Mtu*DAH7PS^{F227D} showed no variation (Figure 7.6). Thus the substitution(s) introduced to each variant have not obviously affected the secondary structure.

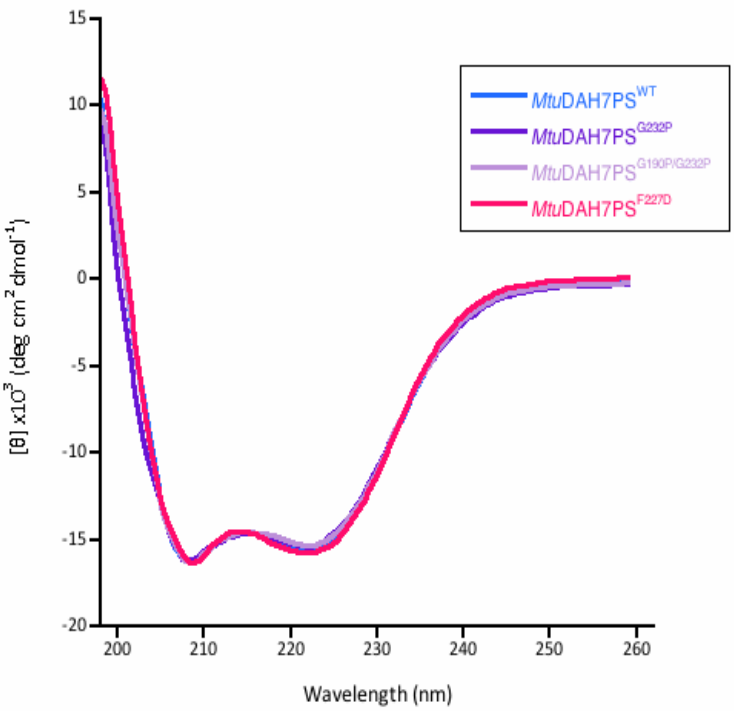

Figure 7.6 CD spectra for *Mtu*DAH7PS^{WT} (blue), *Mtu*DAH7PS^{G232P} (purple), *Mtu*DAH7PS$^{G190P/G232P}$ (light purple) and *Mtu*DAH7PS^{F227D} (pink).

7.4. Quaternary structure analysis

The first variant of *Mtu*DAH7PS to be purified was *Mtu*DAH7PS^{G232P}. During the final step of the purification, SEC, it was noted that *Mtu*DAH7PS^{G232P} eluted at ~180 mL, approximately 20 mL later than *Mtu*DAH7PS^{WT}. As SEC separates different species by size, this means the molecular mass *Mtu*DAH7PS^{G232P} is lower than typically observed under the same conditions for *Mtu*DAH7PS^{WT}. A higher elution volume and lower molecular mass are most likely due to *Mtu*DAH7PS^{G232P} adopting a different oligomeric structure to *Mtu*DAH7PS^{WT}. *Mtu*DAH7PS$^{G190P/G232P}$ and *Mtu*DAH7PS^{F227D} were also found to elute from the SEC column at ~180 mL. In order to verify whether the quaternary structure of the *Mtu*DAH7PS variants truly differed from *Mtu*DAH7PS^{WT} the variants were analysed by SAXS, native PAGE and AUC.

7.4.1. SAXS analysis

SAXS analysis was carried out on all three *Mtu*DAH7PS variants under the standard conditions stated for the wild type enzyme, detailed in Section 9.7.5The SAXS scattering profiles of *Mtu*DAH7PS^{G232P}, *Mtu*DAH7PS$^{G190P/G232P}$ and *Mtu*DAH7PS^{F227D} were almost identical to each other when overlaid (Figure 7.7). The scattering profiles of the *Mtu*DAH7PS variants varied greatly from the SAXS scattering profile of *Mtu*DAH7PS^{WT} and the theoretical scattering profile predicted by CRYSOL for tetrameric *Mtu*DAH7PS (PDB code: 3NV8).[103]

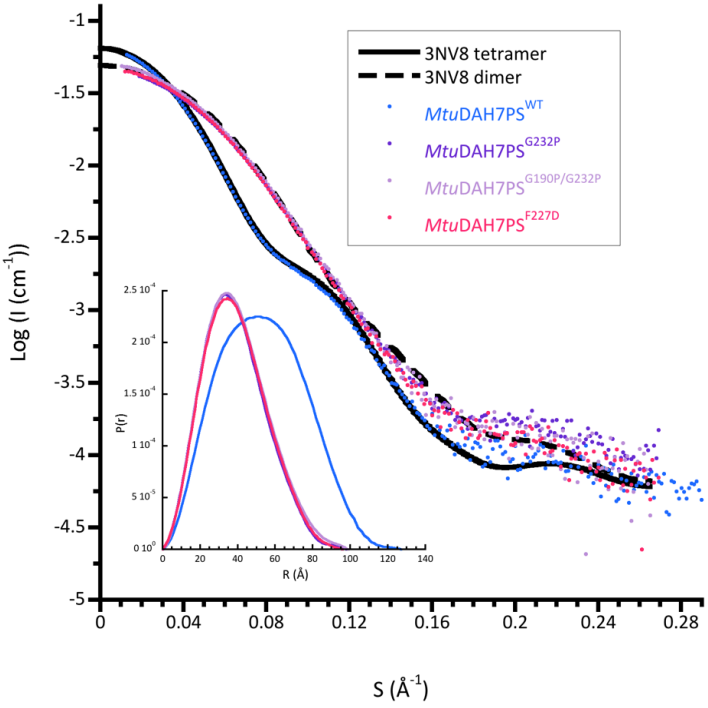

Figure 7.7 SAXS profiles of *Mtu*DAH7PS^{WT} (blue), *Mtu*DAH7PS^{G232P} (purple), *Mtu*DAH7PS$^{G190P/G232P}$ (light purple) and *Mtu*DAH7PS^{F227D} (pink). Also shown is the theoretical scattering for the tetrameric (black) and dimeric (black dash) *Mtu*DAH7PS from PDB code 3NV8. Inset pair-wise distribution profiles.

Comparison of the SAXS scattering profiles of the variant enzymes with the theoretical scattering profile predicted by CRYSOL for the dimer of *Mtu*DAH7PS showed they were in good agreement. The dimer formed in the asymmetric unit of the *Mtu*DAH7PS crystal coordinates (PDB code: 3nv8) was used for the CRYSOL analysis, as the substitutions introduced to the variants most likely disrupt the tetramer interface. The χ^2 values calculated by CRYSOL for the fit of *Mtu*DAH7PS^{G232P} and

*Mtu*DAH7PS$^{G190P/G232P}$ to the predicted scattering of the *Mtu*DAH7PS dimer were 0.986 and 0.806 respectively, indicating a very good fit to the dimeric crystal structure. Thus the average structure of *Mtu*DAH7PS^{G232P} and *Mtu*DAH7PS$^{G190P/G232P}$ in solution is a dimeric at the measured concentrations (Table 7.1). The χ^2 for *Mtu*DAH7PS^{F227D} was 2.36, suggesting that there is some deviation of the average structure of *Mtu*DAH7PS^{F227D} in solution from the crystallographic coordinates of the *Mtu*DAH7PS dimer.

The parameters determined from the SAXS experimental data for the three *Mtu*DAH7PS variants differed from the wild type enzyme, but were remarkably similar to each other. The D_{max} of the three variant enzymes was smaller than *Mtu*DAH7PS^{WT}, as was the R_g, the real space R_g and the Porod volume (Table 7.1). Analysis by SAXS MoW showed the Porod volume of the *Mtu*DAH7PS variants was consistent with the mass of the *Mtu*DAH7PS dimer. The analysis of the SAXS data for the *Mtu*DAH7PS^{G232P}, *Mtu*DAH7PS$^{G190P/G232P}$ and *Mtu*DAH7PS^{F227D} showed the average quaternary structure of all three variants was dimeric. There was no convincing evidence to suggest other oligomeric species were present in solution at the concentrations (4.5 – 6 mg/mL) analysed.

The quaternary structure of *Mtu*DAH7PS^{G232P}, *Mtu*DAH7PS$^{G190P/G232P}$ and *Mtu*DAH7PS^{F227D} collected at the concentrations required for SAXS was shown to be almost exclusively dimeric in solution. The lack of evidence of tetramer formation at the high concentrations of the variant enzymes required for the SAXS analysis of *Mtu*DAH7PS indicates the introduced substitutions, Gly232Pro and Phe227Asp, most likely prevent tetramer formation.

Table 7.1 SAXS parameters calculated from analysis of the scattering profiles of *Mtu*DAH7PS variants using PRIMUS, GNOM, MoW, and CRYSOL. Values were obtained by analysis of one set of SAXS data.

***Mtu*DAH7PS**	**Wild type**	**G232P**	**G190P/ G232P**	**F227D**
Guinier analysis				
R_g (Å)	41.6 ± 0.3	29.8 ± 0.1	30.7 ± 0.2	29.8 ± 0.1
I (0) (cm^{-1})	0.168 ± 0.001	0.074 ± 0.001	0.053 ± 0.001	0.066 ± 0.001
Pair distribution analysis				
Real Space R_g (Å)	40.9 ± 0.2	29.6 ± 0.1	30.2 ± 0.1	28.83 ± 0.07
D_{max} (Å)	127	98	99	96
V_p, (Da)	282700	144500	137500	150518
Molecular weight estimates from SAXS MoW analysis				
M_w from V_p (Da)	199 100	89800	92900	91800
Nō of Subunits	4	2	2	2
CRYSOL analysis with Tetrameric 3NV8				
R_{gE} (Å)	42.4 ± 0.2	41.6 ± 0.2	41.9 ± 0.2	29.8 ± 0.2
R_{gT} (Å)	40.6	29.6 ± 0.2	30.4 ± 0.2	39.8
χ^2	0.996	40.0	39.9	51.4
CRYSOL analysis with dimeric 3NV8				
R_{gE} (Å)	41.7 ± 0.2	29.6 ± 0.2	30.2 ± 0.2	29.9 ± 0.2
R_{gT} (Å)	30.7	29.1	29.4	29.3
χ^2	13.3	0.986	0.806	2.36

7.4.2. Native PAGE

To evaluate the quaternary structure of the *Mtu*DAH7PS variants at low concentrations (< 250 ng/mL) blue native PAGE was employed. The blue native PAGE was carried out under the conditions stated in Section 9.7.2. All three *Mtu*DAH7PS variants display a protein band at ~100 kDa and a second at ~50 kDa (Figure 7.8), consistent with the molecular masses of the *Mtu*DAH7PS dimer and monomer respectively. The result is similar to *Mtu*DAH7PS^{WT}. This shows despite the *Mtu*DAH7PS variants being dimeric at high concentrations, at low concentrations they exist as both monomeric and dimeric species in solution. Furthermore the ratio present of the two oligomeric species in each variant enzyme is approximately the same as the wild type enzyme in solution at low concentration.

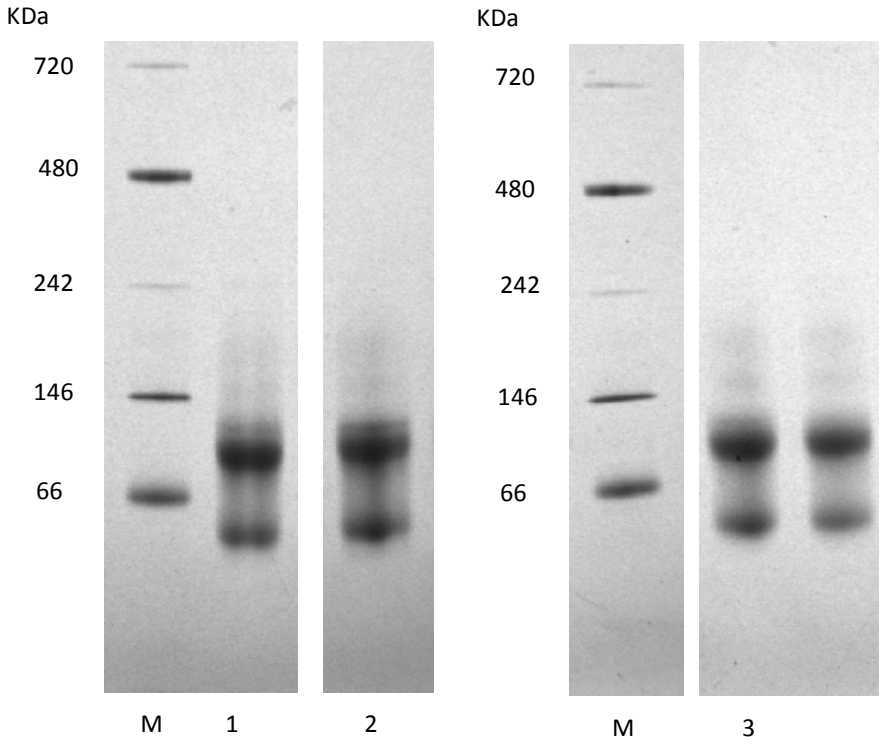

Figure 7.8 Blue native PAGE gel; Lane M displays the molecular weight marker; Lane 1 *Mtu*DAH7PS^{WT}; Lane2 *Mtu*DAH7PS^{F227D}; Lane 3 *Mtu*DAH7PS^{G232P} and Lane 4 *Mtu*DAH7PS$^{G190P/G232P}$.

7.4.3. AUC analysis

AUC was used to gain better insight into the quaternary structure of *Mtu*DAH7PS^{G232P} in solution. Sedimentation velocity experiments were carried out at the three concentrations 0.09, 0.6 and 0.9 mg/mL, under the conditions previously described for the wild type enzyme in Section 9.7.7. The AUC data was fitted to a continuous distribution *c*(*s)* model, which showed the quaternary structure of *Mtu*DAH7PS^{G232P} varied with concentration (Figure 7.9A). At the lowest analysed concentration, 0.09 mg/mL, the sedimentation coefficient (*s*) of the peak was 4.0 ± 0.4 S, which corresponded to a molecular mass of ~54 kDa, in good agreement with monomeric mass of *Mtu*DAH7PS (~51 kDa). At 0.6 mg/mL the peak had an *s* value of 5.0 ± 0.6 S and had broadened. At 0.9 mg/mL the main peak had an *s* value of 5.7 ± 0.1 S (with a calculated molecular mass of ~75^{4}kDa) and a shoulder at 4.1 ± 0.6 S. These results showed *Mtu*DAH7PS^{G232P} exists as a mixture of monomer and dimer in

solution, with portion of dimer increasing, and the portion of monomer decreasing with increasing concentration.

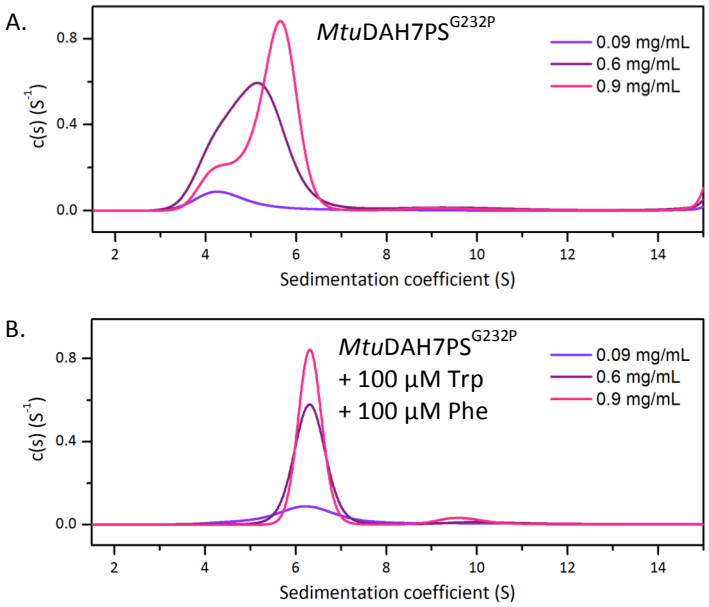

Figure 7.9 Normalised c(s) distribution functions from AUC data for *Mtu*DAH7PS^{G232P} in the absence (A.) and presence (B.) of 100 µM Trp and 100 µM Phe. *Mtu*DAH7PS^{G232P} was analysed at 0.09 mg/mL (violet), 0.6 mg/mL (purple) and 0.9 mg/mL (pink). AUC data, fits and residuals are provided in Appendix II.

When samples were spiked with 100 µM each of Trp and Phe analysis showed only one peak at ~6.1 S for all concentrations (Figure 7.9B). This peak gave a calculated molecular mass of ~92 kDa. The molecular mass of dimeric *Mtu*DAH7PS is expected to be ~102 kDa. Hence, the addition of Trp and Phe had stabilised the dimeric structure of *Mtu*DAH7PS^{G232P}. As Phe binds at the dimer interface, Phe was most likely primarily responsible for the stabilisation of the *Mtu*DAH7PS^{G232P} dimer by strengthening the interactions between the two subunits. The effect of Trp and Phe alone on the quaternary structure of the dimeric *Mtu*DAH7PS variants is yet to be established.

a

7.5. Kinetic parameters

The substitutions introduced to the three dimeric *Mtu*DAH7PS variants had devastating consequences on their catalytic ability. The E4P-dependent Michaelis-Menten kinetics was determined using the standard kinetic assays conditions initially used for the wild type enzyme in Section 9.9.1.

The E4P-dependent Michaelis-Menten kinetics displayed a huge rise in the Michaelis constant (K_m) for all three dimeric variants of *Mtu*DAH7PS (Table 7.2). For *Mtu*DAH7PS^{G232P} and *Mtu*DAH7PS$^{G190P/G232P}$ the K_m^{E4P} had to 330 µM and 390 µM respectively. *Mtu*DAH7PS^{F227D} was the most severely affected with the K_m^{E4P} increasing to 590 ± 60 µM. All three dimeric enzymes showed that a considerably higher concentration of E4P was required for effective catalysis than by *Mtu*DAH7PS^{WT}.

There was also an unanticipated improvement in the k_{cat} of all three dimeric variants (Table 7.2). The improvement in k_{cat} indicates the maximum rate of catalysis at high substrate concentrations is not adversely affected; in fact it may have improved. If any improvement to catalysis has occurred as a result of preventing tetramer formation it was insufficient to compensate for the decreased affinity of the variant enzymes for E4P. *Mtu*DAH7PS^{G232P}, *Mtu*DAH7PS$^{G190P/G232P}$ and *Mtu*DAH7PS^{F227D} were all found to have very low catalytic efficiencies with respect to E4P.

Table 7.2 Kinetic parameters of *Mtu*DAH7PS^{WT}, *Mtu*DAH7PS^{G232P}, *Mtu*DAH7PS$^{G190P/G232P}$ and *Mtu*DAH7PS^{F227D} determined from Michaelis-Menten kinetics. Data for K_m^{E4P} was obtained using the ternary complex rate equation. Michaelis-Menten plots are shown in Appendix I. Values have been determined from a single set of kinetic data. Error represents error of curve fitting to the data set by least squares fit.

***Mtu*DAH7PS**	K_m^{E4P} (µM)	K_m^{PEP} (µM)	k_{cat} (s^{-1})	**Catalytic Efficiency** k_{cat}/K_m^{E4P} ($s^{-1}mM^{-1}$)	k_{cat}/K_m^{PEP} ($s^{-1}mM^{-1}$)
Wild type	28 ± 2	37 ± 4	4.7 ± 0.1	170 ± 20	130 ± 20
G232P	330 ± 10	90 ± 20	14.3. ± 0.2	43 ± 2	160 ± 40
G190P/G232P	390 ± 30	60 ± 20	12.3 ± 0.4	32 ± 4	210 ± 70
F227D	590 ± 60	80 ± 20	8.0 ± 0.4	14 ± 2	100 ± 30

For the determination of Michaelis-Menten kinetics of enzyme systems involving two substrates the alternate substrate ideally needs to be held in excess, usually at a concentration between three and ten times the estimated K_m. For the dimeric *Mtu*DAH7PS variants this would require unworkable E4P concentrations in excess of 1.5 mM to determine the K_m^{PEP}. As an alternative the ternary complex equation provided by GraFit 5.0 (Erthicus) was used (Equation 7.1). Derived from the general rate equation of Alberty the ternary complex rate equation from Grafit models a generalised two-substrate irreversible enzyme reaction with a mechanism involving the formation of a ternary complex between the two substrates and the enzyme in non-saturating substrate conditions.[128] Three sets of Michaelis-Menten kinetics were used to determine the determine K_m^{PEP}, each at a different E4P concentration, 150, 300 and 500 µM (Figure 7.10) When this data was fitted to the ternary complex rate equation the K_m^{PEP} could be determined, without needing excessively high and problematic E4P concentrations. The K_m^{PEP} was determined for each dimeric variant and found to be greater than *Mtu*DAH7PS^{WT}. Indicating greater PEP concentrations were required by the dimeric *Mtu*DAH7PS variants for effective catalysis.

$$\upsilon = \frac{V_{\max}[\mathrm{A}][\mathrm{B}]}{K'_{\mathrm{A}}K_B + K_{\mathrm{B}}[\mathrm{A}] + K_{\mathrm{A}}[\mathrm{B}] + [\mathrm{A}][\mathrm{B}]}$$

Equation 7.1 The ternary complex equation from GraFit 5.0. V_{max} the maximum possible rate, υ the measured rate. A is the variable substrate (PEP) and B is substrate held constant (E4P) for each set of Michaelis-Menten kinetics.[A] and [B] represents the concentration of the relative substrate and K_A and K_B are the Michaelis constants determined for the respective substrate (concentration of specified substrate that gives ½ V_{max}. K_A' is the apparent dissociation constant of substrate A.

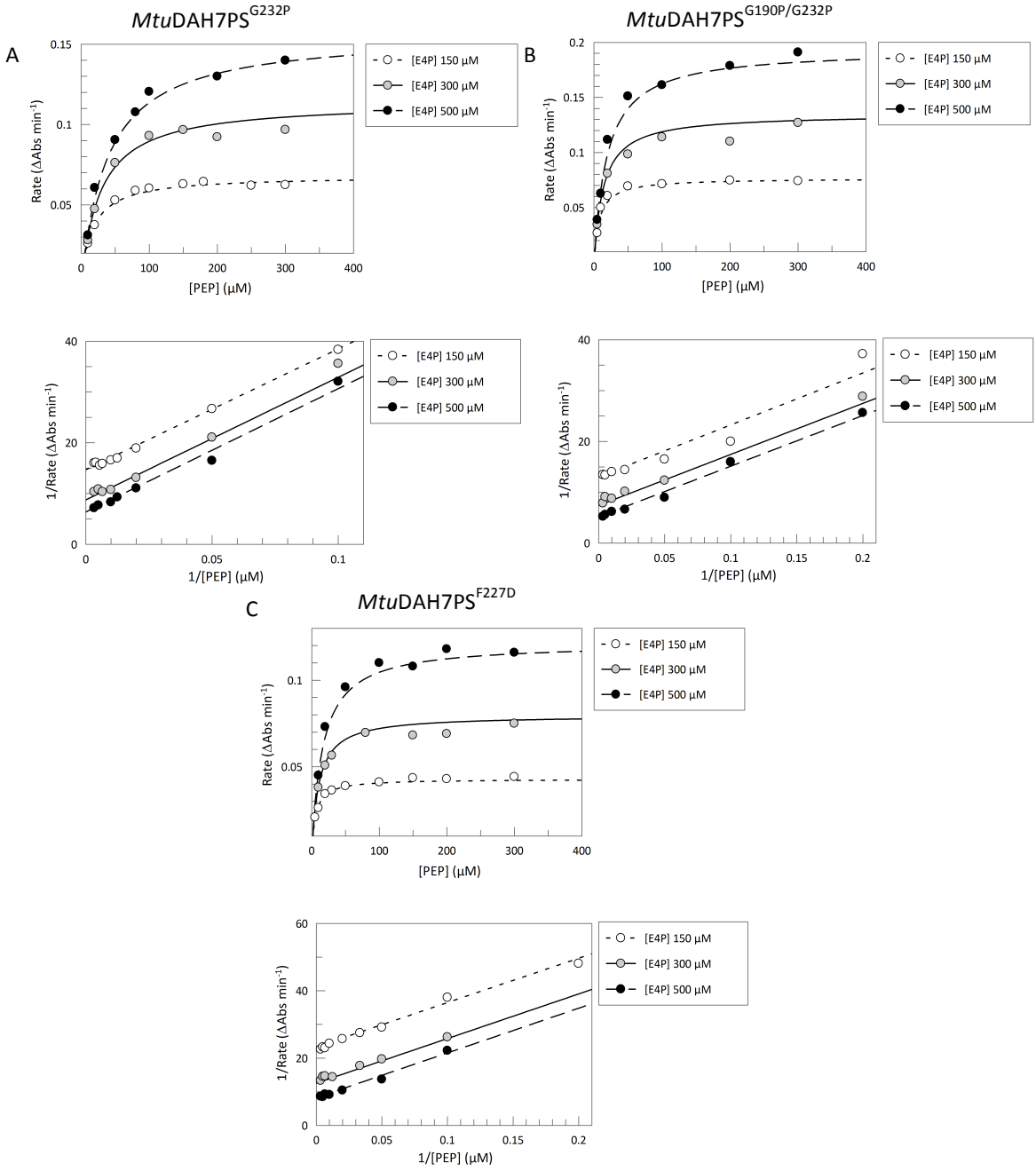

Figure 7.10 Ternary complex kinetics used to determine the K_m^{PEP} for A. *Mtu*DAH7PS^{G232P}; B. *Mtu*DAH7PS$^{G190P/G232P}$ and C. *Mtu*DAH7PS^{F227D}. Michaelis-Menten kinetics is shown in the top plot, and Lineweaver-Burke plots below. E4P concentrations were held constant at 150, 300 and 500 μM for each set of kinetic data.

Overall the dimeric *Mtu*DAH7PS variants were much poorer catalysts than *Mtu*DAH7PS^{WT} or any other *Mtu*DAH7PS variant produced. As all three dimeric *Mtu*DAH7PS variants displayed poor catalytic activity, the dimeric quaternary structure of the enzymes was most likely responsible for the poor catalytic activity as opposed to the substitutions themselves. The inability of *Mtu*DAH7PS^{G232P},

*Mtu*DAH7PS$^{G190P/G232P}$ and *Mtu*DAH7PS^{F227S} to form the *Mtu*DAH7PS tetramer in solution severely handicapped their ability to bind E4P, and to a lesser extent PEP. Intriguingly dimeric *Mtu*DAH7PS variants were able to turnover the substrates to product faster than *Mtu*DAH7PS^{WT}.

7.6. Feedback regulation of dimeric *Mtu*DAH7PS variants

7.6.1. Disruption of feedback inhibition

The initial set of inhibition studies were conducted using the standard conditions, for which the substrate concentrations are held at 150 µM, as outline in Section 9.9.3. These conditions have been used previously for all *Mtu*DAH7PS variants.[48,91] All three dimeric *Mtu*DAH7PS variants showed an increased sensitivity to Phe, reducing activity to 50-60 % (Figure 7.11A). Interestingly only *Mtu*DAH7PS^{G232P} and *Mtu*DAH7PS$^{G190P/G232P}$ showed heightened sensitivity to Tyr. Thus the Gly232Pro (and Gly190Pro) substitution(s) have affected the enzymes sensitivity to Tyr. Whereas the disruption to the quaternary structure of the *Mtu*DAH7PS variants may be responsible for the change in sensitivity to Phe, due to *Mtu*DAH7PS^{F227D} also exhibiting increased sensitivity to Phe. The dimeric *Mtu*DAH7PS variants also showed no evidence of synergistic regulation when multiple aromatic amino acids were present. The lack of synergistic regulation in all three dimeric *Mtu*DAH7PS variants illustrated that the tetrameric structure of *Mtu*DAH7PS is essential for synergistic regulation. The fine-tuning of the molecular dynamics of *Mtu*DAH7PS in response to the aromatic amino acids is believed to be responsible for the inhibition of *Mtu*DAH7PS activity.[71,115]The *Mtu*DAH7PS tetramer probably facilitates the correct molecular motion or conformational fluctuations of the subunits that allows allosteric ligand binding and communication of allosteric binding within and between subunits.

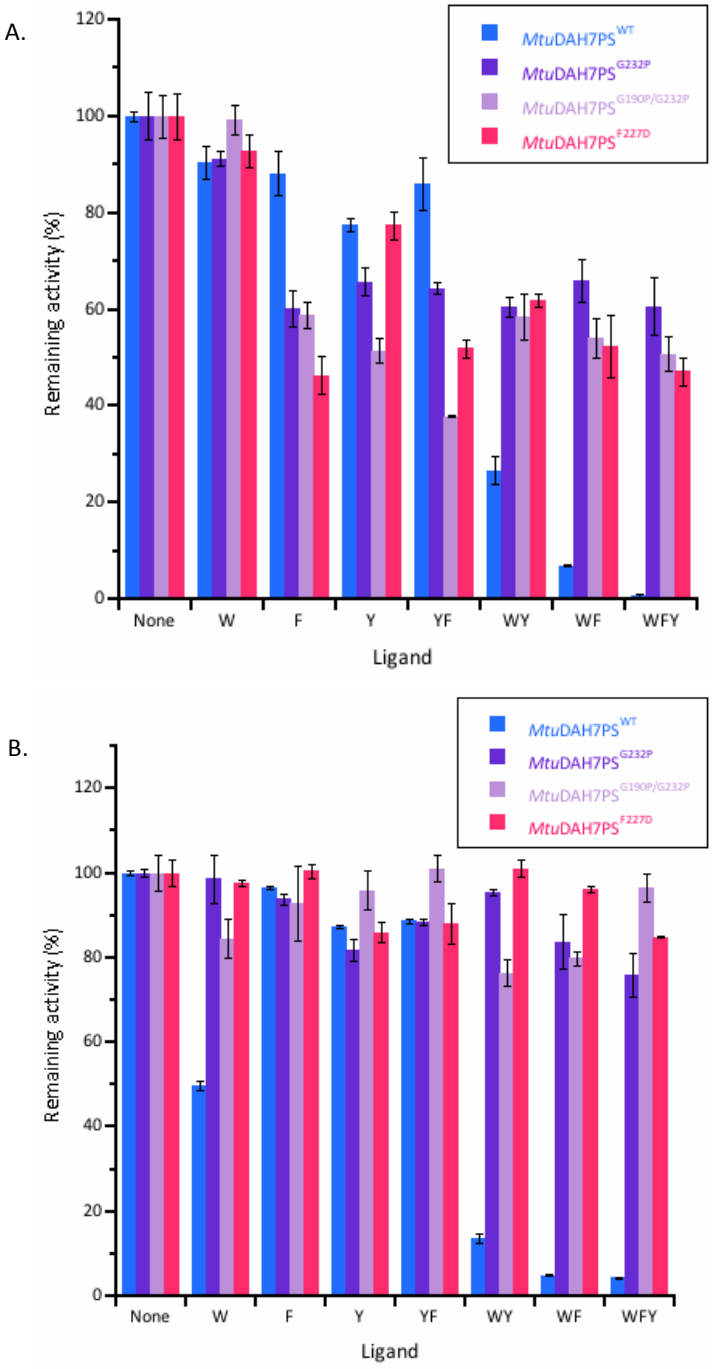

Figure 7.11 Remaining activity of *Mtu*DAH7PS^{WT} (blue), *Mtu*DAH7PS^{G232P} (purple), *Mtu*DAH7PS$^{G190P/G232P}$ (light purple) and *Mtu*DAH7PS^{F227D} (pink) in the presence of various single, binary and ternary combinations of aromatic amino acids. The aromatic amino acids are represented by their one letter code; Trp, W; Phe, F and Tyr, Y. Each letter also represents 200 µM of the corresponding aromatic amino acids. Assays conducted in the presence of A. 150 µM E4P and PEP and B. 1800 µM E4P and 150 µM PEP. Error bars depict the standard deviation of at least duplicate measurements. P-values provided in appendix V.

The regulatory response of *Mtu*DAH7PS has previously been shown to be highly dependent on E4P concentration.[48] An absolute concentration of 150 µM E4P was originally chosen to illustrate the

synergistic inhibition of *Mtu*DAH7PS whilst conserving E4P stocks. However, the huge drop in the affinity of the dimeric *Mtu*DAH7PS variants for E4P (Section 7.5) complicated the interpretation of the inhibition studies. The concentration of 150 µM E4P used in these assays was less than half the K_m^{E4P} determined for any of the dimeric *Mtu*DAH7PS variants. For *Mtu*DAH7PS^{WT} and most other *Mtu*DAH7PS variants 150 µM E4P was equivalent to three-five times the K_m^{E4P}. Consequently, assays conducted at a concentration of 150 µM E4P for the dimeric *Mtu*DAH7PS variants evaluated the inhibitory response at a completely different area of the Michaelis-Menten curve compared to the wild type enzyme. To address any possible discrepancies in inhibition due to surveying a different portion of the Michaelis-Menten curve the inhibition studies were also conducted at a concentration of 1800 µM E4P, a value between three to five times the K_m^{E4P} of the dimeric variants.

To ensure such high concentrations of E4P did not adversely affect *Mtu*DAH7PS inhibition, high E4P concentration (1800 µM) inhibition studies were also carried out on the wild type enzyme (Figure 7.11B). *Mtu*DAH7PS^{WT} displayed very similar regulatory behaviour at both E4P concentrations. The only exception was *Mtu*DAH7PS^{WT} that the addition of Trp alone, with the remaining *Mtu*DAH7PS^{WT} activity reduced to ~49 %. All three dimeric *Mtu*DAH7PS variants were insensitive to the presence of any single, binary or ternary combination of aromatic amino acids at the higher E4P concentration of 1800 µM. Hence the dimeric *Mtu*DAH7PS variants appear to be poorly regulated.

7.6.2. Effect of ligand on dimeric *Mtu*DAH7PS kinetic parameters

The E4P-dependent kinetics of *Mtu*DAH7PS^{WT} displayed cooperativity, only in the presence of Trp and Phe (or Tyr).[48] To ascertain if the dimeric *Mtu*DAH7PS variants were capable of cooperative E4P binding the E4P-dependent kinetics of *Mtu*DAH7PS$^{G190P/G232P}$ were determined in the presence of Trp and Phe. Assays were conducted under standard assay conditions detailed in Section Inhibition studies, with and the addition of 200 µM Trp and 200 µM Phe. PEP concentration was held at 300 µM for the collection of the E4P-dependent kinetic data. Only one set of kinetic data was required to

identify if the plot was sigmoidal shape and to see how the kinetic parameters changed with respect to unliganded enzyme.

The E4P-dependent kinetics of *Mtu*DAH7PS$^{G190P/G232P}$ in the presence of Trp and Phe fitted the standard Michaelis-Menten equation and showed no sign of cooperative E4P binding (Figure 7.12). Hence it is likely that the formation of the *Mtu*DAH7PS tetramer is essential for effective communication of ligand binding at the allosteric binding sites to the active site. The E4P catalytic efficiency of *Mtu*DAH7PS$^{G190P/G232P}$ was harmed by the presence of Trp and Phe. The K_m^{E4P} increased to ~990 µM and the k_{cat} roughly halved to ~6.8 s^{-1} (Table 7.3). As *Mtu*DAH7PS$^{G190P/G232P}$ only showed sensitivity to Phe in the inhibition studies, Phe is most likely responsible for the observed inhibitory effect. The Gly190Pro/Gly232Pro substitutions disrupted the quaternary structure of *Mtu*DAH7PS$^{G190P/G232P}$ and possibly the flexibility of the loops that precede and succeed the α2a and α2b helices. As two changes may have occurred to *Mtu*DAH7PS$^{G190P/G232P}$ it was difficult to absolutely define which was responsible for the loss of E4P cooperativity. But given cooperativity has long been associated with multi-subunit complexes it is highly likely that the change in quaternary structure is the primary cause.[2,128] Analysis of E4P-dependent kinetics of *Mtu*DAH7PS^{F227D} in the presence of Trp and Phe would help to confirm if tetramer formation is necessary for E4P cooperativity.

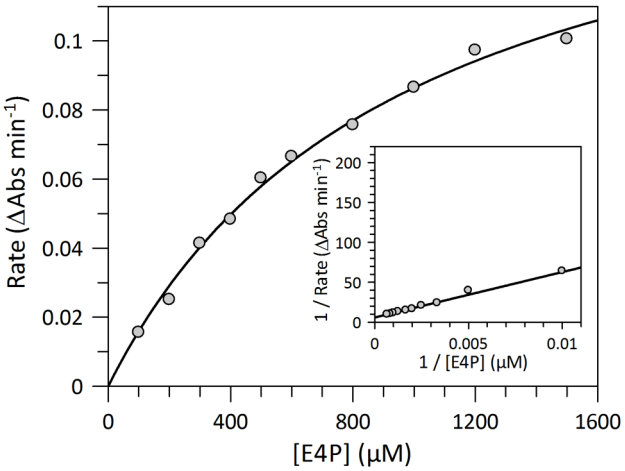

Figure 7.12 Michaelis-Menten plot, with Lineweaver burke insert, of the E4P-dependent kinetics of *Mtu*DAH7PS$^{G190P/G232P}$ in the presence of 200 µM of Trp and 200 µM Phe. The concentration of PEP was held at 300 µM.

Table 7.3 E4P-dependent kinetic parameters for *Mtu*DAH7PS^{WT} and *Mtu*DAH7PS$^{G190P/G232P}$ with and without 200 µM Trp and 200 µM Phe, determined from the Michaelis-Menten kinetics (Appendix I). Values were determined from a single set of kinetic data with error bars depicted the error of of curve fitting to the data set by least squares fit.

***Mtu*DAH7PS**	K_m^{E4P} (µM)	k_{cat} (s^{-1})	Catalytic Efficiency k_{cat}/K_m^{E4P} ($s^{-1}mM^{-1}$)
Wild type	28 ± 2	4.7 ± 0.1	170 ± 20
G190P/G232P	390 ± 30	12.3 ± 0.4	32 ± 4
G190P/G232P WF	990 ± 90	6.8 ± 0.3	7.0 ± 0.9

7.7. Thermal stability

DSF was used to assess the thermal stability of the *Mtu*DAH7PS variants in the presence of various combinations of ligands, Section 9.8.1. The dimeric variants have lower T_m than *Mtu*DAH7PS^{WT} (Figure 7.13). The *Mtu*DAH7PS tetramer has additional interactions across the tetramer interface, which needs to be broken, compared to the *Mtu*DAH7PS dimer. The more interactions to be broken the more energy (heat) is required to thermally denature the protein. If a substantial portion of *Mtu*DAH7PS^{WT} can access the *Mtu*DAH7PS tetramer under the DSF assay conditions it would explain the higher T_m of *Mtu*DAH7PS^{WT} compared to the dimeric *Mtu*DAH7PS variants. *Mtu*DAH7PS^{F227D} was less thermally stable than *Mtu*DAH7PS^{G232P} or *Mtu*DAH7PS$^{G190P/G232P}$. The introduction of the negatively charged Asp residue in place of the neutral Phe may repel dimeric units from each other, preventing or reducing transient interactions across the tetramer interface and reducing thermal stability further. Gly190Pro was previously shown to stabilise the *Mtu*DAH7PS tetramer stability and increased the enzymes thermal stability (Section 5.4.3). The ~2 ˚C difference in T_m between *Mtu*DAH7PS^{G232P} and *Mtu*DAH7PS$^{G190P/G232P}$ suggests the Gly190Pro substitution may also offer thermal stability to the *Mtu*DAH7PS dimer.

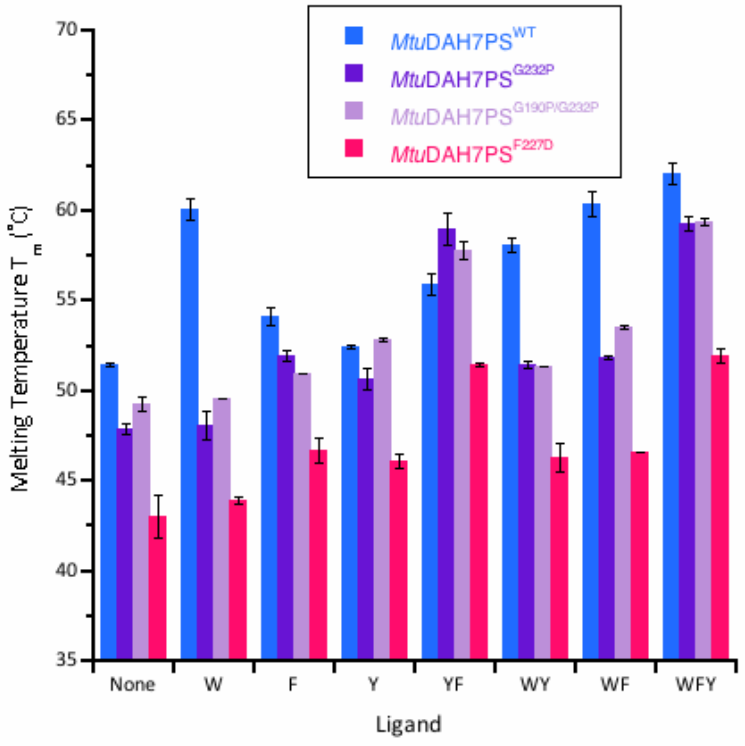

Figure 7.13 The effect of individual, binary and ternary combinations of aromatic amino acids on the thermal stability of *Mtu*DAH7PS^{WT} (blue) and *Mtu*DAH7PS^{G232P} (purple), *Mtu*DAH7PS$^{G190P/G232P}$ (light purple) and *Mtu*DAH7PS^{F227D} (pink). The aromatic amino acids are represented by their one letter code; Trp, W; Phe, F and Tyr, Y. Each letter also represents 200 µM of the corresponding aromatic amino acids. Error bars depict the standard deviation of triplicate measurements. P-values provided in appendix V.

The addition of Trp to the assay buffer had little effect on the determined T_m of any of the dimeric *Mtu*DAH7PS variants (Figure 7.13). The increase in T_m determined for *Mtu*DAH7PS^{G232P} and *Mtu*DAH7PS$^{G190P/G232P}$ was less than 0.3 ˚C. A DSF assay was conducted with the addition of 1 mM Trp to the assay buffer and *Mtu*DAH7PS$^{G190P/G232P}$ T_m was 51.1 ± 0.4 ˚C, less than a ~2 ˚C increase in thermal stability. The small shift in T_m means Trp either binds very weakly or Trp binding offers little improvement in thermal stability to the dimeric *Mtu*DAH7PS variants. *Mtu*DAH7PS^{F227D} showed a modest ~0.9 ˚C increase in T_m in the presence of 200 mM Trp. The behaviour of *Mtu*DAH7PS^{F227D} is similar to *Mtu*DAH7PS^{G232P} and *Mtu*DAH7PS$^{G190P/G232P}$, thus the change in quaternary structure of the *Mtu*DAH7PS variants was most likely responsible for their poorer response to Trp.

The addition of either Phe or Tyr caused an increase in thermal stability between 2-3.5 ˚C, for each dimeric *Mtu*DAH7PS variant, *Mtu*DAH7PS^{WT} displayed an increase in thermal stability of ~2.6 ˚C. The

increase in T_m in the presence of Phe or Tyr suggests that the Phe- and Tyr-selective bindings sites, sites 1 and 2, are intact in the *Mtu*DAH7PS dimeric variants. Interestingly the increase in thermal stability in the presence of Phe was lower for *Mtu*DAH7PS$^{G190P/G232P}$ than *Mtu*DAH7PS^{G232P}, which may be an indication that the substitution of Gly190 has affected Phe binding. The thermal stability gained from Phe and Tyr binding to the dimeric *Mtu*DAH7PS variants was additive when both Phe and Tyr were present. Although the additive effect of Tyr and Phe was seen for the wild type enzyme and *Mtu*DAH7PS^{F227D} (each showed an increase of ~4.4 ˚C and ~3.7 ˚C respectively), the gain in stability for *Mtu*DAH7PS^{G232P} and *Mtu*DAH7PS$^{G190P/G232P}$ was much more dramatic, ~8.5 ˚C and ~11.1 ˚C respectively. The increased T_m in the presence of Phe and Tyr suggests that the Gly232Pro substitution influences ligand binding.

7.8. Binding affinities

ITC was used to gain a more detailed insight into the dimeric *Mtu*DAH7PS variants ability to bind the aromatic amino acids. The experimental protocol is detailed in Section 9.8.2. Trp and Phe were shown to bind to *Mtu*DAH7PS^{G232P} (Figure 7.14A-B) and *Mtu*DAH7PS^{F227D} (Figure 7.15G-H) and all three aromatic amino acids were shown to bind *Mtu*DAH7PS$^{G190P/G232P}$ (Figure 7.14D-F, Table 7.4). The K_d determined between Tyr and *Mtu*DAH7PS$^{G190P/G232P}$ was 42 ± 9 µM, indicating the loss of tetrameric structure has not negatively impacted Tyr binding. Tyr binding was only evaluated for *Mtu*DAH7PS$^{G190P/G232P}$. As *Mtu*DAH7PS$^{G190P/G232P}$ shares a similar dimeric structure to *Mtu*DAH7PS^{G232P} and *Mtu*DAH7PS^{F227D} and DSF showed a change in thermal stability in the presence of Tyr for all there dimeric *Mtu*DAH7PS variants it is not unreasonable to assume Tyr binding is also largely unaffected in these variants. Ideally ITC should be carried out to verify this assumption. The K_d values between Phe and *Mtu*DAH7PS^{G232P} or *Mtu*DAH7PS^{F227D} were 17 ± 2 µM and 15.9 ± 0.9 µM respectively, whereas the K_d of Phe in *Mtu*DAH7PS$^{G190P/G232P}$ was slightly lower. The ability of the three *Mtu*DAH7PS variants to bind Phe has therefore not been adversely affected by the inability of the variant enzymes to form the tetrameric *Mtu*DAH7PS structure. As Tyr and Phe can bind to the dimeric *Mtu*DAH7PS variants without penalty it is highly likely the Phe- and Tyr-selective sites, site 1 and site 2, remain relatively intact in the *Mtu*DAH7PS dimer.

Most remarkably all three dimeric *Mtu*DAH7PS variants have retained the ability to bind Trp, albeit weakly, with the K_d for Trp binding to the variant enzymes ranging between 150-200 μM (Table 7.4). Unfortunately, although ITC may have shown that Trp can bind it does not reveal which of the three distinct allosteric binding sites of *Mtu*DAH7PS Trp occupies. In an attempt to establish if Trp bound to the Phe-selective site, site 1, the variant enzymes were pre-incubated with Phe. As Phe preferentially binds to site 1, Trp would have to compete with Phe to occupy site 1 and this competition should have been reflected in increased K_d for Trp in the variant enzyme in the presence of Phe. However, the small increase in K_d observed between Trp and *Mtu*DAH7PS^{F227D} preincubated with Phe was within error of the determined K_d in the absence of a Phe. The K_d between Trp and *Mtu*DAH7PS^{G232P} preincubated with Phe increased to 210 ± 30 μM (Figure 7.14C, Figure 7.15I, Table 7.4). Given site 1 is known to be the Phe binding site a more dramatic increase in the K_d I was expected if we were to confidently identify competition between Trp and Phe.

The lack of unequivocal evidence for competition between the Trp and Phe suggest Trp does not bind to site 1. It is most probable the Trp site can still bind Trp. The huge reduction in the affinity for Trp by the dimeric *Mtu*DAH7PS variants is likely due to the disruption of the tetramer interface directly affecting the Trp site. However, Trp may instead bind to the Tyr-selective site, site 2. This possibility is yet to be discounted experimentally and cannot be ruled out. It should also be noted that preincubation of *Mtu*DAH7PS^{G232P} or *Mtu*DAH7PS^{F227D} with Phe did not improve Trp binding as seen previously for *Mtu*DAH7PS^{WT}. The loss of tetramer structure appears to have prevented communication between site 1 and the Trp site, resulting in the loss of cooperative Trp binding in the presence of Phe.

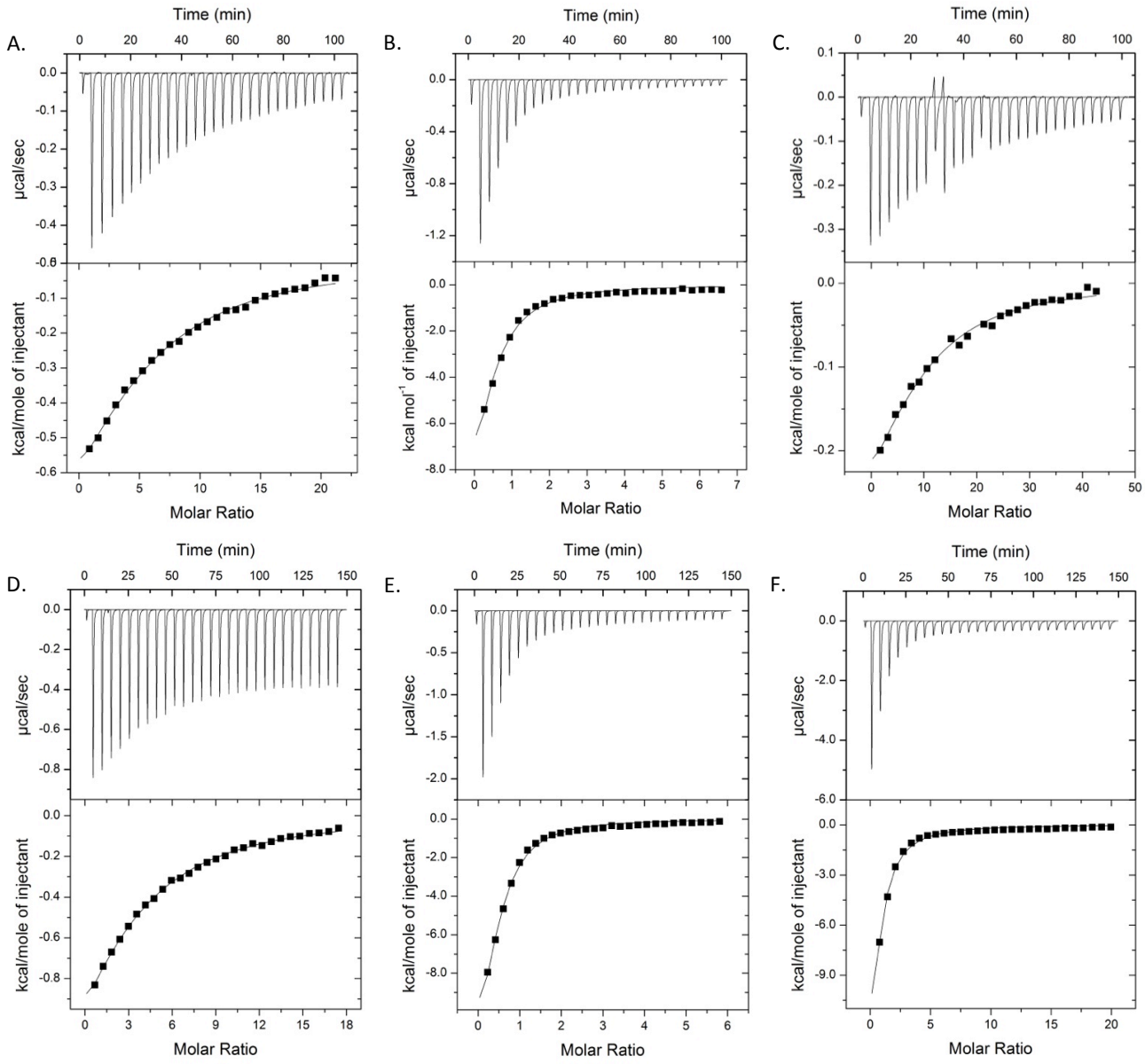

Figure 7.14 ITC data for the interaction of A. 30 µM *Mtu*DAH7PS^{G232P} with 3 mM Trp titrant; B. 28 µM of *Mtu*DAH7PS^{G232P} with 900 µM Phe titrant; C. 24 µM *Mtu*DAH7PS^{G232P} and a background of 50 µM Phe present in the cell with a 5 mM Trp titrant; D. 37 µM *Mtu*DAH7PS$^{G190P/G232P}$ with 3 mM Trp titrant; E. 33 µM of *Mtu*DAH7PS$^{G190P/G232P}$ with 900 µM Phe titrant and F. 32 µM *Mtu*DAH7PS$^{G190P/G232P}$ with a 3 mM Tyr titrant.

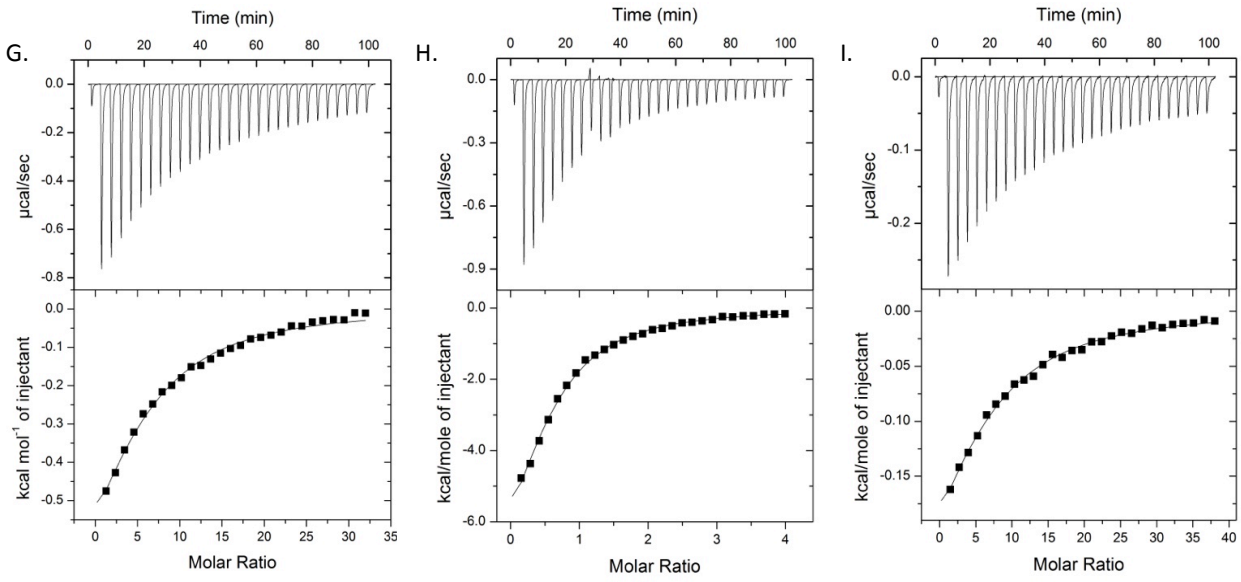

Figure 7.15 (Figure 7.14 cont.) ITC data for the interaction of G. 32 µM *Mtu*DAH7PS^{F227D} with 5 mM Trp titrant; H. 32 µM of *Mtu*DAH7PS^{F227D} with 600 µM Phe titrant and I. 28 µM *Mtu*DAH7PS^{F227D} and a background of 50 µM Phe present in the cell with a 5 mM Trp titrant.

Table 7.4 Dissociation constants determined by ITC for *Mtu*DAH7PS^{WT}, *Mtu*DAH7PS^{G232P}, *Mtu*DAH7PS$^{G190P/G232P}$ and *Mtu*DAH7PS^{F227D}. * Indicates results determined previously by Richard Hutton and — Indicates no background ligand or analysis not conducted. Values were determined from a single ITC experiment. Error represents error of curve fitting to the data set by least squares fit.

Titrated ligand	Background ligand	*Mtu*DAH7PS			
		Wild type K_d (µM)	G232P K_d (µM)	G190P/G232P K_d (µM)	F227D K_d (µM)
Trp	—	4.7 ± 0.1*	150 ± 10	180 ± 10	200 ± 20
Trp	Phe	1.08 ± 0.03*	210 ± 30	—	220 ± 20
Phe	—	21 ± 1*	17 ± 2	11.3 ± 0.2	15.9 ± 0.9
Tyr	—	39 ± 1	—	42 ± 9	—

7.9. Activation of *Mtu*CM activity

In the interest of determining how effectively the dimeric *Mtu*DAH7PS variants interact with *Mtu*CM kinetic assays were conducted monitoring *Mtu*CM activity, under the standard conditions detailed in Section 9.9.1. *Mtu*DAH7PS^{G232P}, *Mtu*DAH7PS$^{G190P/G232P}$ and *Mtu*DAH7PS^{F227D} were all very poor enhancers of *Mtu*CM activity (

Figure 7.16A). A 200-fold molar excess of a dimeric *Mtu*DAH7PS variant resulted in the *Mtu*CM activity being activated by a maximum of approximately ten-fold. This level of activation was considerably less than the activation of *Mtu*DAH7PS^{WT} achieved under the same conditions.

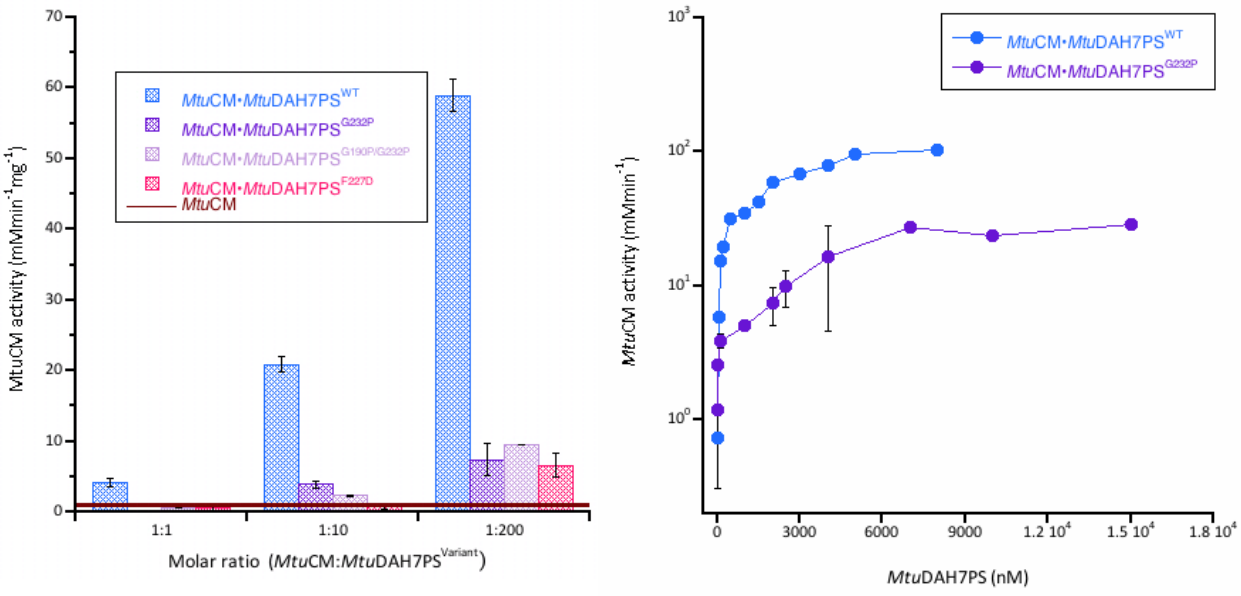

Figure 7.16 A. Activation of *Mtu*CM activity in the presence of either equimolar, ten-fold or 200-fold molar excess of *Mtu*DAH7PS^{WT} (blue hash) and *Mtu*DAH7PS^{G232P} (purple hash), *Mtu*DAH7PS$^{G190P/G232P}$ (light purple hash) and *Mtu*DAH7PS^{F227D} (pink hash). The burgundy line indicates the activity of *Mtu*CM alone. Assays conducted with 150 µM chorismic acid and 60 nM *Mtu*CM except for reactions requiring a 200-fold excess of *Mtu*DAH7PS where 10 nM of *Mtu*CM was used and *Mtu*CM alone where 90 nM was used and the results normalised. Error bars depict the standard deviation of duplicate measurements. B. *Mtu*CM activity in the presence of increasing concentration of *Mtu*DAH7PS^{WT} (blue dots) or *Mtu*DAH7PS^{G232P} (purple dots). Single point assays were conducted with 10 nM *Mtu*CM and 150 µM chorismic acid. Error bars depict the standard deviation of duplicate measurements.

To ascertain if this poor activation could be overcome by increasing the concentration of the dimeric *Mtu*DAH7PS variants the *Mtu*CM activation profile for *Mtu*DAH7PS^{G232P} was examined more closely.

The activation of *Mtu*CM with increasing *Mtu*DAH7PS^{G232P} concentration was plotted (Figure 7.16B). The kinetic assays were conducted in the standard kinetic buffer of 50 mM BTP 1mM TCEP pH 7.5 with 10 nM *Mtu*CM, 150 µM PEP and initiated with 150 µM chorismic acid and varying concentrations of either *Mtu*DAH7PS^{G232P} or *Mtu*DAH7PS^{WT}. The experimental data showed *Mtu*DAH7PS^{G232P} was incapable of enhancing *Mtu*CM activity to the same extent as the wild type enzyme.

The *Mtu*CM binding site is located across the tetramer interface of *Mtu*DAH7PS. *Mtu*DAH7PS^{G232P}, *Mtu*DAH7PS$^{G190P/G232P}$ and *Mtu*DAH7PS^{F227D} have all been shown to be primarily dimeric in solution. The dimeric *Mtu*DAH7PS variants would not be able to interact appropriately with *Mtu*CM, resulting in the observed loss in their ability to activate *Mtu*CM activity and form the *Mtu*CM•*Mtu*DAH7PS complex. The *Mtu*DAH7PS dimer may not be able to induce the *Mtu*CM active site conformational changes required for optimal catalysis.

7.10. Regulation of *Mtu*CM

The *Mtu*CM inhibition studies in the presence of a ten-fold molar excess of *Mtu*DAH7PS variant were conducted using the standard protocol outlined in Section 9.9.3, except that the chorismic acid concentration was adjusted to 250 µM due to the poor activation of *Mtu*CM activity in the presence of the dimeric *Mtu*DAH7PS variants. *Mtu*DAH7PS$^{G190P/G232P}$ was not analysed as protein stocks had been exhausted. *Mtu*DAH7PS^{G232P} and *Mtu*DAH7PS^{F227D} displayed no evidence of inhibition in the presence of any single or combination of aromatic amino acids (Figure 7.17). The lack of inhibition may mean the transmission of ligand binding across the *Mtu*CM•*Mtu*DAH7PS interface is dependent on *Mtu*DAH7PS accessing the tetramer structure. However, the lack of inhibition was more likely an indication that very little *Mtu*CM•*Mtu*DAH7PS complex had formed in solution. Further insight could be gained by repeating the *Mtu*CM inhibition studies with a higher molar excess of *Mtu*DAH7PS, i.e. 200-fold to force more complex formation.

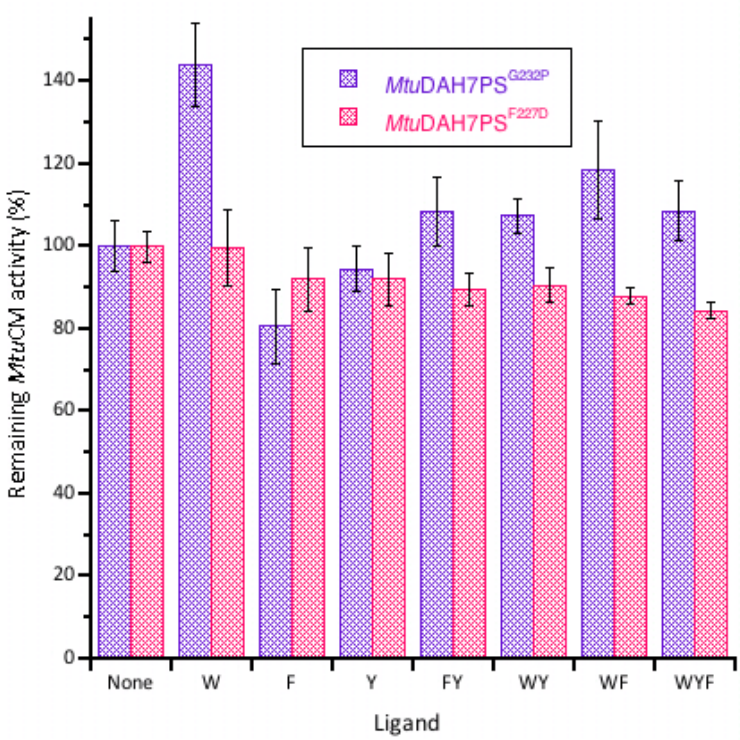

Figure 7.17 Remaining *Mtu*CM activity in the presence of various single, binary and ternary combinations of aromatic amino acids and a ten-fold excess of *Mtu*DAH7PS^{G232P} (purple hash) or *Mtu*DAH7PS^{F227D} (pink hash). The aromatic amino acids are represented by their one letter code; Trp, W; Phe, F and Tyr, Y. Each letter also represents 200 µM of the corresponding aromatic amino acids. Assays conducted in the presence of 250 µM chorismic acid and 60 nM *Mtu*CM. Error bars depict the standard deviation of duplicate measurements. P-values provided in appendix V.

Intriguingly *Mtu*DAH7PS^{G232P} was a better activator of *Mtu*CM activity in the presence of Trp. As the Trp site is located at the tetramer interface it is possible Trp binding would encourage tetramer formation. It is tempting to attribute the improved activation of *Mtu*CM activity to Trp shifting the quaternary structure equilibrium of *Mtu*DAH7PS^{G232P} towards tetramer formation however further evidence, such as AUC, is required to support this conclusion.

7.11. Chapter summary

*Mtu*DAH7PS^{G232P}, *Mtu*DAH7PS$^{G190P/G232P}$ and *Mtu*DAH7PS^{F227D} were all successfully prepared and purified. AUC, native PAGE and SAXS all showed the quaternary structure of the three variant enzymes had been disrupted. At high concentrations (>1 mg/mL) the *Mtu*DAH7PS dimer was

favoured, and at low concentration (< 0.6 mg/mL) the *Mtu*DAH7PS monomer was favoured. The Gly232Pro substitution located on the α2b-β3 loop had unintentionally disturbed the tetramer interface, preventing *Mtu*DAH7PS tetramer formation. Conversely the Phe227Asp substitution was successfully engineered to disrupt the tetramer interface by causing repulsion between the hydrophobic pocket that would normally bind Phe227 and the Asp that replaced it. CD showed there was no change to the secondary structure of any of the variant enzymes as a result of the introduced substitutions. Successful preparation of *Mtu*DAH7PS^{F227D} helped to distinguish which properties of *Mtu*DAH7PS^{G232P} and *Mtu*DAH7PS$^{G190P/G232P}$ are due to their introduced substitution(s) and which are due to the disruption of their quaternary structure.

All three dimeric *Mtu*DAH7PS variants were active with similar kinetic parameters. The variant enzymes all exhibited poor activity, primarily because the concentration of E4P required for effective catalysis had increased by over ten-fold. The concentration of PEP required for effective catalysis had also increased but more modestly. Intriguingly the turnover number for the dimeric variants was significantly higher than *Mtu*DAH7PS^{WT}, which helped to compensate for the poor affinity of the enzymes for E4P. As all three variant enzymes share similar kinetic parameters it is highly likely the change in quaternary structure is responsible for the loss in E4P affinity. The E4P-dependent kinetics of *Mtu*DAH7PS$^{G190P/G232P}$ showed no cooperativity in the presence of Trp and Phe. The lack of cooperative E4P binding suggests the tetrameric *Mtu*DAH7PS structure may be important for signalling between the allosteric binding sites and the active site.

DSF, ITC, AUC and inhibition studies collectively showed all three aromatic amino acids could bind to the three variant enzymes. Phe and Tyr binding had not been adversely affected, whilst Trp binding was significantly weakened. The Trp binding site is located very near the tetramer interface, with several residues contributing to both the Trp binding site and the tetramer interface. Consequently, changes to the quaternary structure may affect the conformation of the binding site and the flexibility of the regions near the Trp binding site, ultimately discouraging Trp binding. Furthermore the Gly232Pro and Phe227Asp substitutions are located close to both the Trp binding site and the tetramer interface and may have inadvertently contributed to the disruption of Trp binding to the Trp

site. Phe and Tyr bind at sites 1 and 2 at the dimer interface and the disruption of the tetramer interface is less likely to affect these binding sites directly. Additionally, AUC revealed Trp and Phe stabilised the dimer formation of *Mtu*DAH7PS^{G232P}. As the Phe-selective binding site, site 1, is located at the dimer interface it is understandable that Phe binding may help strengthen interactions between the two subunits. ITC also revealed that Phe did not improve Trp binding to *Mtu*DAH7PS^{G232P} or *Mtu*DAH7PS^{F227D}; evidence that the *Mtu*DAH7PS tetramer is required for signal transmission between the allosteric binding sites.

Inhibition studies of *Mtu*DAH7PS activity conducted at 150 µM E4P showed *Mtu*DAH7PS^{G232P}, *Mtu*DAH7PS$^{G190P/G232P}$ and *Mtu*DAH7PS^{F227D} were sensitive to the presence of Phe and Tyr, but showed no evidence of synergistic inhibition. The lack of synergy is consistent with the lack of synergy observed by ITC for *Mtu*DAH7PS^{G232P} and *Mtu*DAH7PS^{F227D}. Due to the huge increase in the K_m^{E4P} the standard inhibition studies of the dimeric *Mtu*DAH7PS variants were conducted at an E4P concentration less than half the K_m^{E4P} for the dimeric variants. For *Mtu*DAH7PS^{WT} the E4P concentration in the inhibition studies was roughly five times the *Mtu*DAH7S^{WT} K_m^{E4P}. To correct for the difference in relative E4P concentrations the inhibition assays were also conducted at an E4P concentration three to five times the K_m^{E4P} of the dimeric *Mtu*DAH7PS variants (1800 µM). At this high concentration of E4P *Mtu*DAH7PS^{G232P}, *Mtu*DAH7PS$^{G190P/G232P}$ and *Mtu*DAH7PS^{F227D} all showed no sensitivity to any single or combination of aromatic amino acids. Thus the sensitivity to Phe and Tyr demonstrated by the dimeric *Mtu*DAH7PS variants in the standard inhibition study was most likely an artefact of the relatively low E4P concentration (150 µM) at which the inhibition studies were conducted. Therefore the *Mtu*DAH7PS tetramer quaternary structure is required for effective regulation of *Mtu*DAH7PS.

*Mtu*DAH7PS^{G232P}, *Mtu*DAH7PS$^{G190P/G232P}$ and *Mtu*DAH7PS^{F227D} poorly boosted *Mtu*CM activity and showed little evidence of regulatory sensitivity. Two *Mtu*CM dimers bind across the tetramer interface of *Mtu*DAH7PS (Figure 7.18). The dimeric *Mtu*CM binds across the interface with one *Mtu*CM subunit bound to each *Mtu*DAH7PS asymmetric dimer and this binding mode is repeated at the opposite side of *Mtu*DAH7PS. The disruption of the tetramer interface by Gly232Pro and

Phe227Asp, has most probably inadvertently disrupted the *Mtu*CM binding site. Since the dimeric *Mtu*DAH7PS variants do not form an appreciable amount of tetramer the *Mtu*CM dimer can only form half the number of contacts, resulting in a much weaker interaction. This weaker interaction between *Mtu*CM and *Mtu*DAH7PS^{WT} may result in a transient *Mtu*CM•*Mtu*DAH7PS^{dimer} complex, with the short time span of the association most likely limiting the benefits of the interaction from being exploited. Moreover, the restricted interactions between the dimeric *Mtu*DAH7PS variants and *Mtu*CM may not invoke the active site rearrangement of *Mtu*CM required for activation. The proposed mechanism of inhibition of *Mtu*CM activity is via breaking or weakening the interaction between *Mtu*CM and *Mtu*DAH7PS preventing proper activation. Hence, it is unlikely *Mtu*CM and the dimeric *Mtu*DAH7PS variants form a sufficient amount of the *Mtu*CM•*Mtu*DAH7PS^{dimer} complex to detect inhibition.

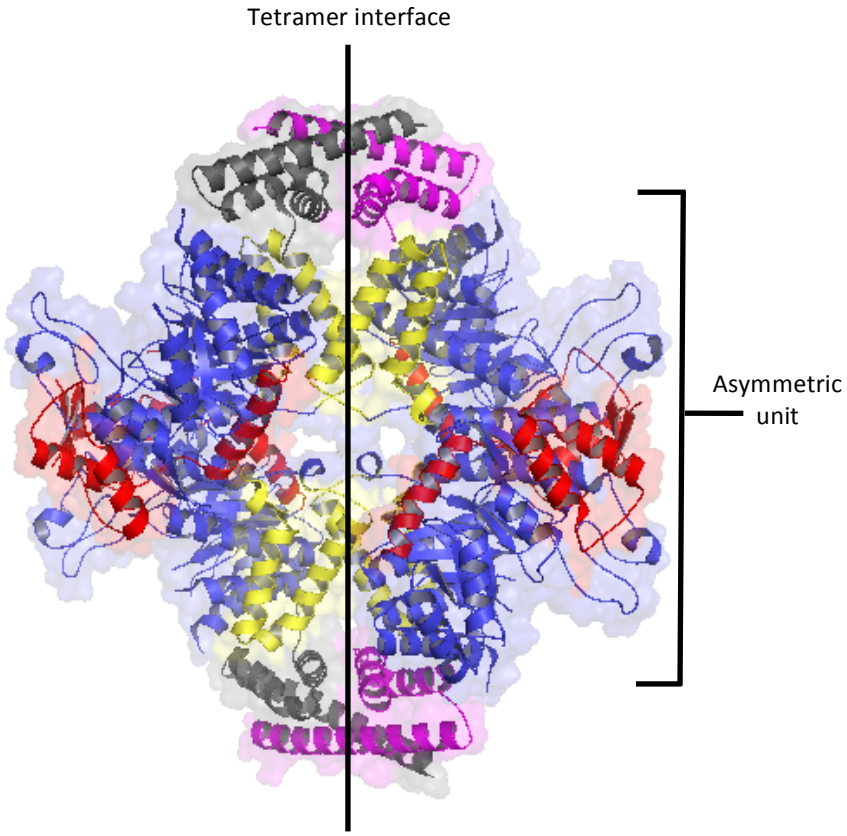

Figure 7.18 Cartoon and surface depiction of the *Mtu*CM bound *Mtu*DAH7PS crystallographic coordinates (PDB code: 2W19). For *Mtu*DAH7PS the core $(\beta/\alpha)_8$ barrel structure is coloured blue, the N-terminal extension is coloured red and the additional helices to the α2-β3 loop are coloured yellow. One subunit of the *Mtu*CM dimer is coloured grey, the second magenta.

*Mtu*DAH7PS^{G232P}, *Mtu*DAH7PS$^{G190P/G232P}$ and *Mtu*DAH7PS^{F227D} exist as a mixture of monomer and dimer in solution. Therefore the introduction of the Gly232Pro or Phe227Asp substitution has clearly disrupted the quaternary structure of the *Mtu*DAH7PS variants. The similarity in the properties of the three variant enzymes showed it is the change in quaternary structure, which is largely responsible for the changes in their observed kinetic and biophysical properties. These dimeric variants have highlighted the necessity of *Mtu*DAH7PS to be able to access the tetrameric structure for proper catalytic and regulatory function. Thus, in all likelihood the tetrameric *Mtu*DAH7PS structure is the most biologically relevant form of the enzyme.

8. Thesis summary and future directions

The functional and structural studies of *Mtu*DAH7PS presented within this thesis have expanded upon previous work on the enzyme by the Parker research group.[48,64,69,71,115,126] The work described in this thesis largely utilised the technique of SDM to generate variant proteins in order to investigate the regulation of *Mtu*DAH7PS so as to better understand how the complex allostery is achieved in the absence of significant conformational change. This thesis also describes investigations into the interactions between *Mtu*DAH7PS and *Mtu*CM first described in 2009.[85]

8.1. *Mtu*DAH7PS is subject to ternary synergistic allostery

Enzymes located at critical points in metabolic pathways are generally tightly regulated to control metabolic flux into the pathway. Enzymes such as DAH7PS, that are located within branched pathways present particular challenges in order to tune enzyme activity to meet cellular requirements without causing a build up of harmful, unstable or unnecessary metabolites. DAH7PS enzymes from different organisms employ different strategies to control entry into aromatic amino acid biosynthesis. It is speculated that in plants DAH7PS activity is controlled primarily at the transcriptional level, although the exact mechanism remains unclear.[70,129-131] Some organisms such as *E. coli* and *S. cerevisiae* utilise multiple DAH7PS isozymes, with each isozyme being regulated by a particular aromatic amino acid.[49,50,132,133] Other organisms encode for a single DAH7PS, which is subject to feedback regulation by specific individual aromatic amino acids. One example is *T. maritima* DAH7PS, which is sensitive to Phe or Tyr but is never completely inhibited by either amino acid, presumably to allow basal levels of synthesis of Trp and other metabolites even when Phe or Tyr are in excess.[47,134] *M. tuberculosis* also encodes a single DAH7PS but this enzyme has developed synergistic allostery, with a far more sophisticated strategy to allow DAH7PS activity to be fine-tuned to meet cellular needs.

Prior to the commencement of this work it had been established that *Mtu*DAH7PS was insensitive to individual aromatic amino acids, but synergistically inhibited by binary combinations of aromatic amino acids that included Trp.[48,63,70] Crystallographic studies had identified three distinct allosteric binding sites; the Trp site, site 1 and site 2.[48,71,91] The Trp site is the only allosteric site Trp has been observed to occupy. The selectivity of sites 1 and 2 was more ambiguous as both Phe and Tyr have been observed to occupy both sites.[48,71,91] Moreover, it was uncertain whether both sites 1 and 2 or if only one of the sites played a part in the allosteric regulation of *Mtu*DAH7PS.

SDM, kinetic analysis and ITC showed that site 1 was able to bind both Phe and Tyr, but had to be occupied by Phe, in combination with Trp bound to the Trp site, to elicit an inhibitory response. These findings have now led to site 1 being designated the Phe-selective site. Site 2 was found to show a higher affinity for Tyr than Phe. Furthermore Tyr, must occupy site 2, in combination with Trp at the Trp site, to elicit an inhibitory response, leading site 2 to be designated the Tyr-selective site. Additionally, it was found the binary synergistic inhibitory response caused by Trp and Phe was augmented by the addition of Tyr, which almost completely abolished *Mtu*DAH7PS activity.

The presence of three distinct allosteric binding sites, each specific to a particular aromatic amino acid, allows *M. tuberculosis* to finely tune *Mtu*DAH7PS activity in response to the cellular concentrations of all three aromatic amino acid end products. Synergistic regulation of enzymes by two effectors is not uncommon. Glutamine phophoribosylpyrophosphate amidotransferase from *B. subtilis* is synergistically feedback regulated by the end products of the *de novo* purine nucleotide synthesis, adenine diphosphate (ADP) and guanine monophosphate (GMP).[135] Aspartate transcarbamoylase from *E. coli* is synergistically regulated by the allosteric effectors pyrimidine cytidine and uracil triphosphates (CTP and UTP), the end products of pyrimidine biosynthetic pathways.[119] However, the highly sophisticated ternary synergistic allosteric regulation observed for *Mtu*DAH7PS is unique amongst characterised regulatory enzymes. Although, the lack of examples of ternary synergistic allosteric regulation in the literature is perhaps a reflection of the difficulty in identifying the necessary conditions to observe the phenomena, as opposed to a lack of its prevalence in nature.

8.2. The synergistic allosteric regulation of *Mtu*DAH7PS involves a highly evolved network of residues to communicate between remote sites

Traditionally the transmission of signals between remote allosteric binding sites and between allosteric binding sites and active sites have largely been understood in terms of conformational change. For instance the binding of Tyr to the DAH7PS from *T. maritime* causes the regulatory domain favour a closed form of the enzyme rather than an open form, effectively blocking the active site.[47,62] The allosteric regulation of proteins that undergo significant structural change is considered to be enthalpically driven, whereas the allosteric regulation of proteins that do not undergo any obvious change in conformation is considered to be entropically driven.[3,6,24] The binding of Trp and Phe to *Mtu*DAH7PS does not cause any significant conformational changes and there are very few structural differences between the liganded and unliganded structures.[48,71] Furthermore, the allosteric binding sites of *Mtu*DAH7PS are remote from the active site and each other. There are very few known well-studied examples of allostery not associated with changes in conformation. One, commonly cited example is the interaction of the catabolite activator protein from *E. coli* with the allosteric effector cyclic adenine monophosphate (cAMP), which results in changes in the enzymes intrinsic motions without significantly altering the structure of the enzyme.[25,136] MD simulations indicate the synergistic allosteric regulation of *Mtu*DAH7PS is largely entropically driven.[71,115] Upon binding of Trp or Phe the rigidity of the alternative allosteric binding pockets changes, improving the binding of Phe or Trp respectively.[71,115] Similarly, upon binding of Trp and Phe, the flexibility of the E4P binding loop (the β2-α2 loop) was predicted to increase, increasing the entropic cost of E4P binding, reducing catalytic activity.[71,115]

The subtle changes in enzyme dynamics that occur upon Trp and Phe binding to *Mtu*DAH7PS are becoming increasingly well understood, but exactly how occupancy at one allosteric site is communicated to the other allosteric sites, and how the occupancy of two or more distinct allosteric sites is communicated to the active site is a more challenging problem to solve. The current general view on allosteric communication is that multiple propagation pathways exist, major and minor, as a

result of proteins existing as population ensembles of different states.[3,18,71,125,136,137] Local stress(s) applied to the allosteric binding sites by ligand binding or by covalent modification triggers propagation of a signal along multiple pathways to other allosteric binding sites and/or the active site.[3,18,125,137]

Computational techniques such as, anisotropic thermal diffusion, SCA and MD simulations are frequently employed to identify potential clusters or residues that may be involved in the communication pathways of a protein.[25,115,122,123,125,138,139] A combination of SCA and MD simulations were used to identify a cluster of coevolved residues that could potentially be critical to the allosteric regulation of *Mtu*DAH7PS.[71,115] This network or cluster of residues is thought to transmit subtle changes in flexibility or molecular motion across the enzyme, ultimately providing entropic control of the affinity of each binding site for its ligand.[23,71] Although insightful, such findings are more meaningful when accompanied by experimental validation. Hence, the roles of four residues belonging to the cluster of residues identified by computational techniques were examined as described in chapter 5. Substitution of any one of the four residues was surprisingly effective at disrupting the synergistic regulation of *Mtu*DAH7PS and/or *Mtu*CM as shown by, kinetic analysis, ITC, and DSF. The substitution of Gly190 for Pro had the most radical effect and rendered *Mtu*DAH7PS insensitive to any combination of allosteric amino acids. Gly190 is located along the α2-α2a loop, and the substitution to Pro was intended to restrict the flexibility of the loop and the adjacent inserted α2a and to a lesser extent the α2b helices. Changes in the flexibility of the α2 α2a loop may impact on the ability of the backbone carbonyl moiety of Ala192, also located along the loop, from hydrogen bonding with the bound Trp ligand. The substitution of Gly190 highlights the importance of the flexibility of the secondary and tertiary structure, and therefore molecular dynamics, for the transmission of signals between allosteric and/or the active site of *Mtu*DAH7PS.

These results imply that the SCA and MD simulations have successfully identified residues critical to the proper function of the synergistic allosteric regulation of *Mtu*DAH7PS. Furthermore, three of the residues targeted were not directly located at either the allosteric binding sites or the active site therefore, these residues must form part of the communication network responsible for transmitting

occupancy of an allosteric binding site to other allosteric binding sites and the active site. The drastic changes to the regulation of *Mtu*DAH7PS (and *Mtu*CM) due to a single residue substitution highlights how highly evolved this communication pathway is.

Additional residues involved in the signalling network could potentially be found by the continuation of this work. SCA and MD analysis provided a series of residues that are candidates for further investigation using SDM and the same kinetic and biophysical techniques described here. The continuation of this work could lead to a map of the molecular pathways within *Mtu*DAH7PS responsible for the signal transfer between allosteric sites, to the active site and to *Mtu*CM. A greater understanding of how allostery is communicated within *Mtu*DAH7PS could potentially be exploited to develop novel anti-TB drugs.

This work not only validates the computational studies on *Mtu*DAH7PS, but also provides a successful example of how computational techniques can be used to successfully identify allosteric communication networks in enzymes that show little or no conformational change. Discoveries of allosteric systems such as *Mtu*DAH7PS that are mediated by subtle changes in molecular dynamics force the traditional views of allostery to be reassessed and evolve into more flexible and robust paradigms.

8.3. The *Mtu*DAH7PS tetramer is the regulated quaternary structure

Not all residues identified as part of the *Mtu*DAH7PS allosteric communication network were amenable to substitution without adversely affecting protein solubility or quaternary structure. Chapter 7 describes the characterisation of *Mtu*DAH7PS variants where the residue substitution disrupted quaternary structure, destabilising the homotetramer. The substitution of Gly232 to Pro proved to be of particular interest. Gly232 is located on the α2b-β3 loop succeeding the inserted α2a and α2b helices. Substitution of Gly232 to Pro was intended to limit the flexibility of this loop and the preceding helices. However, an unintended consequence of the Gly232Pro substitution was the

disruption to the quaternary structure, *Mtu*DAH7PS^{G232P} (and *Mtu*DAH7PS$^{G190P/G232P}$) could not form the tetramer. AUC, SAXS and native PAGE show these *Mtu*DAH7PS variants are primarily dimeric in solution. There is a link between the allosteric network responsible for signalling ligand occupancy at the allosteric sites and the control of quaternary structure and these findings imply quaternary structure is important to the regulation of *Mtu*DAH7PS.

The serendipitous formation of the dimeric *Mtu*DAH7PS variants provided an unexpected opportunity to characterise the properties of the *Mtu*DAH7PS dimer. Kinetic and biophysical analysis showed that all dimeric *Mtu*DAH7PS variants possessed a significantly reduced catalytic efficiency and showed very poor regulatory sensitivity. The engineering of another *Mtu*DAH7PS variant (*Mtu*DAH7PS^{F227D}) intended to only disrupt the tetramer interface of *Mtu*DAH7PS, also prevented tetramer formation, and this confirmed that the changes in properties observed of *Mtu*DAH7PS^{G232P} were due to the change in quaternary structure and not the substitution of Gly232.

In chapter 2 AUC results showed that *Mtu*DAH7PS^{WT} exists as a mixture of oligomeric states in solution, with increases in protein concentration favouring tetramer formation. The addition of the allosteric ligands, Trp and/or Phe, stabilised the formation of the tetramer at all protein concentrations analysed. This stabilisation is understandable given the allosteric binding sites are located at the dimer and tetramer interfaces.[48,69] Similarly in chapter 6 AUC and SAXS analyses demonstrated that *Mtu*DAH7PS^{K123M} exists as a mixture of primarily monomer and tetramer, but the addition of Phe promoted formation of the tetramer. The stabilisation of the *Mtu*DAH7PS tetramer in the presence of ligand and the poor activity and regulation of the dimeric *Mtu*DAH7PS variants, described in chapter 7, suggests the tetramer is the regulated species.

Previous work has shown that *Mtu*CM binds to *Mtu*DAH7PS across the tetramer interface, which infers the necessity for the formation of the *Mtu*DAH7PS tetramer for the *Mtu*CM•*Mtu*DAH7PS complex to form.[85] The dimeric *Mtu*DAH7PS variants were found to be very poor activators of *Mtu*CM activity and in chapter 3 AUC analyses are presented that show that *Mtu*CM stabilised the formation

of the *Mtu*DAH7PS^{WT} tetramer at all protein concentrations used. These findings are consistent with the formation of the *Mtu*CM•*Mtu*DAH7PS complex being accessed via the *Mtu*DAH7PS tetramer.

In chapter 3 it was hypothesised that *Mtu*DAH7PS inhibited the activity of *Mtu*CM by causing the *Mtu*CM•*Mtu*DAH7PS complex to dissociate when Phe bound *Mtu*DAH7PS. Native PAGE and AUC studies support this proposed hypothesis. This hypothesis implies that the unliganded *Mtu*DAH7PS species is not equivalent to the liganded (Phe-bound) *Mtu*DAH7PS species. Hence either a small conformational change, such as a twist across the tetramer interface or a significant increase in the molecular motion of the α2b, α7 and α8 helices (and their associated loops) located at the *Mtu*CM•*Mtu*DAH7PS interface must weaken the interactions between *Mtu*CM and *Mtu*DAH7PS. It should be noted that Trp alone does not cause the same changes to the *Mtu*DAH7PS tetramer as Phe, as indicated by the insensitivity of the *Mtu*CM•*Mtu*DAH7PS complex to Trp. This different kinetic behaviour suggests Trp may stabilise a tetramer species, with similar affinity for *Mtu*CM as the unliganded *Mtu*DAH7PS, but with an increased affinity for other allosteric ligands.

As stated previously the AUC showed unliganded *Mtu*DAH7PS^{WT} exists as a mixture of monomer, dimer and tetramer. The stability of the dimeric *Mtu*DAH7PS variants, their regulatory properties, and their catalytic abilities calls into question the biological relevance of the *Mtu*DAH7PS dimer. The tetramer is clearly the relevant regulatory structure, has a higher catalytic efficiency, and is required to interact with *Mtu*CM. The observation of the dimer may simply be an artefact of an *in vitro* environment. The localised cellular concentration within the bacterium cells, salt concentrations, pH, ancillary proteins and cofactors can all influence the quaternary structure a protein adopts *in vivo,* factors that are hard to predict and mimic in a laboratory setting. However, the existence of two distinct tetrameric *Mtu*DAH7PS species does not preclude the possibility that these different conformations are accessed via the dimer or even via the monomer. These possibilities are more akin to the morpheein model of allostery.[5,12,94] The stability of the *Mtu*DA7PS dimer and the ease with which the tetramer interface can be disrupted to prevent tetramer formation (even accidently) supports the viability of a morpheein-like model of allostery via a dimeric intermediate.

The original MWC view has now been expanded and enzymes are now generally considered to exist as protein ensemble of conformational states.[3,20,140] The binding of an allosteric effectors to a protein that exists at equilibrium may vary the overall amplitude and frequency of fluctuations about the mean species or alter the average conformation of the equilibrium.[3,17,20,22,137] The current model is more robust and does not restrict or require the shift in the population ensemble of a protein from occurring via dissociation and of a proteins oligomeric state and reassembly into a new oligomeric state/different conformation. A complex model of different species where the distribution can be altered by ligand, protein partner or substrate binding is better suited to modelling the allosteric regulation of *Mtu*DAH7PS. The experimental findings from this and previous studies have helped to shape our current understanding of how allosteric function is communicated within *Mtu*DAH7PS. Molecular dynamics and quaternary structure clearly play a significant role in the transmission of occupancy at one or more allosteric site to other allosteric sites and the active site.

8.4. CM complex and dissociation

Our understanding of how the thousands of enzyme-catalysed reactions within the *in vivo* cellular environment are interconnected and regulated to meet the cells overall needs is continuously developing but is still not well understood.[141] Cells were once thought to consist of collection of soluble proteins, substrates, cofactors and products within the cellular matrix that relied primarily on diffusion for the right components to come together and react.[2] However, as our understanding of cellular organisation advances, the number of examples of strategic use of compartmentalisation, membrane-bound systems and formation of multimolecular complexes by cells in order to organise and control the enzymes of particular pathways is growing.[2,141-143] An excellent example of the highly organised nature of the cellular environment is the respiratory enzymes of eukaryotic cells that form multimolecular complexes, most of which are membrane bound and localised within the mitrochondria.[2,144,145]

Enzymes from a vast array of metabolic pathways including glycolysis, Krebs cycle, *de novo* purine biosynthesis, DNA repair and replication have been shown to form multimolecular

complexes.[2,140,141,143] There are several obvious advantages to the formation of multimolecular complexes. Complex formation may offer a kinetic advantage to the enzymes by permitting the channelling of metabolites between sequential enzymes.[2,141] Complex formation may also increase the overall stability of each enzyme and reduce the risk of enzyme degradation via proteolysis.[1,2,146] Furthermore the formation of multienzyme complexes affords the cell another mechanism by which to regulate and control enzyme activity: through the association and dissociation of the complex.[147,148] Complex formation may be required for the proper function for some enzymes, whereas for others complex formation may inhibit enzyme activity.[147,148]

In 2009 Sasso *et al.* showed *Mtu*DAH7PS formed a non-covalent complex with *Mtu*CM, which dramatically boosted the catalytic efficiency of *Mtu*CM and bestowed it with regulatory sensitivity to Phe and Tyr.[85] In chapter 4 studies were detailed that demonstrated that *Mtu*DAH7PS boosted *Mtu*CM activity by over 100 fold and endowed *Mtu*CM with regulatory sensitivity to Phe and Tyr, consistent with previous work.[85] This study additionally showed *Mtu*DAH7PS synergistically regulated *Mtu*CM activity when Trp was present in combination with either Phe and/or Tyr. The work described in chapter 4 further expanded upon the findings reported previously by showing conclusively that the allosteric sites of *Mtu*DAH7PS were responsible for the synergistic regulation of *Mtu*CM. The *Mtu*DAH7PS variants generated in chapter 3, engineered to disrupt ligand binding at site 1 or site 2, were utilised in these experiments to show that site 1, and to a lesser extent site 2, were essential for the inhibitory response on *Mtu*CM activity by Phe and Tyr respectively.

Arguably one of the most exciting findings of this work was that the binding of Phe to *Mtu*DAH7PS weakens or alters the interaction between *Mtu*CM and *Mtu*DAH7PS, encouraging the dissociation of *Mtu*CM from *Mtu*DAH7PS. The disruption to the *Mtu*CM•*Mtu*DAH7PS was revealed by a variety of techniques including kinetic analysis, native PAGE and AUC. Control of enzyme activity or protein function of a multienzyme complex via association and dissociation is not unprecedented. One well known example is the suppression of protein synthesis by dissociation of the ribosome in response to cell stress, such as a limited supply of adenosine triphosphate (ATP).[2,149]

As stated in Section 0, the fact that the Phe-bound *Mtu*DAH7PS and unliganded *Mtu*DAH7PS exhibit different affinities for *Mtu*CM suggests their tetramer properties are not the same. One possibility is that Phe binding causes changes to the molecular dynamics of the residues of *Mtu*DAH7PS located at the *Mtu*CM•*Mtu*DAH7PS interface, and this change discourages *Mtu*CM binding. MD simulations predicted that Phe binding leads to increased flexibility of the β7-α7 and β8-α8 loops, which are involved in forming the *Mtu*CM•*Mtu*DAH7PS interface.[71] However, the binding of Trp and Phe, which synergistically inhibit *Mtu*CM activity, reduces the flexibility of these loops, resulting in similar or less flexibility of the β7-α7 and β8-α8 loops, as is predicted for the unliganded enzyme.[71]

Alternatively Phe binding may alter the *Mtu*DAH7PS tetramer species, by altering the nature of the interactions between *Mtu*CM and *Mtu*DAH7PS at the *Mtu*CM•*Mtu*DAH7PS interface, disfavouring the interaction with *Mtu*CM and/or activation of *Mtu*CM activity. The crystallographic coordinates for *Mtu*DAH7PS show no obvious evidence of a twist in the conformation of the *Mtu*DAH7PS tetramer as a result of Phe binding, but subtle changes in conformation could be hidden due to crystal packing effects.[48,69,91] Phe binding does cause a small shift in the β0-strand of one subunit relative β0-strand of the other subunit across the dimer interface of *Mtu*DAH7PS on Phe binding, which is best illustrated by the relative positions of Trp3 in each subunit (Figure 8.1A). This shift may reflect a slight twist of the two subunits across the dimer interface in the plane of the tetramer interface (Figure 8.1B). [48,69,91] Any twisting, even if only slight, at the dimer interface would probably change the interactions of the tetramer interface and the overall tetramer conformation slightly. If substantial enough, this change could be responsible for the reduced affinity of Phe-bound *Mtu*DAH7PS for *Mtu*CM.

However, the SAXS data presented in chapter 2 showed no evidence of *Mtu*DAH7PS^{WT} undergoing any conformational change due to the addition of 200 μM Trp, Phe and Tyr. The change that occurred to the SAXS profile for *Mtu*DAH7PS^{N237A} on the addition of Trp was described in Chapter 6, prove that the *Mtu*DAH7PS tetramer is flexible and can change on ligand binding. The lack of change observed between the SAXS profile for *Mtu*DAH7PS^{WT} with and without Trp, Phe and Tyr does not eliminate the possibility a small conformational change is occurring. SAXS data with a better signal to noise may be required to visualise such subtle changes in conformation.

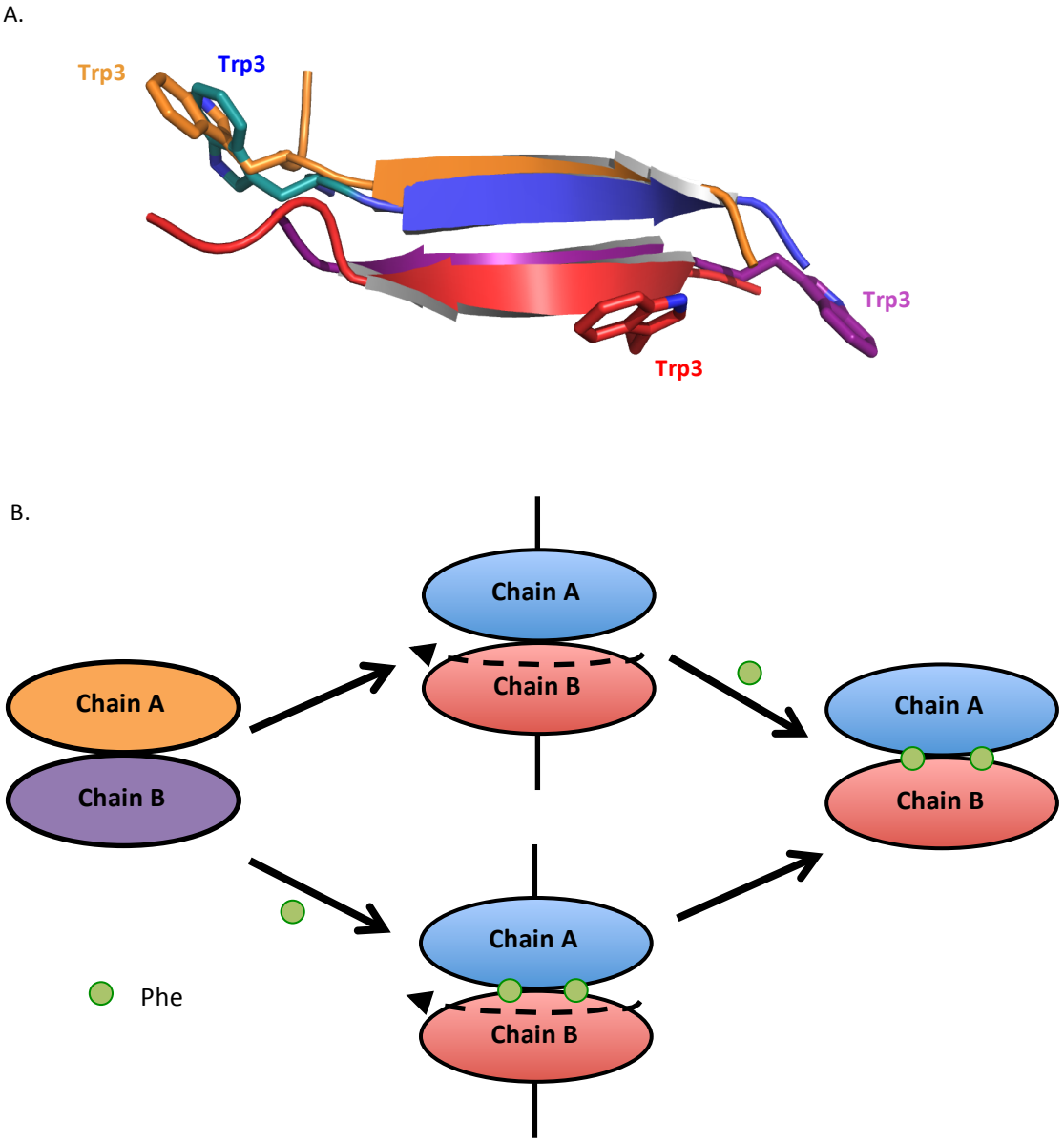

Figure 8.1 A. The antiparallel β-sheet formed between the β0-strands of the two subunits of the dimer interface of *Mtu*DAH7PS shown in cartoon form. Phe binding causes the β0-strand of one subunit to move by about one peptide unit relative to the β0-strand of the other subunit as illustrated by considering the relative positions of Trp3 on each β0-strand. The dimer interface is located between the two subunits of the crystallographic asymmetric unit. The side chain of Trp3 shown in Teal has been modelled in by PyMol. Hypothetically this movement could cause the dimer interface to twist slightly. The crystal structure from *Mtu*DAH7PS bound with Trp- and Phe-bound (PDB code: 3KGF) has each subunit coloured red and blue and the unliganded *Mtu*DAH7PS crystal structure (PDB code: 3NV8) has each subunit coloured orange and purple. Phe is shown as green spheres. B. A schematic representation of the slight twist that may occur at the dimer interface in either in response to Phe binding or in order for Phe to bind. This twist changes the dimer conformation, and therefore the tetramer conformation, reducing *Mtu*DAH7PS affinity for *Mtu*CM. The dimeric subunit shown in orange an purple represents unliganded *Mtu*DAH7PS and the dimeric subunit shown in red and blue represents the Phe-bound *Mtu*DAH7PS dimer subunit. The green sphere represents Phe.

8.5. Future directions

There are various options that could be pursued in order expand upon the research into the regulation of *Mtu*DAH7PS presented in this thesis. The three questions below are particularly pertinent, and addressing these could significantly enhance the extent of our understanding of this sophisticated regulatory system.

8.5.1. Does a twist at the dimer interface of *Mtu*DAH7PS occur?

The hypothesis that the dimeric interface of *Mtu*DAH7PS undergoes a slight twist on Phe binding has been proposed within this body of work. As yet no convincing evidence exists to support this hypothesis, but there are several techniques that could be used in order to observe the twist including ^{19}F, ^{2}H, and/or a combination of ^{15}N, ^{13}C and ^{1}H nuclear magnetic resonance (NMR), pulsed electron-electron double resonance (PELDOR) and fluorescence resonance energy transfer (FRET).[150-152] PELDOR is an electron paramagnetic resonance technique used to measure the strength of spin coupling between spin labels to determine the distance between the spin-labels.[152] A spin-label would need to be covalently attached to each *Mtu*DAH7PS subunit near the dimer interface before PELDOR could be carried out. FRET is a phenomenon that occurs when the emission and absorption spectra of two different chromophores overlap.[153,154] The amount of FRET signal depends on the relative orientation and distance between the chromophores, enabling the technique to be used as a highly sensitive 'spectroscopic ruler'.[153,154] FRET also requires each *Mtu*DAH7PS subunit to be labelled, covalently or non-covalently, near the dimer interface with either a chromophore donor or acceptor. The necessity of subunit labelling for both PELDOR and FRET is a distinct disadvantage, as this modification risks disrupting or preventing ligand binding or the *Mtu*DAH7PS quaternary structure itself. The choice of label(s) and their placement will need to be carefully considered for either technique.

FRET and PELDOR could also be used to measure the interaction between *Mtu*CM and *Mtu*DAH7PS. Monitoring changes that occur across the *Mtu*CM•*Mtu*DAH7PS on Phe binding could also reveal a change in *Mtu*DAH7PS tetramer conformation and confirm that Phe binding does cause *Mtu*CM to dissociate from *Mtu*CM.

8.5.2. How is the allosteric regulation of *Mtu*DAH7PS transmitted across the *Mtu*CM•*Mtu*DAH7PS interface to *Mtu*CM?

This work has clearly established that the allosteric binding sites of *Mtu*DAH7PS are responsible for the regulation of *Mtu*CM, and that occupancy at the allosteric binding sites of *Mtu*DAH7PS is transmitted along a network of residues to other allosteric sites and to the *Mtu*CM•*Mtu*DAH7PS interface (*Mtu*CM binding site). It is still unclear exactly which residues of *Mtu*DAH7PS and *Mtu*CM are responsible for the transmission of the allosteric signal across the interface. The most obvious candidates for investigation are the six residue pairs that form polar contacts across the *Mtu*CM•*Mtu*DAH7PS interface. SDM and kinetic analysis could be used to evaluate the role of these residues. However, changes in these residues risks completely disrupting *Mtu*CM binding. SCA and MD simulations could be used to identify alternative targets that perhaps do not form such crucial interactions between *Mtu*CM and *Mtu*DAH7PS.

8.5.3. Is the highly sophisticated allostery of *Mtu*DAH7PS a common feature of microbial type II DAH7PS enzymes?

*Mtu*DAH7PS is currently the only structurally characterised type II DAH7PS and is by far the best functionally characterised type II enzyme. A broader question to be considered is whether all type II DAH7PS enzymes demonstrate synergistic allostery or form multienzyme complexes with other enzymes of the aromatic amino acid biosynthetic pathway. This question is complicated by the fact that many microbial organisms possess a combination of type I and type II DAH7PS, and/or may possess multiple open reading frames encoding the type II DAH7PSs.[70] Often these organisms have

DAH7PS enzymes that are associated with the production of secondary metabolites as well as for the primary metabolism of the aromatic amino acids.[70] Thus investigation of a broad range of type II DAH7PS enzymes from a variety of organisms, such as those listed below, is required to better understand the functional and structural characteristics of the type II DAH7PS family and lead to the classification of new sub-types within the type II DAH7PS family.

One of two DAH7PSs from *C. glutamicum* (*Cgl*DAH7PS) is a type II DAH7PS, and is reportedly only inhibited by Trp. However, when *Cgl*DAH7PS forms a complex with the CM from the same organism the *Cgl*DAH7PS activity is boosted and it is bestowed with additional sensitivity to prephenate.[88-90] This response appears to be a variation of the symbiotic regulation observed for *Mtu*DAH7PS and *Mtu*CM.

The type II DAH7PS from *Helicobacter pylori* (*Hpy*DAH7PS) has also been functionally characterised by members of the Parker research group.[63] Despite sharing a 67 % sequence similarity with *Mtu*DAH7PS, *Hpy*DAH7PS is insensitive to the presence of any individual or combination of aromatic amino acids. If *Hpy*DAH7PS is allosterically inhibited, the right allosteric inhibitor or combination of inhibitors is yet to be found. Further investigation of *Hpy*DAH7PS is needed to assess whether a binding partner is required for allosteric regulation such as *Hpy*CM. Structural characterisation of *Hpy*DAH7PS could also determine whether it has allosteric binding sites that are similar to *Mtu*DAH7PS and therefore whether allosteric regulation would be expected.

The genome of *Pseudomonas aeruginosa* also encodes for at least two DAH7PS enzymes, one of these is a type II DAH7PS (*Pae*DAH7PS).[70] Sequence alignment shows *Pae*DAH7PS is missing part of the sequence that aligns with the Trp binding site of *Mtu*DAH7PS.[70] Functional and structural characterisation of this *Pae*DAH7PS is yet to be undertaken. It is unlikely that *Pae*DAH7PS will be synergistically regulated if it is truly lacking a Trp binding site, but could still form a multienzyme complex as seen for *Cgl*DAH7PS and *Cgl*CM that bestows *Pae*DAH7PS with regulatory sensitivity. *Pae*DAH7PS could also be involved with the biosynthesis of secondary metabolites and may be subject to feedback regulation from different metabolites.

8.6. Concluding remarks

*Mtu*DAH7PS exhibits a remarkably sophisticated regulatory mechanism that tightly controls not only the activity of *Mtu*DAH7PS itself, but also of its partner enzyme *Mtu*CM. These studies have furthered our understanding of the mechanism of allosteric regulation employed by *Mtu*DAH7PS. Importantly, these studies have started to address how *Mtu*DAH7PS is regulated and how allosteric regulation is communicated between the allosteric sites, to the active site and to *Mtu*CM. This knowledge could eventually contribute to the rational design of drugs that mimic allosteric effectors or disrupt the allosteric regulation of the target enzyme. For *Mtu*DAH7PS this could mean the development of anti-TB drugs that target its allosteric binding sites designed to inhibit both *Mtu*DAH7PS and *Mtu*CM.

9. Experimental details

9.1. General experimental

9.1.1. Water

All buffers and solutions made using water filtered by Millipore Milli-Q water system. Any water used for the purpose of PCR was autoclaved prior to use.

9.1.2. pH measurement

The pH of solutions was determined using a Denver Instruments UB-10 Ultra-Basic pH meter with either a standard or micro-probe. The addition of either HCl or NaOH solution was used to adjust the pH of the solutions if necessary, with the exceptions of buffers for CD where H_2SO_4 was used in place of HCl.

9.1.3. Centrifugation

Centrifugation was performed by either Sorvall Evolution RC (Thermo Scientific), Heraeus Multifuge 1 S-R (Thermo Scientific) Heraeus Fresco 17 (Thermo Scientific) or a Minispin® Centrifuge (Eppendorf).

9.1.4. Culture media

All *E. coli* cells were grown in Lysogeny-Broth (LB). LB media was prepared by dissolving 20 g/L LB (Lennox L) base in Milli-Q water and sterilised by autoclaving at 121 ˚C, 15 psi for 20 min. The appropriate antibiotics were added just prior to use.

LB-agar plates were prepared by dissolving 20 g/L LB (Lennox L) base and 15 g/L agar in Milli-Q water and sterilising by autoclaving at 121 ˚C, 15 psi for 20 min. The LB-agar mixture was then heated in a

microwave until boiling and left to cool in a 60 ˚C oven. The mixture was allowed to cool to ~50 ˚C on the bench and the appropriate antibiotics were added just prior to pouring the plates into round petri dishes and allowing to set. Plates were stored for up to a week at 4 ˚C.

9.1.5. Antibiotic stocks

Stock solutions of ampicillin and chloramphenicol were prepared and stored at -80 ˚C. Ampicillin (100 mg/mL) was prepared in Milli-Q water and chloramphenicol (50 mg/mL) was made in ~95 % ethanol (analytical grade).

9.1.6. Generation of protein structure figures

Figures of protein structures were created using PyMOL (version 1.5, Schrödinger LLC).[155]

9.2. Site-directed mutagenesis and transformations

9.2.1. Primers

Primers were designed using the QuikChange® Primer Design Tool (Agilent technologies) (Table 9.1) and synthesised by Invitrogen. Primers were stored at 300 mM in autoclaved Milli-Q water.

Table 9.1 Sequence of primers designed for site-directed mutagenesis.

Substitution	Strand	Primer Sequence 5'→3'
Arg171Ala	sense	gtcgcggctggtcgcggcttacgctaac
	antisense	gttagcgtaagccgcgaccagccgcgac
Arg256Ala	sense	gtgctcgactacgaggccgccatgttgaggtt
	antisense	aacctcaacatggcggcctcgtagtcgagcac
Gly190Pro	sense	gctgacttcgtcgcccctggcgtcgctg
	antisense	cagcgacgccaggggcgacgaagtcagc
Val103Ala	sense	catattcggggcaatgcccgtgccttgttgcag
	antisense	ctgcaacaaggcacgggcattgccccgaatatg
Tyr131Ala	sense	catcgccggtcaggccgcgaagcctcgg
	antisense	ccgaggcttcgcggcctgaccggcgatg
Asn175Ala	sense	gctggtccgggcttacgctgccgccagtgcg
	antisense	cgcactggccggcagcgtaagcccggaccagc
Lys123Met	sense	cagcatgccagtggtgatggtggcccg
	antisense	cgggccaccatcaccactggcatgctg
Asn237Ala	sense	ggcggtctgtagagcgcggtcggccacc
	antisense	ggtggccgaccgcgctctacagaccgcc
Gly232Pro	sense	gcggttcatgagtgcctgtccggtggccgac
	antisense	gtcggccaccggacaggcactcatgaaccgc
Phe227Asp	sense	ccacaggcactcatgtcccgcagcccacgatc
	antisense	gatcgtgggctgcgggacatgagtgcctgtgg

9.2.2. Site-directed mutagenesis

Site-directed mutagenesis (SDM) was used to introduce amino acid substitutions into the pProExHta-*Mtu*DAH7PS plasmid. The mutagenesis was performed using the QuickChange® Lightning Site-Directed Mutagenesis Kit (Stratagene) following the manufacturers recommended protocol for 50 µL reactions. For *Mtu*DAH7PS containing a single amino acid substitution the pProExHta-*Mtu*DAH7PS plasmid was used as the DNA template. To generate the double amino acid substituted *Mtu*DAH7PS$^{G190P/G232P}$ the pProExHta-*Mtu*DAH7PS^{G190P} plasmid was used as the template. The single amino acid substitutions were introduced using synthetic oligonucleotide primers. These primers were used to amplify the whole plasmid via a thermocycling reaction performed using a Veriti®96-well Thermal Cycler (Applied Biosystems). After thermocycling the SDM product was treated with

Dpn1 (Stratagene) for 5 min at 37 ˚C to digest the template DNA. The Dpn1 treated SDM product was then transformed into *E. coli* OneShot Top10 cells (Invitrogen) for storage. For protein expression the SDM products for the *Mtu*DAH7PS variants were transformed into *E. coli* BL21(DE3) pGroESL cells.

9.2.3. Agarose gel electrophoresis

Either pre-cast E-Gel® 1.2 % (w/v) agarose gels (Invitrogen) or self-cast 1 % agarose gels were used for agarose gel electrophoresis. Reaction products were loaded on to E-Gel's® without dye and run as directed by the manufacturer. The E-Gel® was run and monitored with an E-Gel R iBase™ and Safe Imager™ (Invitrogen).

Self-cast 1 % agarose gels were prepared by heating 0.3 g of agarose in 30 mL of tris-acetate-EDTA (TAE) buffer until dissolved. The solution was then cooled ~50 ˚C before adding SYBR Safe® DNA stain, poured into a mould and allowed to set. For the self-cast gels samples were prepared by adding a 6x sample loading buffer. Electrophoresis performed using a Mini-Sub® Cell GT (Bio-Rad). Samples were run in TAE buffer for 60 min at 80 V. Gel bands were visualised and photographed under UV light with a Molecular Imager® Gel Doc™ XR (BioRad).

TAE buffer:

60 mM Tris-HCl, 1 mM EDTA, 20 mM acetic acid.

Sample loading dye (6x):

60 mM Tris-HCl, 60 mM EDTA, 0.2 % (w/v) orange G, 0.05 % (w/v) xylene cyanol ff and 60 % (v/v) glycerol.

9.2.1. Chemical transformation of *E. coli* cells

Prior to the transformation the chemically competent cells were allowed to thaw on ice. Transformations were carried out by gently mixing 2 µL of Dpn1 treated mutagenesis product (40-80 ng/µL)) with 50 µL of chemically competent cells and incubating on ice for 30 min. The cells were heat-shocked at 42 ˚C for ~35 s and then incubated on ice for a further 2 min. 200 µL of super

optimal broth (SOC) medium was added to the cells, mixed gently and incubated at 37 ˚C for 1 h. The cells were then spread on LB-agar plates containing the appropriate antibiotics for antibiotic-resistance selection. The plates were incubated overnight at 37 ˚C. *E. coli* Oneshot Top10 cells (Invitrogen) were used for plasmid storage and propagation, and *E.coli* BL21(DE3) cells were used for the expression of *Mtu*CM.

SOC medium:

> 2 % (w/v) tryptone, 0.5% (w/v) yeast extract, 10 mM NaCl, 2.5 mM KCl, 10 mM $MgSO_4$ and 20 mM glucose.

9.2.2. Preparation of chemically competent cells

Chemically competent cells were prepared by inoculating a 5 mL LB culture from a glycerol stock of the desired cell line and grown overnight at 37 ˚C with the appropriate antibiotics if applicable. 2 mL from this culture was used to inoculate a 100mL LB culture, with the appropriate antibiotics added, grown at 37 ˚C until the culture reached an optical density at 600 nm (OD_{600}) between 0.3-0.4. The culture was then transferred to a sterile 50 mL tube and centrifuged at 2000 g, 4 ˚C for 15 min. All plasticware and solutions used here on were pre-chilled and kept on ice in order to maintain cell health until the cells were flash frozen. After centrifugation the media was poured off and discarded. The cells were carefully resuspended, on ice, in 50 mL of sterile 0.1 M $CaCl_2$ and incubated on ice for 30 min. Cells were then centrifuged again at 4000 rpm, 4 ˚C for 15 min and the supernatant discarded. The cell pellet was gently resuspended in 5 mL 0.1 M $CaCl_2$ and incubated for a further 2 h on ice before being gently mixed with pre- chilled sterile 60% (v/v) glycerol to a final concentration of 15% (v/v). The cells were then pipetted into 50 µL, flash frozen in liquid nitrogen and stored at -80 ˚C.

9.2.1. Electroporation of *E.coli* BL21 (DE3) pGroESL cells

Prior to electroporation the electro-competent *E. coli* BL21 (DE3) pGroESL cells were thawed on ice. Once thawed the cells were gently mixed with 2 µL (40-80 ng/mL) of the Dpn1 treated mutagenesis

product and transferred into a chilled 0.2 cm gap electroporation cuvette (BioRad). The mixture was incubated on ice for 2 min before electroporation was performed using a BioRad Gene Pulser (200 Ω, 25 µF 2.5 kV) with a time constant of ~4.6 ms. 500 µL of SOC media was immediately added to the cuvette and gently mixed. The cells were then transferred to a sterile 1.5 mL Eppendorf tube and incubated at 37 ˚C for 1 h. The cells were then spread onto pre-warmed LB-agar plates with the appropriate antibiotics (100 µg/mL ampicillin and 25 µg/mL chloramphenicol) and incubated at 37 ˚C overnight.

9.2.2. Preparation of *E.coli* BL21 (DE3) pGroESL electro-competent cells

Electro-competent BL21 (DE3) pGroESL cells were prepared by inoculating a 5 mL preculture (with 25 µg/mL chloramphenicol) with a scraping from a BL21 (DE3) pGroESL cell glycerol stock and left to grow overnight at 37 ˚C. 2 mL from this culture was then used to inoculate a 100 mL LB culture (with 25 µg/mL chloramphenicol), which was grown at 37 ˚C until the OD_{600} reached ~0.5. The culture was then transferred to a sterile falcon tube and centrifuged at 6400 g, 4 ˚C for 5 min. All plasticware and solutions used here on were pre-chilled and kept on ice in order to maintain cell health until the cells were flash frozen. The supernatant was discarded, and the cells gently resuspended in 100 mL chilled and sterile 1 mM HEPES pH 7.0 buffer. The cells were centrifuged again at 6400 g, 4 ˚C for 5 min, the supernatant discarded and the cell pellet resuspended in 50 mL chilled HEPES buffer. The cells were centrifuged again at 6400 g, 4 ˚C for 5 min, the supernatant discarded and the cell pellet resuspended in 4 mL cold sterile glycerol (10 % (v/v)). The cells were centrifuged for the final time at 7700 g, 4 ˚C for 10 min and the supernatant discarded. The cell pellet was resuspended in 500 µL of glycerol (10 % (v/v)) and pipetted into 50 µL aliquots, flash frozen in liquid nitrogen and stored at -80 ˚C.

9.2.3. Plasmid preparation and isolation

When required for DNA sequencing or for transformations plasmids were extracted and purified from 5 mL LB cultures. The 5 mL cultures were inoculated with *E. coli* OneShot Top10 cells containing the

target plasmid and grown overnight at 37 ˚C. 3 mL of the incubated cultures were harvested for the cells by centrifuging in sterile 1.5 mL Eppendorf tubes at 17000 g for 1 min at room temperature. The supernatant was discarded. The plasmids were extracted and purified from the cells using a High Pure Plasmid Isolation Kit (Roche) by following the manufacturer's procedure. Isolated plasmids were stored at -20 ˚C.

9.2.4. DNA sequencing

DNA sequencing services were provided by Canterbury Sequencing, and performed using an ABI3100 Genetic Analyser (Applied Systems Inc.) and following a procedure derived from the Sanger chain termination protocol. Double stranded plasmid samples were prepared in 6 µL aliquots at 40-50 ng/mL per sequencing run. Generic pPro (sense and antisense) primers were used for sequencing at concentration of 3.2 mM.

9.2.5. Glycerol stocks

In order to maintain a viable cell stock, *E. coli* cells transformed with *Mtu*DAH7PS or *Mtu*CM containing plasmids were stored at -80 ˚C as glycerol stocks. Glycerol stocks were prepared by inoculating a 5 mL culture, with appropriate antibiotics, with the desired *E. coli* cells. The 5 mL culture was incubated overnight at 37 ˚C. 800 µL of this culture was mixed with 400 µL sterile 50 % (v/v) glycerol in a sterile 1.5 mL Eppendorf tube and flash frozen with liquid nitrogen prior to storage.

9.3. *E. coli* cell growth, induction and harvesting

9.3.1. Growth of *E. coli* cells

E. coli BL21 (DE3) cells containing the plasmid encoding the gene for *Mtu*CM were ampicillin resistant, whist *E. coli* BL21 (DE3) pGroESL cells containing the pPro Ex-Hta plasmid encoding the gene for *Mtu*DAH7PS were resistant to ampicillin and chloramphenicol.

100 mL LB cultures containing the appropriate antibiotics (ampicillin (100 µg/mL) and/or chloramphenicol (25 µg/mL)) were inoculated with scraping from the appropriate glycerol stock and grown overnight at 37 ˚C with shaking at 170-180 rpm. 25 mL of this small culture was used to inoculate 1L of LB media cultures containing ampicillin (100 µg/mL) and chloramphenicol (25 µg/mL) in 2-3 L baffled flasks. Typically 4L of culture was prepared and grown at 37 ˚C, with shaking at 170-180 rpm until the OD_{600} reached 0.4-0.6, which usually took about 3 h. The temperature was lowered to 23 ˚C 20-30 min before induction.

9.3.2. Induction of protein expression

A physiological analogue of lactose isopropyl β-D-1-thiogalactopyranoside (IPTG) was added to the cell culture to activate the *lac* promoter, thereby activating gene expression of the target protein (*Mtu*CM or *Mtu*DAH7PS). IPTG was added to the 1L cultures to give a final concentration of 0.1 mM for the expression of *Mtu*DAH7PS from *E. coli* BL21 (DE3) pGroESL cells and 0.5 mM for the expression of *Mtu*CM from *E. coli* BL21 (DE3) cells. The induced cultures were incubated at 23 ˚C overnight, with shaking at 170-180 rpm, overnight.

9.3.3. Cell harvesting

Cell cultures were harvested in 1 L flasks by centrifugation at 14000 g for 20 min at 4 ˚C. The supernatant was discarded and the cell pellet scraped out of the flasks and either immediately lysed or stored at -80 ˚C until needed.

9.4. General purification experimental

9.4.1. Fast protein liquid chromatography (FPLC)

FPLC was carried out using either the Bio-Rad Biologic Duoflow or GE Healthcare AKTApurifier™ protein chromatography systems at 4 ˚C unless otherwise stated. All buffers, solvents and samples for FPLC were filtered through a 0.2 µM filter just prior to use. Samples were applied to columns using a

10 or 50 mL Superloop™ (GE Healthcare). Sample elution was monitored at both 260 and 280 nm and identified peaks assessed by SDS-PAGE to determine if the protein of interest was present.

9.4.2. Preparation of TEV protease

Recombinant Tobacco etch virus (TEV) protease [156] was purified from *E. coli* BL21 (DE3) cells containing the plasmids pRIL and pRK793. pRIL allows *E. coli* to better produce rare codons and pRK793 encodes for TEV protease. A scraping of these cells was used to grow a 50 mL LB culture, containing ampicillin (100 µg/mL) and chloramphenicol (25 µg/mL), overnight at 37 ˚C with shaking at 170-180 rpm. 1 L of LB, containing ampicillin (100 µg/mL) and chloramphenicol (25 µg/mL), was inoculated with about 20 mL of this small culture and grown at 37 ˚C with shaking at 170-180 rpm until the OD_{600} was ~0.6. The *E. coli* cells were then induced IPTG (final concentration 0.5 mM), and incubated overnight at 23 ˚C with shaking at 170-180 rpm.

Cells were then harvested, resuspended in TEV HisTrap A buffer and lysed by sonication as described later for *Mtu*DAH7PS (Section 9.5.1). The TEV protease was then purified from the soluble *E. coli* proteins by a single IMAC step using a 5 mL HisTrap™ HP column (GE Healthcare). The procedure for the IMAC was the same as previously described for *Mtu*DAH7PS using a linear gradient for elution except TEV HisTrap A and B buffers were used. The eluted fractions containing TEV protease were pooled and buffer exchanged into TEV storage buffer and concentrated to ~ 1 mg/mL before being flash frozen in liquid nitrogen in 1 mL aliquots and stored at -80 ˚C.

TEV HisTrap A buffer:

> 50 mM potassium phosphate, 500 mM KCl, 25 mM imidazole and 10 % (v/v) glycerol at pH 8.0

TEV HisTrap B buffer:

> 50 mM potassium phosphate, 500 mM KCl, 500 mM imidazole and 10 % (v/v) glycerol at pH 8.0

TEV storage buffer:

> 25 mM potassium phosphate, 200 mM KCl, 10 mM dithiothreitol (DTT), 2 mM ethylenediaminetetraacetic acid (EDTA) and 10 % (v/v) glycerol at pH 8.0

9.4.3. Determination of *Mtu*DAH7PS concentration

The concentration of protein samples was measured using a Nanodrop ND-1000 spectrophotometer. The concentration was calculated from the absorbance at 280 nm using the molar extinction coefficient determined for each protein. The molar extinction coefficients for each protein were determined from the protein sequences using the ProtParam tool on the ExPASy Proteomics Server (Table 9.2).[157] The molar extinction coefficient determined for *Mtu*DAH7PS^{WT} was used to assess the concentration of all *Mtu*DAH7PS variants, as the single or double residue substitutions were found to have a negligible effect on the calculated molar extinction coefficient.

Table 9.2 Molar extinction coefficients determined for *Mtu*DAH7PS and *Mtu*CM at 280 nm measured in water using the ProtParam tool on the ExPASy Proteomics Server.[157]

Protein	Molar extinction coefficient $M^{-1}cm^{-1}$
*Mtu*DAH7PS	41160
*Mtu*CM	1490

9.4.4. Determination of *Mtu*CM concentration

Due to the low molar extinction coefficient of *Mtu*CM there is a large error associated with spectroscopic determination of protein concentration. As an alternative the concentration of *Mtu*CM samples were determined by the method of Bradford, using bovine serum albumin as a standard.[158] 20 µL of protein sample was added to 1 mL of Bradford agent pre-equilibrated to room temperature. Samples were then gently shaken and incubated at room temperature for 5 min prior to absorbance readings at 595 nm being taken in triplicate. The absorbance readings of the standards were plotted by Cary UV software, the software also calculated the protein concentration of the sample by fitting to the curve produced by bovine serum albumin.

Contamination of *Mtu*CM samples with a small portion of GST-tag results in the Bradford method overestimating the concentration of *Mtu*CM. To adjust for this contamination the kinetic activity of each purification batch of *Mtu*CM was also determined and the concentration normalised to the

activity of a highly pure preparation of *Mtu*CM (as shown by SDS-PAGE) used as a standard. Kinetic assays were conducted with a final concentration of *Mtu*CM of 1 ng/mL in kinetic assay buffer (50 mM BTP with 1 mM TCEP at pH 7.5) with 150 µM chorismic acid, 150 µM PEP and 100 µM $MnSO_4$.

9.4.5. SDS-PAGE

NuPAGE® 10% Bis-Tris 1mm x 12-well pre-cast gels (Invitrogen) were used for Sodium dodecyl sulphate-polyacrylamide (SDS-PAGE). SDS-PAGE was performed using an XCell SureLock™ Electrophoresis Cell (Invitrogen). Protein samples were mixed with NuPAGE® LDS Sample Buffer (4x) and DTT, centrifuged to mix and placed in boiling water for 5 min before loading onto a gel. Electrophoresis of *Mtu*DAH7PS protein samples was conducted in NuPAGE® MOPS SDS Running Buffer (Invitrogen) and run at 200 V for 50 min. Electrophoresis of *Mtu*CM protein samples was conducted in NuPAGE® MES SDS Running Buffer (Invitrogen) and run at 200 V for 35 min. A sample of the Novex® Sharp Pre-Stained Protein Standards was included on each SDS-PAGE gel for the determination of the molecular weight of protein bands.

9.4.6. Visualisation of PAGE gels

Gels were stained by heating in microwave oven on high for ~1 min in a staining solution and then shaken for 15-30 min at room temperature. Gels were then rinsed in water and placed in destaining solution, heated for 1 min in the microwave oven on high for ~ 1 min and shaken for 1-2 hours or until sufficiently destained at room temperature before being rinsed with water and stored in water. Gels were viewed and imaged with a Molecular Imager Gel Doc XR (Bio-Rad).

Staining solution:

1 % (w/v) Coomassie brilliant blue R-250, 40 % methanol (v/v) and 10 % (v/v) glacial acetic acid

Destaining solution:

40 % (v/v) methanol and 10 % (v/v) glacial acetic acid.

9.4.7. Protein concentration and buffer exchange

*Mtu*DAH7PS protein solutions were concentrated using 10000 Da molecular weight cut-off (MWCO) devices, and *Mtu*CM protein solutions were concentrated using 5000 Da MWCO (Vivaspin 2 (GE Healthcare) or Vivaspin 500 or Vivaspin 20 (Sartorius Stedim Biotech) or Amicon® Ultra-4 (Millipore)). Concentrators were rinsed with Milli-Q water prior to use.

Buffer exchange of protein solutions was achieved by concentrating a sample volume to ~5 mL and diluting to ~18 mL with desired buffer and repeating until the percentage of old buffer in solution was less than 5 %.

9.5. Purification of *Mtu*DAH7PS and *Mtu*DAH7PS variants

9.5.1. Cell lysis

Harvested cells were thoroughly resuspended in 10 mL of cold lysis buffer per 1 g of cell pellet and then either lysed by sonication or cell disruption. Cell disruption was found to achieve more reliable and complete cell lysis and was used preferentially for the lysis of *E. coli* BL21 (DE3) pGroESL cells containing the plasmid for *Mtu*DAH7PS.

Sonication was performed on ice, using an Omni-Ruptor 4000 Ultrasonic Homogenizer (Omni International). Sonication was conducted for 5 min intervals at ~35 % pulse, 80-90 % power and repeated 4-6 times with a 2-5 5 min wait between cycles to reduce the risk of over-heating the sample.

Prior to cell disruption the resuspended cells were incubated with 2 µL of benzonase for 5 min. Cell disruption was performed by passing the resuspended cells through an M-110P Microfluidiser® (Microfluidics) 2-3 times at a pressure of 18000 psi. The interaction chamber of the Microfluidiser® was packed with ice, and the samples were collected and kept on ice between reapplication to reduce the risk of over-heating the sample and denaturing the target protein.

The soluble fraction of the cell lysate was separated by centrifugation at 24000 g, 4 ˚C for 60 min. The cell pellet was discarded. The supernatant was then filtered through a 0.2 µm filter (Millipore) and stored until ready to be purified. To reduce the risk of proteolysis chromatography was carried out as soon as possible, and protease inhibitors were included in the lysis buffer.

Lysis buffer:

50 mL HisTrap A buffer (Section 9.5.2) and a Complete™ Protease Inhibitor Cocktail Tablet (Roche).

9.5.2. Immobilised metal affinity chromatography

The purification of *Mtu*DAH7PS and *Mtu*DAH7PS utilised IMAC to isolate the polyhistidine tagged *Mtu*DAH7PS (*Mtu*DAH7PS^{H6}) from other soluble *E. coli* proteins (Section 2.3,Figure 2.3). Following the separation of the *Mtu*DAH7PS^{H6}, the polyhistidine tag was cleaved and removed from the protein sample by IMAC.

The first round of IMAC was performed using a 5 mL HisTrap™ HP column prepacked with pre-charged Ni Sepharose™ High Performance resin. The column was washed with 5 column volumes of water prior to use. Thereafter the column was equilibrated with 5 column volumes of HisTrap A buffer before sample application. Weakly bound proteins and contaminants were washed off the column with 3-5 columns of HisTrap A buffer. Proteins bound to the column were eluted with steadily increasing imidazole concentration i.e. a linear gradient. The proportion of HisTrap B buffer mixed with HisTrap A buffer increased from 0 to 100 % over 10 column volumes. The column was then washed with 3-5 columns volumes of HisTrap B buffer. The columned was then washed with 5 column volumes of HisTrap A buffer ready for the next stage of IMAC. The eluted protein of interest (*Mtu*DAH7PS^{H6}) was immediately collected and pooled ready for treatment with TEV protease.

After TEV protease cleavage the protein sample was reapplied to a 5 mL HisTrap™ HP column (GE Healthcare), to remove the cleaved polyhistidine tag and the TEV protease. Prior to application of the sample the column was pre-equilibrated with 5 column volumes of HisTrap A buffer. The unbound

protein, including *Mtu*DAH7PS, was washed off the column with 3-5 column volumes of HisTrap A buffer. The unbound fraction was collected and pooled ready for the next stage of purification. Any bound protein was washed off the column with 3-5 column volumes of HisTrap B buffer. The column was then washed with 5 column volumes of HisTrap A buffer and 5 column volumes of water prior to storage in 20 % ethanol.

HisTrap A buffer:

> 20 mM 1,3- bis[tris(hydroxymethyl)methylamino]propane (BTP), 150 mM NaCl, 100 µM $MnSO_4$, 100 µM phophoenolpyruvate (PEP), 200 µM tris(2-carboxyethyl)phosphine (TCEP) and 20 mM imidazole at pH 7.5.

HisTrap B buffer:

> 20 mM BTP, 150 mM NaCl, 100 µM $MnSO_4$, 100 µM PEP, 200 µM TCEP and 500 mM imidazole at pH 7.5.

9.5.3. Cleavage of the polyhistidine tag

TEV protease was used to cleave the N-terminal polyhistidine tag from *Mtu*DAH7PS^{H6}. The fractions, containing *Mtu*DAH7PS, eluted from the first IMAC were pooled. This pooled fraction typically had a total volume between 15-20 mL, and was diluted to 50 mL with SEC buffer (Section 9.5.4) to reduce the concentration of imidazole, permitting better TEV protease activity. Typically 1 mg of TEV protease ($1/10^{th}$ – $1/100^{th}$ of the concentration (mg/mL) of the protein of interest) was added to the pooled fractions, gently mixed and incubated overnight at 4 ˚C. The pooled fraction was then reapplied to the IMAC column to remove the cleaved polyhistidine tag and TEV protease.

9.5.4. Size exclusion chromatography

SEC was used as a polishing step to separate any remaining *E. coli* proteins in the protein sample from *Mtu*DAH7PS based on size. The pooled fractions containing the cleaved protein from the second IMAC step was concentrated to a volume of less than 13 mL or until a maximum concentration of 5 mg/mL was reached. A HiLoad™ 26/60 Superdex™ 200 prep grade column (GE Healthcare) was equilibrated with 1 column volume of SEC buffer prior to loading the cleaved protein sample onto the column. The

sample was eluted with 1 column volume of SEC buffer and the fractions containing *Mtu*DAH7PS were pooled and concentrated to between 3-5 mg/mL. The SEC column was stored in 20 % ethanol.

SEC buffer:

10 mM BTP, 150 mM NaCl, 200 µM $MnSO_4$, 200 µM PEP and 200 µM TCEP at pH 7.5.

9.5.5. Storage of purified *Mtu*DAH7PS

The pooled fractions of *Mtu*DAH7PS from SEC were concentrated to between 2-5 mg/mL and then pipetted into 100 or 200 µL aliquots, flash frozen in liquid nitrogen and stored at -80 ˚C.

9.6. Purification of *Mtu*CM

9.6.1. Cell lysis

Harvested cells were thoroughly resuspended in 10 mL cold lysis buffer per 1 g of cell pellet and lysed by sonication. Sonication was performed on ice, using an Omni-Ruptor 4000 Ultrasonic Homogeniser (Omni International). Sonication was conducted for 5 min intervals at ~35 % pulse, 70-80 % power and repeated 4-5 times with 5-10 min breaks between cycles to reduce the risk of over-heating the sample.

The soluble fraction of the cell lysate was separated by centrifugation at 24000 g, 4 ˚C for 35 min. The cell pellet was discarded. The supernatant was then filtered through a 0.2 µm filter (Millipore) and stored until ready to be purified. To reduce the risk of proteolysis chromatography was carried out as soon as possible, and protease inhibitors were included in the lysis buffer.

Lysis buffer:

50 mL GSTrap A1 buffer and a Complete™ Protease Inhibitor Cocktail Tablet (Roche).

9.6.2. Affinity chromatography

The purification of *Mtu*CM also utilised affinity chromatography to separate the glutathione *S*-transferase (GST) tagged *Mtu*CM (*Mtu*CM^{GST}) from other soluble *E. coli* proteins (Section 4.2, Figure 4.4). Once isolated *Mtu*CM^{GST}, was treated with TEV protease to cleave the GST tag. IMAC was used to remove the cleaved GST tag.

The first round of IMAC was performed using a 5 mL GSTrap^{TM} HP column prepacked with Glutathione Sepharose^{TM} High Performance resin. The column was washed with 5 column volumes of water prior to use. Thereafter the column was equilibrated with 5 column volumes of GSTrap A1 buffer before sample application. Weakly bound proteins and contaminants were washed off the column with 3-5 columns of GSTrap A1 buffer. Proteins bound to the column were eluted with increasing imidazole concentration i.e. a linear gradient. The proportion of GSTrap B buffer mixed with GSTrap A1 buffer increased from 0 to 100 % over 10 column volumes. The column was then washed with 3-5 columns volumes of GSTrap B buffer. The columned was then washed with 5 column volumes of GSTrap A2 buffer ready for the next stage of IMAC. The eluted protein of interest (*Mtu*CM^{GST}) was immediately collected and pooled ready for treatment with TEV protease.

Separation of the cleaved GST tag proved to be problematic due to an affinity between *Mtu*CM and the cleaved GST tag. To overcome this glycerol was added to the GSTrap A1 buffer (GSTrap A2 buffer), FPLC was conducted at room temperature and the four GSTraps were connected in series to maximise GST tag recovery during each IMAC step. After each round of IMAC the protein washed off the column was inspected by SDS-PAGE to ascertain the amount of GST tag present in the protein samples. If significant contamination was present the *Mtu*CM protein solution would undergo another round of IMAC.

After TEV protease cleavage the protein sample was reapplied to a 4x 5 mL GSTrap^{TM} HP columns (GE Healthcare) connected in series (for a total column volume of 20 mL), pre-equilibrated with 5 column volumes of GSTrap A2 buffer, to remove the cleaved GST tag. The unbound protein, including *Mtu*CM,

was washed off the column with 3-5 column volumes of GSTrap A2 buffer. The unbound fraction was collected and pooled. Any bound protein was washed off the column with 3-5 column volumes of GSTrap B buffer. The column was then washed with 5 column volumes of GSTrap A. If the *Mtu*CM protein sample contained significant GST tag contamination it was concentrated to ~10 mL and underwent further iterations of IMAC until the sample appeared to be sufficiently pure. The *Mtu*CM sample was then concentrated to ~5 mL ready for SEC. Meanwhile, the column was then washed with 5 column volumes of GSTrap A1 or GSTrap A2 buffer and 5 column volumes of water prior to storage in 20 % ethanol.

In some instances SEC did not sufficiently remove the remaining cleaved GST tag and the *Mtu*CM sample underwent another 1 or 2 iterations of IMAC using 4 x 5 mL GSTtap^{TM}s in series. When analysed by SDS-PAGE and found to be sufficiently pure the *Mtu*CM sample was concentrated to ~3-6 mL before being desalted to remove any glycerol in the buffer.

GSTrap A1 buffer:

10 mM phosphate buffer and 5 mM KCl at pH 7.5.

GSTrap A2 buffer:

10 mM phosphate buffer and 5 mM KCl and 1 % (v/v) glycerol at pH 7.5.

GSTrap B buffer:

50 mM Tris-HCl, 150 mM NaCl, and 10 mM reduced glutathione at pH 7.5

9.6.3. Cleavage of GST-tag

TEV protease was used to cleave the N-terminal GST tag from *Mtu*CM^{GST}. The fractions, containing *Mtu*DAH7PS, eluted from the first IMAC were pooled. This pooled fraction typically had a total volume between 10-15 mL, and was diluted to ~50 mL with SEC buffer (Section 9.6.4) to reduce the concentration of reduced glutathione. Typically 0.5 mg of TEV protease (1/10th – 1/100th of the concentration (mg/mL) of the protein of interest) was added to the pooled fractions, gently mixed

and incubated overnight at 4 ˚C. The pooled fraction was then reapplied to the IMAC column to remove the cleaved GST tag as described above in Section 9.6.2.

9.6.4. Size exclusion chromatography

The pooled fractions containing the cleaved protein from the IMAC step to remove the cleaved GST tag was concentrated to a volume of less than 5 mL. The protein sample was applied to a SEC column to remove any remaining GST tag and the TEV protease. A HiLoad™ 16/60 Superdex™ 75 prep grade column (GE Healthcare) was equilibrated with 1 column volume of SEC buffer prior to loading the cleaved protein sample onto the column. The sample was eluted with 1 column volume of SEC buffer and the fractions containing *Mtu*CM were pooled. The SEC column was stored in 20 % ethanol. The pooled *Mtu*CM fractions were concentrated to between 0.5-2 mg/mL and purity was verified by SDS-PAGE. If sufficiently pure the *Mtu*CM sample was prepared for storage. If significant GST tag contamination was present in the sample the *Mtu*CM sample underwent further rounds of IMAC.

SEC buffer:

10 mM BTP, 150 mM NaCl, 200 µM $MnSO_4$, 200 µM PEP and 200 µM TCEP at pH 7.5.

9.6.5. Desalting

*Mtu*CM samples that were insufficiently purified by SEC were subjected to further IMAC to remove any remaining GST tag. The GSTrap A2 buffer required for IMAC contains glycerol and reintroduces glycerol to the *Mtu*CM sample. This glycerol must be removed from the buffer prior to storage as it was shown to interfere in the inhibition studies of *Mtu*CM•*Mtu*DAH7PS activity. The *Mtu*CM was desalted with a PD-10 Sephadex™ G-25 column (GE Healthcare) using the manufacturer's gravity-fed protocol. The column was equilibrated with 5 column volumes of SEC buffer before the protein sample was applied. The protein was eluted with 2 column volumes of SEC buffer, and *Mtu*CM containing fractions collected and pooled (*Mtu*CM was usually eluted in a single block from 2.5-6 mL).

The column was then washed with 5 column volumes of water and stored in 20% ethanol. The collected *Mtu*CM sample was then pooled and concentrated to 0.5-2 mg/mL ready for storage.

9.6.6. Storage of purified *Mtu*CM

*Mtu*CM samples ready for storage were concentrated to between 0.5-2 mg/mL before being pipetted into 10, 50 or 100 µL aliquots, flash frozen in liquid nitrogen and stored at -80 ˚C.

9.7. Structural characterisation

9.7.1. Mass spectrometry

The mass of the purified proteins was measured by electrospray ionisation using a Bruker maXis™ 3G (Bruker Daltonics). Protein samples were buffer exchanged into Milli-Q water and diluted to 1 mg/mL for analysis.

9.7.2. Blue native PAGE of *Mtu*DAH7PS

Blue native PAGE was performed using NativePAGE™ Novex® 4-16 % Bis-Tris Protein 1 mm 10 wells Gels. Native PAGE was performed using an XCell SureLock™ Electrophoresis Cell (Invitrogen). The manufacturer's experimental setup and protocol was used including the 20x NativePAGE™ Running Buffer and 20x NativePAGE™ cathode buffer additive for electrophoresis. Samples were prepared by mixing with 4x NativePAGE™ Sample Buffer prior to loading on the gels. NativeMark™ Unstained Protein Standard was mixed with the 4x NativePAGE™ Sample Buffer and loaded on the gel for the determination of the native molecular weight of the target protein. The gels were stained and destained as described for SDS-PAGE gels (Section 9.4.6)

9.7.3. Native PAGE of the *Mtu*CM•*Mtu*DAH7PS complex

Native PAGE was performed using Amersham™ ECL™ 12 % 15-well gels (GE Healthcare). The gels were run in 50 mM Tris buffer with 175 mM alanine at pH 9.2 using an EDL™ Gel Box at 160 V 90 min. Samples were prepared to give a final concentration of ~ 6 µM *Mtu*DAH7PS and 18-24 µM *Mtu*CM when mixed with a 2x loading dye. The samples were allowed incubate for 5 min before being loaded onto the gel. NativeMark™ Unstained Protein Standard was mixed with the 2x loading dye and also loaded onto the gel as native molecular weight standards. The gels were stained and destained as described for SDS-PAGE gels (Section 9.4.6)

Loading dye:

125 mM Tris-HCl, 20 % (v/v) glycerol and 2 mg bromophenol blue at pH 6.5 and made to 10 mL with Milli-Q water.

9.7.4. Circular dichroism

CD experiments were carried out using a JASCO J-815 Spectropolarimeter. The CD spectrum of each protein was collected from 260 to 195 nm, with a 0.5 nm data pitch, 1 s response and 1 nm bandwidth. Samples were prepared at 0.03 mg/mL in a 3 mL quartz cuvette with a 1 cm path length. Data was collected at 25 ˚C in 10 mM Tris buffer at pH 7.5 pH adjusted with H_2SO_4. The CD spectrum of each protein had the spectrum of the buffer subtracted and was smoothed by performing a five-point moving average.

9.7.5. Small angle X-ray scattering data collection

SAXS data was collected at the Australian Synchrotron SAXS/WAXS beamline equipped with a Pilatus Synchrotron detector (1 M, 170 x 170 mm, effective pixel size, 172 x 172 µm). The wavelength of the X-rays was 1.0332 Å. The sample-detector distance was set to 1.6 m, which provides an s range of 0.0126-0.6014 $Å^{-1}$. *s* is defined as the magnitude of the scattering vector and is related to the scattering angle (2θ) and the wavelength (λ) by $s=(4\pi/\lambda)\sin\theta$. Protein samples were analysed at ~6

mg/mL in SEC buffer (Section 9.5.4) and filtered through a 0.2 µM filter just prior to analysis to minimise the amount of aggregates in the protein solution. SAXS data was collected for each protein following it's elution from a Superdex^{TM} 200 5/150 column, equilibrated previously with 1 column volume of SEC buffer. The SAXS data was collected from a 1.5 mm glass capillary at 27 ˚C at 2 s intervals. For some experiments SEC buffer and the protein sample were supplemented with the stated concentration of aromatic amino acids (200 µM or 1 mM). Two-dimensional intensity plots from the tip of the peak of the SEC analysis were radially averaged, normalised to sample transmission and background subtracted in ScatterBrain (www.synchrotron.org.au/index.php/aussyncbeamlines/saxswaxs/software-saxswaxs).

9.7.6. SAXS data analysis

Scattering intensity (I) was plotted against s. All samples were checked for non-linearity in the increase of intensity at low s to check for aggregation or concentration dependent scattering. Guinier fits were linear for $s \cdot R_g < 1.3$ (R_g is the radius of gyration) as calculated by PRIMUS.[101] An indirect Fourier transform was performed by GNOM to provide the pair wise distribution function (P(r)) which determined both the relative probabilities of distance between scattering centres and the maximum dimension of the scattering particle (D_{max}).[102]

Theoretical scattering profiles were generated from atomic coordinates and compared with the experimental scattering profile using CRYSOL.[103] For scattering profiles that possibly consist as mixtures of quaternary structures theoretical scattering profiles were generated and compared to the experimental scattering profile by OLIGOMER.[159] OLIGOMER was used to predict the approximate proportion of each oligomeric structure in present. To assess and compare the quality of fits determined by CRYSOL or OLIGOMER the χ^2 values for the fits were compared.[160]

9.7.7. Analytical ultracentrifugation

Sedimentation velocity experiments were performed using a Beckman Coulter model XL-I analytical ultracentrifuge equipped with UV-visible scanning optics. Reference samples (i.e. buffer) were 400 µL and protein samples were 380 µL. Samples were loaded into 12 mm double-sector cells with quartz windows, and the cells were mounted in an An-50 Ti eight-hole rotor. All *Mtu*DAH7PS samples were prepared by dialysis overnight into the AUC buffer whilst samples containing a mixture of *Mtu*CM and *Mtu*DAH7PS were dialysed for 2-4 h into the AUC buffer due to the instability of *Mtu*CM. Samples collected in the presence of 100 µM of any of the aromatic amino acids were spiked with the amino acid (both the protein sample and the buffer reference sample) just prior to analysis.

All AUC experiments were carried out by Ali Nazmi, I performed all sample preparation. Ali was also kind enough to assist with the analysis of the experimental data.

Protein samples were prepared at three different concentrations between 0.09 and 1.0 mg/mL and centrifuged at 50000 rpm at 20 ˚C. Absorbance data was collected in continuous mode at 278 or 279 nm without averaging. AUC data was fitted to a continuous distribution *c*(*s*) model using SEDFIT.[107,161] The ratios of the frictional coefficients (f/f_0) calculated by SEDFIT from fitting the *c*(*s*) models are tabulated below (Table 9.3). The partial specific volume (v) of the proteins, buffer density (1.005 gmL^{-1}) and buffer viscosity (1.021 cp) were calculated using the program SEDNTERP.[162] The v of the *Mtu*CM•*Mtu*DAH7PS complex was calculated from the equation (Equation 9.1) below:

$$\bar{v} = \frac{\bar{v}_1 . Mw_1 + \bar{v}_2 . Mw_2}{M_1 + M_2}$$

Equation 9.1 Equation to calculate the partial specific volume for AUC. Where v_1 and Mw_1 are the partial specific volume and molecular weight of *Mtu*DAH7PS and v_2 and Mw_2 are the partial specific volume and molecular weight of *Mtu*CM respectively.

AUC Buffer:

50 mM Tris buffer with 150 mM NaCl and 200 µM $MnSO_4$ at pH 7.5.

Table 9.3 Frictional coefficient ratios (f/f_0) calculated from fitting the continuous size (c(s)) distribution model to the AUC data by SEDFIT.

Sample	[*Mtu*DAH7PS] (mg/mL)	f/f_0	Sample	[*Mtu*DAH7PS] (mg/mL)	f/f_0
Chapter 2			*Chapter 4 cont.*		
*Mtu*DAH7PS^{WT}	0.2	1.13	*Mtu*DAH7PS^{WT} + *Mtu*CM +100 µM Phe	0.2	1.28
*Mtu*DAH7PS^{WT}	0.4	1.19	*Mtu*DAH7PS^{WT} + *Mtu*CM +100 µM Phe	0.4	1.33
*Mtu*DAH7PS^{WT}	1.0	1.23	*Mtu*DAH7PS^{WT} + *Mtu*CM +100 µM Phe	0.6	1.21
*Mtu*DAH7PS^{WT}+ 100 µM Phe	0.2	1.18	*Mtu*DAH7PS^{WT}	0.6	1.23
*Mtu*DAH7PS^{WT}+ 100 µM Phe	0.4	1.15	*Chapter5*		
*Mtu*DAH7PS^{WT}+ 100 µM Phe	1.0	1.12	*Mtu*DAH7PS^{G190P}	0.1	1.24
*Mtu*DAH7PS^{WT}+ 100 µM Trp	0.2	1.25	*Mtu*DAH7PS^{G190P}	0.25	1.34
*Mtu*DAH7PS^{WT}+ 100 µM Trp	0.4	1.18	*Mtu*DAH7PS^{G190P}	1.0	1.34
*Mtu*DAH7PS^{WT}+ 100 µM Trp	1.0	1.18	*Mtu*DAH7PS^{V103A}	0.1	1.25
*Mtu*DAH7PS^{WT} + 100 µM Phe + 100 µM Trp	0.2	1.35	*Mtu*DAH7PS^{V103A}	0.3	1.40
*Mtu*DAH7PS^{WT} + 100 µM Phe + 100 µM Trp	0.4	1.23	*Mtu*DAH7PS^{V103A}	1.0	1.32
*Mtu*DAH7PS^{WT} + 100 µM Phe + 100 µM Trp	1.0	1.13			
Chapter 4			*Chapter 6*		
*Mtu*DAH7PS^{WT} + 4x *Mtu*CM	0.2	1.23	*Mtu*DAH7PS^{K123M}	0.3	1.20
*Mtu*DAH7PS^{WT} + 4x *Mtu*CM	0.4	1.25	*Mtu*DAH7PS^{K123M}	0.6	1.18
*Mtu*DAH7PS^{WT} + 4x *Mtu*CM	0.6	1.23	*Mtu*DAH7PS^{K123M}	1.0	1.19
*Mtu*DAH7PS^{WT} + *Mtu*CM	0.2	1.30	*Chapter 7*		
*Mtu*DAH7PS^{WT} + *Mtu*CM	0.4	1.26	*Mtu*DAH7PS^{G232P}	0.09	1.38
*Mtu*DAH7PS^{WT} + *Mtu*CM	0.6	1.35	*Mtu*DAH7PS^{G232P}	0.6	1.28
*Mtu*DAH7PS^{WT} + 0.5x *Mtu*CM	0.2	1.46	*Mtu*DAH7PS^{G232P}	0.9	1.26
*Mtu*DAH7PS^{WT} + 0.5x *Mtu*CM	0.4	1.10	*Mtu*DAH7PS^{G232P} + 100 µM Phe + 100 µM Trp	0.09	1.25
*Mtu*DAH7PS^{WT} + 0.5x *Mtu*CM	0.6	1.29	*Mtu*DAH7PS^{G232P} + 100 µM Phe + 100 µM Trp	0.6	1.23
*Mtu*DAH7PS^{WT} + 4x *Mtu*CM +100 µM Phe	0.4	1.32	*Mtu*DAH7PS^{G232P} + 100 µM Phe + 100 µM Trp	0.9	1.24

9.7.8. IMAC pull down assay

A pull-down assay is an *in vitro* method to determine whether a physical interaction occurs between two proteins in this case *Mtu*DAH7PS and *Mtu*CM by utilising the affinity of one binding partner for a particular resin or surface. *Mtu*DAH7PS was purified without cleavage of the polyhistidine tag allowing the enzyme to retain an affinity for resin of a HisTrap^{TM} HP column. *Mtu*CM has no inherent

affinity for the HisTrap™ HP resin and therefore can only bind to the HisTrap™ HP column via *Mtu*DAH7PS^{H6}.

A 200 µL mixture of *Mtu*DAH7PS and *Mtu*CM was prepared to give a final concentration of 10 µM *Mtu*DAH7PS and ~30 µM *Mtu*CM. The mixture was gently mixed and incubated for 15 min at 4 ˚C. A 200 µL sample of each separate protein was also prepared. In this control, *Mtu*DAH7PS was applied to the column at ~10 µM. The sample concentration of *Mtu*CM was increased to ~60 µM to allow the elution of *Mtu*CM from the column to be more easily identified by monitoring the UV absorbance at 280 nm.

The pull down assay protocol is similar to that of an IMAC purification step. The protein samples were applied (~200 µL) to a 5mL HisTrap™ HP column (GE Healthcare) previously equilibrated with 5 column volumes of Histrap A buffer (Section 9.5.2). The column was washed with 2-3 column volumes of Histrap A buffer to remove any unbound protein. Any bound protein was then eluted off the column with 2-3 column volumes of Histrap B buffer (Section 9.5.2).

To assess if Phe prevented the complex from forming a second mixture of the same concentrations was also prepared and spiked to a final concentration of 1 mM Phe and allowed to incubate for 15 min at 4 ˚C prior to application to the column. The HisTrap A buffer for this pull down assay was also spiked to a final concentration of 1 mM Phe.

Fractions were collected during both the wash and elution steps and analysed on an SDS-PAGE gel to identify the whether *Mtu*CM and/or *Mtu*DAH7PS was present.

9.8. Biophysical characterisation

9.8.1. Differential scanning fluorimetry

DSF was performed using a Bio-Rad iCycler iQ5™ Multicolour Real-Time PCR Detection System. Samples were prepared in a 96-well plate to give a final volume of 25 µL. Each well contained 20 µL SEC buffer (supplemented with the appropriate amino acid(s) to give a final amino acid concentration of either 200 µM, 500 µM or 1 mM), 4 µL of protein at 1 mg/mL and 1 µL of 250x SYPRO Orange dye. The plate was sealed and subjected to a thermal cycling program that heated the plated from 20 to 95 ˚C in 0.2 ˚C increments over 4 h. Each protein sample was measured in triplicate and compared to a negative control in which no protein sample was present. Melting temperatures were manually calculated at the temperature at which the maximum inflection occurred along the generated melting curve of each protein sample. Statistical analysis way performed via a two-tailed student t-test with a 95 % confidence interval.

9.8.2. Isothermal titration calorimetry

The affinity between *Mtu*DAH7PS variants and the aromatic amino acids was assessed by ITC and performed using a VP-ITC unit (MicroCal; GE Healthcare). All solutions were filtered through a 0.2 µm filter (Millipore) and degassed under vacuum. All protein samples were analysed in SEC buffer at 25 ˚C. The experimental set-up for each experiment is detailed in Table 9.4. Heats of dilution experiments were carried out for each run and subtracted from the integrated data before curve fitting was carried out. Iterative curve fitting to either the one- or two-site models provided by MicroCal was performed by Origin 7.0 software.

Examples of the heat of dilution for each ligand (Trp, Phe and Tyr) are displayed in appendix IV.

Table 9.4 ITC experimental set-up. * Number of injection excludes the first small volume injection. –indicates no background ligand was present.

Protein	Background ligand	Titrated Ligand	Number of injections*
Chapter 2			
38 µM *Mtu*DAH7PS^{WT}	20 µM Trp	3 mM Tyr	28 x 10 µL
49 µM *Mtu*DAH7PS^{WT}	400 µM Tyr	250 µM Trp	28 x 10 µL
40 µM *Mtu*DAH7PS^{WT}	400 µM Tyr	1 mM Phe	28 x 10 µL
Chapter 3			
30 µM *Mtu*DAH7PS^{R171A}	–	2 mM Phe	28 x 10 µL
30 µM *Mtu*DAH7PS^{R171A}	–	3 mM Tyr	56 x 5 µL
30 µM *Mtu*DAH7PS^{R171A}	50 µM Phe	3 mM Tyr	28 x 10 µL
40 µM *Mtu*DAH7PS^{R171A}	–	3 mM Trp	56 x 5 µL
30 µM *Mtu*DAH7PS^{R256A}	–	900 µM Phe	28 x 10 µL
60 µM *Mtu*DAH7PS^{R256A}	–	2 mM Tyr	28 x 10 µL
50 µM *Mtu*DAH7PS^{R256A}	50 µM Phe	3 mM Tyr	28 x 10 µL
30 µM *Mtu*DAH7PS^{R256A}	–	300 µM Trp	28 x 10 µL
Chapter 5			
81 µM *Mtu*DAH7PS^{G190P}	–	1 mM Trp	28 x 10 µL
49 µM *Mtu*DAH7PS^{G190P}	–	2 mM Phe	28 x 2 µL
38 µM *Mtu*DAH7PS^{G190P}	100 µM Phe	1 mM Trp	28 x 10 µL
38 µM *Mtu*DAH7PS^{Y131A}	–	500 µM Trp	28 x 10 µL
38 µM *Mtu*DAH7PS^{Y131A}	–	1 mM Phe	28 x 10 µL
38 µM *Mtu*DAH7PS^{Y131A}	100 µM Phe	500 µM Trp	28 x 10 µL
Chapter 6			
38 µM *Mtu*DAH7PS^{N237A}	–	800 µM Trp	28 x 10 µL
41 µM *Mtu*DAH7PS^{N237A}	–	1 mM Phe	28 x 10 µL
40 µM *Mtu*DAH7PS^{N237A}	–	2.5 mM Tyr	28 x 10 µL
38 µM *Mtu*DAH7PS^{N237A}	50 µM Phe	800 µM Trp	28 x 10 µL
41 µM *Mtu*DAH7PS^{N237A}	20 µM Trp	1 mM Phe	28 x 10 µL
38 µM *Mtu*DAH7PS^{N237A}	20 µM Trp	2.5 mM Tyr	28 x 10 µL
Chapter 7			
30 µM *Mtu*DAH7PS^{G232P}	–	3 mM Trp	28 x 10 µL
28 µM *Mtu*DAH7PS^{G232P}	–	900 µM Phe	28 x 10 µL
24 µM *Mtu*DAH7PS^{G232P}	50 µM Phe	5 mM Trp	28 x 10 µL
37 µM *Mtu*DAH7PS$^{G190P/G232P}$	–	3 mM Trp	28 x 10 µL
33 µM *Mtu*DAH7PS$^{G190P/G232P}$	–	900 µM Phe	28 x 10 µL
32 µM *Mtu*DAH7PS$^{G190P/G232P}$	–	3 mM Tyr	28 x 10 µL
32 µM *Mtu*DAH7PS^{F227D}	–	5 mM Trp	28 x 10 µL
32 µM *Mtu*DAH7PS^{F227D}	–	600 µM Phe	28 x 10 µL
28 µM *Mtu*DAH7PS^{F227D}	50 µM Phe	5 mM Trp	28 x 10 µL

9.9. Kinetic analysis

9.9.1. Standard kinetic assays

Measurement of Mtu*DAH7PS activity*

The assays used to measure *Mtu*DAH7PS activity were based on the assay developed by Celia Webby and further improved by Richard Hutton.[48,69,70] The kinetic parameters and measurements of *Mtu*DAH7PS activity were measured by monitoring the loss of PEP at 232 nm (ε = 2.8 x 10^3 M^{-1} cm^{-1} at 30 ˚C) in the presence of E4P using a Varian Cary 100 UV-visible spectrophotometer using quartz cuvettes with a 1 cm or 1 mm pathlength and standard assay conditions. The reaction mixtures contained 100 µM $MnSO_4$, 300 µM PEP (unless stated otherwise or varied to determine the K_m^{PEP}) and E4P at 300 µM (unless stated otherwise or varied to determine the K_m^{E4P}). Reactions were initiated with enzyme. For assays not intended to determine K_m values PEP and E4P concentrations were held at 150 µM. PEP and E4P solutions were made up in assay buffer.

Measurement of Mtu*CM activity*

The assays used to measure *Mtu*CM activity were developed by Richard Hutton based on the assays performed by Sasso *et. al*..[85] Kinetic parameters of *Mtu*CM activity were determined by monitoring the loss of chorismic acid (Sigma) at 274 nm (ε = 2.630 M^{-1} cm^{-1} at 30 ˚C) in the same assay buffer as *Mtu*DAH7PS and in the presence of $MnSO_4$ (100 µM), PEP (150 µM) and 25 µM or 150 µM chorismic acid. For the determination of the chorismic acid K_m the chorismic acid concentration was varied.

Measurement of Mtu*CM or* Mtu*DAH7PS activity of the* Mtu*CM*•Mtu*DAH7PS complex*

For study of the complexes, *Mtu*CM activity was determined with a 1:10 ratio for *Mtu*CM to *Mtu*DAH7PS and *Mtu*DAH7PS activity was determined with a 10:1 ratio of *Mtu*CM to *Mtu*DAH7PS, and allowed to incubate at 303 K in the presence of all assay components (except the initiating substrate, chorismic acid, or E4P respectively) for five min. Assays were also conducted to measure *Mtu*CM activity in the presence of 1:1 or 1:200 ratios of *Mtu*CM to *Mtu*DAH7PS or as *Mtu*DAH7PS concentration was varied between 10 nm and 4 µM under the standard assay conditions. The effect of NaCl on the *Mtu*CM activity of a 1:10 mixture of *Mtu*CM to *Mtu*DAH7PS was determined under standard assays conditions with the addition of the NaCl to give a final concentration between 0-1.5 mM. Reactions were initiated with 150 µM chorismic acid.

Determination of Michaelis-Menten kinetics in the presence of aromatic amino acids

For Michaelis-Menten kinetics determined in the presence of one or a combination of aromatic amino acids the amino acid solutions were added to the standard assay conditions to a concentrations to give a final concentration of 200 µM (unless stated otherwise). Kinetic measurements were then conducted as described in the absence of aromatic amino acids.

Chorismic acid, PEP, and E4P solutions were made up in assay buffer and the $MnSO_4$ solution was made up in Milli-Q water. All assay solutions were filtered through a 0.2 µM (Millipore) filter prior to use. Initial reaction rates were determined by a least-squares fit of the initial-rate data. K_m and k_{cat} values were determined by fitting the data to the Michaelis-Menten equation (Equation 9.2), ternary complex equation (Equation 9.3) or the Hill equation (Equation 9.4) using the software GraFit 5.0 (Erithacus software) or Kaleidagraph (Synergy).

Michaelis-Menten kinetic equation

$$v = \frac{V_{max}[S]}{K_m + [S]}$$

Hill equation

$$v = \frac{V_{max}[S]^n}{K^n + [S]^n}$$

Ternary complex kinetic equation

$$v = \frac{V_{max}[A][B]}{(KK_B + K_B[A] + K_A[B] + [A][B])}$$

Equation 9.2 The Michaelis-Menten kinetic equation, **Equation 9.3** The Hill equation and **Equation 9.4** The ternary complex kinetic equation. υ is the reaction velocity, V_{max} is the maximum velocity of an enzyme, [S] substrate concentration, K_m is the Michaelis constant, n is the Hill coefficient, K is the apparent association constant. For the ternary complex kinetic equation A and B refer to alternate substrates.

9.9.2. Determination of substrate concentrations

The concentration of substrates (PEP, E4P and chorismic acid) was determined enzymatically using the appropriate assay conditions and the relevant enzyme. Assays were conducted in the presence of 100 µM $MnSO_4$. A known volume of substrate solutions, typically 5 µL, for which substrate concentration was to be determined, was added to the assay. For the measurement of PEP and E4P the other substrate was held in excess. Reaction was imitated with enzyme and allowed to progress until complete consumption of the limiting substrate had taken place. To ensure the desired substrate was limiting more of the limited substrate was added to the cuvette. For efficiency *Mtu*DAH7PS was used to activate *Mtu*CM activity for the measurement of chorismic acid concentration.

The change in absorbance was noted between the start and end of the reactions. The change in absorbance caused by the addition of enzyme to initiate the reactions was allowed for and the total change in absorbance was used to determine the concentration of substrate by applying the Beer-Lambert law using the appropriate substrate extinction coefficient. All measurements for the determination of substrate concentration were conducted in triplicate.

9.9.3. Inhibition studies

Solutions of L-Phe, L-Tyr and L-Trp were made up in Milli-Q water and filtered through a 0.2 µm filter (Millipore). The appropriate amino acid solution(s) were added to the standard assay reaction mixtures to give a final concentration of 200 µM unless stated otherwise for all inhibitor studies. Steady-state kinetics were conducted in the presence of one, two or all three aromatic amino acids. The assay conditions contained 150 µM PEP, 150 or 1800 µM E4P and 100 µM $MnSO_4$ in assay buffer for measurements of *Mtu*DAH7PS activity.

For the measurement of the inhibition of *Mtu*CM activity the assay conditions contained 150 µM PEP, 150 µM chorismic acid and 100 µM $MnSO_4$ in assay. The final concentration of *Mtu*CM in each cuvette was ~3 µM. Reactions were initiated with chorismic acid.

For reactions measuring the inhibition of *Mtu*CM activity of the *Mtu*CM•*Mtu*DAH7PS complex activity was determined with a 1:10 ratio of *Mtu*CM to *Mtu*DAH7PS with *Mtu*CM concentration held a 60 nM. When measuring the inhibition of *Mtu*DAH7PS activity of the complex a 10:1 ratio of *Mtu*CM to *Mtu*DAH7PS was used *Mtu*DAH7PS was held at 40 nM.

Statistical analysis way performed via a two-tailed student t-test with a 95 % confidence interval.

9.9.4. Kinetic determination of dissociation constant between *Mtu*CM and *Mtu*DAH7PS

The kinetic parameters were determined by measuring CM activity at various concentrations of *Mtu*DAH7PS under the standard assay conditions described above either in the presence or absence of 200 µM Phe. The *Mtu*CM concentration was held at 10 nM (90 nM in the absence of *Mtu*DAH7PS). For each *Mtu*DAH7PS concentration at least seven points were used to determine the Michaelis-Menten kinetic parameters used to find the catalytic efficiency (k_{cat}/K_m) of *Mtu*CM activity. Each set of Michaelis-Menten kinetics was conducted in duplicate. The $K_{d\ app}$ was derived using an equation (Equation 9.5) adapted from Taira and Benkovic as outlined by Sasso *et al.* and assumes a 1:1 stoichiometry of *Mtu*CM to *Mtu*DAH7PS.[85,114] The program KaleidaGraph (Synergy Software) was used to iteratively fit the derived equation, shown below:

$$\upsilon = \upsilon_{CM} + \left([CM]_0 + [DS]_0 + K_{d,app} - \sqrt{([CM]_0 + [DS]_0 + K_{d,app})^2 - 4[CM]_0[DS]_0}\right) \bullet \frac{\upsilon_{CM \bullet DS} - \upsilon_{CM}}{2[CM]_0}$$

Equation 9.5 Equation for the determination of the apparent dissociation constant if the *Mtu*CM•*Mtu*DAH7PS complex υ, υ_{CM} and $\upsilon_{CM•DS}$ are the corresponding catalytic efficiencies, $[CM]_0$ and $[DS]_0$ are the total concentrations of *Mtu*CM and *Mtu*DAH7PS^{WT} respectively. $K_{d,app}$ is the apparent dissociation constant of the complex.

The data was fitted to Equation 9.5, using $\upsilon_{CM•DS}$ and $K_{d,app}$ as the fitting parameters, by the iterative curve fitting software KaleidaGraph (Synergy Software). Sasso *et al.* adapted work by Taira and Benkovic to derive this equation allowing the determination of the apparent *Mtu*CM•*Mtu*DAH7PS dissociation constant for a 1:1 stoichiometry.[85,114]

Appendix I – Michaelis-Menten plots of kinetic data

In this section the kinetic data for the each enzyme is presented as Michaelis-Menten plots with the Lineweaver-Burke plot inset. The data has been fitted to Michaelis-Menten kinetics using the software GraFit 5.0 (Erithicus).

Chapter 2

*Mtu*DAH7PS^{WT}

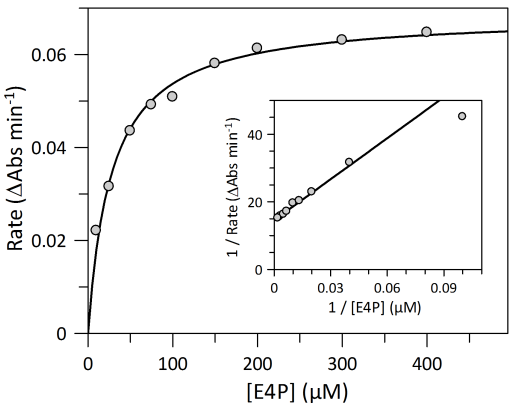

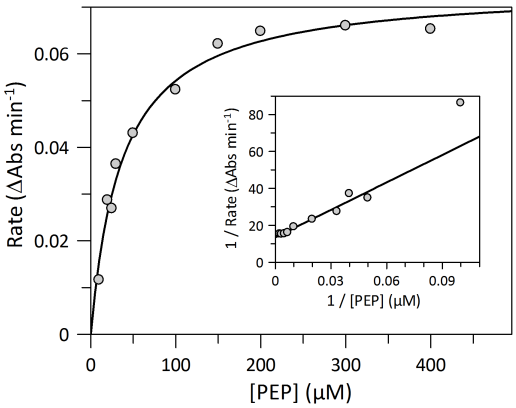

Chapter 3

*Mtu*DAH7PS^{R171A}

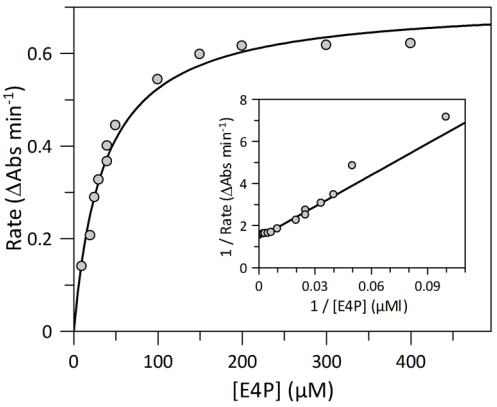

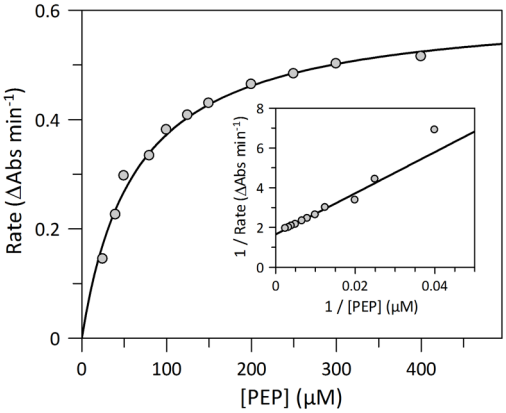

*Mtu*DAH7PS^{R256A}

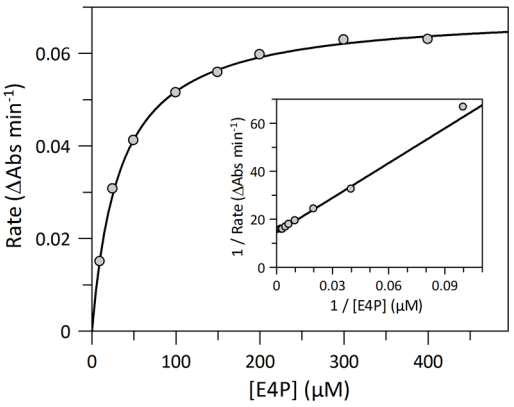

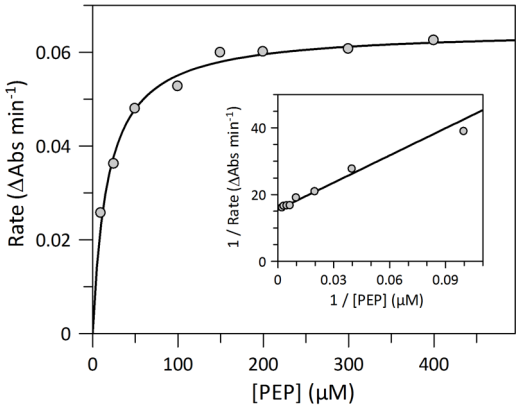

Chapter 4

*Mtu*CM alone

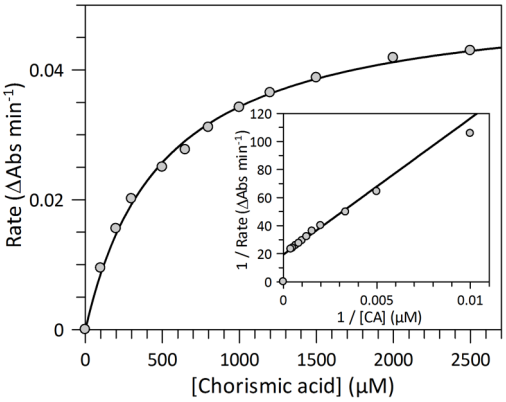

*Mtu*CM + 10 x *Mtu*DAH7PS

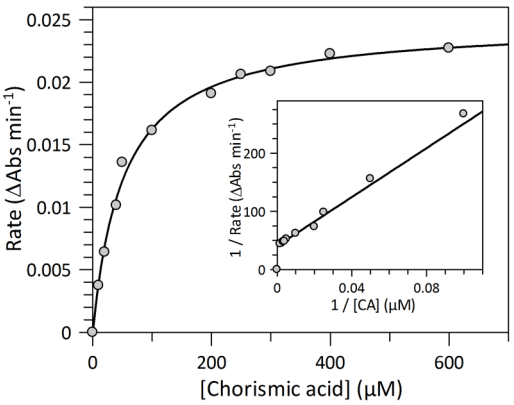

*Mtu*CM + 200 x *Mtu*DAH7PS

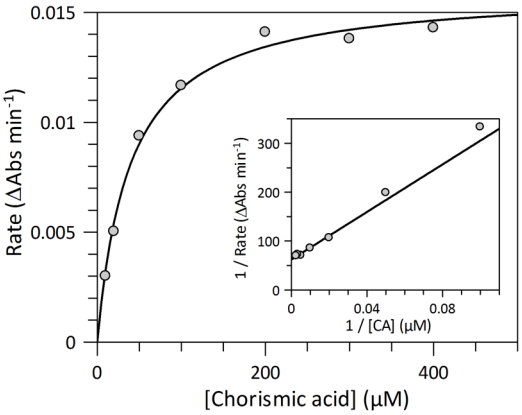

*Mtu*CM + 10 x *Mtu*DAH7PS + 200 μM Phe

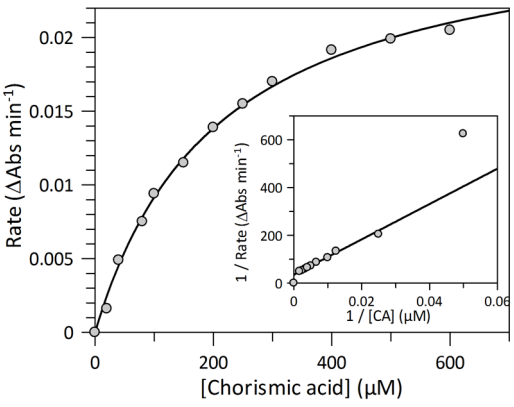

*Mtu*CM + 10 x *Mtu*DAH7PS + 100 μM Phe + 100 μM Tyr

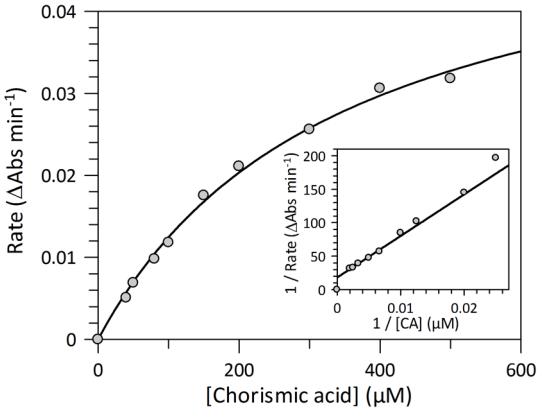

*Mtu*CM + 10 x *Mtu*DAH7PS + 200 µM Phe + 200 µM Tyr

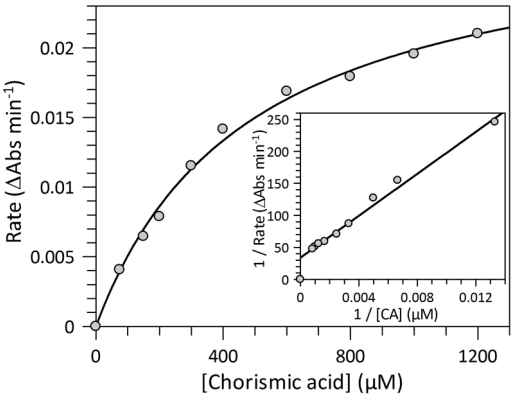

*Mtu*CM + 10 x *Mtu*DAH7PS + 200 µM Tyr

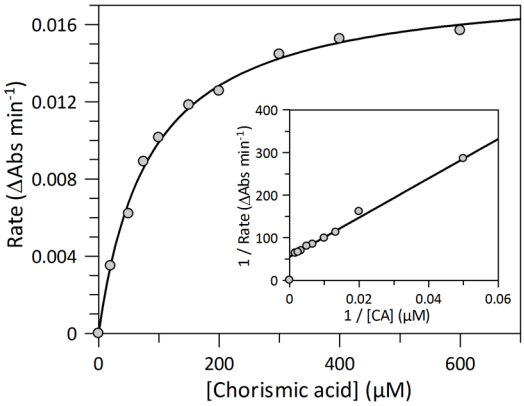

*Mtu*DAH7PS + 10 x *Mtu*CM

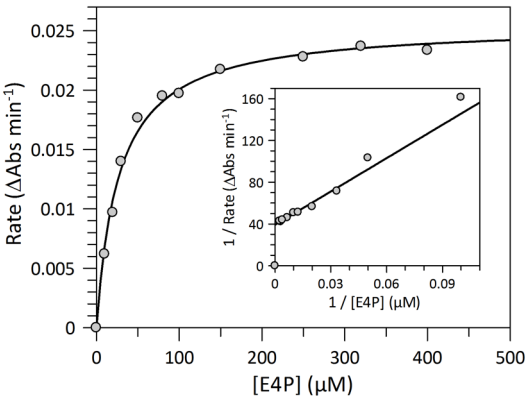

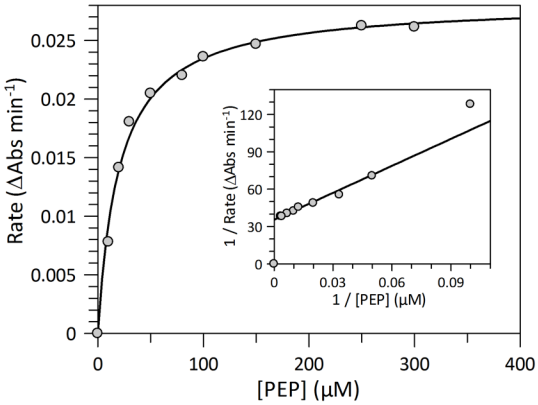

*Mtu*CM + 10 x *Mtu*DAH7PS^{R171A}

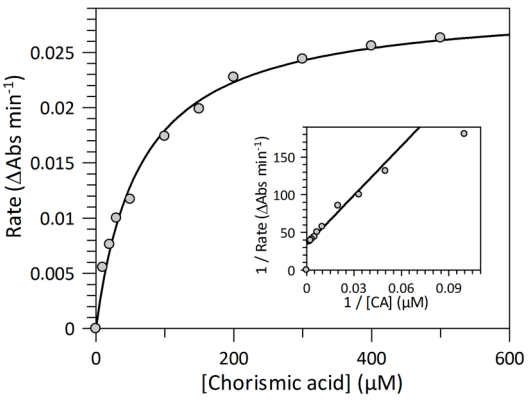

*Mtu*CM + 10 x *Mtu*DAH7PS^{R256A}

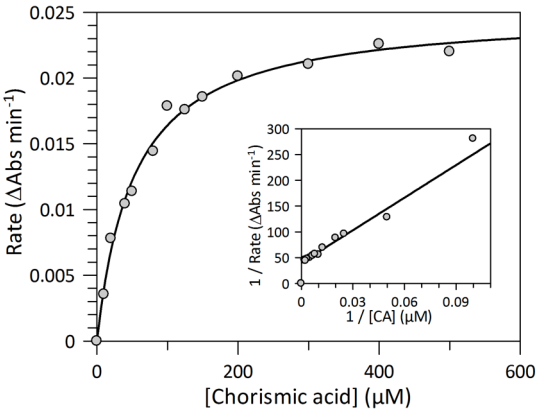

*Mtu*DAH7PS^{R171A} + 10 x *Mtu*CM

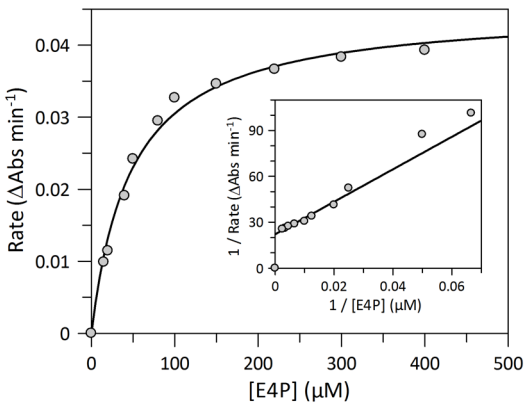

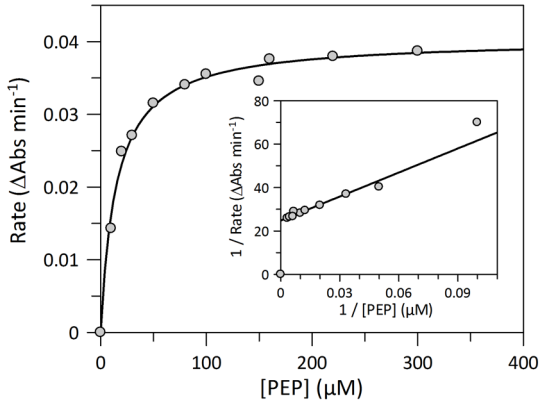

*Mtu*DAH7PS^{R256A} + 10 x *Mtu*CM

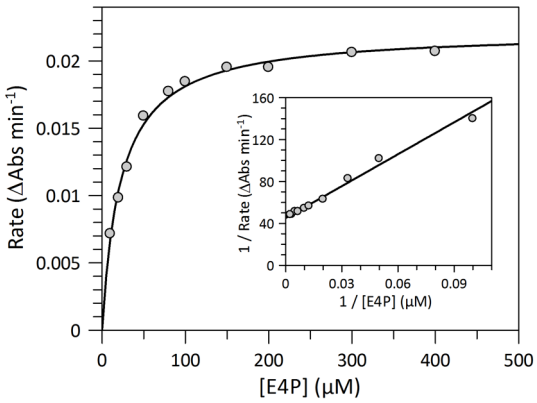

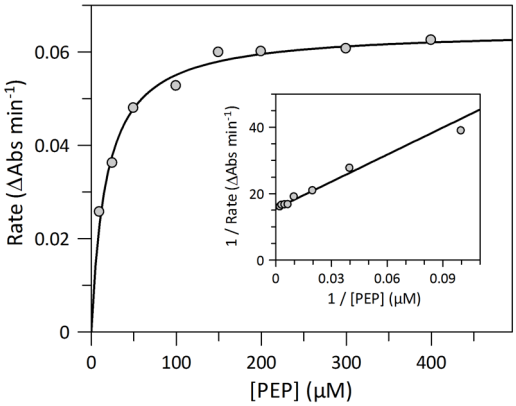

Chapter 5

*Mtu*DAH7PS^{G190P}

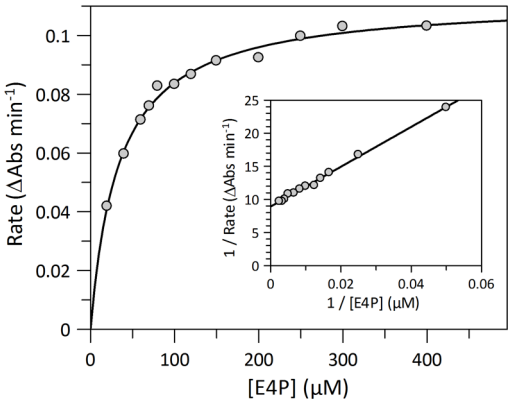

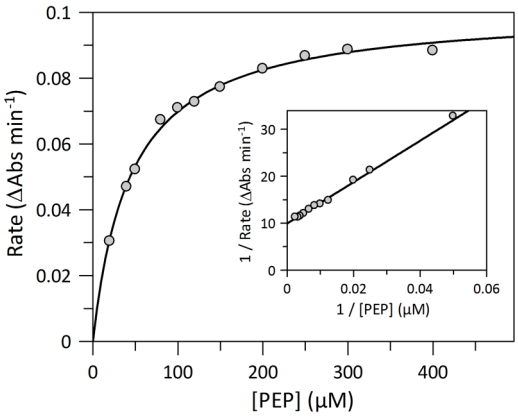

*Mtu*DAH7PS^{V103A}

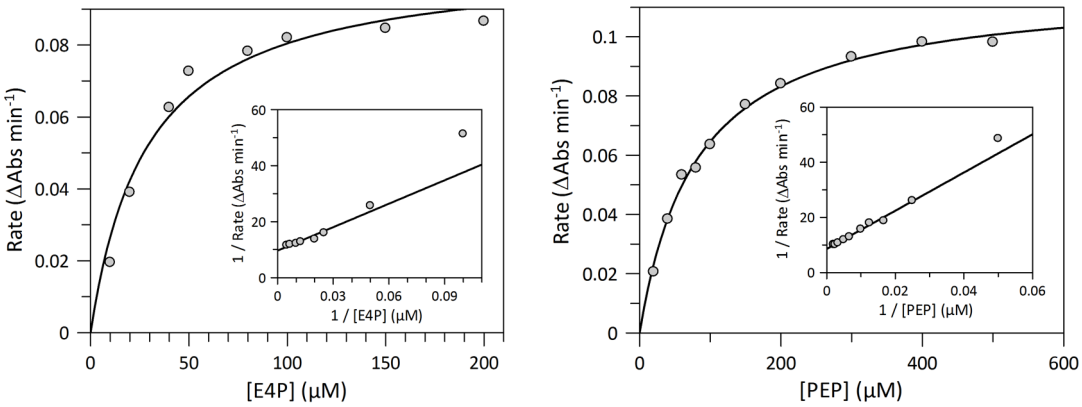

*Mtu*DAH7PS^{Y131A}

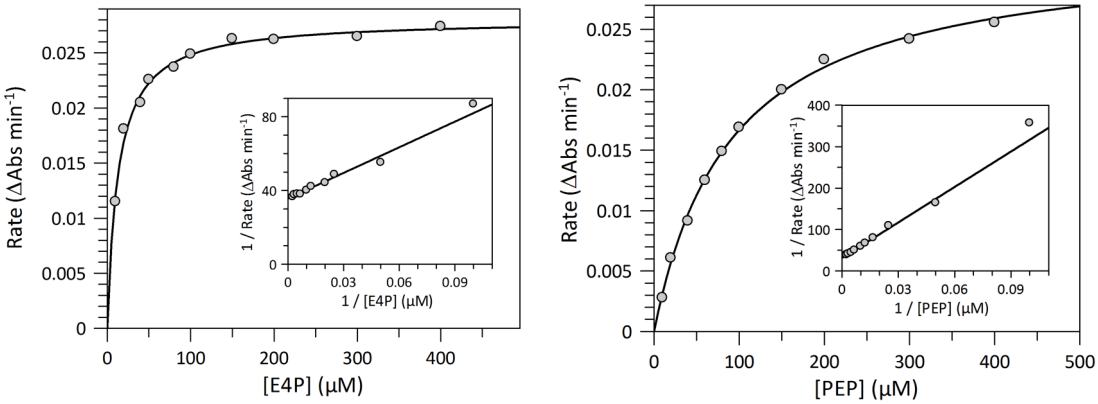

*Mtu*DAH7PS^{N175A}

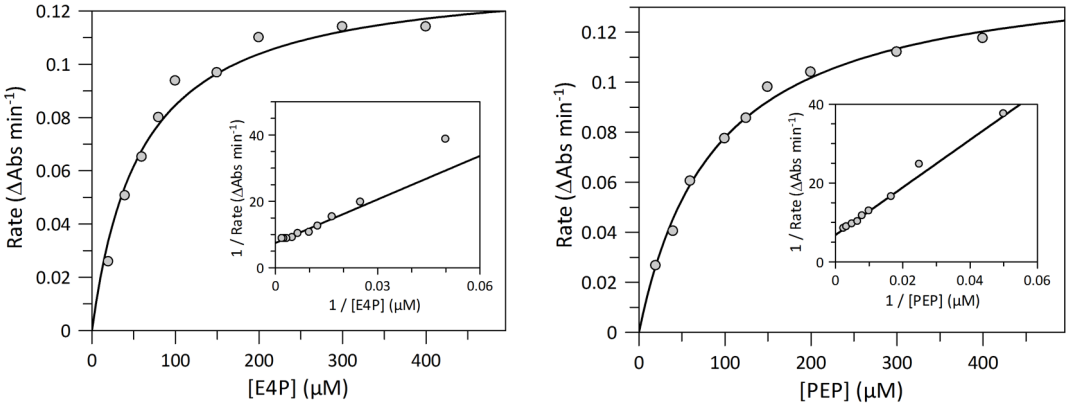

Chapter 6

*Mtu*DAH7PS^{N237A}

*

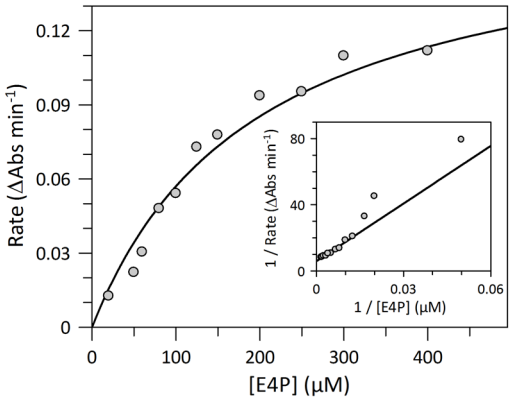

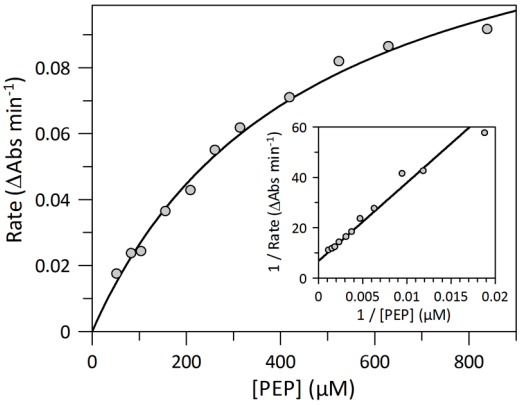

*Mtu*DAH7PS^{K123M}

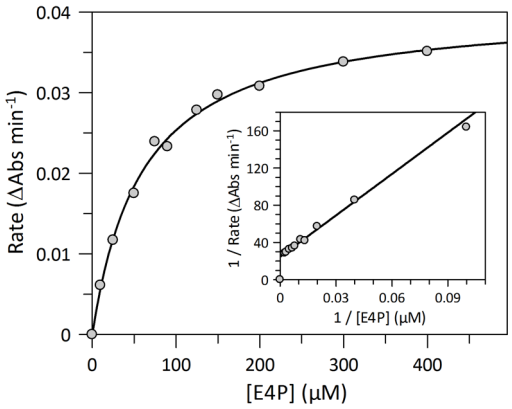

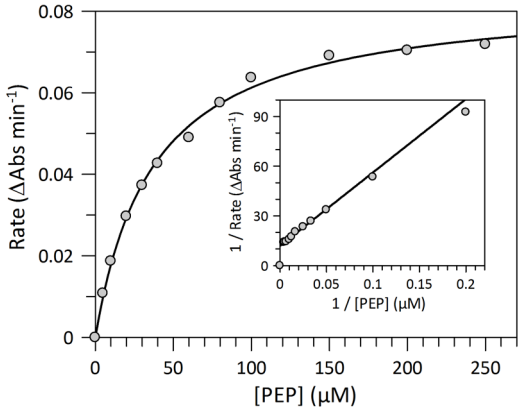

*Mtu*DAH7PS^{N237A} + 200 μM Trp*

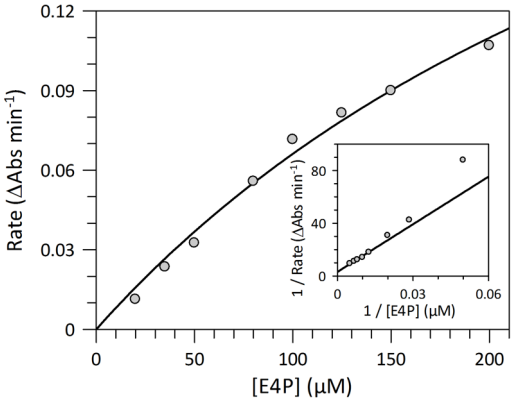

*Mtu*DAH7PS^{K123M} + 200 μM Phe

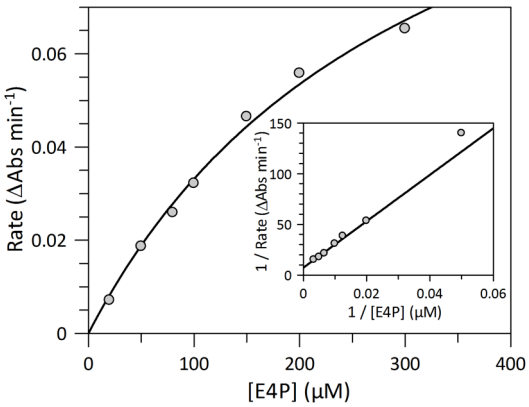

* Kinetic data was also fitted to the Hill equation, data plot and fit shown in chapter 6.

***Mtu*DAH7PS^{K123M} + 10 x *Mtu*CM**

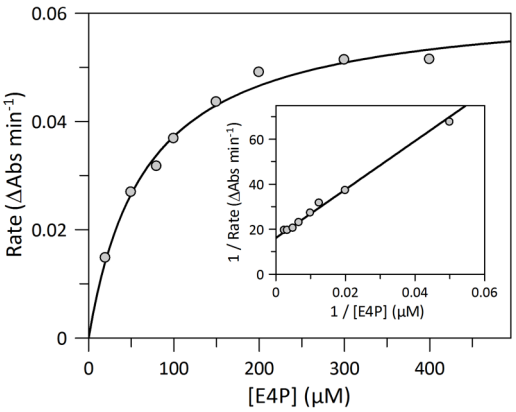

Chapter 7

***Mtu*DAH7PS^{G232P}**

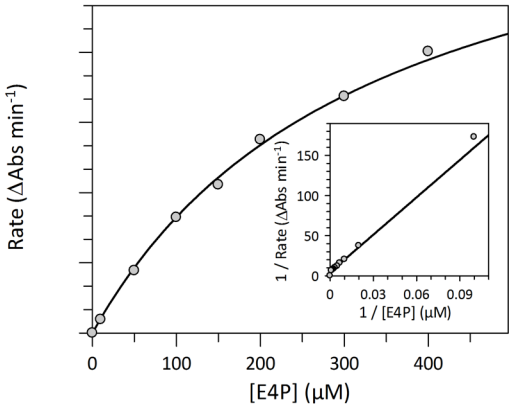

***Mtu*DAH7PS$^{G190P/G232P}$**

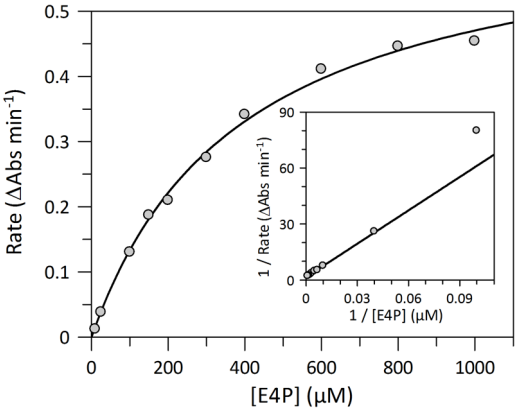

***Mtu*DAH7PS^{F227D}**

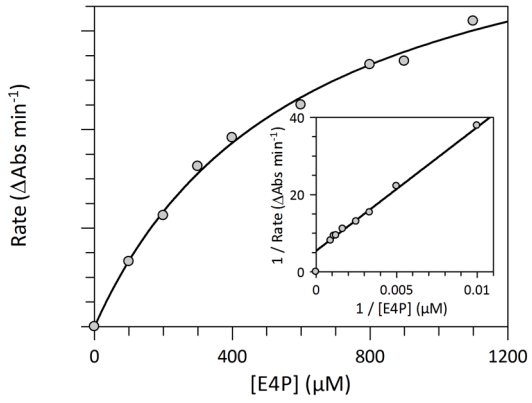

***Mtu*DAH7PS$^{G190P/G232P}$ + 200 μM Trp + 200 μM Phe**

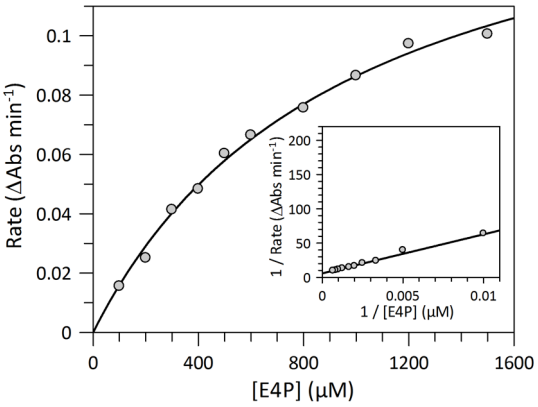

Appendix II – AUC distribution and residual data

In this section the data for the sedimentation velocity experiments is presented. Plotted is the continuous distribution *c*(*s*) model fitted (coloured lines) to the experimental data (black dots) using SEDFIT. The residuals for the fits are also plotted above the AUC data.

Chapter 2

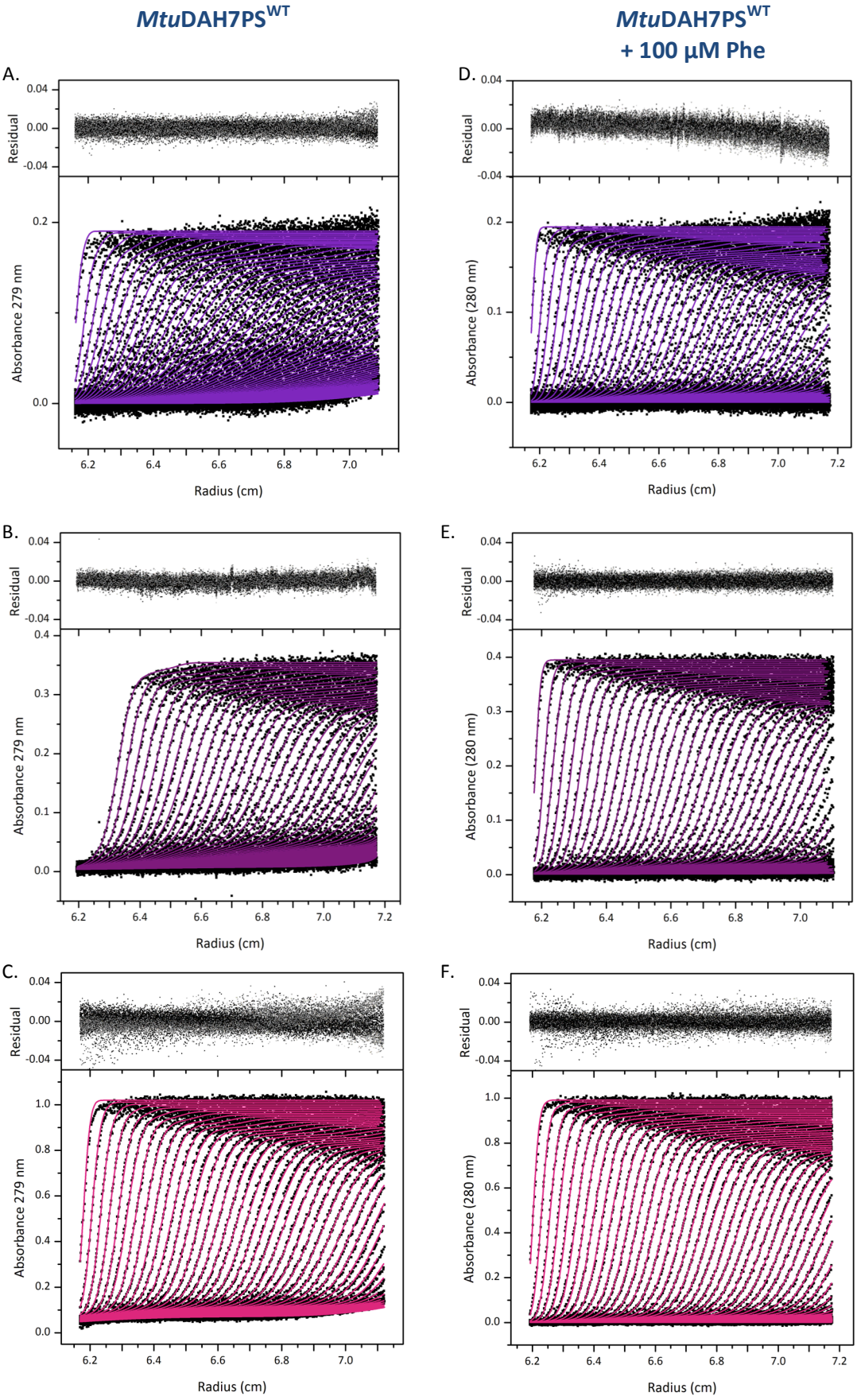

Figure AII.1 Left *Mtu*DAH7PS^{WT} at 0.2 mg/mL (A.) 0.4 mg/mL (B.) and 1.0mg/mL (C.). Right *Mtu*DAH7PS^{WT} + 100 µM Phe at 0.2 mg/mL (D.) 0.4 mg/mL (E.) and 1.0 mg/mL (F.)

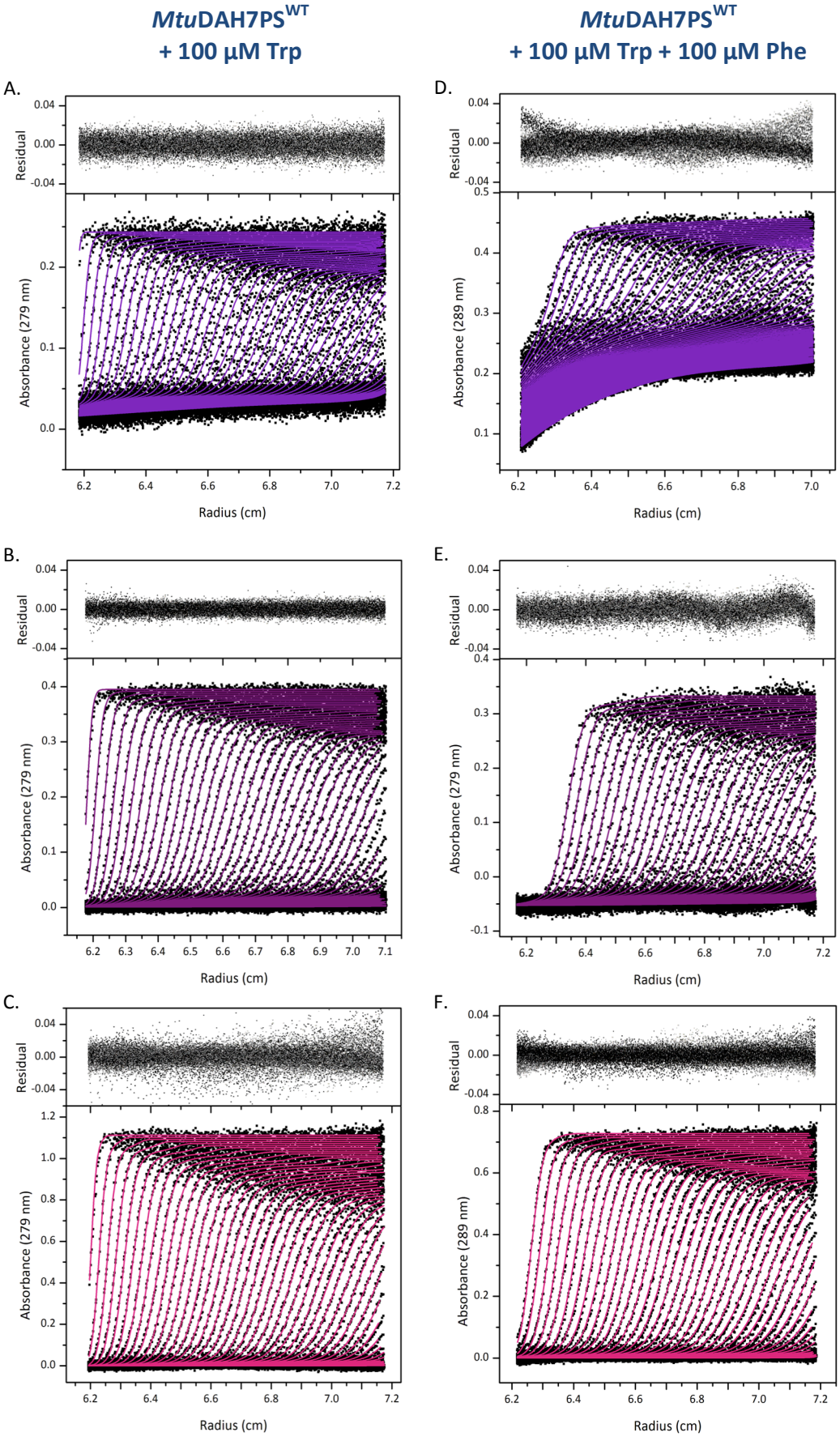

Figure AII.2 Left *Mtu*DAH7PS^{WT} + 100 µM Trp at 0.2 mg/mL (A.) 0.4 mg/mL (B.) and 1.0 mg/mL (C.). Right *Mtu*DAH7PS^{WT} + 100 µM Trp + 100 µM Phe at 0.2 mg/mL (D.) 0.4 mg/mL (E.) and 1.0 mg/mL (F.).

Chapter 4

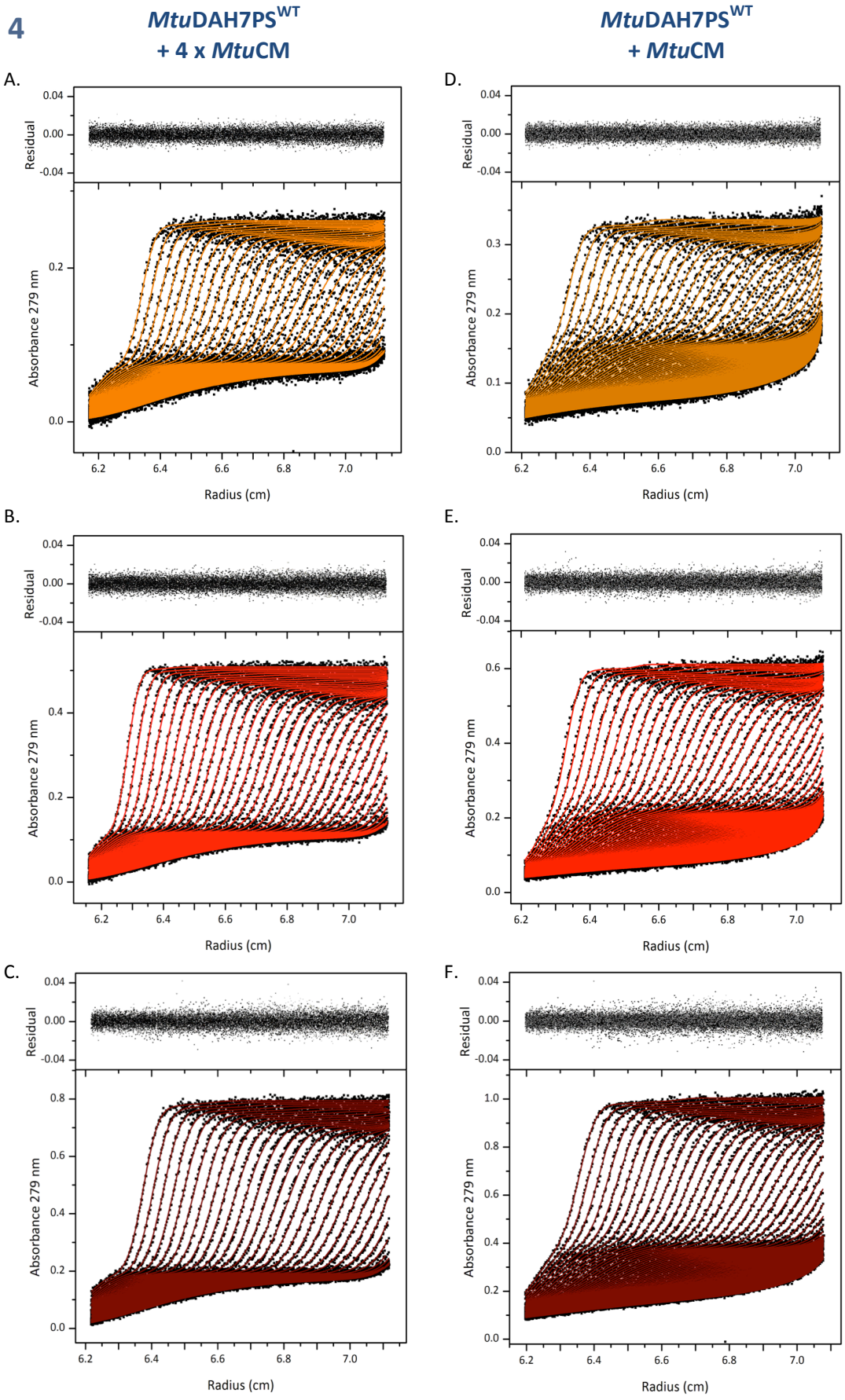

Figure AII.3 Left *Mtu*DAH7PS^{WT} + four-fold molar excess of *Mtu*CM at 0.2 mg/mL (A.) 0.4 mg/mL (B.) and 0.6 mg/mL (C.). Right *Mtu*DAH7PS^{WT} + equimolar amount of *Mtu*CM at 0.2 mg/mL (D.) 0.4 mg/mL (E.) and 0.6 mg/mL (F.).

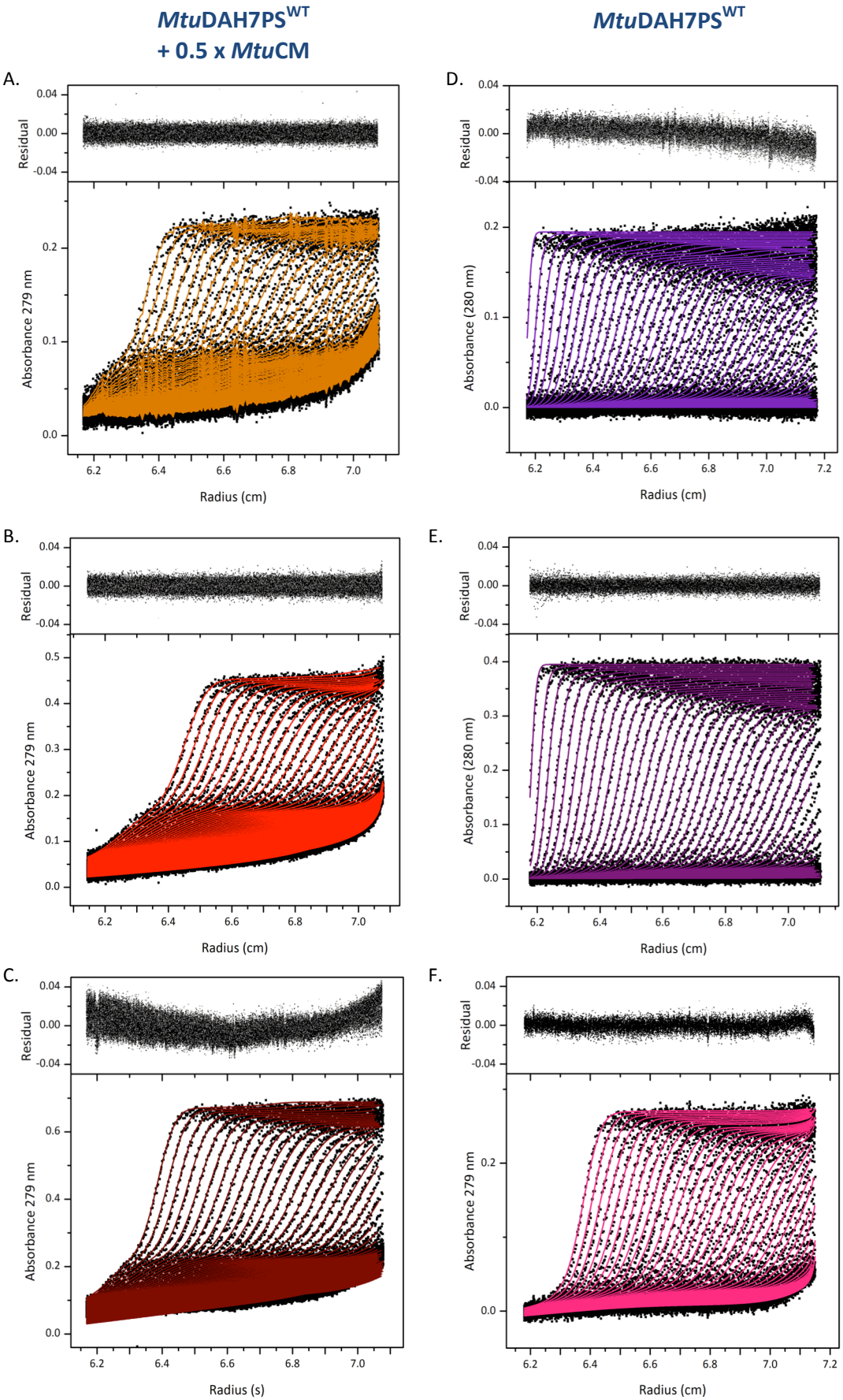

Figure AII.4 Left *Mtu*DAH7PS^{WT} + half the molar amount of *Mtu*CM at 0.2 mg/mL (A.) 0.4 mg/mL (B.) and 0.6 mg/mL (C.). Right *Mtu*DAH7PS^{WT} at 0.2 mg/mL (D.) 0.4 mg/mL (E.) and 0.6 mg/mL (F.).

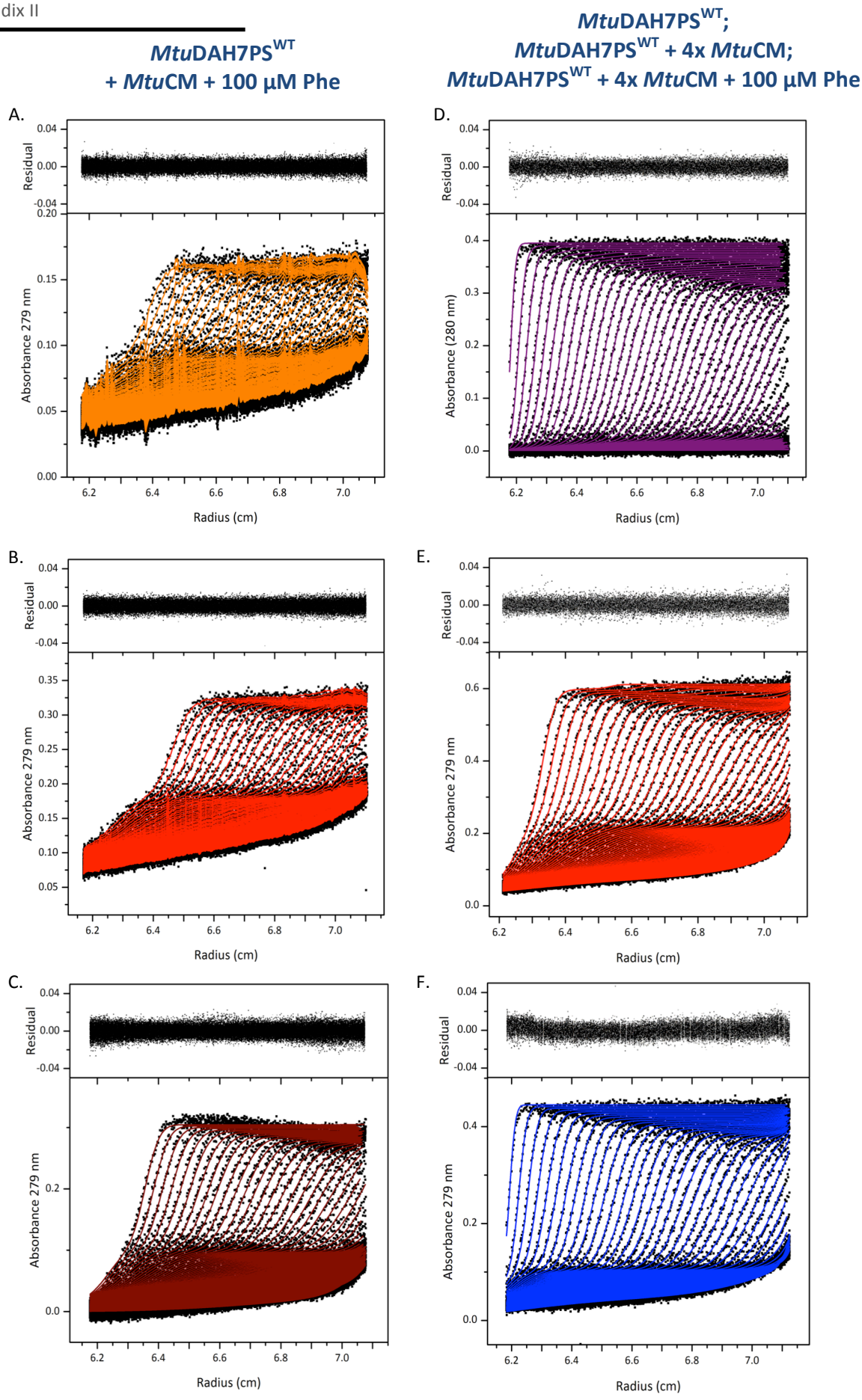

Figure AII.5 Left *Mtu*DAH7PS^{WT} + equimolar amount of *Mtu*CM + 100 µM Phe at 0.2 mg/mL (A.) 0.4 mg/mL (B.) and 0.6 mg/mL (C.). Right *Mtu*DAH7PS^{WT} at 0.4 mg/mL (D.) *Mtu*DAH7PS^{WT} + four-fold molar excess of *Mtu*CM at 0.4 mg/mL (E.) and *Mtu*DAH7PS^{WT} + four-fold molar excess of *Mtu*CM + 100 µM Phe at 0.4 mg/mL (F.).

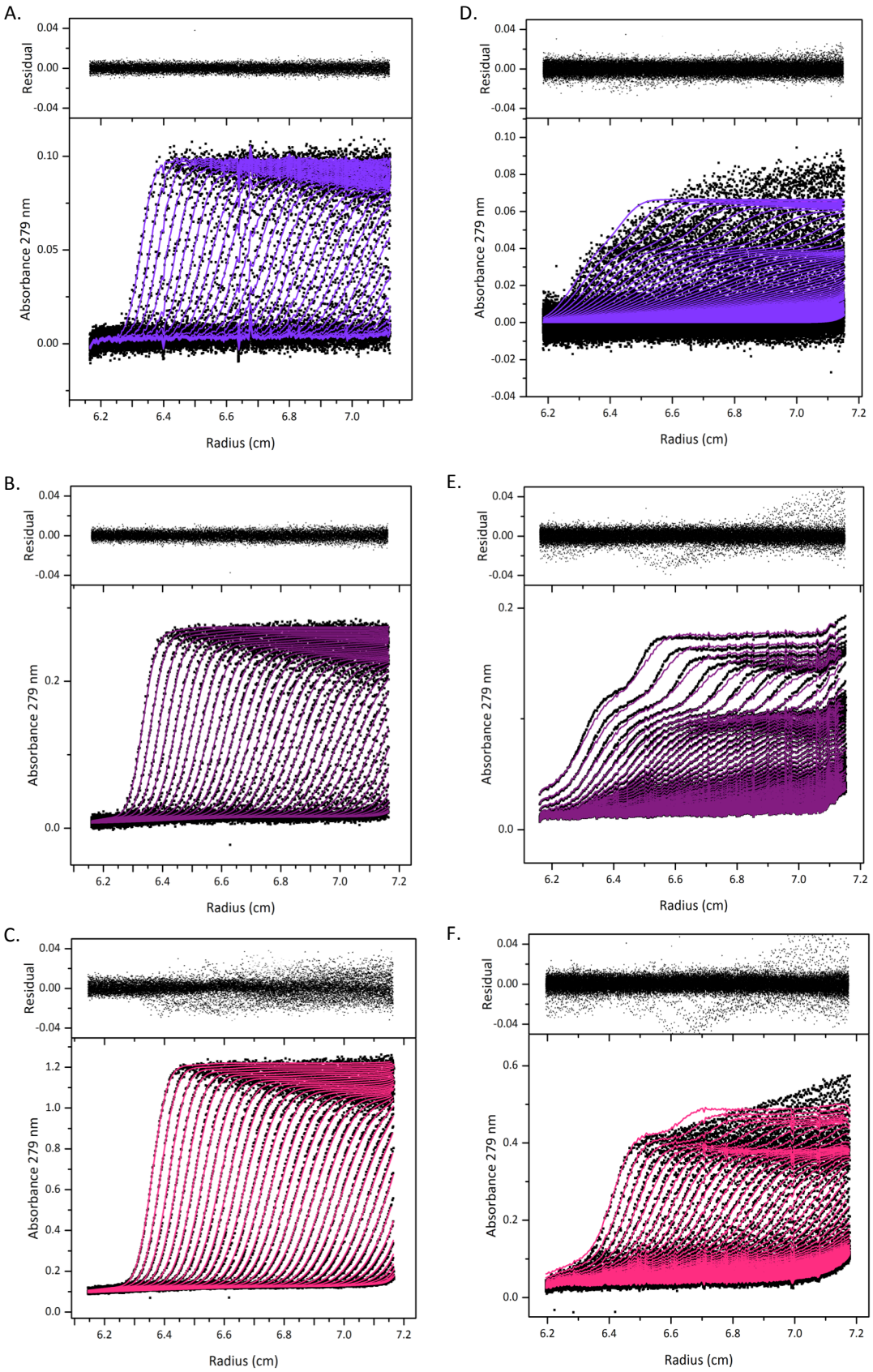

Figure AII.6 Left *Mtu*DAH7PS^{G190P} at 0.1 mg/mL (A.) 0.25 mg/mL (B.) and 1.0 mg/mL (C.). Right *Mtu*DAH7PS^{V103A} at 0.1 mg/mL (D.) 0.3 mg/mL (E.) and 1.0 mg/mL (F.).

Chapter 6

*Mtu*DAH7PS^{K123M}

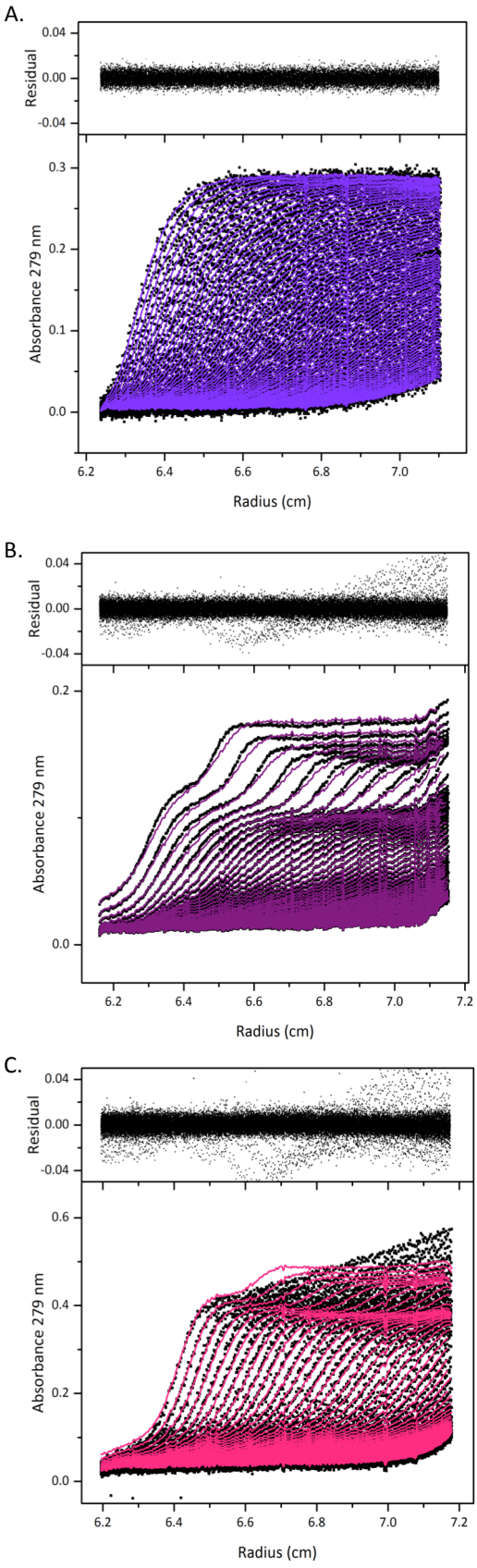

Figure AII.7 *Mtu*DAH7PS^{K123M} at 0.3 mg/mL (A.) 0.6 mg/mL (B.) and 1.0 mg/mL (C.).

Appendix III – Protein-Protein interface interactions

In this section the PDBsum analysis, which schematically depicts the interactions between residues at a protein-protein interface. Dashed orange lines represent a hydrogen bond, and the solid blue line represents a hydrogen bond between residue pairs. The four subunits of *Mtu*DAH7PS have been identified as chains A-D and the two subunits of *Mtu*CM as chains E and F as shown in the schematic below (Figure AIII.1).

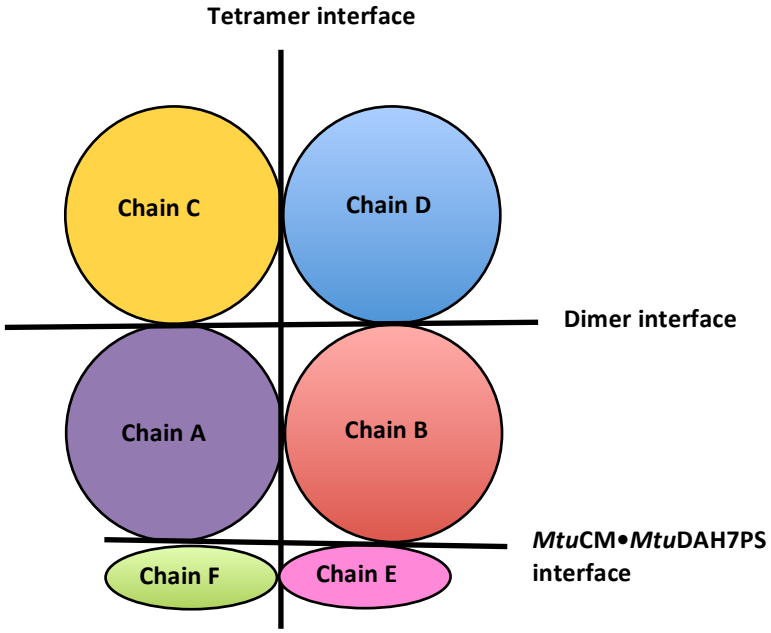

Figure AIII.1 Schematic of the dimer, tetramer and *Mtu*CM•*Mtu*DAH7PS interfaces. The subunits of *Mtu*DAH7PS have been identified as chains A-D, and the two subunits of *Mtu*CM have been identified as chains E and F.

Chapter 2

Interactions at the dimer interface

*Mtu*DAH7PS^{WT}
(PDB code: 3NV8)

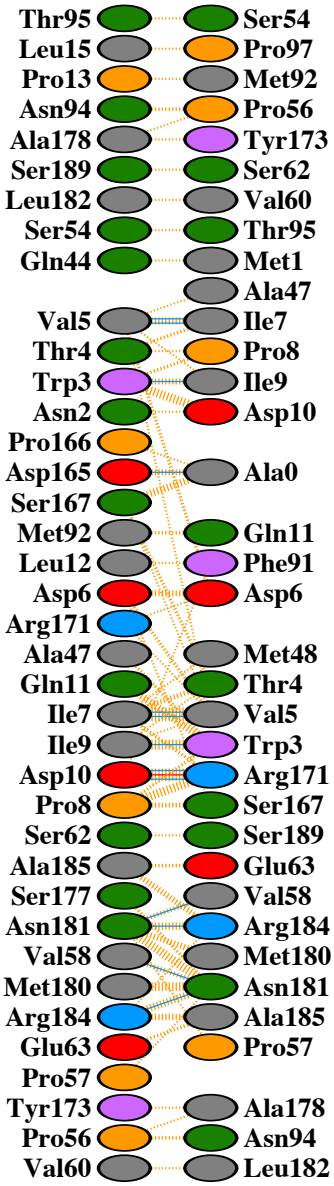

*Mtu*DAH7PS^{WT}+ Trp + Phe
(PDB code: 3KGF)

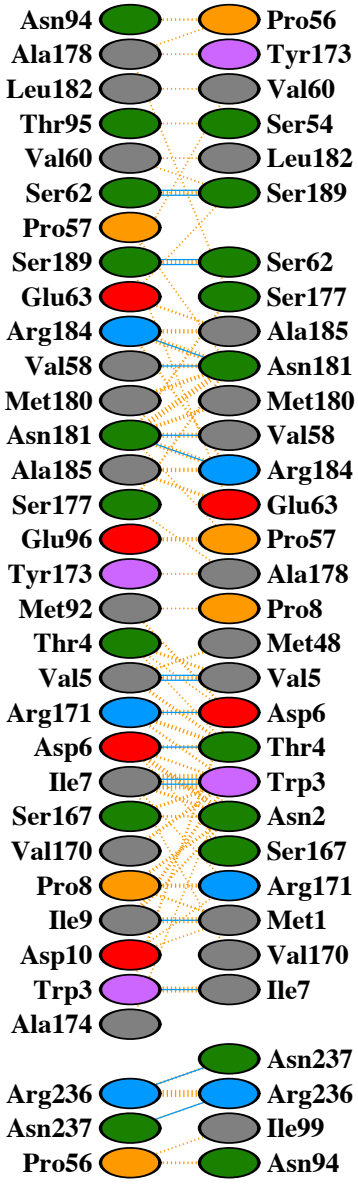

Interactions at the tetramer interface

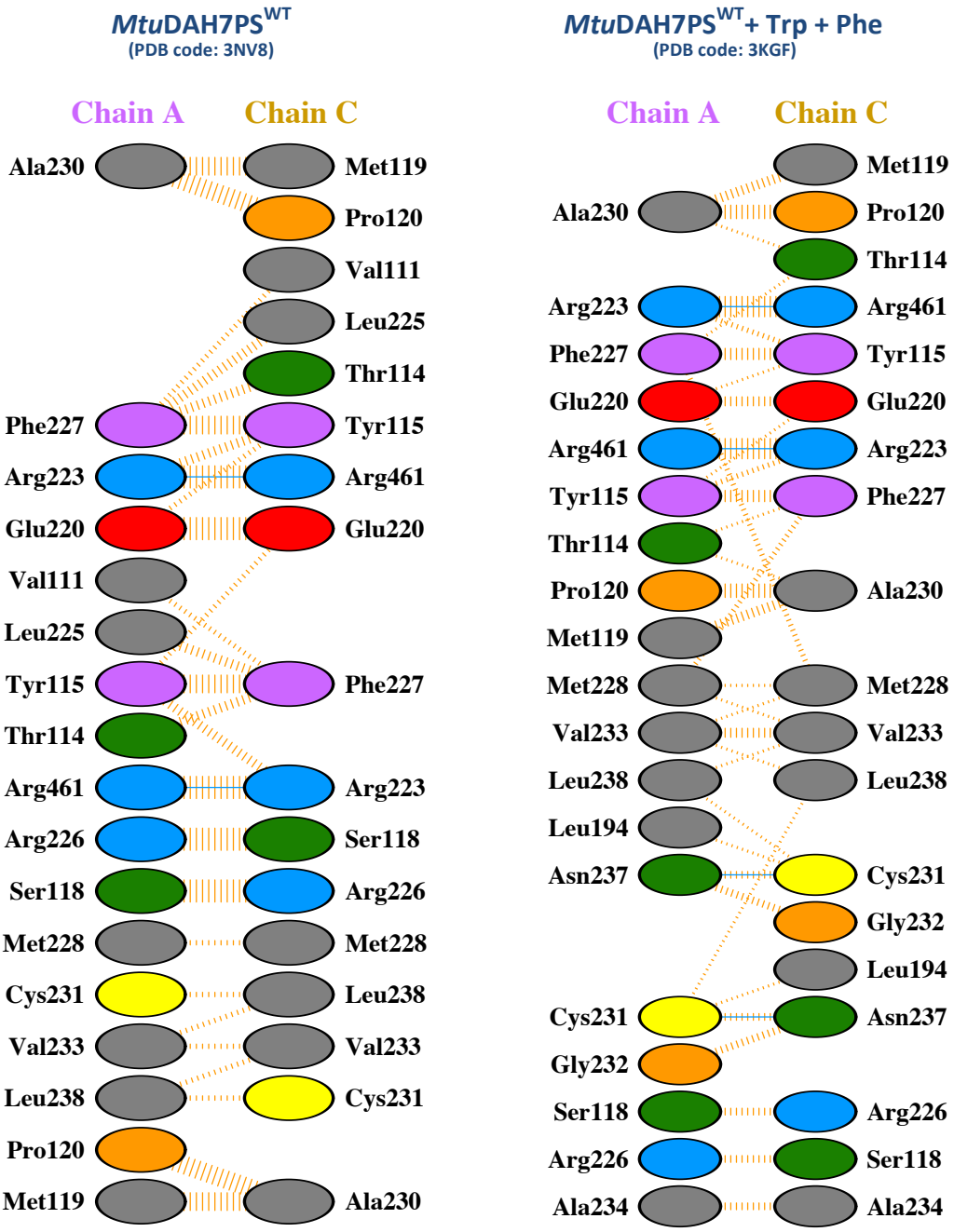

Chapter 4

Interactions at the *Mtu*CM•*Mtu*DAH7PS interface

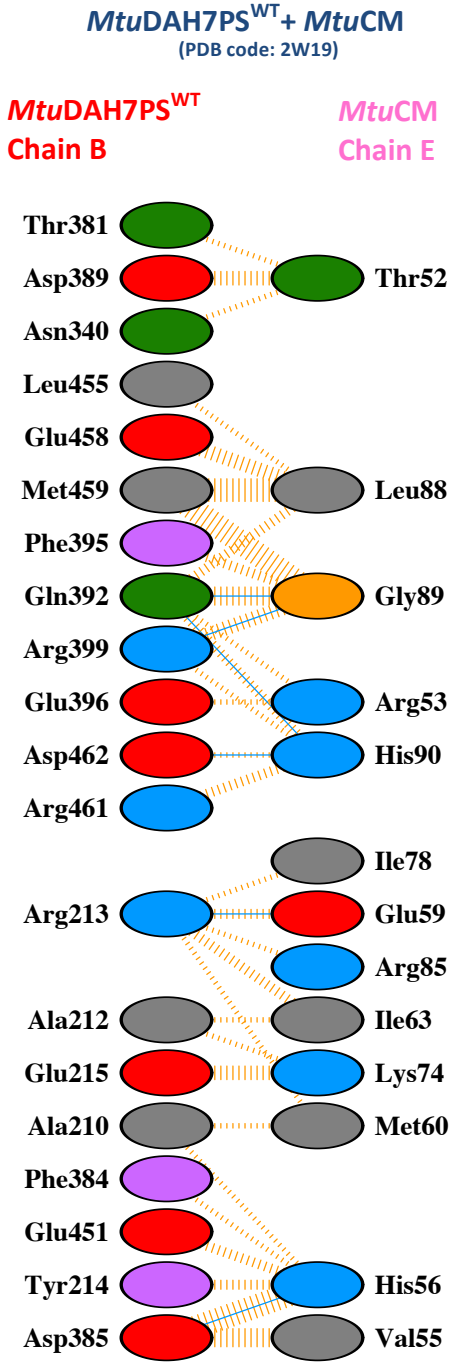

Appendix IV – ITC heats of dilution

In this section an example of the heat of dilution (HOD) for each ligand, Trp, Phe and Tyr, used in the ITC analysis of *Mtu*DAH7PS^{WT} and the *Mtu*DAH7PS variants are shown

HOD for 300 µM Trp

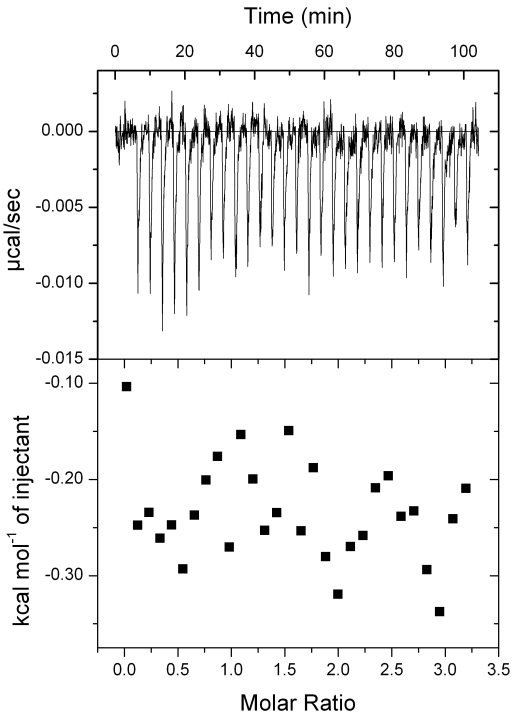

HOD for 900 µM Phe

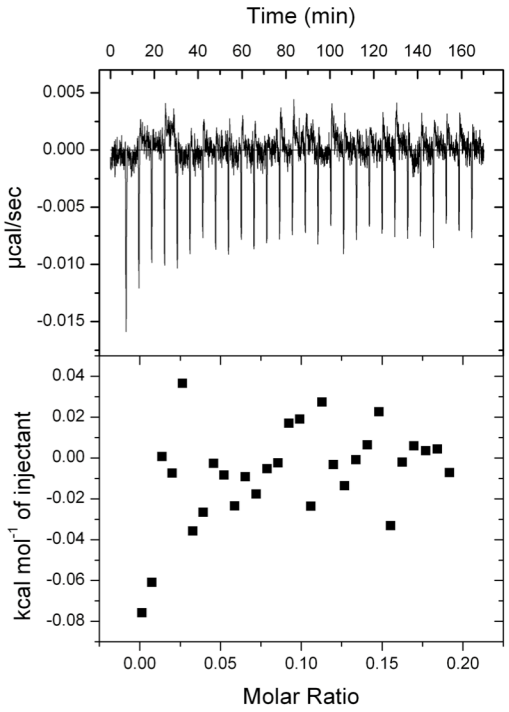

HOD for 2 mM Tyr

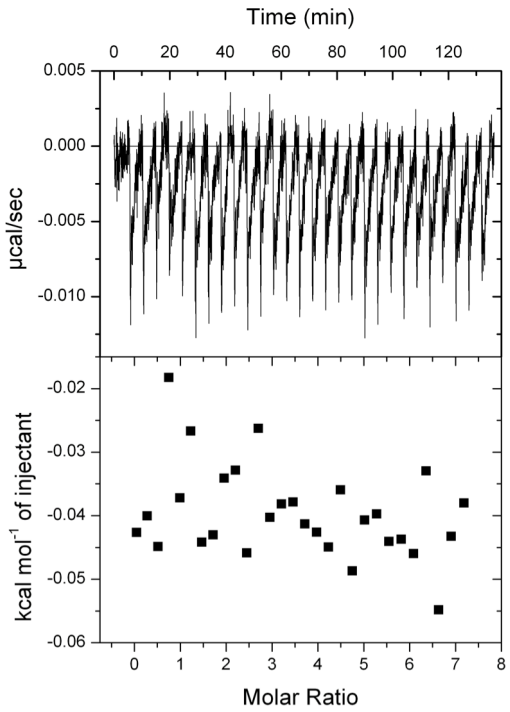

Appendix V – Student t-test analysis of DSF and kinetic data

In this section the p-values determined via a two-tailed student t-test performed on the DSF and kinetic data have been tabulated. A 95 % confidence interval was used.

DSF student t-test analysis

Chapter 2	Ligand	Mean T_m (˚C)	Error (˚C)	P value 0.5
MtuD WT	None	51.5	0.1	
MtuD WT	W	60.1	0.6	0.00
MtuD WT	F	54.1	0.5	0.01
MtuD WT	Y	52.5	0.1	0.01
MtuD WT	WF	60.4	0.7	0.00
MtuD WT	WY	58.1	0.4	0.00
MtuD WT	YF	55.9	0.6	0.00
MtuD WT	WFY	62.1	0.6	0.00
MtuD WT	500W	63.6	0.5	0.00
MtuD WT	1000W	66.5	0.1	0.00
MtuD WT	500F	58.9	0.1	0.00
MtuD WT	1000F	62.5	0.1	0.00
MtuD WT	500Y	49.5	0.4	0.02
MtuD WT	1000Y	42.7	0.8	0.00
Chapter 3	**Ligand**	**Mean T_m (˚C)**	**Error (˚C)**	**P value 0.5**
MtuD R171A	None	51.1	0.1	
MtuD R171A	W	58.6	0.0	0.00
MtuD R171A	F	51.2	0.0	0.18
MtuD R171A	Y	51.6	0.0	0.02
MtuD R171A	WF	57.7	0.1	0.00
MtuD R171A	WY	58.8	0.0	0.00
MtuD R171A	FY	51.7	0.1	0.04
MtuD R171A	WFY	58.5	0.1	0.00
MtuD R256A	None	50.8	0.0	
MtuD R256A	W	58.2	0.5	0.00
MtuD R256A	F	53.2	0.5	0.02
MtuD R256A	Y	50.9	0.1	0.18
MtuD R256A	WF	60.7	0.1	0.00
MtuD R256A	WY	58.3	0.8	0.00
MtuD R256A	YF	52.7	0.6	0.03
MtuD R256A	WFY	60.1	0.3	0.00
Chapter 4	**Ligand**	**Mean T_m (˚C)**	**Error (˚C)**	**P value 0.5**
MtuCM	None	54.7	0.4	
MtuCM	W	52.9	1.2	0.20
MtuCM	F	52.8	0.0	0.02
MtuCM	Y	48.1	0.8	0.01
MtuCM	YF	50.3	0.5	0.01
MtuCM	WFY	51.9	1.2	0.03
Chapter 5	**Ligand**	**Mean T_m (˚C)**	**Error (˚C)**	**P value 0.5**
MtuD G190P	None	52.6	0.0	
MtuD G190P	W	57.4	0.0	ND
MtuD G190P	F	58.5	0.1	0.00
MtuD G190P	Y	53.6	0.0	ND
MtuD G190P	WF	60.4	0.0	ND
MtuD G190P	WY	58.2	0.2	0.00
MtuD G190P	YF	61.7	0.1	0.00
MtuD G190P	WFY	63.2	0.0	0.00
MtuD G190P	500W	64.6	0.2	0.00
MtuD G190P	1000W	67.1	0.1	0.00

Chapter 5	Ligand	Mean T_m (˚C)	Error (˚C)	P value 0.5
MtuD Y131A	None	44.9	0.5	
MtuD Y131A	W	52.3	0.1	0.00
MtuD Y131A	F	42.7	0.6	0.00
MtuD Y131A	Y	49.4	0.0	0.00
MtuD Y131A	WF	53.1	0.8	0.00
MtuD Y131A	WY	53.8	0.2	0.00
MtuD Y131A	YF	49.4	0.0	0.00
MtuD Y131A	WFY	53.9	0.1	0.00
MtuD V103A	None	40.2	0.0	
MtuD V103A	W	51.2	0.3	0.00
MtuD V103A	F	44.2	0.5	0.01
MtuD V103A	Y	48.4	0.0	ND
MtuD V103A	WF	54.4	0.0	ND
MtuD V103A	WY	51.6	0.0	ND
MtuD V103A	YF	54.1	0.1	0.00
MtuD V103A	WFY	57.2	0.3	0.00
MtuD N175A	None	44.1	0.5	
MtuD N175A	W	51.3	0.1	0.00
MtuD N175A	F	44.3	0.6	0.46
MtuD N175A	Y	49.3	0.5	0.01
MtuD N175A	WF	51.4	0.0	0.00
MtuD N175A	WY	54.5	0.1	0.00
MtuD N175A	YF	48.9	0.3	0.00
MtuD N175A	WFY	54.3	0.1	0.00
Chapter 6	**Ligand**	**Mean T_m (˚C)**	**Error (˚C)**	**P value 0.5**
MtuK123M	None	47.8	0.0	
MtuK123M	W	48.0	0.0	0.00
MtuK123M	F	51.3	0.4	0.00
MtuK123M	Y	46.9	0.3	0.03
MtuK123M	WF	51.7	0.1	0.00
MtuK123M	WY	47.5	0.1	0.04
MtuK123M	YF	54.7	0.6	0.00
MtuK123M	WFY	55.1	0.5	0.00
MtuD N237A	None	51.2	0.2	
MtuD N237A	W	52.6	0.7	0.04
MtuD N237A	F	55.9	0.5	0.01
MtuD N237A	Y	56.9	0.8	0.01
MtuD N237A	WF	56.2	0.3	0.00
MtuD N237A	WY	56.5	0.1	0.00
MtuD N237A	YF	59.2	0.3	0.00
MtuD N237A	WFY	59.1	0.2	0.00
Chapter 7	**Ligand**	**Mean T_m (˚C)**	**Error (˚C)**	**P value 0.5**
MtuD G232P	None	47.9	0.3	
MtuD G232P	W	48.1	0.8	0.53
MtuD G232P	F	52.0	0.3	0.00
MtuD G232P	Y	50.7	0.6	0.01
MtuD G232P	WF	51.9	0.1	0.00
MtuD G232P	WY	51.5	0.2	0.00
MtuD G232P	YF	59.0	0.9	0.00
MtuD G232P	WFY	59.3	0.4	0.00

Chapter 7 cont.	Ligand	Mean T_m (˚C)	Error (˚C)	P value 0.5
MtuD G190P/G232P	None	49.3	0.4	
MtuD G190P/G232P	W	49.6	0.0	0.30
MtuD G190P/G232P	F	51.0	0.0	0.02
MtuD G190P/G232P	Y	52.9	0.1	0.01
MtuD G190P/G232P	WF	53.5	0.1	0.01
MtuD G190P/G232P	WY	51.4	0.0	0.01
MtuD G190P/G232P	YF	57.8	0.5	0.00
MtuD G190P/G232P	WFY	59.4	0.2	0.00
MtuD G190P/G232P	500W	49.9	0.6	0.33
MtuD G190P/G232P	1000W	51.1	0.4	0.02
MtuD F227D	None	43.0	1.2	
MtuD F227D	W	43.9	0.2	0.38
MtuD F227D	F	46.7	0.7	0.02
MtuD F227D	Y	46.1	0.4	0.08
MtuD F227D	WF	46.6	0.0	0.04
MtuD F227D	WY	46.3	0.8	0.11
MtuD F227D	YF	51.5	0.1	0.01
MtuD F227D	WFY	52.0	0.4	0.01

Student t-test analysis on DAH7PS kinetic data

Chapter 2	Ligand	Mean rate (%)	Error (%)	P value 0.5
MtuD WT	None	100.0	1.1	
MtuD WT	W	90.6	3.4	0.03
MtuD WT	F	88.1	4.6	0.06
MtuD WT	Y	77.5	1.5	0.00
MtuD WT	YF	85.9	5.4	0.06
MtuD WT	WY	26.7	2.8	0.00
MtuD WT	WF	6.9	0.1	0.00
MtuD WT	WFY	0.6	0.3	0.00
MtuD WT	WFF	1.9	0.2	0.00
MtuD WT	WYY	11.7	4.7	0.00
Chapter 3	**Ligand**	**Mean rate (%)**	**Error (%)**	**P value 0.5**
MtuD R171A	None	100.0	1.9	
MtuD R171A	W	95.8	0.9	0.02
MtuD R171A	F	94.6	3.3	0.02
MtuD R171A	Y	73.1	3.1	0.00
MtuD R171A	YF	79.0	2.3	0.01
MtuD R171A	WY	76.8	0.6	0.00
MtuD R171A	WF	60.9	2.6	0.00
MtuD R171A	WFY	23.7	2.7	0.00
MtuD R171A	WFF	86.8	3.6	0.03
MtuD R171A	WYY	54.9	7.0	0.01
MtuD R256A	None	100.0	2.2	
MtuD R256A	W	99.8	0.5	0.89
MtuD R256A	F	84.4	2.7	0.00
MtuD R256A	Y	90.0	2.0	0.01
MtuD R256A	YF	82.0	5.6	0.03
MtuD R256A	WY	98.4	3.1	0.58
MtuD R256A	WF	17.6	1.6	0.00
MtuD R256A	WFY	15.3	0.6	0.00
MtuD R256A	WFF	12.9	2.2	0.00
MtuD R256A	WYY	99.5	4.3	0.90
Chapter 4	**Ligand**	**Mean rate (%)**	**Error (%)**	**P value 0.5**
MtuD MtuCM	None	100.0	5.5	
MtuD MtuCM	W	225.8	1.7	0.01
MtuD MtuCM	F	139.9	1.8	0.02
MtuD MtuCM	Y	155.8	0.1	0.03
MtuD MtuCM	YF	106.1	4.5	0.37
MtuD MtuCM	WY	48.2	3.2	0.00
MtuD MtuCM	WF	6.1	0.2	0.02
MtuD MtuCM	WFY	4.1	1.5	0.02
MtuD H6	None	100.0	3.2	
MtuD H6	W	96.6	3.6	0.45
MtuD H6	F	95.4	1.7	0.15
MtuD H6	Y	89.3	6.7	0.16
MtuD H6	YF	75.0	1.9	0.01
MtuD H6	WY	66.4	1.4	0.00
MtuD H6	WF	19.3	0.5	0.00
MtuD H6	WFY	7.2	1.7	0.00

Chapter 5	Ligand	Mean rate (%)	Error (%)	P value 0.5
MtuD G190P	None	100.0	2.3	
MtuD G190P	W	93.5	3.1	0.03
MtuD G190P	F	106.8	4.3	0.15
MtuD G190P	Y	88.8	5.2	0.11
MtuD G190P	YF	87.9	3.4	0.06
MtuD G190P	WY	90.6	1.8	0.00
MtuD G190P	WF	99.8	4.3	0.87
MtuD G190P	WFY	83.6	0.5	0.01
MtuD Y131A	None	100.0	0.9	
MtuD Y131A	W	116.4	1.7	0.05
MtuD Y131A	F	168.6	6.5	0.04
MtuD Y131A	Y	112.9	2.0	0.08
MtuD Y131A	YF	194.4	1.7	0.01
MtuD Y131A	WY	90.5	5.2	0.22
MtuD Y131A	WF	114.6	0.4	0.02
MtuD Y131A	WFY	41.6	4.4	0.03
MtuD V103A	None	100.0	3.9	
MtuD V103A	W	104.8	2.8	0.54
MtuD V103A	F	99.9	3.0	0.28
MtuD V103A	Y	103.4	0.7	0.26
MtuD V103A	YF	83.0	0.2	0.04
MtuD V103A	WY	75.8	3.1	0.08
MtuD V103A	WF	19.5	7.5	0.05
MtuD V103A	WFY	3.6	0.0	0.01
MtuD N175A	None	100.0	4.5	
MtuD N175A	W	84.2	5.2	0.22
MtuD N175A	F	94.8	4.5	0.43
MtuD N175A	Y	98.7	1.6	0.52
MtuD N175A	YF	97.8	0.1	0.36
MtuD N175A	WY	11.7	0.9	0.00
MtuD N175A	WF	59.4	3.7	0.08
MtuD N175A	WFY	15.2	0.1	0.02
Chapter 6	**Ligand**	**Mean rate (%)**	**Error (%)**	**P value 0.5**
MtuD K123M	None	100.0	3.1	
MtuD K123M	W	84.5	5.0	0.08
MtuD K123M	F	30.3	2.3	0.00
MtuD K123M	Y	38.0	3.4	0.00
MtuD K123M	YF	26.1	3.9	0.00
MtuD K123M	WY	35.4	1.6	0.00
MtuD K123M	WF	29.6	0.6	0.00
MtuD K123M	WFY	24.6	3.4	0.00
MtuD N237A	None	100.0	3.5	
MtuD N237A	W	121.1	0.7	0.00
MtuD N237A	F	22.4	0.3	0.01
MtuD N237A	Y	28.9	2.9	0.02
MtuD N237A	YF	21.0	1.0	0.01
MtuD N237A	WY	30.2	3.3	0.02
MtuD N237A	WF	3.2	0.8	0.00
MtuD N237A	WFY	1.9	0.4	0.00

Chapter 7	Ligand	Mean rate (%)	Error (%)	P value 0.5
MtuD G232P	None	100.0	4.9	
MtuD G232P	W	91.2	1.6	0.12
MtuD G232P	F	60.1	3.8	0.00
MtuD G232P	Y	65.7	2.9	0.00
MtuD G232P	YF	64.4	1.2	0.01
MtuD G232P	WY	60.5	2.1	0.00
MtuD G232P	WF	65.9	4.4	0.01
MtuD G232P	WFY	60.6	5.9	0.02
MtuD G190P/G232P	None	100.0	4.5	
MtuD G190P/G232P	W	99.3	3.0	0.86
MtuD G190P/G232P	F	58.9	2.7	0.01
MtuD G190P/G232P	Y	51.5	2.5	0.00
MtuD G190P/G232P	YF	37.9	0.3	0.00
MtuD G190P/G232P	WY	58.5	4.7	0.02
MtuD G190P/G232P	WF	54.1	4.2	0.01
MtuD G190P/G232P	WFY	50.8	3.7	0.01
MtuD F227D	None	100.0	4.7	
MtuD F227D	W	92.7	3.4	0.53
MtuD F227D	F	46.4	4.0	0.01
MtuD F227D	Y	77.5	2.9	0.06
MtuD F227D	YF	51.9	1.9	0.04
MtuD F227D	WY	61.8	1.4	0.09
MtuD F227D	WF	52.4	6.5	0.00
MtuD F227D	WFY	47.1	3.0	0.02
1800 µM E4P				
MtuD G232P	None	100.0	1.0	
MtuD G232P	W	98.6	5.6	0.74
MtuD G232P	F	93.8	1.2	0.01
MtuD G232P	Y	81.8	2.5	0.04
MtuD G232P	YF	88.4	0.7	0.07
MtuD G232P	WY	95.3	0.7	0.16
MtuD G232P	WF	83.7	6.5	0.20
MtuD G232P	WFY	76.0	5.1	0.08
G190P/G232P	None	100.0	4.2	
G190P/G232P	W	84.4	4.6	0.01
G190P/G232P	F	92.9	8.9	0.58
G190P/G232P	Y	95.9	4.6	0.05
G190P/G232P	YF	101.0	3.2	0.88
G190P/G232P	WY	76.4	3.0	0.02
G190P/G232P	WF	79.8	1.6	0.13
G190P/G232P	WFY	96.5	3.2	0.62
MtuD F227D	None	100.0	3.1	
MtuD F227D	W	97.5	0.8	0.38
MtuD F227D	F	100.4	1.8	0.75
MtuD F227D	Y	86.0	2.3	0.17
MtuD F227D	YF	88.1	4.7	0.28
MtuD F227D	WY	101.0	2.0	0.05
MtuD F227D	WF	96.0	0.7	0.38
MtuD F227D	WFY	84.8	0.2	0.03
		100.0	2.4	0.02

Chapter 7 cont.	Ligand	Mean rate (%)	Error (%)	P value 0.5
MtuD WT	None	100.0	0.6	
MtuD WT	W	49.9	1.1	0.02
MtuD WT	F	96.5	0.3	0.04
MtuD WT	Y	87.3	0.2	0.02
MtuD WT	YF	88.6	0.4	0.04
MtuD WT	WY	13.6	1.0	0.00
MtuD WT	WF	4.9	0.1	0.00
MtuD WT	WFY	4.3	0.2	0.00

Student t-test analysis on CM kinetic data

Chapter 4	Ligand	Mean rate (%)	Error (%)	P value 0.5
MtuCM	None	100.0	2.2	
MtuCM	F	102.2	2.3	0.47
MtuCM	W	99.9	3.1	0.97
MtuCM	Y	98.1	0.6	0.52
MtuCM	WF	99.1	1.4	0.60
MtuCM	FY	99.4	1.8	0.17
MtuCM	WY	97.2	0.0	0.44
MtuCM	WFY	98.0	2.2	0.35
150				
MtuCM -DWT	None	100.0	0.2	
MtuCM -DWT	F	63.1	0.1	0.06
MtuCM -DWT	W	94.0	3.0	0.46
MtuCM -DWT	Y	88.1	0.4	0.19
MtuCM -DWT	WF	38.8	1.2	0.05
MtuCM -DWT	FY	35.1	0.5	0.05
MtuCM -DWT	WY	60.6	2.7	0.04
MtuCM -DWT	WFY	29.5	2.6	0.05
25				
MtuCM -DWT	None	100.0	3.9	
MtuCM -DWT	F	16.4	2.0	0.00
MtuCM -DWT	W	93.1	10.0	0.12
MtuCM -DWT	Y	59.5	9.1	0.03
MtuCM -DWT	WF	2.2	1.8	0.00
MtuCM -DWT	FY	6.4	2.2	0.00
MtuCM -DWT	WY	23.1	7.9	0.00
MtuCM -DWT	WFY	1.0	0.7	0.00
MtuCM -DR171A	None	100.0	7.7	
MtuCM -DR171A	F	83.8	5.2	0.00
MtuCM -DR171A	W	109.4	5.5	0.42
MtuCM -DR171A	Y	118.6	3.8	0.34
MtuCM -DR171A	WF	79.3	8.9	0.01
MtuCM -DR171A	FY	79.8	2.5	0.01
MtuCM -DR171A	WY	93.3	10.8	0.21
MtuCM -DR171A	WFY	92.1	11.7	0.06

Chapter 4 cont.	Ligand	Mean rate (%)	Error (%)	P value 0.5
MtuCM -DR256A	None	100.0	1.2	
MtuCM -DR256A	F	20.9	2.7	0.00
MtuCM -DR256A	W	90.7	3.7	0.04
MtuCM -DR256A	Y	97.7	2.8	0.47
MtuCM -DR256A	WF	19.4	5.6	0.00
MtuCM -DR256A	FY	27.8	12.2	0.00
MtuCM -DR256A	WY	86.8	1.3	0.01
MtuCM -DR256A	WFY	17.2	0.9	0.00
Chapter 5	**Ligand**	**Mean rate (%)**	**Error (%)**	**P value 0.5**
MtuCM -DG190P	None	100.0	1.0	
MtuCM -DG190P	F	24.1	1.8	0.00
MtuCM -DG190P	W	136.8	7.7	0.03
MtuCM -DG190P	Y	88.6	6.4	0.01
MtuCM -DG190P	WF	105.2	5.7	0.03
MtuCM -DG190P	FY	16.3	3.3	0.00
MtuCM -DG190P	WY	123.5	1.7	0.50
MtuCM -DG190P	WFY	51.3	4.1	0.00
MtuCM -DY131A	None	100.0	14.1	
MtuCM -DY131A	F	74.9	3.4	0.07
MtuCM -DY131A	W	82.8	5.9	0.08
MtuCM -DY131A	Y	57.3	8.6	0.01
MtuCM -DY131A	WF	54.5	3.8	0.02
MtuCM -DY131A	FY	21.3	3.3	0.01
MtuCM -DY131A	WY	71.0	0.9	0.06
MtuCM -DY131A	WFY	16.4	0.6	0.01
MtuCM -DV103A	None	100.0	5.2	
MtuCM -DV103A	F	45.9	1.7	0.03
MtuCM -DV103A	W	110.0	4.4	0.03
MtuCM -DV103A	Y	93.4	8.7	0.59
MtuCM -DV103A	WF	59.9	9.2	0.16
MtuCM -DV103A	FY	16.8	2.7	0.01
MtuCM -DV103A	WY	77.0	0.0	0.10
MtuCM -DV103A	WFY	28.4	2.0	0.00
MtuCM -DN175A	None	100.0	2.3	
MtuCM -DN175A	F	70.1	1.2	0.05
MtuCM -DN175A	W	4.6	1.3	0.00
MtuCM -DN175A	Y	76.9	8.8	0.12
MtuCM -DN175A	WF	3.2	2.2	0.02
MtuCM -DN175A	FY	41.3	3.8	0.01
MtuCM -DN175A	WY	39.8	18.8	0.35
MtuCM -DN175A	WFY	29.2	0.4	0.01
Chapter 6	**Ligand**	**Mean rate (%)**	**Error (%)**	**P value 0.5**
MtuCM -DK123M	None	100.0	9.6	
MtuCM -DK123M	F	11.3	2.5	0.01
MtuCM -DK123M	W	126.6	5.7	0.00
MtuCM -DK123M	Y	4.4	4.7	0.01
MtuCM -DK123M	WF	0.0	9.2	0.01
MtuCM -DK123M	FY	2.5	7.3	0.00
MtuCM -DK123M	WY	2.4	0.4	0.00
MtuCM -DK123M	WFY	6.3	0.2	0.00

Chapter 6 cont.	Ligand	Mean rate (%)	Error (%)	P value 0.5
MtuCM -DN237A	None	100.0	9.8	
MtuCM -DN237A	F	4.3	3.8	0.00
MtuCM -DN237A	W	196.0	12.8	0.01
MtuCM -DN237A	Y	26.0	9.7	0.00
MtuCM -DN237A	WF	3.2	8.5	0.01
MtuCM -DN237A	FY	12.8	7.5	0.00
MtuCM -DN237A	WY	10.1	1.2	0.02
MtuCM -DN237A	WFY	2.5	0.5	0.01
Chapter 7	**Ligand**	**Mean rate (%)**	**Error (%)**	**P value 0.5**
MtuCM -DG232P	None	100.0	6.1	
MtuCM -DG232P	F	80.6	5.0	0.35
MtuCM -DG232P	W	144.0	4.1	0.00
MtuCM -DG232P	Y	94.5	2.5	0.23
MtuCM -DG232P	WF	118.4	11.8	0.03
MtuCM -DG232P	FY	108.6	8.3	0.07
MtuCM -DG232P	WY	107.4	4.1	0.01
MtuCM -DG232P	WFY	108.6	1.2	0.01
MtuCM –DF227D	None	100.0	2.0	
MtuCM –DF227D	F	92.0	5.5	0.20
MtuCM –DF227D	W	99.7	9.1	0.98
MtuCM –DF227D	Y	92.0	4.5	0.14
MtuCM –DF227D	WF	88.0	0.1	0.08
MtuCM –DF227D	FY	89.4	2.0	0.17
MtuCM –DF227D	WY	90.7	2.0	0.25
MtuCM –DF227D	WFY	84.4	0.1	0.04

Bibliography

1 Campbell, M. K. & Farrell, S. *Biochemistry*. 8th edn, (Cengage Learning, 2013).

2 Garrett, R. H. & Grisham, C. M. *Biochemistry*. 3rd edn, (Thomson Brooks/Cole, 2005).

3 Nussinov, R. & Tsai, C. J. Allostery in disease and in drug discovery. *Cell* **153**, 293-305 (2013).

4 Cornish-Bowden, A. Understanding allosteric and cooperative interactions in enzymes. *FEBS J.* **281**, 621-632 (2014).

5 Jaffe, E. K. Morpheeins-a new structural paradigm for allosteric regulation. *Trends Biochem. Sci.* **30**, 490-497 (2005).

6 Okazaki, K. & Takada, S. Dynamic energy landscape view of coupled binding and protein conformational change: induced-fit versus population-shift mechanisms. *Proc. Natl. Acad. Sci. U. S. A.* **105**, 11182-11187 (2008).

7 Monod, J., Wyman, J. & Changeux, J. P. On the nature of allosteric transitions: a plausible model. *J. Mol. Biol.* **12**, 88-118 (1965).

8 Changeux, J. P. 50 years of allosteric interactions: the twists and turns of the models. *Nat. Rev. Mol. Cell Biol.* **14**, 819-829 (2013).

9 Koshland, D. E., Jr., Nemethy, G. & Filmer, D. Comparison of experimental binding data and theoretical models in proteins containing subunits. *Biochemistry* **5**, 365-385 (1966).

10 Cui, Q. & Karplus, M. Allostery and cooperativity revisited. *Protein Sci.* **17**, 1295-1307 (2008).

11 Perica, T. *et al.* The emergence of protein complexes: quaternary structure, dynamics and allostery. Colworth Medal Lecture. *Biochem. Soc. Trans.* **40**, 475-491.

12 Selwood, T. & Jaffe, E. K. Dynamic dissociating homo-oligomers and the control of protein function. *Arch. Biochem. Biophys.* **519**, 131-143.

13 Haber, J. E. & Koshland, D. E., Jr. Relation of protein subunit interactions to the molecular species observed during cooperative binding of ligands. *Proc. Natl. Acad. Sci. U. S. A.* **58**, 2087-2093 (1967).

14 Eigen, M. New looks and outlooks on physical enzymology. *Q. Rev. Biophys.* **1**, 3-33 (1968).

15 Tsai, C. J. & Nussinov, R. A unified view of "how allostery works". *PLoS Comput Biol* **10**, e1003394 (2014).

16 Peracchi, A. & Mozzarelli, A. Exploring and exploiting allostery: models, evolution, and drug targeting. *Biochim. Biophys. Acta* **1814**, 922-933 (2011).

17 Gunasekaran, K., Ma, B. & Nussinov, R. Is allostery an intrinsic property of all dynamic proteins? *Proteins* **57**, 433-443 (2004).

18 Swain, J. F. & Gierasch, L. M. The changing landscape of protein allostery. *Curr. Opin. Struct. Biol.* **16**, 102-108 (2006).

19 Changeux, J. P. Allostery and the Monod-Wyman-Changeux model after 50 years. *Annu Rev Biophys* **41**, 103-133 (2012).

20 Goodey, N. M. & Benkovic, S. J. Allosteric regulation and catalysis emerge via a common route. *Nat. Chem. Biol.* **4**, 474-482 (2008).

21 Hilser, V. J., Dowdy, D., Oas, T. G. & Freire, E. The structural distribution of cooperative interactions in proteins: analysis of the native state ensemble. *Proc. Natl. Acad. Sci. U. S. A.* **95**, 9903-9908 (1998).

22 Tsai, C. J., del Sol, A. & Nussinov, R. Allostery: absence of a change in shape does not imply that allostery is not at play. *J. Mol. Biol.* **378**, 1-11 (2008).

23 del Sol, A., Tsai, C. J., Ma, B. & Nussinov, R. The origin of allosteric functional modulation: multiple pre-existing pathways. *Structure* **17**, 1042-1050 (2009).

24 McLeish, T. C., Rodgers, T. L. & Wilson, M. R. Allostery without conformation change: modelling protein dynamics at multiple scales. *Phys. Biol.* **10**, 056004 (2013).

25 Kalodimos, C. G. Protein function and allostery: A dynamic relationship. *Ann. N. Y. Acad. Sci.* **1260**, 81-86 (2012).

26 Wood, M. R., Hopkins, C. R., Brogan, J. T., Conn, P. J. & Lindsley, C. W. "Molecular switches" on mGluR allosteric ligands that modulate modes of pharmacology. *Biochemistry* **50**, 2403-2410 (2011).

27 Lavu, S., Boss, O., Elliott, P. J. & Lambert, P. D. Sirtuins-novel therapeutic targets to treat age-associated diseases. *Nat Rev Drug Discov* **7**, 841-853 (2008).

28 Zorn, J. A. & Wells, J. A. Turning enzymes ON with small molecules. *Nat. Chem. Biol.* **6**, 179-188 (2010).

29 Smith, N. J. & Milligan, G. Allostery at G protein-coupled receptor homo- and heteromers: uncharted pharmacological landscapes. *Pharmacol. Rev.* **62**, 701-725 (2010).

30 Johannessen, C. M. *et al.* COT drives resistance to RAF inhibition through MAP kinase pathway reactivation. *Nature* **468**, 968-972 (2010).

31 Global tuberculosis report 2013. (World Health Organisation, WHO Press, Geneva, 2013).

32 Zaman, K. Tuberculosis: A Global Health Problem. *J. Health Popul. Nutr.* **28**, 111-113 (2010).

33 Chang, K. C. & Yew, W. W. Management of difficult multidrug-resistant tuberculosis and extensively drug-resistant tuberculosis: update 2012. *Respirology* **18**, 8-21 (2013).

34 Centers for Disease, C. & Prevention. Emergence of Mycobacterium tuberculosis with extensive resistance to second-line drugs-worldwide, 2000-2004. Report No. 0149-2195, 301-305 (2006).

35 Lange, C. *et al.* Management of patients with multidrug-resistant/extensively drug-resistant tuberculosis in Europe: a TBNET consensus statement. *Eur. Respir. J.* (2014).

36 Eker, B. *et al.* Multidrug- and Extensively Drug-Resistant Tuberculosis, Germany. *Emerg. Infect. Dis.* **14**, 1700-1706 (2008).

37 Velayati, A. A. *et al.* Emergence of new forms of totally drug-resistant tuberculosis bacilli: super extensively drug-resistant tuberculosis or totally drug-resistant strains in iran. *Chest* **136**, 420-425 (2009).

38 Cegielski, P. *et al.* Challenges and controversies in defining totally drug-resistant tuberculosis. *Emerg. Infect. Dis.* **18**, e2 (2012).
39 Udwadia, Z. F., Amale, R. A., Ajbani, K. K. & Rodrigues, C. Totally drug-resistant tuberculosis in India. *Clin. Infect. Dis.* **54**, 579-581 (2012).
40 Velayati, A. A., Farnia, P. & Masjedi, M. R. The totally drug resistant tuberculosis (TDR-TB). *Int J Clin Exp Med* **6**, 307-309 (2013).
41 Klopper, M. *et al.* Emergence and spread of extensively and totally drug-resistant tuberculosis, South Africa. *Emerg. Infect. Dis.* **19**, 449-455 (2013).
42 Roberts, C. W. *et al.* Shikimate pathway in apicomplexan parasites - Reply. *Nature* **397**, 220-220 (1999).
43 Roberts, C. W. *et al.* The shikimate pathway and its branches in apicomplexan parasites. *J. Infect. Dis.* **185**, S25-S36 (2002).
44 Campbell, S. A. *et al.* A complete shikimate pathway in *Toxoplasma gondii*: an ancient eukaryotic innovation. *Int. J. Parasitol.* **34**, 5-13 (2004).
45 Parish, T. & Stoker, N. G. The common aromatic amino acid biosynthesis pathway is essential in *Mycobacterium tuberculosis*. *Microbiology-Sgm* **148**, 3069-3077 (2002).
46 Bentley, R. The Shikimate Pathway - a Metabolic Tree with Many Branches. *Crit. Rev. Biochem. Mol. Biol.* **25**, 307-384 (1990).
47 Cross, P. J., Dobson, R. C., Patchett, M. L. & Parker, E. J. Tyrosine latching of a regulatory gate affords allosteric control of aromatic amino acid biosynthesis. *J. Biol. Chem.* **286**, 10216-10224 (2011).
48 Webby, C. J. *et al.* Synergistic allostery: a sophisticated regulatory network for the control of aromatic amino acid biosynthesis in *Mycobacterium tuberculosis*. *J. Biol. Chem.* **285**, 30567-30576 (2010).
49 Shumilin, I. A., Kretsinger, R. H. & Bauerle, R. H. Crystal structure of phenylalanine-regulated 3-deoxy-D-*arabino*-heptulosonate 7-phosphate synthase from *Escherichia coli*. *Structure* **7**, 865-875 (1999).
50 Shumilin, I. A., Zhao, C., Bauerle, R. & Kretsinger, R. H. Allosteric inhibition of 3-deoxy-D-*arabino*-heptulosonate 7-phosphate synthase alters the coordination of both substrates. *J. Mol. Biol.* **320**, 1147-1156 (2002).
51 Hartmann, M. *et al.* Evolution of feedback-inhibited beta/alpha barrel isoenzymes by gene duplication and a single mutation. *Proc. Natl. Acad. Sci. U. S. A.* **100**, 862-867 (2003).
52 Walker, G. E., Dunbar, B., Hunter, I. S., Nimmo, H. G. & Coggins, J. R. Evidence for a novel class of microbial 3-deoxy-D-*arabino*-heptulosonate 7-phosphate synthase in *Streptomyces coelicolor* A3(2), *Streptomyces rimosus* and *Neurospora crassa*. *Microbiology-Uk* **142**, 1973-1982 (1996).
53 Jensen, R. A., Xie, G., Calhoun, D. H. & Bonner, C. A. The correct phylogenetic relationship of KdsA (3-deoxy-D-*manno*-octulosonate 8-phosphate synthase) with one of two independently evolved classes of AroA (3-deoxy-D-*arabino*-heptulosonate 7-phosphate synthase). *J. Mol. Evol.* **54**, 416-423 (2002).
54 Subramaniam, P. S., Xie, G., Xia, T. & Jensen, R. A. Substrate ambiguity of 3-deoxy-D-*manno*-octulosonate 8-phosphate synthase from *Neisseria gonorrhoeae* in the context of its membership in a protein family containing a subset of 3-deoxy-D-*arabino*-heptulosonate 7-phosphate synthases. *J. Bacteriol.* **180**, 119-127 (1998).

55 Light, S. H. & Anderson, W. F. The diversity of allosteric controls at the gateway to aromatic amino acid biosynthesis. *Protein Sci.* **22**, 395-404 (2013).

56 Shumilin, I. A., Bauerle, R. & Kretsinger, R. H. The high-resolution structure of 3-deoxy-D-*arabino*-heptulosonate 7-phosphate synthase reveals a twist in the plane of bound phosphoenolpyruvate. *Biochemistry* **42**, 3766-3776 (2003).

57 Wagner, T., Shumilin, I. A., Bauerle, R. & Kretsinger, R. H. Structure of 3-deoxy-D-*arabino*-heptulosonate 7-phosphate synthase from *Escherichia coli*: comparison of the Mn(2+)*2-phosphoglycolate and the Pb(2+)*2-phosphoenolpyruvate complexes and implications for catalysis. *J. Mol. Biol.* **301**, 389-399 (2000).

58 Konig, V., Pfeil, A., Braus, G. H. & Schneider, T. R. Substrate and metal complexes of 3-deoxy-D-*arabino*-heptulosonate 7-phosphate synthase from *Saccharomyces cerevisiae* provide new insights into the catalytic mechanism. *J. Mol. Biol.* **337**, 675-690 (2004).

59 Cross, P. J. *et al. Neisseria meningitidis* expresses a single 3-deoxy-D-*arabino*-heptulosonate 7-phosphate synthase that is inhibited primarily by phenylalanine. *Protein Sci.* **22**, 1087-1099 (2013).

60 Schofield, L. R. *et al.* Substrate ambiguity and crystal structure of *Pyrococcus furiosus* 3-Deoxy-D-*arabino*-heptulosonate 7-phosphate synthase: an ancestral 3-Deoxyald-2-ulosonate-phosphate synthase? *Biochemistry* **44**, 11950-11962 (2005).

61 Light, S. H., Halavaty, A. S., Minasov, G., Shuvalova, L. & Anderson, W. F. Structural analysis of a 3-deoxy-D-*arabino*-heptulosonate 7-phosphate synthase with an N-terminal chorismate mutase-like regulatory domain. *Protein Sci.* **21**, 887-895 (2012).

62 Shumilin, I. A., Bauerle, R., Wu, J., Woodard, R. W. & Kretsinger, R. H. Crystal structure of the reaction complex of 3-deoxy-D-*arabino*-heptulosonate 7-phosphate synthase from *Thermotoga maritima* refines the catalytic mechanism and indicates a new mechanism of allosteric regulation. *J. Mol. Biol.* **341**, 455-466 (2004).

63 Webby, C. J., Patchett, M. L. & Parker, E. J. Characterisation of a recombinant type II 3-deoxy-D-*arabino*-heptulosonate 7-phosphate synthase from *Helicobacter pylori*. *Biochem. J.* **390**, 223-230 (2005).

64 Webby, C. J., Lott, J. S., Baker, H. M., Baker, E. N. & Parker, E. J. Crystallisation and preliminary X-ray crystallographic analysis of 3-deoxy-D-*arabino*-heptulosonate 7-phosphate synthase from *Mycobacterium tuberculosis*. *Acta Crystallogr Sect F Struct Biol Cryst Commun* **61**, 403-406 (2005).

65 Zhou, L. *et al.* Structure and characterisation of the 3-deoxy-D-*arabino*-heptulosonate 7-phosphate synthase from *Aeropyrum pernix*. *Bioorg. Chem.* **40**, 79-86 (2012).

66 Grant, G. A. The ACT domain: a small molecule binding domain and its role as a common regulatory element. *J. Biol. Chem.* **281**, 33825-33829 (2006).

67 Wu, J., Sheflyan, G. Y. & Woodard, R. W. *Bacillus subtilis* 3-deoxy-D-*arabino*-heptulosonate 7-phosphate synthase revisited: resolution of two long-standing enigmas. *Biochem. J.* **390**, 583-590 (2005).

68 Wu, J. & Woodard, R. W. New insights into the evolutionary links relating to the 3-deoxy-D-*arabino*-heptulosonate 7-phosphate synthase subfamilies. *J. Biol. Chem.* **281**, 4042-4048 (2006).

69 Webby, C. J., Baker, H. M., Lott, J. S., Baker, E. N. & Parker, E. J. The structure of 3-deoxy-D-*arabino*-heptulosonate 7-phosphate synthase from *Mycobacterium tuberculosis* reveals a common catalytic scaffold and ancestry for type I and type II enzymes. *J. Mol. Biol.* **354**, 927-939 (2005).

70 Webby, C. J. *Structural & functional characterisation of 3-deoxy-D-arabino-heptulosonate 7-phosphate synthase from Helicobacter pylori & Mycobacterium tuberculosis.* Doctor of Philosophy thesis, Massey University, (2006).

71 Jiao, W., Hutton, R. D., Cross, P. J., Jameson, G. B. & Parker, E. J. Dynamic cross-talk among remote binding sites: the molecular basis for unusual synergistic allostery. *J. Mol. Biol.* **415**, 716-726 (2012).

72 Guilford, W. J., Copley, S. D. & Knowles, J. R. On the mechanism of the chorismate mutase reaction. *J. Am. Chem. Soc.* **109**, 5013-5019 (1987).

73 Zhang, X., Zhang, X. & Bruice, T. C. A definitive mechanism for chorismate mutase. *Biochemistry* **44**, 10443-10448 (2005).

74 Lee, A. Y., Stewart, J. D., Clardy, J. & Ganem, B. New insight into the catalytic mechanism of chorismate mutases from structural studies. *Chemistry and Biology* **2**, 195-203 (1995).

75 Chook, Y. M., Ke, H. & Lipscomb, W. N. Crystal structures of the monofunctional chorismate mutase from *Bacillus subtilis* and its complex with a transition state analog. *Proc. Natl. Acad. Sci. U. S. A.* **90**, 8600-8603 (1993).

76 Lee, A. Y., Karplus, P. A., Ganem, B. & Clardy, J. Atomic structure of the buried catalytic pocket of *Escherichia coli* chorismate mutase. *J. Am. Chem. Soc.* **117**, 3627-3628 (1995).

77 Qamra, R., Prakash, P., Aruna, B., Hasnain, S. E. & Mande, S. C. The 2.15 Å crystal structure of *Mycobacterium tuberculosis* chorismate mutase reveals an unexpected gene duplication and suggests a role in host-pathogen interactions. *Biochemistry* **45**, 6997-7005 (2006).

78 Okvist, M. *et al.* 1.6 A crystal structure of the secreted chorismate mutase from *Mycobacterium tuberculosis*: novel fold topology revealed. *J. Mol. Biol.* **357**, 1483-1499 (2006).

79 MacBeath, G., Kast, P. & Hilvert, D. A small, thermostable, and monofunctional chorismate mutase from the archeon *Methanococcus jannaschii*. *Biochemistry* **37**, 10062-10073 (1998).

80 Gu, W. *et al.* The aroQ and pheA domains of the bifunctional P-protein from *Xanthomonas campestris* in a context of genomic comparison. *Microbial & comparative genomics* **2**, 141-158 (1997).

81 Xue, Y., Lipscomb, W. N., Graf, R., Schnappauf, G. & Braus, G. The crystal structure of allosteric chorismate mutase at 2.2 Å resolution. *Proc. Natl. Acad. Sci. U. S. A.* **91**, 10814-10818 (1994).

82 Sträter, N., Schnappauf, G., Braus, G. & Lipscomb, W. N. Mechanisms of catalysis and allosteric regulation of yeast chorismate mutase from crystal structures. *Structure* **5**, 1437-1452 (1997).

83 Prakash, P., Aruna, B., Sardesai, A. A. & Hasnain, S. E. Purified recombinant hypothetical protein coded by open reading frame Rv1885c of *Mycobacterium tuberculosis* exhibits a monofunctional AroQ class of periplasmic chorismate mutase activity. *J. Biol. Chem.* **280**, 19641-19648 (2005).

84 Sasso, S., Ramakrishnan, C., Gamper, M., Hilvert, D. & Kast, P. Characterisation of the secreted chorismate mutase from the pathogen *Mycobacterium tuberculosis*. *FEBS J.* **272**, 375-389 (2005).

85 Sasso, S. *et al.* Structure and function of a complex between chorismate mutase and DAHP synthase: efficiency boost for the junior partner. *Embo Journal* **28**, 2128-2142 (2009).

86 Kim, S. K. *et al.* A comparative biochemical and structural analysis of the intracellular chorismate mutase (Rv0948c) from *Mycobacterium tuberculosis* H(37)R(v) and the secreted chorismate mutase (y2828) from *Yersinia pestis*. *FEBS J.* **275**, 4824-4835 (2008).

87 Schneider, C. Z., Parish, T., Basso, L. A. & Santos, D. S. The two chorismate Mutases from both *Mycobacterium tuberculosis* and *Mycobacterium smegmatis*: Biochemical analysis and limited regulation of promoter activity by aromatic amino acids. *J. Bacteriol.* **190**, 122-134 (2008).

88 Li, P. P. *et al.* Interaction between DAHP synthase and chorismate mutase endows new regulation on DAHP synthase activity in *Corynebacterium glutamicum*. *Appl. Microbiol. Biotechnol.* **97**, 10373-10380 (2013).

89 Li, P. P., Liu, Y. J. & Liu, S. J. Genetic and biochemical identification of the chorismate mutase from *Corynebacterium glutamicum*. *Microbiology* **155**, 3382-3391 (2009).

90 Liao, H. F., Lin, L. L., Chien, H. R. & Hsu, W. H. Serine 187 is a crucial residue for allosteric regulation of *Corynebacterium glutamicum* 3-deoxy-D-*arabino*-heptulosonate 7-phosphate synthase. *FEMS Microbiol. Lett.* **194**, 59-64 (2001).

91 Blackmore, N. J. *et al.* Three sites and you are out: Ternary synergistic allostery controls aromatic amino acid biosynthesis in *Mycobacterium tuberculosis*. *J. Mol. Biol.* **425**, 1582-1592 (2013).

92 Drury, L. J. *et al.* Monomeric and dimeric CXCL12 inhibit metastasis through distinct CXCR4 interactions and signaling pathways. *Proc. Natl. Acad. Sci. U. S. A.* **108**, 17655-17660 (2011).

93 Lawrence, S. H., Ramirez, U. D., Selwood, T., Stith, L. & Jaffe, E. K. Allosteric inhibition of human porphobilinogen synthase. *J. Biol. Chem.* **284**, 35807-35817 (2009).

94 Mouilleron, S. *et al.* Structural basis for morpheein-type allosteric regulation of *Escherichia coli* glucosamine-6-phosphate synthase: equilibrium between inactive hexamer and active dimer. *J. Biol. Chem.* **287**, 34533-34546 (2012).

95 Panja, S. & Woodson, S. A. Hexamer to monomer equilibrium of *E. coli* Hfq in solution and its impact on RNA annealing. *J. Mol. Biol.* **417**, 406-412 (2012).

96 Pretel, E., Camporeale, G. & de Prat-Gay, G. The non-structural NS1 protein unique to respiratory syncytial virus: a two-state folding monomer in quasi-equilibrium with a stable spherical oligomer. *PLoS One* **8**, e74338 (2013).

97 Trempe, J. F., Shenker, S., Kozlov, G. & Gehring, K. Self-association studies of the bifunctional N-acetylglucosamine-1-phosphate uridyltransferase from *Escherichia coli*. *Protein Sci.* **20**, 745-752 (2011).

98 Freyer, M. W. & Lewis, E. A. Isothermal titration calorimetry: experimental design, data analysis, and probing macromolecule/ligand binding and kinetic interactions. *Methods Cell Biol.* **84**, 79-113 (2008).

99 Grossoehme, N. E., Spuches, A. M. & Wilcox, D. E. Application of isothermal titration calorimetry in bioinorganic chemistry. *J Biol Inorg Chem* **15**, 1183-1191 (2010).

100 Lewis, E. A. & Murphy, K. P. Isothermal titration calorimetry. *Methods Mol. Biol.* **305**, 1-15 (2005).

101 Konarev, P. V., Volkov, V. V., Sokolova, A. V., Koch, M. H. J. & Svergun, D. I. PRIMUS: a Windows PC-based system for small-angle scattering data analysis. *J. Appl. Crystallog.* **36**, 1277-1282 (2003).

102 Svergun, D. Determination of the regularisation parameter in indirect-transform methods using perceptual criteria. *J. Appl. Crystallog.* **25**, 495-503 (1992).

103 Svergun, D., Barberato, C. & Koch, M. H. J. CRYSOL - a program to evaluate X-ray solution scattering of biological macromolecules from atomic coordinates. *J. Appl. Crystallog.* **28**, 768-773 (1995).

104 Fischer, H., de Oliveira Neto, M., Napolitano, H. B., Polikarpov, I. & Craievich, A. F. Determination of the molecular weight of proteins in solution from a single small-angle X-ray scattering measurement on a relative scale. *J. Appl. Crystallog.* **43**, 101-109 (2010).

105 Gasteiger, E. *et al.* in *The proteomics protocols handbook* Ch. 52, 571-607 (Humana Press, 2005).

106 Scott, D. J. & Schuck, P. in *Analytical ultracentrifugation: techniques and methods* (eds David J. Scott, Stephen E. Harding, & Arthur J. Rowe) 1-25 (The Royal Society of Chemistry, 2005).

107 Schuck, P., Perugini, M. A., Gonzales, N. R., Howlett, G. J. & Schubert, D. Size-distribution analysis of proteins by analytical ultracentrifugation: strategies and application to model systems. *Biophys. J.* **82**, 1096-1111 (2002).

108 Golemis, E. *Protein-protein interactions : a molecular cloning manual*. (Cold Spring Harbor Laboratory Press, 2002).

109 Ralston, G. *Introduction to analytical ultracentrifugation*. (Beckham, unknown).

110 Greenfield, N. J. Using circular dichroism spectra to estimate protein secondary structure. *Nat Protoc* **1**, 2876-2890 (2006).

111 Atkins, P. & de Paula, J. *Elements of physical chemistry*. Fourth edn, (Oxford University Press, 2005).

112 Okvist, M., Sasso, S., Roderer, K., Kast, P. & Krengel, U. A novel noncovalent complex of chorismate mutase and DAHP synthase from *Mycobacterium tuberculosis*: protein purification, crystallisation and X-ray diffraction analysis. *Acta Crystallograph. Sect. F-Struct. Biol. and Cryst. Commun.* **65**, 1048-1052 (2009).

113 Vagenende, V., Yap, M. G. & Trout, B. L. Mechanisms of protein stabilisation and prevention of protein aggregation by glycerol. *Biochemistry* **48**, 11084-11096 (2009).

114 Taira, K. & Benkovic, S. J. Evaluation of the importance of hydrophobic interactions in drug-binding to dihyrdrofolate-reductase. *J. Med. Chem.* **31**, 129-137 (1988).

115 Jiao, W. *The use of moelcular modelling to study enzymic action* PhD thesis, Univerisity of Canterbury, (2011).

116 Bennett, B. D. *et al.* Absolute metabolite concentrations and implied enzyme active site occupancy in *Escherichia coli*. *Nat. Chem. Biol.* **5**, 593-599 (2009).

117 Nguyen Bich, N. *et al.* Structural basis for the influence of a single mutation K145N on the oligomerization and photoswitching rate of Dronpa. *Acta Crystallogr D Biol Crystallogr* **68**, 1653-1659 (2012).

118 Maity, A. *et al.* Adaptability in protein structures: structural dynamics and implications in ligand design. *J. Biomol. Struct. Dyn.* **33**, 298-321 (2015).

119 Kantrowitz, E. R. Allostery and cooperativity in *Escherichia coli* aspartate transcarbamoylase. *Arch. Biochem. Biophys.* **519**, 81-90 (2012).

120 Ciaccio, C., Coletta, A., De Sanctis, G., Marini, S. & Coletta, M. Cooperativity and allostery in haemoglobin function. *IUBMB Life* **60**, 112-123 (2008).

121 Petit, C. M., Zhang, J., Sapienza, P. J., Fuentes, E. J. & Lee, A. L. Hidden dynamic allostery in a PDZ domain. *Proc. Natl. Acad. Sci. U. S. A.* **106**, 18249-18254 (2009).

122 Estabrook, R. A. *et al.* Statistical coevolution analysis and molecular dynamics: identification of amino acid pairs essential for catalysis. *Proc. Natl. Acad. Sci. U. S. A.* **102**, 994-999 (2005).

123 Bradley, M. J., Chivers, P. T. & Baker, N. A. Molecular Dynamics Simulation of the *Escherichia coli* NikR Protein: Equilibrium Conformational Fluctuations Reveal Interdomain Allosteric Communication Pathways. *J. Mol. Biol.* **378**, 1155-1173 (2008).

124 Süel, G. M., Lockless, S. W., Wall, M. A. & Ranganathan, R. Evolutionarily conserved networks of residues mediate allosteric communication in proteins. *Nat. Struct. Biol.* **10**, 59-69 (2003).

125 Lockless, S. W. & Ranganathan, R. Evolutionarily conserved pathways of energetic connectivity in protein families. *Science* **286**, 295-299 (1999).

126 Reichau, S. *Inhibition and regulation of Mycobacterium tuberculosis 3-deoxy-D-arabino-heptulosonate 7-phosphate synthase* PhD thesis, University of Canterbury, (2013).

127 Laskowski, R. A. *et al.* PDBsum: a Web-based database of summaries and analyses of all PDB structures. *Trends Biochem. Sci.* **22**, 488-490 (1997).

128 Palmer, T. *Enzymes: Biochemistry, biotechnology and clinical chemistry*. 1st edn, (Horwood Publishing LTD, 2001).

129 Entus, R., Poling, M. & Herrmann, K. M. Redox regulation of Arabidopsis 3-deoxy-D-*arabino*-heptulosonate 7-phosphate synthase. *Plant Physiol* **129**, 1866-1871 (2002).

130 Zhang, Z. Z. *et al.* Molecular characterisation and expression analysis on two isogenes encoding 3-deoxy-D-*arabino*-heptulosonate 7-phosphate synthase in grapes. *Mol. Biol. Rep.* (2010).

131 Weaver, L. M. & Herrmann, K. M. Dynamics of the shikimate pathway in plants. *Trends Plant Sci.* **2**, 346-351 (1997).

132 Schnappauf, G., Hartmann, M., Kunzler, M. & Braus, G. H. The two 3-deoxy-D-*arabino*-heptulosonate 7-phosphate synthase isoenzymes from *Saccharomyces cerevisiae* show different kinetic modes of inhibition. *Arch. Microbiol.* **169**, 517-524 (1998).

133 Shumilin, I. A., Kretsinger, R. H. & Bauerle, R. Purification, crystallisation, and preliminary crystallographic analysis of 3-deoxy-D-*arabino*-heptulosonate-7-phosphate synthase from *Escherichia coli*. *Proteins* **24**, 404-406 (1996).

134 Wu, J., Howe, D. L. & Woodard, R. W. *Thermotoga maritima* 3-deoxy-D-*arabino*-heptulosonate 7-phosphate (DAHP) synthase - The ancestral eubacterial DAHP synthase? *J. Biol. Chem.* **278**, 27525-27531 (2003).

135 Meyer, E. & Switzer, R. L. Regulation of *Bacillus subtilis* glutamine phosphoribosylpyrophosphate amidotransferase activity by end products. *J. Biol. Chem.* **254**, 5397-5402 (1979).

136 Popovych, N., Sun, S., Ebright, R. H. & Kalodimos, C. G. Dynamically driven protein allostery. *Nat. Struct. Mol. Biol.* **13**, 831-838 (2006).

137 Kern, D. & Zuiderweg, E. R. The role of dynamics in allosteric regulation. *Curr. Opin. Struct. Biol.* **13**, 748-757 (2003).

138 Ota, N. & Agard, D. A. Intramolecular signaling pathways revealed by modeling anisotropic thermal diffusion. *J. Mol. Biol.* **351**, 345-354 (2005).

139 Gandhi, P. S., Chen, Z., Mathews, F. S. & Di Cera, E. Structural identification of the pathway of long-range communication in an allosteric enzyme. *Proc. Natl. Acad. Sci. U. S. A.* **105**, 1832-1837 (2008).

140 Nussinov, R., Ma, B. & Tsai, C. J. A broad view of scaffolding suggests that scaffolding proteins can actively control regulation and signaling of multienzyme complexes through allostery. *Biochim. Biophys. Acta* **1834**, 820-829 (2013).

141 Srere, P. A. & Ovadi, J. Enzyme-enzyme interactions and their metabolic role. *FEBS Lett.* **268**, 360-364 (1990).

142 Srere, P. A. Complexes of sequential metabolic enzymes. *Annu. Rev. Biochem.* **56**, 89-124 (1987).

143 Friedrich, P. & Hajdu, J. An overview of supramolecular enzyme organisation. *Biochem. Soc. Trans.* **15**, 973-977 (1987).

144 Kim, H. J., Khalimonchuk, O., Smith, P. M. & Winge, D. R. Structure, function, and assembly of heme centers in mitochondrial respiratory complexes. *Biochim. Biophys. Acta* **1823**, 1604-1616 (2012).

145 Efremov, R. G. & Sazanov, L. A. The coupling mechanism of respiratory complex I - a structural and evolutionary perspective. *Biochim. Biophys. Acta* **1817**, 1785-1795 (2012).

146 Makino, D. L., Halbach, F. & Conti, E. The RNA exosome and proteasome: common principles of degradation control. *Nat. Rev. Mol. Cell Biol.* **14**, 654-660 (2013).

147 Kruger, B. *et al.* Metabolic adaptation and protein complexes in prokaryotes. *Metabolites* **2**, 940-958 (2012).

148 An, S., Kyoung, M., Allen, J. J., Shokat, K. M. & Benkovic, S. J. Dynamic regulation of a metabolic multi-enzyme complex by protein kinase CK2. *J. Biol. Chem.* **285**, 11093-11099 (2010).

149 Storey, K. B. in *Functional Metabolism* 383-413 (John Wiley & Sons, Inc., 2005).

150 Danielson, M. A. & Falke, J. J. Use of 19F NMR to probe protein structure and conformational changes. *Annu. Rev. Biophys. Biomol. Struct.* **25**, 163-195 (1996).

151 Wüthrich, K. Protein structure determination in solution by NMR spectroscopy. *J. Biol. Chem.* **265**, 22059-22062 (1990).

152 Bode, B. E., Dastvan, R. & Prisner, T. F. Pulsed electron-electron double resonance (PELDOR) distance measurements in detergent micelles. *J Magn Reson* **211**, 11-17 (2011).

153 Truong, K. & Ikura, M. The use of FRET imaging microscopy to detect protein-protein interactions and protein conformational changes *in vivo*. *Curr. Opin. Struct. Biol.* **11**, 573-578 (2001).

154 Stryer, L. Fluorescence energy transfer as a spectroscopic ruler. *Annu. Rev. Biochem.* **47**, 819-846 (1978).

155 The PyMOL molecular graphics system v. 1.5 (2011).

156 Kapust, R. B. *et al.* Tobacco etch virus protease: mechanism of autolysis and rational design of stable mutants with wild type catalytic proficiency. *Protein Eng.* **14**, 993-1000 (2001).

157 Gasteiger, E. *et al.* ExPASy: the proteomics server for in-depth protein knowledge and analysis. *Nucleic Acids Res.* **31**, 3784-3788 (2003).

158 Bradford, M. M. A rapid and sensitive method for the quantitation of microgram quantities of protein utilizing the principle of protein-dye binding. *Anal. Biochem.* **72**, 248-254 (1976).

159 Mertens, H. D. & Svergun, D. I. Structural characterisation of proteins and complexes using small-angle X-ray solution scattering. *J. Struct. Biol.* **172**, 128-141.

160 Mills, R. D. *et al.* Domain organisation of the monomeric form of the Tom70 mitochondrial import receptor. *J. Mol. Biol.* **388**, 1043-1058 (2009).

161 Schuck, P. Size-distribution analysis of macromolecules by sedimentation velocity ultracentrifugation and Lamm equation modeling. *Biophys. J.* **78**, 1606-1619 (2000).

162 Laue, T. M., Shah, D. B., Ridgeway, T. M. & Pelletier, S. L. in *Analytical ultracentrifugation in biochemistry and polymer science* 90-125 (The Royal Society of chemistry, 1992).